

UNIVERSITY OF CALIFORNIA

Los Angeles

Synthesis of Metal Complexes Supported by Ferrocene-based Ligands for Tandem Catalysis and
Applications toward Liquid Cell Quantum Sensing

A dissertation submitted in partial satisfaction of the
requirements for the degree of Doctor of Philosophy
in Chemistry

by

Yi Shen

2023

© Copyright by

Yi Shen

2023

ABSTRACT OF THE DISSERTATION

Synthesis of Metal Complexes Supported by Ferrocene-based Ligands for Tandem Catalysis and Applications toward Liquid Cell Quantum Sensing

by

Yi Shen

Doctor of Philosophy in Chemistry

University of California, Los Angeles, 2023

Professor Paula L. Diaconescu, Chair

Developing methodologies to synthesize high-value products efficiently from simple substrates with control over the reactivity and selectivity is highly favored by the chemical industry. Employing assisted tandem catalysis, where serial reactions can be carried out in one pot, to achieve streamlined complex syntheses significantly reduces the number of steps and waste. Harnessing spatial and temporal control in catalysis enables approaches toward one-pot transformations and allows the integration of several catalytic processes. Ferrocene-based ligand-supported metal complexes represent a promising class of catalysts that can incorporate redox control over catalytic processes. We have developed a redox-controlled selective hydroamination reaction catalyzed by (thiolfan*)Zr(NEt₂)₂ (thiolfan*= 1, 1'-bis (2,4-di-*tert*-butyl-6-thiophenoxy)

ferrocene). *In situ* switching of the catalyst's state during the reaction enables selectivity toward different substrates (Chapter 2).

Incorporating the greenhouse gas CO₂ into N-carboxyanhydrides (NCAs) followed by subsequent NCA utilization illustrates the possibility of integrating two synthetic steps in one vessel to afford a valuable material with possible CO₂ recycling. To demonstrate the immense potential of integrating multi-step transformations in one pot, we developed a set of sustainable conditions for NCA synthesis (Chapter 3). Moreover, several metal catalysts supported by ferrocene-based ligands were found to catalyze NCA polymerization in the presence of a co-catalyst. To establish an integrated system composed of two incompatible processes, we aimed to compartmentalize the active reagents for each step. The structure of the ferrocene-based pro-ligand was modified for surface anchoring. Our efforts toward immobilizing ferrocene-supported metal catalysts onto conductive surfaces pave the way of achieving spatiotemporal control over the processes of NCA synthesis and polymerization (Chapter 4).

In addition to the redox-switchable characteristic, ferrocene-based compounds provide a unique platform to support lanthanides and engender distinctive optical properties to them. We synthesized and characterized a series of ytterbium complexes displaying an ultra-narrow absorption in the ultraviolet-visible (UV-Vis) region. The extraordinarily narrow linewidth observed for (thiolfan)YbCl(THF) (thiolfan = 1,1'-bis(2,4-di-*tert*-butyl-6-thiomethylenephenoxy)ferrocene) allows us to investigate its applications toward magnetic field and liquid cell quantum sensing (Chapter 5).

The dissertation of Yi Shen is approved.

Justin R. Caram

Yu Huang

Chong Liu

Paula L. Diaconescu, Committee Chair

University of California, Los Angeles

2023

TABLE OF CONTENT

ACKNOWLEDGMENTS	x
VITA.....	xiv
Chapter 1. Introduction.....	1
1.1 One-pot strategy toward integrating multiple transformations and applications in polymerization	1
1.2 Spatiotemporal control and switchable catalysis	6
1.3 Summary of this work.....	11
Chapter 2. Zirconium complexes supported by a ferrocene-based ligand as redox switches for hydroamination reactions.....	14
2.1 Introduction.....	14
2.2 Results and discussion	18
2.3 Conclusion and outlook	25
2.4 Experimental section.....	26
2.5 Appendix A.....	34
Chapter 3. Synthesis of <i>N</i> -carboxyanhydrides from <i>ortho</i> -aromatic amino acids and CO ₂	78
3.1 Introduction.....	78
3.2 Results and discussion	83
3.3 Conclusion and outlook	92
3.4 Experimental section.....	93
3.5 Appendix B	107
Chapter 4. Surface immobilization of ferrocene-based compounds.....	111
4.1 Introduction.....	111

4.2	Results and discussion	114
4.3	Conclusion and outlook	131
4.4	Experimental section.....	132
4.5	Appendix C	149
Chapter 5. Ytterbium(III) complexes with ultra-narrow absorption: steps toward magnetic field and liquid cell quantum sensing.....		202
5.1	Introduction.....	202
5.2	Results and discussion	207
5.3	Conclusion and outlook	220
5.4	Experimental section.....	221
5.5	Appendix D.....	226
References.....		245

LIST OF FIGURES, SCHEMES, CHARTS, AND TABLES

Figure 1.1.....	3
Figure 1.2.....	6
Figure 1.3.....	7
Figure 1.4.....	8
Figure 1.5.....	10
Figure 2.1.....	14
Figure 2.2.....	15
Figure 2.3.....	16
Scheme 2.1.....	19
Figure 2.4.....	20
Table 2.1.....	22
Scheme 2.2.....	24
Figure 2.5.....	25
Figure 3.1.....	79
Figure 3.2.....	80
Figure 3.3.....	81
Figure 3.4.....	83
Scheme 3.1.....	84
Table 3.1.....	85
Table 3.2.....	86
Figure 3.5.....	89
Figure 3.6.....	90

Figure 3.7	91
Figure 4.1	112
Figure 4.2	114
Figure 4.3	116
Scheme 4.1	116
Figure 4.4	117
Figure 4.5	118
Table 4.1	119
Scheme 4.2	120
Figure 4.6	123
Figure 4.7	126
Figure 4.8	129
Figure 4.9	131
Figure 4.10	132
Figure 5.1	204
Figure 5.2	205
Figure 5.3	206
Scheme 5.1	208
Figure 5.5	210
Figure 5.6	212
Figure 5.7	213
Figure 5.8	214
Figure 5.9	217

ACKNOWLEDGMENTS

After completing the writing of the main body of this dissertation, I realized that my journey of graduate study is approaching the end. Every piece of knowledge I acquired during this process holds immense value, and I will cherish the memories of the challenges I faced throughout this path. The sleepless nights, the setbacks in experiments, the unexpected results, the skeptical voice from others and myself, and the moments of exhaustion that made me stand in front of my glovebox in tears; these memories will stay with me. However, amidst the struggles, there were also moments that sparked brightly in my memory. The satisfaction of solving a difficult problem, the joy of uncovering a solution to a puzzling experiment, the thrill of obtaining a beautiful crystal, the pride of presenting my work before a diverse audience, and the elation of publishing a paper. I experienced both hardships and triumphs, much like many others on this journey. Yet, despite the challenges, I wholeheartedly enjoyed every aspect of it. As I look back, I realized how far I have come to reach this point. It would have been impossible without the invaluable help and support I received from the people around me.

I received the most support from my Ph.D. advisor, Paula. There were many moments when I felt I was lost in my research and my life. She is the one who brought me back on track. She exemplifies exceptional patience in her interactions with students and offers meticulous guidance to everyone she mentors. Her words about graduate study being a transformative learning process, shaping aspiring scientists into both skilled researchers and better individuals, remain etched in my mind. Undoubtedly, Paula's mentorship has played a vital role in shaping the scientist I am today, as I owe nearly all my knowledge of scientific approaches to her invaluable teaching. Paula taught me to possess self-confidence and be fearless to stand in front of people, shaping me from a timid girl into a confident scientist.

My other genius co-advisor Chong also provided me with endless support in my graduate study. He is always willing to lend a patient ear to my grievances, whether they pertained to science or life. Undeniably, he stands among the most brilliant individuals I have encountered, yet he possesses a remarkable balance of intelligence, warmth, and empathy. He dedicates himself to resolving students' challenges to the best of his abilities. I am deeply grateful for his intellectual guidance and the overall support he provided.

I also appreciate the guidance and help I received from my other committee members Prof. Justin R. Caram and Prof. Yu Huang. The pieces of advice I received during my second-year oral examination from Justin and Prof. Huang remain in my memory. Their guidance was invaluable as they encouraged me to adopt a broader perspective when approaching my research and to consider long-term planning for my future. I also appreciate the collaborations with professors from outside institutions. I received invaluable advice from Prof. Loi Do, Prof. Jeffery A. Byers, Prof. Dunwei Wang, and Prof. Alex Miller that reinforced my scientific skills in many aspects.

I want to express my sincere gratitude to previous group members for their unwavering support and willingness to lend a helping hand at all times. Dr. Scott Shepard, my undergraduate mentor, directed me into scientific research. I started becoming an independent researcher following his guidance. Dr. Junnian Wei, Dr. Stephanie Quan, Dr. Jonathan Brosmer, and Dr. Mark Abubekеров provided me with invaluable assistance in the lab. Their expertise and willingness to share knowledge have been instrumental in advancing my scientific understanding. I am also indebted to Dr. Ruxi Dai, Dr. Amy Lai, and Dr. Zach Hern for their guidance, support, and expertise generously shared throughout this journey. I am also incredibly grateful to our current group members for their encouragement and willingness to help. Shiyun, Jenny, George, Hootan, Ramzi, and Joon are excellent co-workers in the lab as they are always responsible for

their jobs and share great ideas on research. Working alongside them has been a source of inspiration and motivation. I also want to thank my undergraduate mentee Varit, who worked with me for three years and contributed a lot to our research. I would also like to mention the visiting scholars Dr. Shuangshuang Li, Dr. Marc Martinez de Sarasa, Arnaud Savoy, Fuyan Ma, and Sisheng Shu; I am grateful for their kind support.

Besides group members, I received emotional and intellectual support from people outside our group. Special thanks to Dr. Shuangning Xu, who I always turn to for help. Throughout our interactions, he has generously shared his knowledge, experience, and insight, providing me with valuable direction and support at every step of my journey. I am immensely grateful to Dr. Xun Guan, Dr. Shengtao Lu, Dr. Danlei Xiang, and Brandon Jolly for their kindness and help along the way. I am genuinely thankful to Dr. Chengzhang Wan, Dr. Xin Mu, and Dr. Xinke Wang. I received invaluable guidance from them, and I am truly grateful for the privilege of learning from these exceptional scientists. Additionally, I received exceptional guidance from my mentors during my internship at *Eli Lilly*. Dr. Tao Liu and Dr. Sarah Anthony taught me how to conduct scientific research in industry, differently than the way I learned in the lab. I sincerely appreciate their generosity and invaluable advice.

I had a great experience working with exceptional collaborators within and outside UCLA, and I would like to acknowledge their efforts. Dr. Christopher J. Reed from CalTech performed the Mössbauer characterization in Chapter 2. Dr. Thi V. Tran co-authored the manuscript and Hieu D. Nguyen from Do Lab at UH contributed to the experiment development and optimization in Chapter 3. Thanks to Dr. Matthew Thompson, Connor Gallin, and Kexing Xiao from the Byers group, Dr. Haochuan Zhang from the Wang group at BC for intellectual support, and James Wilkes for preparing coated electrode plates in Chapter 4. Thanks to Yu Mu from the Wang group for the

help in preparing the published review related to Chapter 4. Thanks to Dr. Leyuan Zhang for the Raman spectroscopy characterization in Chapter 4. Dr. Ashley Shin, Dr. Changling Zhao, and Claire E. Dickerson contributed to the spectroscopy and computational studies in Chapter 5 and co-authored the submitted manuscript. Special thanks to Dr. Paul H. Oyala at CalTech who helped with the EPR studies in Chapter 2 and Chapter 5. Without his dedication, those studies would have been impossible to conduct.

I also received a tremendous amount of help from technicians and staff at UCLA. Many thanks to Dr. Robert (Bob) Taylor and Dr. Ta-Chung (TC) Ong for NMR spectroscopy training and advice. Dr. Greg Khitrov provided insightful suggestions and helped with mass spectrometry characterizations. Dr. Chong Hyun (Paul) Chang performed ICP-MS analysis for the research conducted in Chapter 4 and Chapter 5. Dr. Ignacio Martini provided training and insightful suggestions on SQUID, IR, SEC, and many other techniques. I sincerely appreciate their help and dedication.

Last but not least, I want to thank my family and friends whom I can always count on. They got my back no matter what. My mom is the most powerful woman I know. She raised my sister and me amidst numerous struggles that I could not imagine dealing with on my own. Her love and sacrifice make her my ultimate role model and hero. My dear friends, who have been by my side throughout this journey and have become integral to it, provided me with encouragement, companionship, and support. I am grateful to have them in my life. Finally, I want to dedicate this work to my dad, who unfortunately could not witness this today, but his encouragement drives me to do my best. To my loved ones and all those who supported me during my graduate studies, I want to extend my appreciation. Without your unwavering support, I would not be standing where I am today. Thank you for being with me every step of the way.

VITA

EDUCATION

University of California Los Angeles
Ph.D. Candidate 2020 - present
Advisor: Prof. Paula Diaconescu Co-advisor: Prof. Chong Liu
University of California Los Angeles
Master of Science 2018
Advisor: Prof. Paula Diaconescu
University of California Los Angeles
Bachelor of Science 2017
Major: Chemistry; GPA: 3.83/4.0

AWARDS

UCLA Chemists Association Dissertation Award 2023
UCLA John Alan Walker Excellence in Research Award 2022
UCLA Jim and Barbara Tsay Excellence in Second Year Research
and Academics Awards 2021
UCLA INFEWS Graduate Traineeship 2018 - present
UCLA Graduate Dean's Scholar Award 2018 - 2020
UCLA Stone Award 2019
UCLA Ethel Terry McCoy Award for Excellence in Chemistry
and Biochemistry 2018
UCLA Departmental Honors 2018
UCLA Raymond & Dorothy Wilson Research Scholar 2017
UCLA Departmental Scholar 2017
UCLA Honors Program 2017
Eleanor Barry Memorial Scholarship 2014 - 2017

INTERNSHIP AND SCHOLARSHIP

Eli Lilly
Intern 2022 Jun - Sep
NSF INFEWS Program
Trainee 2018 - present
CalTeach UCLA
Intern 2015

PUBLICATIONS

Deng, S.; **Shen, Y.**; Chantranuwathana, V.; Nguyen, H. D.; Tran, T. V.; Vasquez, K.; Byers, J.; Do, L. H.; Diaconescu, P. L., **ortho-Aromatic polyamides by ring-opening polymerization of N-carboxyanhydrides, submitted.**

Li, S.; Davis, A. R.; Adhami, N.; Roshandel, H.; **Shen, Y.**; Co, N.; Liu, Y.; Diaconescu, P. L., **Application of a ferrocene-chelating heteroscorpionate ligand in nickel mediated radical polymerization, revision requested.**

Shin, A. J.;* Zhao, C.;* **Shen, Y.**;* Dickerson, C.;* Li, B.; Bim, D.; Atallah, T. L.; Oyala, P. H.; He, Y.; Roshandel, H.; Alson, L. K.; Alexandrova, A. N.; Diaconescu, P. L.; Campbell, W. C.; Caram, J. R., **Toward liquid cell quantum sensing: Ytterbium (III) complexes with ultra-narrow absorption, submitted, *authors contributed equally.**

Shen, Y.; Mu, Y.; Wang, D.; Liu, C.; Diaconescu, P. L., **Tuning catalyst reactivity through molecular modification of organometallic complexes on the electrode surface**, *ACS Appl. Mater. Interfaces*. **2023**, *15*, 28851-28878. Tran, T. V.; **Shen, Y.;** Nguyen, H. D.; Deng, S.; Roshandel, H.; Cooper, M. D.; Waston, J. R.; J. Byers, J.; Diaconescu, P. L.; Do, L. H., **N-carboxyanhydrides directly from amino acids and carbon dioxide and their tandem reactions to therapeutic alkaloids**, *Green Chemistry*. **2022**, *24*, 9245-9252.

Lai, A.; Hern, Z. C.; **Shen, Y.;** Dai, R.; Diaconescu, P. L., **Metal complexes for redox switching and control of reactivity**. In *Reference Module in Chemistry, Molecular Sciences and Chemical Engineering*, Elsevier: **2021**.

Shen, Y.; Shepard, S. M.; Reed, C. J.; Diaconescu, P. L., **Zirconium complexes supported by ferrocene-based ligand as redox switches for hydroamination reactions**, *Chem. Commun.* **2019**, *55*, 5587-5590.

Kirlikovali, K. O.; Cho, E.; Downard, T. J.; Grigoryan, L.; Han, Z.; Hong, S.; Jung, D.; Quintana, J. C.; Reynoso, V.; Ro, S.; **Shen, Y.;** Swartz, K.; Sahakyan, E. T.; Wixtrom, A. I.; Yoshida, B.; Rheingold, A. L.; Spokoyny, A. M., **Buchwald–Hartwig amination using Pd(i) dimer precatalysts supported by biaryl phosphine ligands**, *Dalton Trans.* **2018**, *47*, 3684-3688.

Chapter 1. Introduction

1.1 One-pot strategy toward integrating multiple transformations and applications in polymerization

In response to global challenges such as the energy crisis, resource shortage, and environmental pollution, the field of catalysis has emerged as a vital discipline.¹⁻⁴ The development of efficient catalysts with outstanding activity and selectivity in chemical production holds great potential in addressing those societal challenges.^{3, 5-7} Catalysis also plays a pivotal role in achieving sustainable chemistry as it offers the opportunity to leverage renewable feedstocks, minimize waste generation, and optimize the resources utilized.⁸ The field of catalysis has evolved in complexity, including the development of multicatalytic systems to meet the quest for new methodologies to minimize energy and environmental impact while achieving efficient chemical production.¹⁰

Nature laid the foundation of an ideal system where multiple catalysts operate in concert either collaboratively or orthogonally to facilitate a sequence of transformations selectively within living cells.¹¹ Inspired by Nature, scientists strive to harness multicatalytic events in one reaction vessel without intermediate steps.^{5, 11} The one-pot strategy combining multiple transformations holds vast potential to streamline complicated chemical syntheses from simple building blocks to value-added products by undergoing a sequence of precisely staged catalytic steps. The coupling of multiple catalytic transformations leading to a single workup reduces the number of iterations and bypasses the need for tedious purifications, resulting in energy and cost savings.^{5, 10, 12} It also alleviates the burden of isolating unstable intermediates. Therefore, integrated one-pot transformations afford a sustainable approach toward complicated chemical production.^{5, 13, 14}

One-pot reactions encompassing multiple catalytic transformations followed by a single workup have been classified into several sub-categories based on the inspiration from Fogg and Santos,¹² Lohr, and Marks,⁵ and Martínez *et al.* (Figure 1.1).¹⁰ Starting with whether all precatalysts/reagents are present at outset, sequential or isolated catalytic events involve a set of transformations catalyzed by multiple catalysts but require a subsequent addition of the second catalyst after the completion of the previous reaction.^{12, 13} Domino/cascade catalysis implies that while all reagents are present at outset, only one catalytic mechanism is involved, often, only one catalyst is required to carry out a series of reactions. Thus, domino catalysis lies at the edge of multicatalysis but is often included to portray a full picture.¹⁰

Tandem or relay catalysis is defined by sequential transformations of the substrates via two or more mechanistically distinct mechanisms.¹² It is further sub-categorized by the number of catalysts in operation. Auto-tandem catalysis involves two or more mechanistically distinct catalytic cycles promoted by a single catalyst where both catalytic events occur spontaneously.¹² Cooperative interactions among various species are possibly observed in this type of system, however, challenges remain in the design of a multi-functional precatalyst featuring well-controlled catalytic activity for different reactions under the same conditions.¹⁰ On the other hand, assisted tandem catalysis utilizes a single precatalyst to execute two or more reactions via distinct mechanisms. However, an intervention of the catalyst state or mechanism is necessary. The intervention can be triggered by external stimuli including the addition of reagents or change in the reaction conditions.^{10, 12}

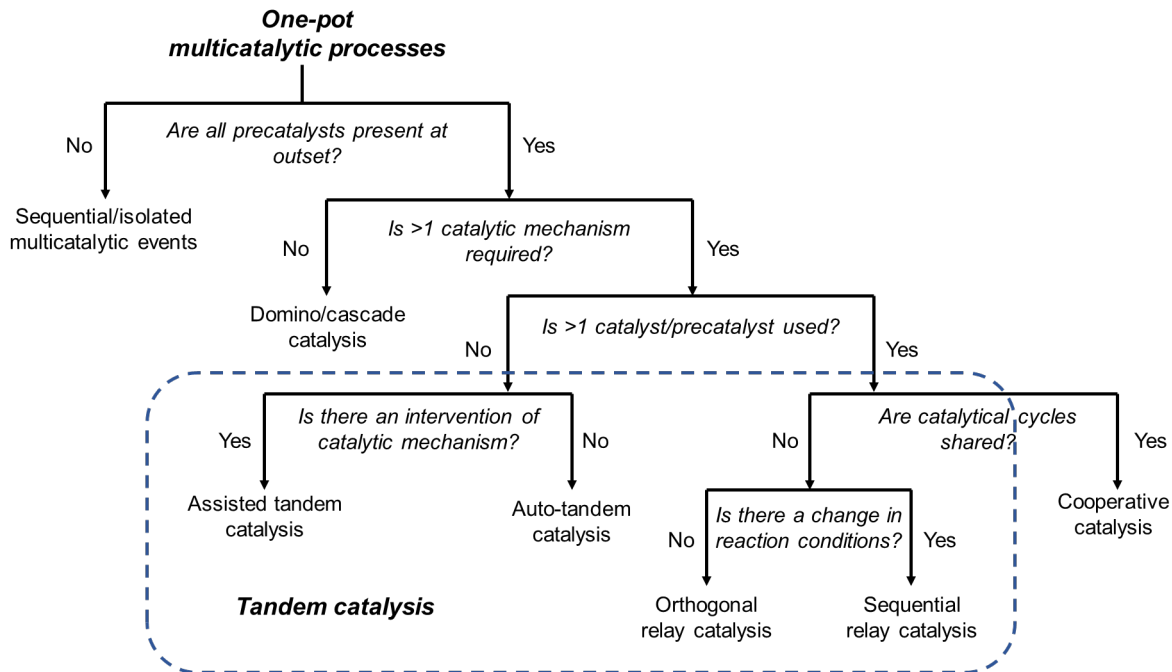


Figure 1.1. Flowchart for classification of one-pot processes.

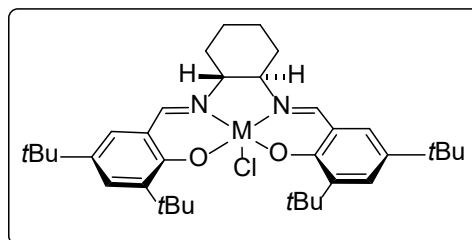
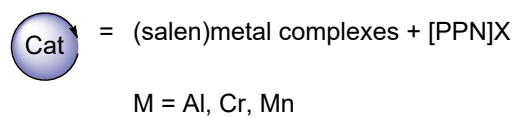
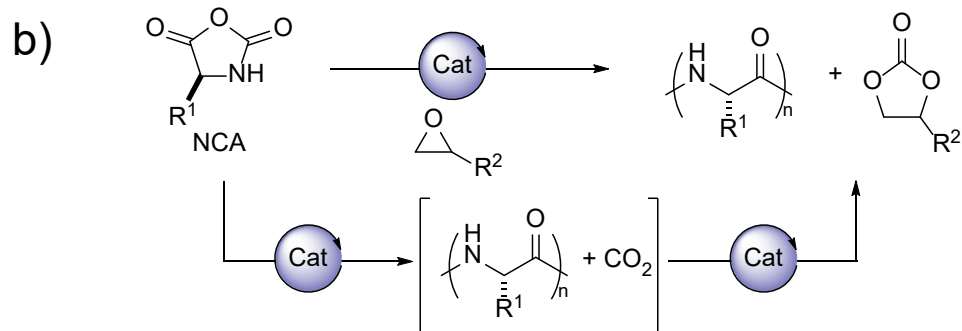
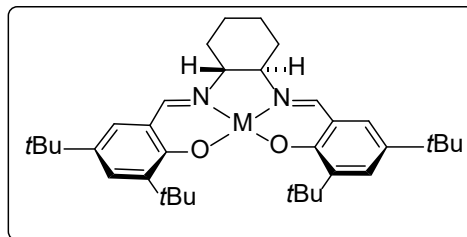
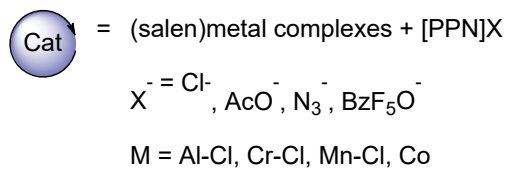
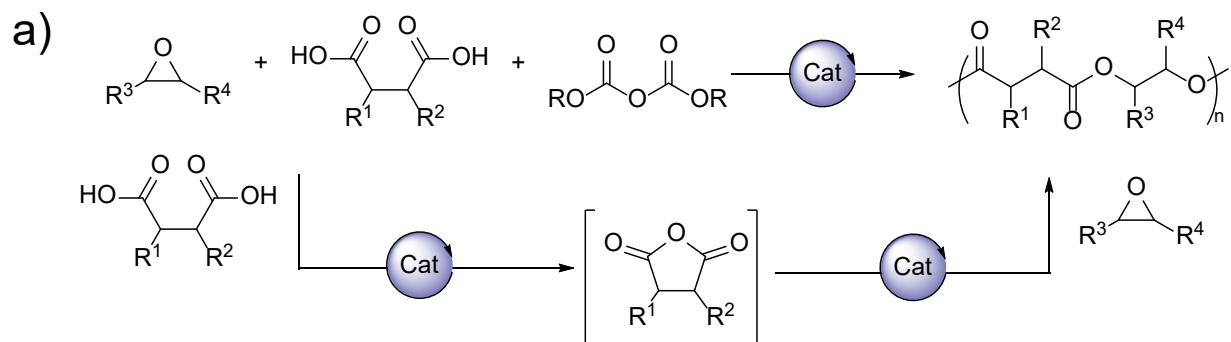
When more than one precatalyst are present at the same time, the process is referred to as orthogonal tandem catalysis.⁵ Orthogonal tandem catalysis implies that at least two catalysts are present and active from the start and they effect one set of the multicatalytic processes via non-interfering catalytic cycles.^{5, 10} In some scenarios, a change in reaction conditions is required to activate the second catalyst, referred to as sequential relay catalysis. A synergy between two catalytic cycles to execute one single reaction with shared intermediates refers to cooperative catalysis.¹⁰

Despite the various approaches toward one-pot transformations, two key challenges remain in integrating multiple transformations into one pot: selectivity and compatibility. It is pivotal to ensure the species present in the system do not inhibit each other while retaining their respective functionality. Moreover, the reaction rate of each step has to be evaluated so that the components

of one catalytic cycle do not hamper the reaction rate of the other cycle that may lead to undesired decomposition or unproductive side reactions.^{13, 14} Therefore, a novel design of a multicatalytic system requires a comprehensive evaluation of a catalyst's reactivity, reaction conditions, mechanisms involved, compatibility with other catalytic cycles, the order of reactions, as well as possible side reactions during the process.

One-pot polymerization

Nature has elegant examples of tandem catalysis in macromolecule synthesis within living cells via multi-enzymatic transformations.^{15, 16} A similar strategy has been extended towards synthetic polymerization from renewable feedstocks (Figure 1.2).^{14, 15, 17-22} The one-pot approach from bio-based monomers to valuable polymers provides an emerging solution for efficient, practical, and versatile production of bio-derived plastics.¹⁵ The coupling of monomer synthesis with a subsequent polymerization to obtain sustainable material directly from renewable resources circumvents the need to isolate the monomer and overcomes thermodynamic limitations through the formation of polymers, representing energy- and resource-efficient integration of distinct catalytic processes. For instance, the cyclization of bio-derived diacids with epoxides yields cyclic anhydrides with functional diversity, which undergo *in situ* ring-opening polymerization to afford biodegradable polyesters (Figure 1.2a).¹⁸ In another scenario, cyclic carbonates were obtained in tandem with the formation of the polypeptide, capturing CO₂ released from ring-opening polymerization of N-carboxyanhydrides (NCAs) (Figure 1.2b).²² Copolymerization of NCA and lactide (LA) could also be achieved in one pot catalyzed by an aluminum catalyst affording polylactide-polypeptide copolymer with interesting properties (Figure 1.2c).²³



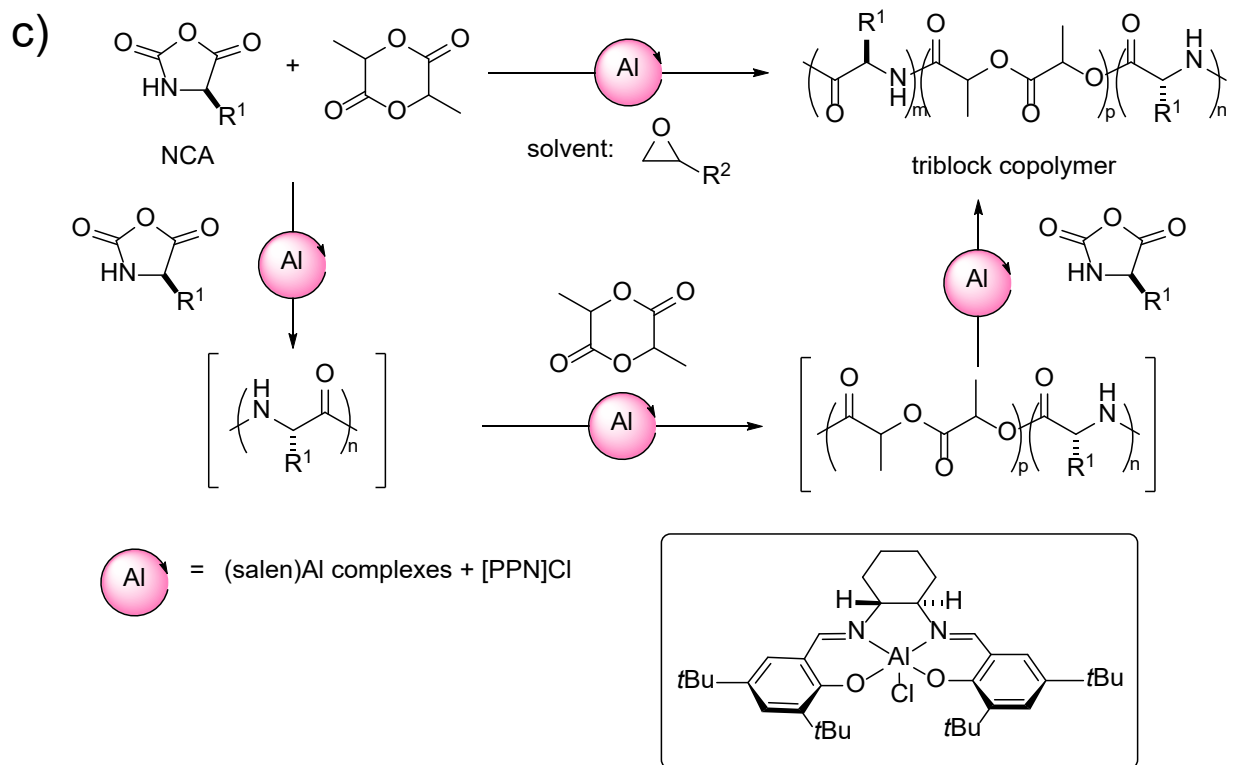


Figure 1.2. One pot synthesis of a) polyesters from epoxides and dicarboxylic acid;¹⁸ b) polypeptides and cyclic carbonates;²² c) copolymer of NCA and lactide.²³ PPN^+ = bis(triphenylphosphine)iminium.

1.2 Spatiotemporal control and switchable catalysis

To implement one-pot strategies towards diverse artificial processes, scientists explored multi-functional catalysts,²⁴⁻²⁸ hybrid catalytic materials,^{9, 16, 29} compartmentalization of incompatible catalysts,³⁰⁻⁴⁰ and switchable catalysts.⁴¹⁻⁵⁰ Except for the rare cases where a multi-functional catalyst or catalytic material is inherently capable of executing consecutive reaction sequences exhibiting exceptional catalytic activity and selectivity without external intervention, the underlying design principle of the current one-pot strategy revolves around achieving spatiotemporal control over the catalytic processes.³¹ Common strategies to address

incompatibility between two catalysts through spatial control focuses on implementing compartmentalization of different type (Figure 1.3). The reagents and catalysts are localized in a confined space through immiscible phases, encapsulated in metal-organic frameworks (MOF), physically separated by membranes, etc. to minimize undesired interference.^{10, 33-38} Physical separation with volatile intermediates being exchanged through the gas phase are also possible.^{30, 51} Solid surfaces such as metal oxides, metal nanoparticles, polymer matrix, and carbon-based material are often exploited to support active sites or to construct hybrid catalytic material.^{39, 52-55}

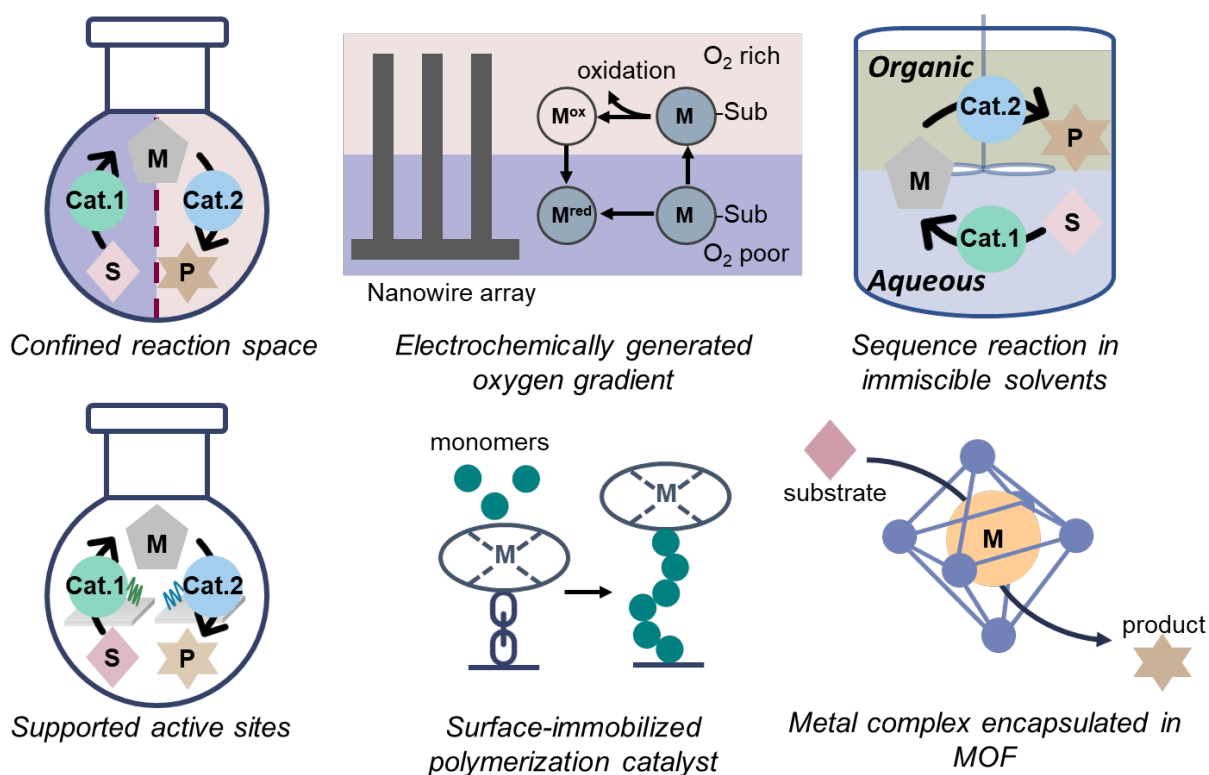


Figure 1.3. Spatial control in one-pot transformations involving different types of compartmentalization strategies.

While spatial control strategies allow catalyst synergy under different reaction conditions, the implementation could be tedious. The circulation of components that are necessary to facilitate

a reaction could be difficult to achieve. On the other hand, temporal control offers a simple approach by allowing sequential addition of reagents to obsolete potential incompatibility. However, it is not suitable for tandem transformations that request all reagents to be present at the outset to proceed, or reactions that require cooperation between steps. Yet, temporal control enabled by switchable catalysts heralds a promising paradigm toward assisted tandem catalysis.^{41, 42, 45, 47, 50, 56} As illustrated in Figure 1.4, a deliberate intervention of the state of a single catalyst through the application of external stimuli results in a switch from one catalytic cycle to the other. Inspired by the exceptional trigger-induced effects, artificial switchable catalysts have been extensively studied incorporating stimuli-responsive features to perform advanced synthetic tasks. The catalytic activity of a single catalyst can be modulated by external stimuli including light, mechanical force, applied potential, and chemical redox reagents, etc.^{41, 42, 44, 57} Judicious combination of switchable catalysts bearing orthogonal activity either toward one reaction or in multiple reactions with external stimulation creates a synthetic platform that could be temporally controlled.

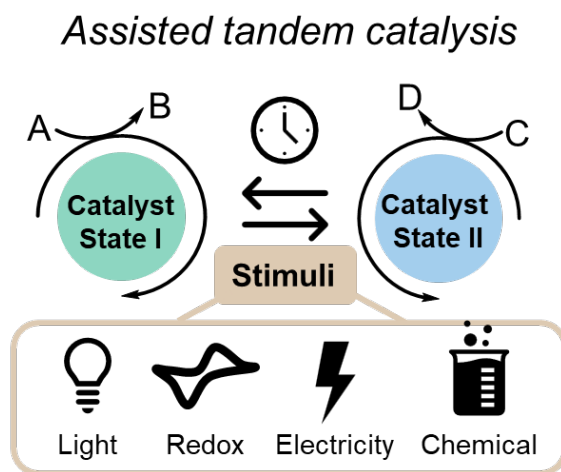


Figure 1.4. Assisted tandem catalysis enabled by stimuli-responsive catalysts.

Switchable polymerization

Among the applications of switchable catalysis, switchable polymerization, emulating the biological process of making sequence-controlled macromolecules, has garnered specific interest. Switchable polymerization holds the potential on increasing the complexity of the obtained structurally diversified material through the incorporation of different building blocks with exceptional control in chemoselectivity, molecular weight, and stereochemistry.^{45, 48, 49, 58-61} Redox switchable polymerization, where the state of a polymerization catalyst can be interconverted via a reversible electron transfer process, results in an alteration of the polymer structure.⁶²⁻⁷¹ Redox control can be achieved based on the oxidation state of the active metal center or manipulations on redox non-innocent supporting ligands of the metal complex. A few examples harnessing redox switchable catalysts in ring-opening polymerization reactions are depicted in **Figure 1.5**.^{62-64, 66, 68, 69, 72-77} It could also be applied to olefin polymerization via ring-opening metathesis, or coordination-insertion.^{64, 65, 67, 71, 78, 79}

Our group has been dedicated to investigating redox switchable ring-opening polymerization with ferrocene-supported metal complexes.⁷²⁻⁸⁴ Followed by the initial report describing the effect of a titanium ferrocene derivative on the rate of lactide polymerization (Figure 1.5a),⁸⁵ our group reported the first examples of on/off switches based on yttrium, indium (Figure 1.5b),⁷² and cerium (Figure 1.5c).⁷³ In the case of the Ti-based system, a difference in the reaction rate of ring-opening polymerization of lactide was observed when using the oxidized (slow) and reduced (fast) catalyst. On the other hand, Y-, In-, and Ce-based systems being developed by the Diaconescu group were able to be completely shut off and turned back on through redox control, enabling our further discovery of obtaining block copolymers leveraging the orthogonal behavior of some of the ferrocene derivatives toward different types of monomers.⁷⁷ Several studies have

been reported on redox switchable copolymerization of lactide, caprolactone, cyclohexene oxide, etc.^{74, 75, 80, 81, 86} Meanwhile, Byers and coworkers conducted research on switching the state of the iron center in the metal catalyst to achieve on/off switch in lactide polymerization. (Figure 1.5d).⁶³ Later, the same scaffold was used to prepare block copolymers.⁶² A similar approach to switching *in situ* between Fe(II) and Fe(III) to modify the rate of polymerization has also been reported by Lang *et al.* (Figure 1.5e).⁸⁷

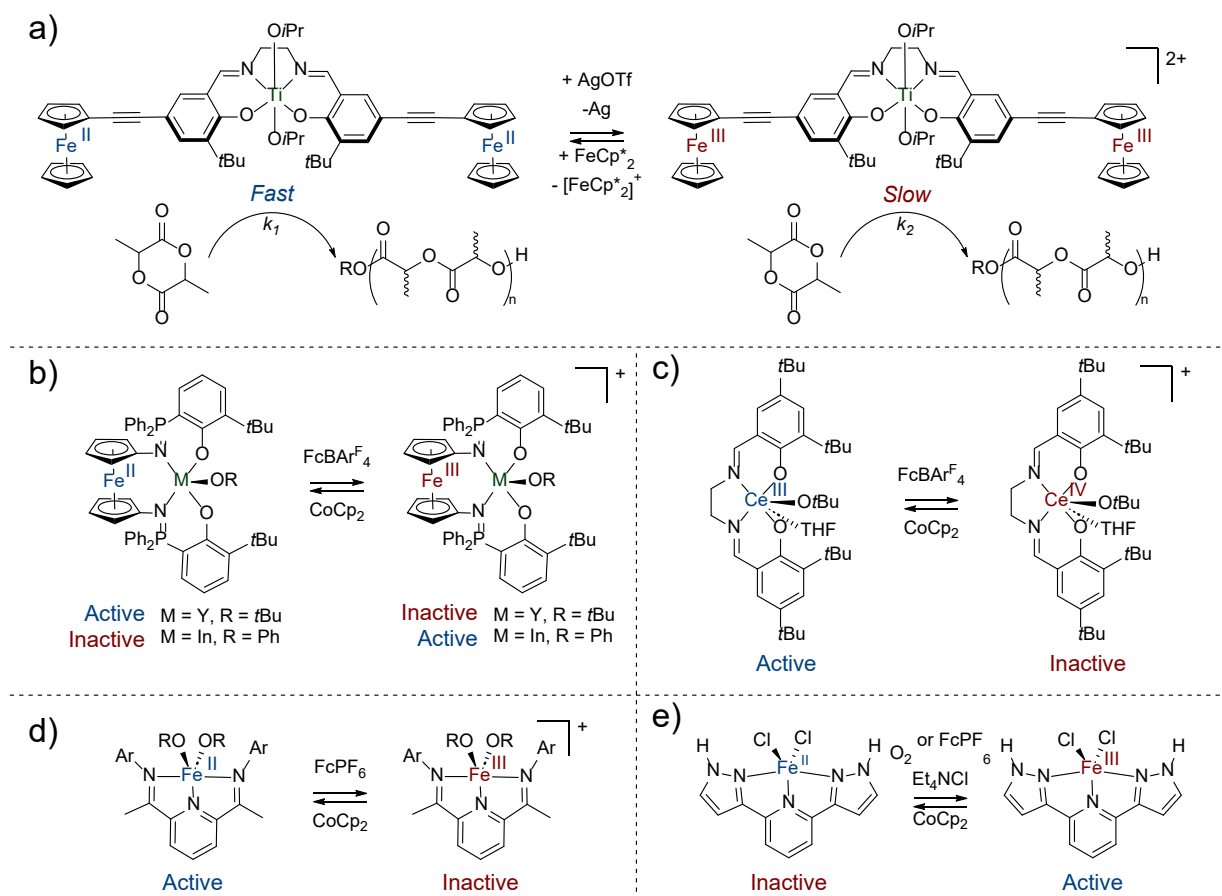


Figure 1.5. Redox-switchable ring-opening polymerization (ROP).⁶⁴ a) Switchable ROP of *rac*-lactide using the Ti-based system;⁸⁵ b) redox switching in the Y- and In-based systems;⁷² c) redox switching in the Ce-based system;⁷³ d), e) redox switching in the Fe-based systems.^{63, 87}

1.3 Summary of this work

In this thesis, we expanded the concept of redox switchable catalysis to small molecule synthesis focusing on hydroamination reactions.⁸⁸ In light of a previous study on redox-controlled hydroalkoxylation reactions,⁸⁹ we developed a ferrocene-based ligand-supported zirconium complex, (thiolfan*)Zr(NEt₂)₂ (thiolfan* = 1, 1'-bis (2,4-di-*tert*-butyl-6-thiophenoxy) ferrocene), and investigated its catalytic activity in selective hydroamination reactions (Figure 1.6).⁸⁸ Orthogonal reactivity was observed for cyclizing primary and secondary aminoalkenes catalyzed by the neutral and oxidized complex, respectively. This work contributes to the field of assisted-tandem catalysis employing a redox switch to achieve temporal control over the reaction.

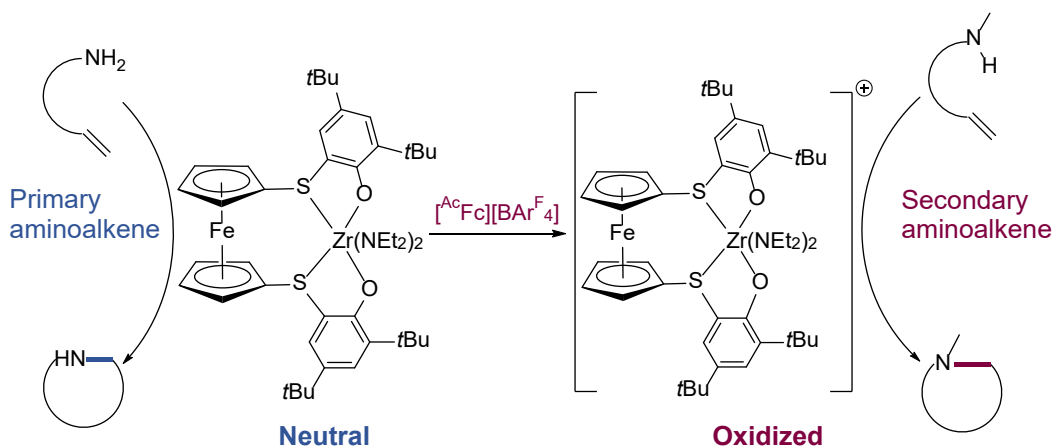


Figure 1.6. A redox-active zirconium complex catalyzes hydroamination reactions selectively.

Moving forward to develop a consecutive one-pot process integrating multi-step transformations in sequence, we attempted to couple NCA synthesis and polymerization. Integrating those two steps allows tandem production of polyamides from amino acid derivatives (Figure 1.7). Our approach started with investigating mild and green conditions to couple amino acid derivatives with CO₂ in order to furnish the necessary monomer,⁹⁰ NCA. Research exploring

the conditions for polymerizing NCA was conducted in the meantime. After the development and optimization of the conditions for each step, we devoted effort to implementing spatial control over the entire reaction sequence through surface immobilization of the catalytic active species. A variety of ferrocene derivatives incorporating surface-anchoring handles were developed for immobilization. Surface functionalization of the designed ferrocene derivatives was investigated through different anchoring methods.

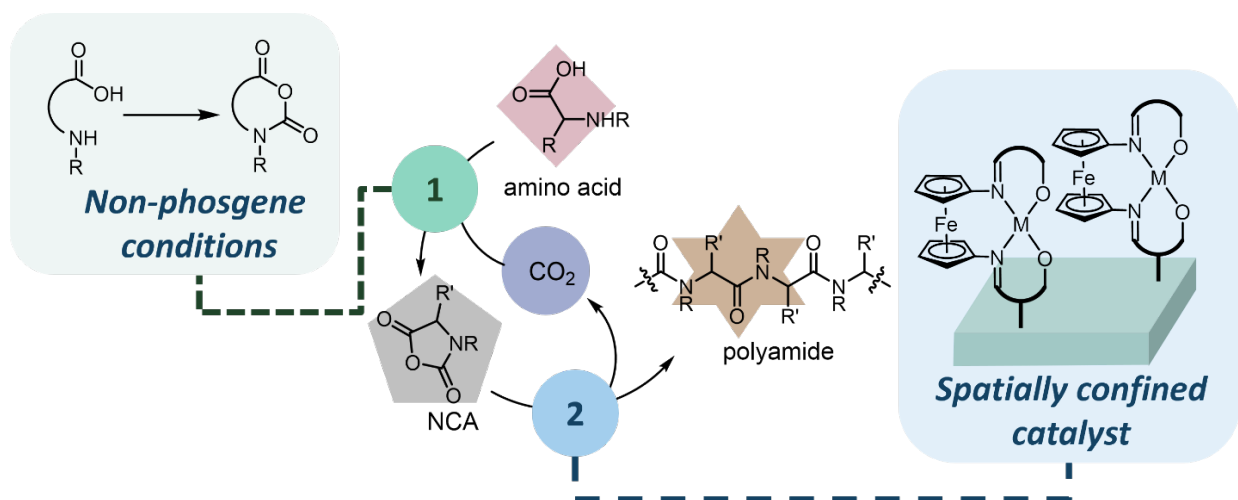


Figure 1.7. Integrating NCA synthesis with subsequent polymerization to obtain polyamide from amino acid.

During the design and development of ferrocene derivatives to achieve temporal and spatial control, we discovered a series of lanthanide complexes supported by ferrocene-based ligands featuring exceptional optical and magnetic properties. Potential applications of the ferrocene derivative-supported lanthanide complexes were investigated for liquid cell quantum sensing and electromagnetic field sensing. Those discoveries are included in Chapter 5 of this thesis. Specifically, Chapter 2 is a version of **Shen, Y.**; Shepard, S. M.; Reed, C. J.; Diaconescu, P. L., **Zirconium complexes supported by ferrocene-based ligand as redox switches for**

hydroamination reactions, *Chem. Commun.* **2019**, *55*, 5587-5590. Chapter 3 is a version of Tran, T. V.; **Shen, Y.**; Nguyen, H. D.; Deng, S.; Roshandel, H.; Cooper, M. D.; Waston, J. R.; J. Byers, J.; Diaconescu, P. L.; Do, L. H., ***N*-carboxyanhydrides directly from amino acids and carbon dioxide and their tandem reactions to therapeutic alkaloids**, *Green Chemistry.* **2022**, *24*, 9245-9252. Chapter 4 is a summary of unpublished work on the surface-immobilization of ferrocene derivatives. Chapter 3 and 4 have content from a submitted manuscript, Deng, S.; **Shen, Y.**; Chantranuwathana, V.; Nguyen, H. D.; Tran, T. V.; Vasquez, K.; Byers, J.; Do, L. H.; Diaconescu, P. L., **ortho-Aromatic polyamides by ring-opening polymerization of *N*-carboxyanhydrides**. Chapter 5 is a version of a manuscript under revision, Shin, A. J.;* Zhao, C.;* **Shen, Y.**;* Dickerson, C.;* Li, B.; Bim, D.; Atallah, T. L.; Oyala, P. H.; He, Y.; Roshandel, H.; Alson, L. K.; Alexandrova, A. N.; Diaconescu, P. L.; Campbell, W. C.; Caram, J. R., **Toward liquid cell quantum sensing: Ytterbium(III) complexes with ultra-narrow absorption**, *authors contributed equally.

Chapter 2. Zirconium complexes supported by a ferrocene-based ligand as redox switches for hydroamination reactions

2.1 Introduction

Incorporating stimuli-responsive features in the design of a metal catalyst enables external control over the catalytic activity toward one-pot transformations without disturbing the reaction sequence.^{41, 42} The integration of a redox-active ligand into a metal complex allows the alteration of the complex's reactivity via chemical or electrochemical redox modifications.⁵⁰ One can expect the electronic properties of the complex to be tuned which potentially induces new activity or selectivity through redox events. The first example using a metallocene redox switch was reported on the influence of catalytic activity for hydrogenation and hydrosilylation reactions.⁹¹ A rhodium complex supported by a cobaltocene-based ligand was demonstrated with higher activity for the hydrogenation of olefins in its neutral state (Figure 2.1). Oxidation on the cobaltocene to a cobaltocenium resulted in better activity in hydrosilylation.

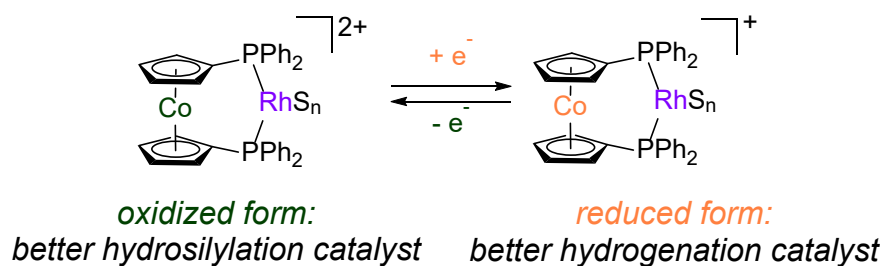


Figure 2.1. The first reported example of a redox switchable catalyst.

Inspired by the pioneering work on harnessing metallocene as a redox switch in the design of a metal catalyst for switchable transformations, tremendous amounts of work have been demonstrated on the development of redox switchable catalysis, primarily on ring-opening polymerizations and olefin polymerization to synthesize block copolymers.^{62-71, 85, 87} Several

advancements have been made in leveraging ferrocene-based ligands to achieve *in situ* redox modification on the catalyst by our group and others.^{65, 66, 69-85, 92} Moreover, inspiring studies on electrochemical switching highlight the versatility of achieving redox-switchable catalysis through diverse approaches (Figure 2.2).^{52, 68, 93}

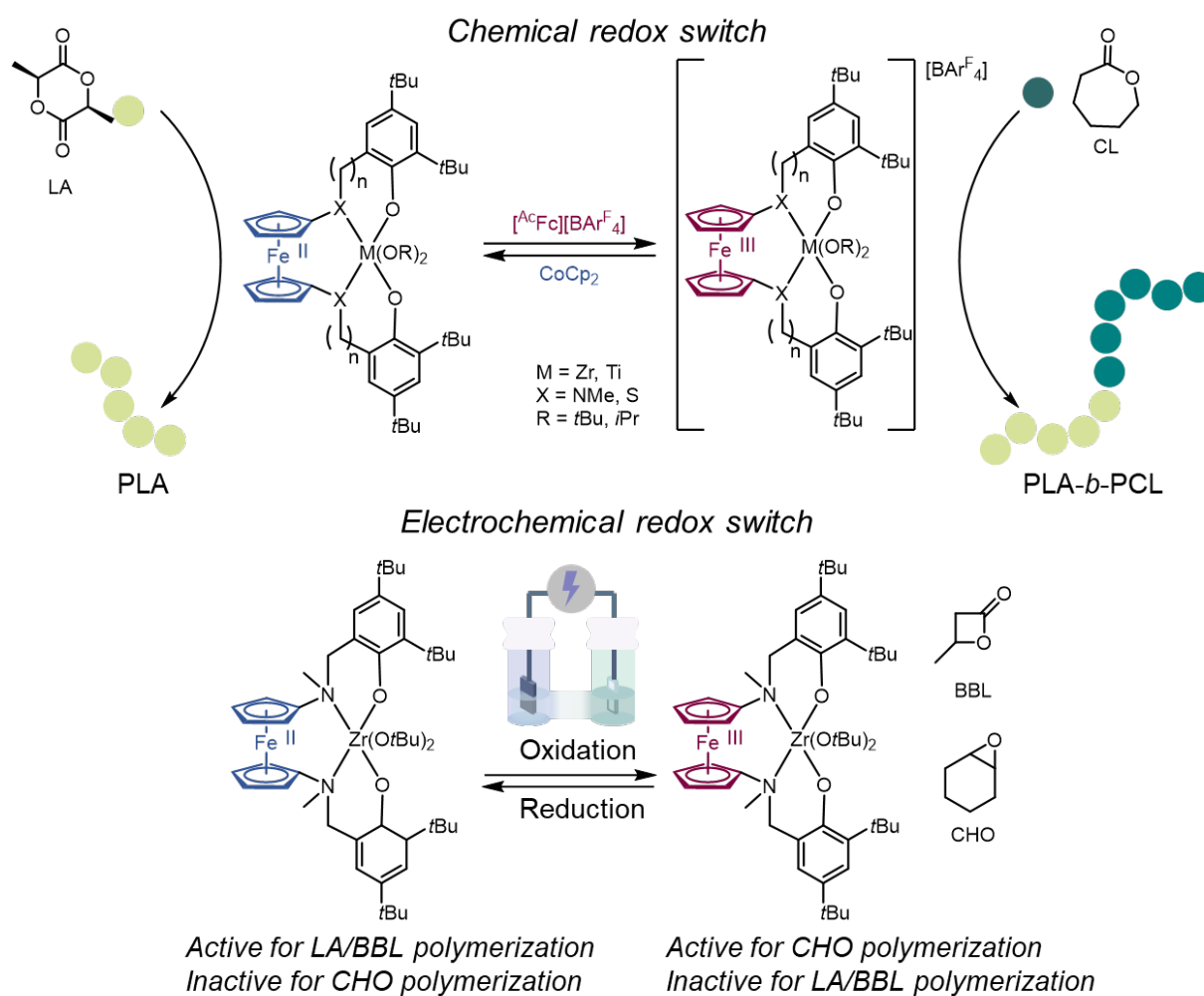


Figure 2.2. Redox-switchable polymerization can be enabled via chemical and electrochemical redox events on the ferrocene backbone.^{80, 93}

Besides polymerization, redox-switchable catalysis has been applied to the organic synthesis of small molecules. Reported examples include the development of redox-switchable

systems for a single reaction where the catalyst's reactivity can be turned on and off triggered by redox events, as well as a one-pot system composing orthogonal reactions. In the latter case, distinct reaction processes could be combined and facilitated by different states of a single catalyst, allowing a sequence of transformations to occur without intermediate isolation. On/off switching on the catalyst's activity has been reported for ring-closing metathesis,⁹⁴⁻⁹⁶ oxazoline, furan, and phenol formation,⁹⁷⁻⁹⁹ cyclization of alkynes,¹⁰⁰ hydroalkoxylation,⁸⁹ hydrosilylation,¹⁰¹ Kumada coupling,¹⁰² Buchwald-Hartwig cross-coupling,¹⁰³ hydroamination,¹⁰⁴ and so on.¹⁰⁵⁻¹¹¹ In most scenarios, the on/off switch of a single catalyst toward one type of reaction is comparatively easy to achieve. As represented in Figure 2.3, a neutral cobalt complex supported by a ferrocene derivative was active toward hydroalkoxylation whereas the reaction could be shut down by chemical oxidation.

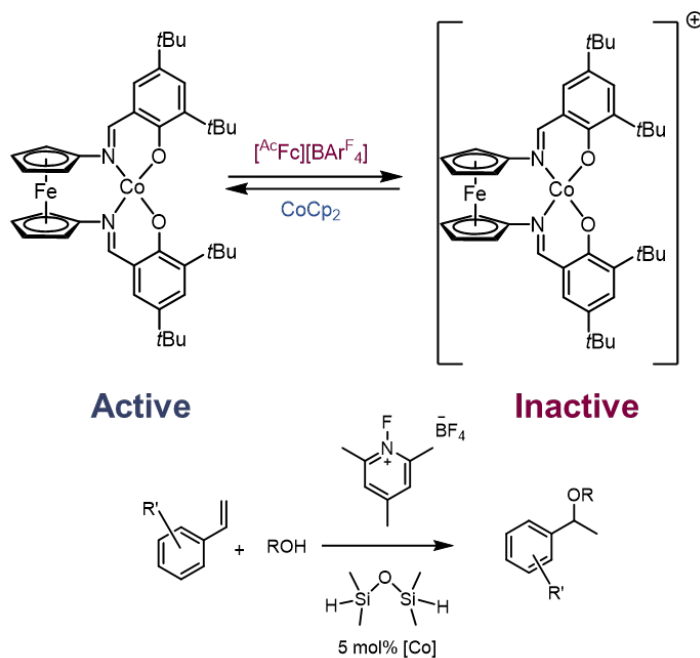


Figure 2.3. Redox-switchable hydroalkoxylation of a cobalt complex supported by a ferrocene-based ligand.⁸⁹

Despite the advantages of combining a sequence of mechanistically different reactions in

tandem, the research field suffers from the complexity of designing a multi-functional single catalyst with the potential to selectively facilitate distinct reactions in the presence of a mixture of substrates and reagents. Therefore, we decided to investigate the possibility of harnessing redox-switchable catalysis in small molecule synthesis focusing on transformations undergoing similar mechanisms. Inspired by the pioneering works on hydrogenation/hydrosilylation⁹¹ and hydroalkoxylation,⁸⁹ we envision incorporating redox-switchable ferrocene derivatives in the design of a metal catalyst for hydroelementation reactions to provide potential control over the reaction outcomes.

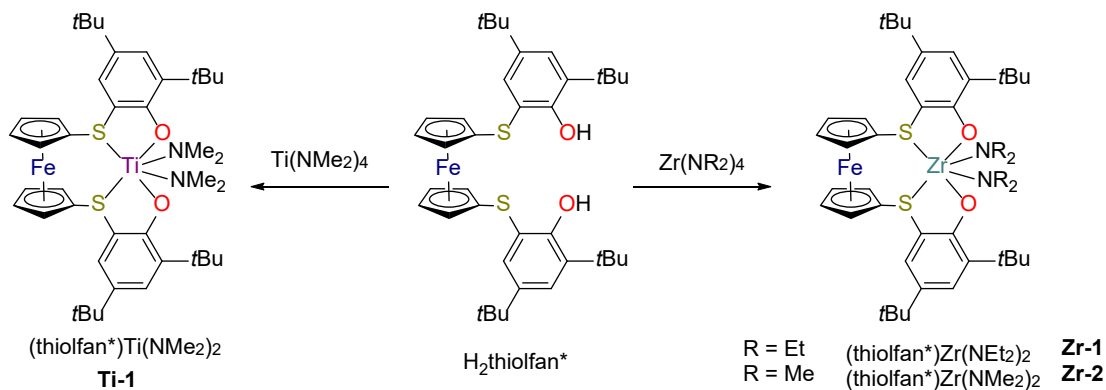
Group IV metal catalysts exhibit exceptional activities in accelerating hydroamination reactions.¹¹²⁻¹²¹ Among the reported examples of zirconium-catalyzed hydroamination reactions, neutral zirconium compounds exclusively catalyze reactions of primary aminoalkenes^{114, 115, 117, 122-125} with a few exceptions.¹²⁶⁻¹²⁹ On the contrary, cationic zirconium complexes exhibit either no selectivity towards the type of substrate,^{112, 113, 128} or selectively catalyze the cyclization of secondary aminoalkenes.^{116, 130} We are interested in the effect of incorporating a redox-switchable backbone on the catalyst's reactivity. Herein, we report the development of an [OSSO]-type zirconium complex, which composes a neutral and a cationic state triggered by redox modifications on the ferrocene backbone. The developed system demonstrated selectivity toward primary and secondary aminoalkene. This chapter is a version of a published manuscript **Shen, Y.; Shepard, S. M.; Reed, C. J.; Diaconescu, P. L., Zirconium complexes supported by ferrocene-based ligand as redox switches for hydroamination reactions, *Chem. Commun.* 2019, 55, 5587-5590.**

2.2 Results and discussion

Synthesis and characterization of Group IV metal complex supported by ferrocene-based ligand

The synthesis of the pro-ligand H₂(thiolfan*) (thiolfan* = 1, 1'-bis (2,4-di-*tert*-butyl-6-thiophenoxy) ferrocene) has been previously published.⁸⁰ Inspired by the exceptional activities of group IV metal catalysts in hydroamination reactions,^{114, 115, 124, 127, 128, 131, 132} we decided to investigate the ferrocene derivative-supported zirconium and titanium metal complexes (Scheme 2.1). The reaction of H₂(thiolfan*) with Zr(NEt₂)₄ was carried out in hexanes at -78 °C followed by 30 min stirring at room temperature. After the volatiles were removed under reduced pressure, the crude could be purified by washing with hexamethyldisiloxane (HMDSO) followed by recrystallization from pentane at -33 °C. The afforded product (thiolfan*)Zr(NEt₂)₂, **Zr-1**, was characterized by NMR spectroscopy (Figure A1-3) and elemental analysis. Similarly, (thiolfan*)Zr(NMe₂)₂ was prepared from the reaction of H₂(thiolfan*) with Zr(NMe₂)₄ in benzene at room temperature for 5 minutes followed by immediate removal of the volatiles under reduced pressure. The crude product (thiolfan*)Zr(NMe₂)₂ was washed with cold pentane three times before recrystallizing from pentane at -33 °C. The afforded (thiolfan*)Zr(NMe₂)₂, **Zr-2**, was characterized by NMR spectroscopy (Figure A5-7). Similarly, the reaction of H₂(thiolfan*) with Ti(NMe₂)₄ was carried out in benzene and stirred at room temperature for 30 min followed by immediate removal of the volatiles under reduced pressure. The crude was dissolved in HMDSO and stored at -33 °C to yield orange-yellow precipitation as (thiolfan*)Ti(NMe₂)₂, **Ti-1**. Alternatively, the reaction could be performed in a mixture of benzene and HMDSO (1:1) by dissolving the pro-ligand in benzene and adding it to a frozen solution of Ti(NMe₂)₄ in HMDSO at liquid nitrogen temperature. The frozen mixture was allowed to slowly warm to room

temperature and stirred for an hour. The volatiles were removed under a reduced pressure and the crude was re-dissolved in HMDSO and filtered through a pipette padded with glass fiber filter paper. Orange-yellow precipitation was obtained after leaving the solution at -33 °C for a week. The obtained compound was characterized by ^1H NMR spectroscopy (Figure A8).



Scheme 2.1. Synthesis of Group IV metal complexes supported by thiolfan*.

To investigate the redox properties of the formed compounds, cyclic voltammetry experiments were performed with 10 mM of metal compounds in the presence of 100 mM of TPABAr^F in *o*-F₂C₆H₄ and referenced to Fc/Fc⁺. Two irreversible oxidations were observed for **Zr-1** and a narrower region chosen for the second scan still revealed one irreversible oxidation event at 0.12 V versus the Fc/Fc⁺ couple (Figure 2.4). We speculated that a possible chemical reaction followed by the electron transfer occurred and caused the decomposition of the oxidized species under electrochemical conditions. Similarly, two irreversible oxidation events were observed for **Zr-2** and the attempt to isolate the first oxidation event reflected an irreversible event at 0.13 V versus the Fc/Fc⁺ couple (Figure A42). In the case of **Ti-1**, three irreversible oxidation events were observed. The attempt to isolate the first oxidation event, unfortunately, still revealed irreversible oxidation at 0.044 V (Figure A43). In all three cases, the oxidized

zirconium complexes under electrochemical conditions were suspected to be unstable and possibly underwent a chemical reaction after electro-oxidation that potentially led to a decomposition of the complex. In addition, chemical oxidation of **Zr-1** using chemical oxidants [^{Ac}Fc][BAR^F], AgOTf, AgBF₄, AgBPh₄, and NOBF₄ followed by the addition of reductant CoCp₂ was conducted. However, no reversible redox event was observed by ¹H NMR spectroscopy (Figure A4). Nonetheless, the reaction of **Zr-1** and an equivalent of [^{Ac}Fc][BAR^F] yielded a paramagnetic compound with the formula [(thiolfan*)Zr(NEt₂)₂][BAR^F], **Zr-1^{ox}**, which was confirmed by elemental analysis.

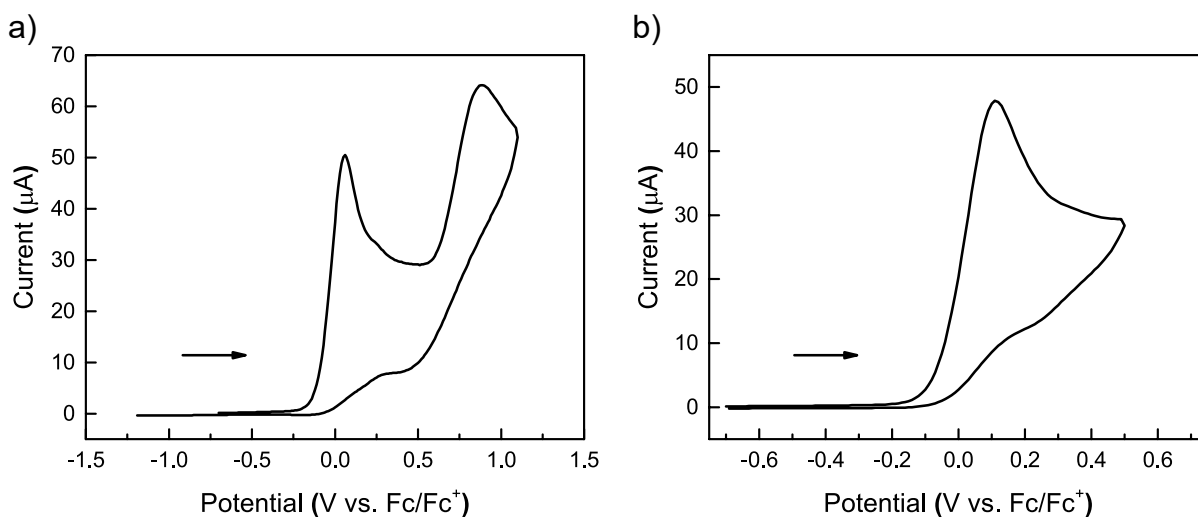


Figure 2.4. Cyclic voltammetry diagram of a) (thiolfan*)Zr(NEt₂)₂ recorded in *o*-F₂C₆H₄ at 100 mV s⁻¹ with 0.1 M TPABAr^F as the electrolyte and referenced to the Fc/Fc⁺ couple; b). a narrower region of the cyclic voltammetry scanned for (thiolfan*)Zr(NEt₂)₂ (right).

To gain a deep understanding of the oxidized compound, we employed ⁵⁷Fe Mössbauer spectroscopy at 80 K, with no applied magnetic field, to study the neutral and oxidized compounds. The results indicated a low-spin iron(II) for both (thiolfan*)Zr(NEt₂)₂ and

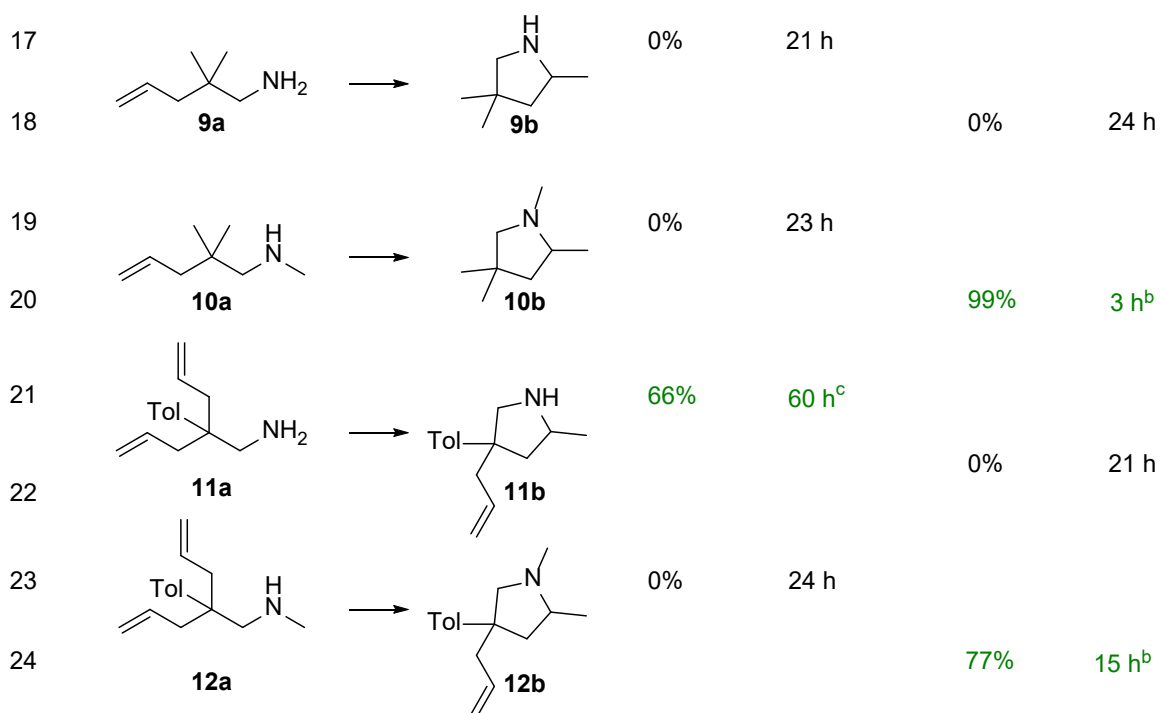
[(thiolfan*)Zr(NEt₂)₂][BAr^F] (Figure A44). Moreover, an X-band EPR spectrum acquired at 77 K revealed the presence of an organic radical ($g = 2.006$, Figure A45). These results suggested that the oxidation possibly occurred at the organic component of the ligand.

Reactivity study of zirconium catalysts in hydroamination reactions

To investigate the reactivity of the group IV metal complexes supported by the ferrocene-based ligands, we chose **Zr-1** and its oxidized form **Zr-1^{ox}** as catalysts for intramolecular hydroamination reactions. A catalytic amount (10 mol%) of **Zr-1** or **Zr-1^{ox}** was added to a J-Young NMR tube with the aminoalkene/alkyne substrate and internal standard, HMB. The reaction was heated to 100 °C in C₆D₆ and monitored by ¹H NMR spectroscopy. **Zr-1** showed reactivity toward cyclizing primary aminoalkene **1a** in 72 h under standard conditions, whereas **Zr-1^{ox}** showed no reactivity (Table 2.1, entries 1 and 2). On the contrary, **Zr-1** displayed no reactivity toward cyclizing secondary aminoalkene **2a** while **Zr-1^{ox}** was able to cyclize **2a** in 20 h (entries 3 and 4). Similar observations were found for another set of substrates **11a** and **12a** where the neutral compound **Zr-1** demonstrated reactivity toward cyclizing the primary aminoalkene **11a** but no reactivity toward secondary aminoalkene **12a**. **Zr-1^{ox}** displayed the orthogonal activity: no reactivity was observed toward **11a**, but 77% conversion was obtained for **12a** (entries 21-24). Unfortunately, no activity was observed for either state of the zirconium catalyst toward cyclizing aminoalkenes **3a-6a**, and **9a** (entries 5-12, and 17-18), while secondary aminoalkene **10a** could be only cyclized in the presence of **Zr-1^{ox}** (entries 19-20). In addition, the hydroamination of aminoalkynes was investigated under the same conditions. However, the primary aminoalkyne can be cyclized in the presence of either **Zr-1** or **Zr-1^{ox}**, while secondary aminoalkyne **8a** could be only cyclized in the presence of **Zr-1^{ox}** (entries 15 and 16).

Table 2.1. Intramolecular hydroaminations catalyzed by **Zr-1** or **Zr-1^{ox}**

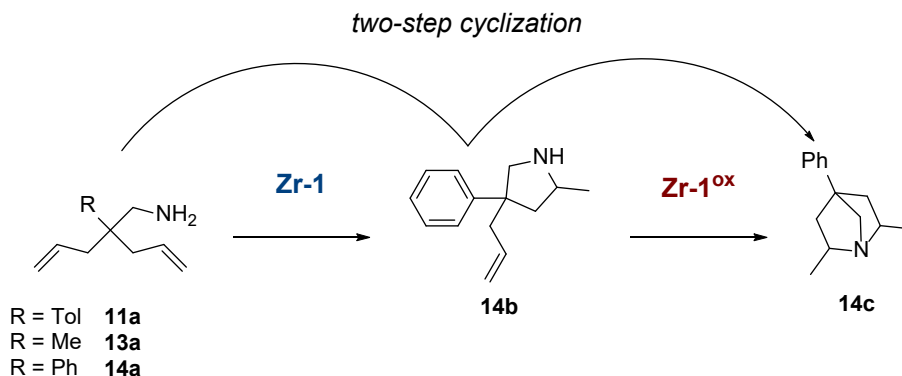
Entry		Neutral state		Oxidized state	
		Conversion	Time	Conversion	Time
1		95%	72 h		
2				0%	20 h
3		0%	16 h		
4				100%	20 h
5		0%	24 h		
6				0%	30 h
7		0%	18 h		
8				0%	20 h
9		0%	21 h		
10				0%	24 h
11		0%	20 h		
12				0%	21 h
13		99%	4 h		
14				99%	2 h
15		0%	20 h		
16				99%	1 h ^b



- a. Reaction conditions: 10 mmol% catalyst, 0.5 mL C₆D₆, 100 °C. Conversions were calculated from the corresponding NMR spectra using hexamethylbenzene (HMB) as an internal standard, except for entry 24, when the conversion was calculated by HRMS because of overlapping peaks in the corresponding NMR spectra. The oxidized state was generated *in situ* by the addition of 0.9 equiv. of [AcFc][BAR^F].
- b. Reactions were carried out in a 4 : 1 by volume C₆D₆ : *o*-C₆H₄F₂ solution.
- c. The reaction was carried out in *o*-C₆H₄F₂.

Control reactions were performed to elucidate the role of chemical oxidants in hydroamination (Table A1). No conversion of **1a** to **1b** was observed while full conversion of **2a** to **2b** was observed in the presence of [AcFc][BAR^F] (Table A1, entries 1 and 3). Furthermore, partial conversion of **2a** to **2b** was observed in the presence of NaFcBAR^F, full conversion was observed with [Fc][BAR^F], while no conversion was observed in the presence of acetyl ferrocene

nor FcPF₆ (Table A1, entries 4-7). Moreover, **7a** and **10a** could also be cyclized in the presence of [AcFc][BAR^F] (Table A1, entries 8-9). We reasoned that those hydroamination reactions were catalyzed by Brønsted acid.^{132, 133} To alleviate the possible effect from the oxidants, we premix the zirconium compound with 0.9 equivalent of [AcFc][BAR^F] and allowed it to fully react before the addition of a substrate.



Scheme 2.2. 2-step cyclization proposed for **Zr-1** and **Zr-1^{ox}**.

Encouraged by the orthogonal activity obtained for **Zr-1** and **Zr-1^{ox}** toward cyclizing **11a** and **12a**, we proposed to enable a redox-controlled two-step cyclization of primary aminoalkenes bearing two unsaturated C=C bonds. As depicted in Scheme 2.2, we envisioned that the first cyclization of the primary aminoalkene could be accomplished in the presence of **Zr-1**, affording a cyclic secondary aminoalkene serving as the starting material for the second cyclization. Upon the addition of the chemical oxidant, *in situ* generation of **Zr-1^{ox}** was expected to enable the second cyclization affording the bicyclic final product. The bicyclic amines hold vast potential as heterocyclic skeletons of greater structural complexity but are more challenging to obtain and usually require to be heated at higher temperatures.^{112, 134, 135} Primary aminoalkenes **11a**, **13a**, and **14a** were investigated in the 2-step cyclization. Although no conversion of **13a** to **13b** was

observed, **14b** was obtained in the presence of **Zr-1** as a mixture of isomers. As previously discussed, **11b** was also obtained under similar conditions. However, tandem synthesis toward **14c** from **14b** catalyzed by **Zr-1^{ox}** via *in situ* oxidation of **Zr-1** was not successful. To deepen our understanding of the second cyclization reaction, we performed the reaction using purified **14b** in the presence of **Zr-1^{ox}**, however, no clear evidence of **14c** formation was observed (Figure A41).

2.3 Conclusion and outlook

In summary, we synthesized Group IV metal complexes supported by ferrocene-based ligand, and their redox property was investigated. Although unfortunately none of the thiolan-supported compounds was redox-switchable, (thiolan*)Zr(NEt₂)₂ was investigated in intramolecular hydroamination reactions comprehensively. Orthogonal reactivity was found for (thiolan*)Zr(NEt₂)₂ and its oxidized form towards primary and secondary aminoalkenes: the neutral compound selectively catalyzes the cyclization of primary aminoalkenes whereas the oxidized compound was only active in cyclizing secondary aminoalkenes (Figure 2.5).

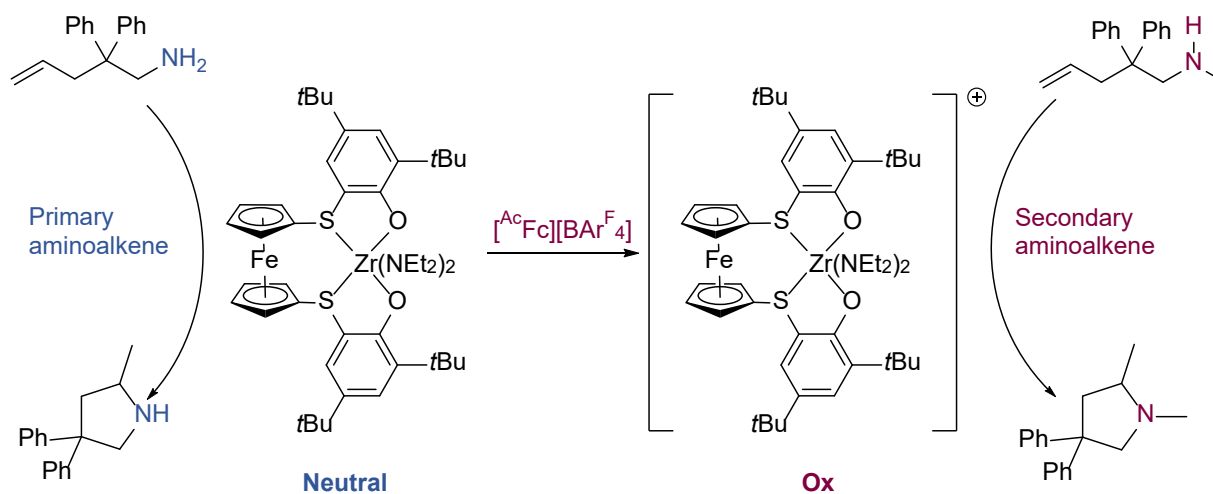


Figure 2.5. A redox-active zirconium complex catalyzed hydroamination reactions selectively.

Although leveraging the selectivity toward primary and secondary aminoalkenes via *in situ* switching the oxidation state of the zirconium catalyst to conduct a 2-step cyclization in tandem was unsuccessful, the findings in the present study contribute to the development of redox switchable catalysts for assisted tandem reactions. Further exploration of a redox-switchable complex holds a vast potential on unlocking the possibility of conducting diverse tandem reactions via a single metal catalyst.

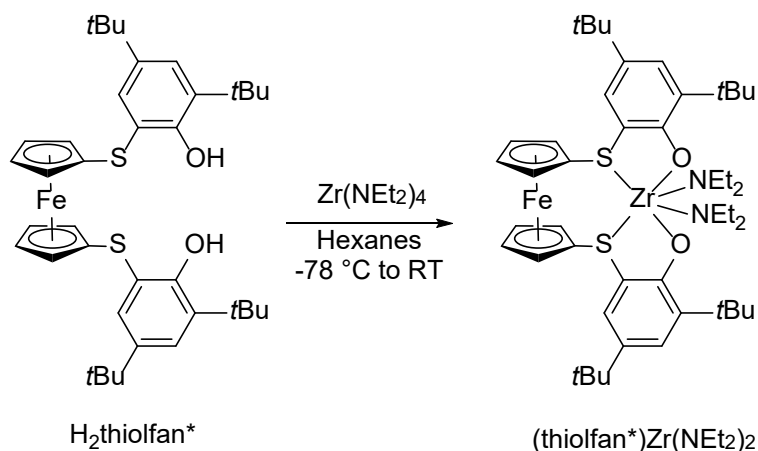
2.4 Experimental section

General considerations

All reactions were performed using standard Schlenk techniques or in an MBraun drybox under a nitrogen atmosphere, unless otherwise noted. All glassware and Celite were stored in an oven at 100 °C overnight before being brought into the drybox. Solvents, except for *n*-pentane, were purified by the method of Grubbs¹³⁶ and transferred to the glovebox without exposure to air. *n*-Pentane was purified by stirring calcium hydride overnight followed by a distillation under a nitrogen atmosphere and transferred into the glovebox without exposure to air. NMR solvents were obtained from Cambridge Isotope Laboratories, degassed, and stored over activated molecular sieves prior to use. NMR spectra were recorded at ambient temperature on Bruker AV-300, AV-400, AV-500, and DRX-500 spectrometers. Chemical shifts are reported with respect to internal solvent, 7.16 ppm (C₆D₆) and 7.26 ppm (CDCl₃) for ¹H NMR spectra. All reagents were acquired from commercial sources and used as received unless otherwise noted. Zr(NEt₂)₄,¹³⁷ NaBAr^F,¹³⁸ and H₂(thiofan*)⁸⁰ were synthesized according to published procedures. Amine substrates were synthesized according to published procedures.^{112, 113, 115, 116, 139-150} Cyclic voltammograms were acquired with a CH Instruments CHI630D potentiostat and

recorded with CH Instruments software (version 13.04). All potentials are given with respect to the ferrocene-ferrocenium couple. Elemental analyses were performed on an Exeter Analytical Inc. CE-440 elemental analyzer. HRMS was recorded on an Agilent 7250 Accurate-mass Q-TOF GC/MS (ESI Source). UV-Vis spectra were recorded on a Hewlett Packard 8453. Zero applied field ^{57}Fe Mössbauer spectra were recorded at 80 K in constant acceleration mode on a spectrometer from See Co (Edina, MN) equipped with an SVT-400 cryostat (Janis, Wilmington, WA). The isomer shifts are relative to the centroid of an α -Fe foil signal at room temperature. Samples were prepared by mixing polycrystalline material (30-40 mg) with boron nitride in a cup fitted with a screw cap. The data were fit to Lorentzian lineshapes using WMOSS (www.wmoss.org). X-band CW EPR spectra were acquired on a Bruker (Billerica, MA) EMX spectrometer using Bruker Win-EPR software (ver. 3.0). Temperature control was achieved using liquid helium and an Oxford Instruments (Oxford, UK) ESR-900 cryogen flow cryostat and an ITC-503 temperature controller.

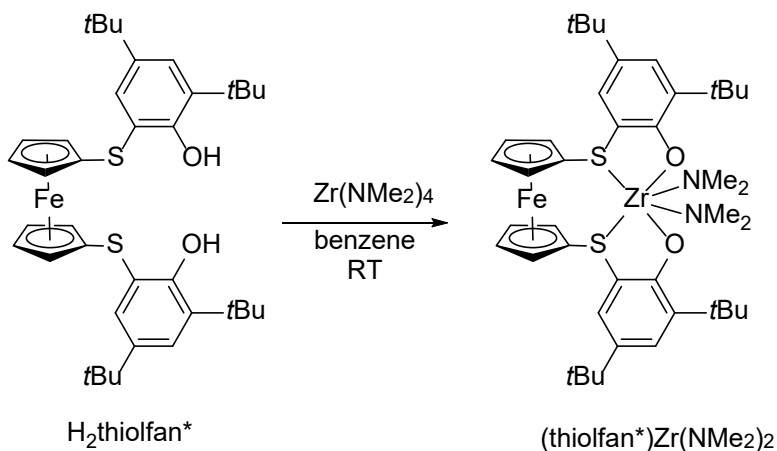
Synthesis of (thiolfan*)Zr(NEt₂)₂, Zr-1



0.201 g (0.31 mmol) of H₂(thiolfan*) was dissolved in 10 mL of hexanes and cooled to -78 °C in a 25 mL vial. 0.101 g (0.31 mmol, 1 equiv.) of Zr(NEt₂)₄ was dissolved in 2 mL of hexanes in a separate vial and cooled to -78°C. The solution of H₂(thiolfan*) was added

dropwise to $\text{Zr}(\text{NEt}_2)_4$ and the reaction solution was stirred at room temperature for 30 min. The volatiles were removed under reduced pressure. The crude yellow solid was washed with HMDSO and recrystallized from *n*-pentane giving 0.2 g (77%) of clean $(\text{thiolfan}^*)\text{Zr}(\text{NEt}_2)_2$. ^1H NMR (C_6D_6 , 500 MHz, 25 °C): δ (ppm) = 7.60 (d, 2H, ArH), 7.58 (d, 2H, ArH), 4.10 (br, 4H, Cp-H), 3.78 (br, 4H, Cp-H), 3.71 (s, 8H, NCH_2CH_3), 1.78 (s, 18H, $\text{C}(\text{CH}_3)_3$), 1.26 (s, 18H, $\text{C}(\text{CH}_3)_3$), 1.07 (t, 12H, NCH_2CH_3). ^{13}C NMR (C_6D_6 , 125 MHz, 25°C): δ (ppm) = 163.0 (ArC), 140.3 (ArC), 137.6, (ArC), 130.6 (ArCH), 125.6 (ArCH), 120.2 (ArC), 89.97 (Cp), 70.5, 68.8, 65.1, 42.5 (NCH_2CH_3), 35.4($\text{C}(\text{CH}_3)_3$), 34.0 ($\text{C}(\text{CH}_3)_3$), 31.3 ($\text{C}(\text{CH}_3)_3$), 29.6 ($\text{C}(\text{CH}_3)_3$), 14.79 (NCH_2CH_3). Anal. Calcd for $(\text{thiolfan}^*)\text{Zr}(\text{NEt}_2)_2$ ($\text{C}_{46}\text{H}_{68}\text{FeN}_2\text{O}_2\text{S}_2\text{Zr}$): C, 61.92%; H, 7.68%; N, 3.14%. Found: C, 62.28%; H, 7.44%; N, 2.50%.

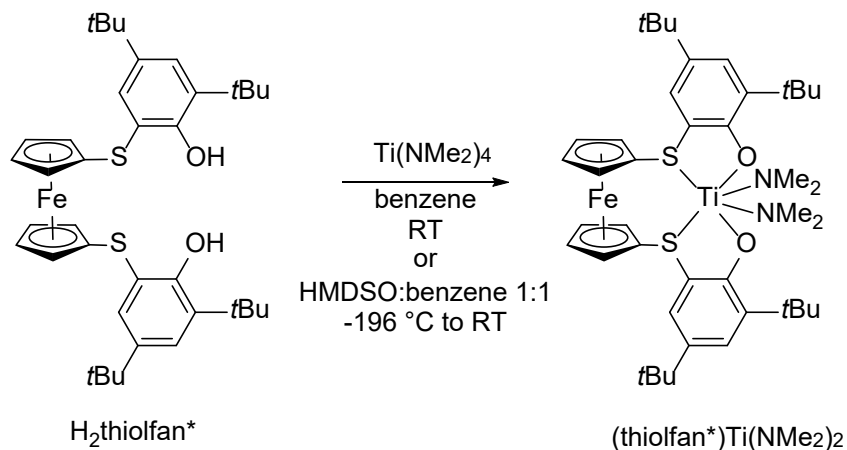
Synthesis of $(\text{thiolfan}^*)\text{Zr}(\text{NMe}_2)_2$, Zr-2



391 mg (0.59 mmol, 1 equiv.) of $\text{H}_2(\text{thiolfan}^*)$ was dissolved in 10 mL benzene at room temperature inside the glovebox and added to the benzene solution of $\text{Zr}(\text{NMe}_2)_4$ (159 mg, 0.59 mmol, 1 equiv.). The reaction solution was stirred at room temperature for 5 min and the volatiles were removed under a reduced pressure. The crude product was washed with cold pentanes and recrystallized from pentanes yielding the yellow solid as $(\text{thiolfan}^*)\text{Zr}(\text{NMe}_2)_2$. ^1H NMR (C_6D_6 , 500 MHz, 298K): δ (ppm) = 7.62 (d, 2H, ArH), 7.58 (d, 2H, ArH), 4.32 (s, 4H, CpH), 3.70 (t,

4H, CpH), 3.29 (s, 12H, NCH₃), 1.79 (s, 18H, C(CH₃)₃), 1.26 (s, 18H, C(CH₃)₃). ¹³C NMR (C₆D₆, 125 MHz, 298K): δ (ppm) = 163.2 (ArC), 140.8 (ArC), 138.2, (ArC), 131.0 (ArCH), 126.1 (ArCH), 120.1 (ArC), 90.1 (Cp), 69.3(Cp), 43.3 (NCH₃), 35.9(C(CH₃)₃), 34.3 (C(CH₃)₃), 31.7 (C(CH₃)₃), 29.9 (C(CH₃)₃).

Synthesis of (thiofan*)Ti(NMe₂)₂, Ti-1



58.7 mg (0.089 mmol, 1 equiv.) of H₂(thiofan*) was dissolved in 2 mL benzene and added to the solution of Ti(NMe₂)₄ (20 mg, 0.089 mmol, 1 equiv.) at room temperature. The reaction was stirred at room temperature for 30 min followed by immediate removing of the volatiles under a reduced pressure. The crude was dissolved in HMDSO and stored at -33 °C to yield orange-yellow precipitation as (thiofan*)Ti(NMe₂)₂. The reaction could also be performed in a mixture of benzene and HMDSO (1:1) by dissolving the pro-ligand in benzene and adding it to a frozen solution of Ti(NMe₂)₄ in HMDSO at liquid nitrogen temperature. The frozen mixture was allowed to slowly warm to room temperature and stirred for an hour. The volatiles were removed under a reduced pressure and the crude was re-dissolved in HMDSO and filtered through a pipette padded with glass fiber filter paper. (thiofan*)Ti(NMe₂)₂ was obtained as orange-yellow precipitation after leaving the solution at -33 °C for a week. ¹H NMR (C₆D₆,

300MHz, 298K): δ (ppm) = 7.35 (d, 2H ArH), 7.32 (d, 2H ArH), 4.47 (s, 4H CpH), 4.10 (t, 4H CpH), 3.36 (s, 12H, N CH₃), 1.69 (s, 18H, C(CH₃)₃), 1.23 (s, 18H, C(CH₃)₃).

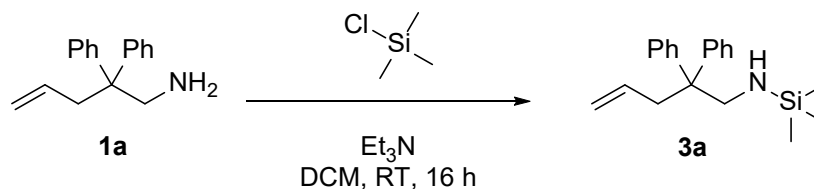
Synthesis of [(thiolfan*)Zr(NEt₂)₂][BAr^F]

0.183 g (0.21 mmol) of (thiolfan*)Zr(NEt₂)₂ was dissolved in 1 mL of *o*-difluorobenzene and added to a 2 mL *o*-difluorobenzene solution of [^AcFc][BAr^F] (0.20 mg, 0.9 eq, 0.1850 mmol) and stirred for 1 hour at room temperature. The volatiles were removed under reduced pressure. The oily product was washed three times with 25 mL of hexanes each time. 2 mL of toluene was added in the last wash to remove acetylferrocene. The resulting solid was dissolved in benzene, the solution was concentrated and layered with hexanes at room temperature overnight. The product was then dried under reduced pressure for 24 h yielding 0.105 mg (32%) of a dark purple solid. Due to the paramagnetic nature of the compound, the NMR spectroscopy analysis was not resolvable. Anal. Calcd for [(thiolfan*)Zr(NEt₂)₂][BAr^F] (C₇₈H₈₀FeN₂O₂S₂BF₂₄Zr): C, 53.37%; H, 4.59%; N, 1.59%. Found: C, 52.71%; H, 4.16%; N, 1.17%.

Synthetic procedure for [^AcFc][BAr^F]

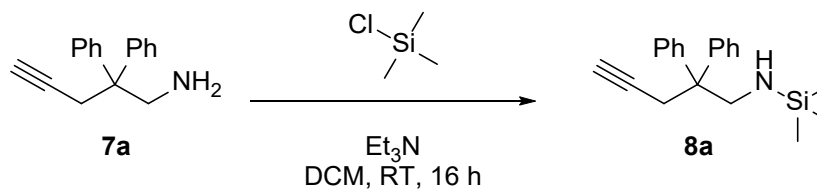
[^AcFc][BAr^F] was synthesized based on previously reported procedures with slight modifications.^{151, 152} 209.3 mg (0.67 mmol) of ^AcFcBF₄ was dissolved in DCM and added to 590.7 mg (0.67 mmol, 1 equiv.) of NaBAr^F in DCM. The reaction mixture was stirred for 2 hours at room temperature and the volatiles were removed under a reduced pressure. The solid was extracted with diethyl ether and the resulting solution was filtered through Celite. [^AcFc][BAr^F] was crystallized from concentrated diethyl ether layered with hexanes at -33 °C yielding dark blue crystals; 611 mg (84%).

Synthesis of *N*-(2,2-diphenylpent-4-en-1-yl)-1,1,1-trimethylsilanamine, 3a



In a nitrogen-filled glovebox, 82 mg (3.4 mmol, 1 equiv.) of 2,2-diphenylpent-4-en-1-amine was dissolved in DCM, to which 70 mg (6.9 mmol, 2 equiv.) of triethylamine and 38 mg (3.4 mmol, 1 equiv.) of TMSCl were added slowly at $-78\text{ }^\circ\text{C}$. the reaction was stirred overnight at room temperature and the solvent was removed under a reduced pressure upon completion. The crude was extracted into hexanes and filtered through celite. The product was concentrated to dryness yielding **3a**. $^1\text{H NMR}$ (C_6D_6 , 300MHz, 298K): δ (ppm) = 7.13-7.09 (m, 10 H, ArH), 5.51-5.06 (m, 1H, $\text{CH}=\text{CH}_2$), 4.95-4.91 (dd, 2H, $\text{CH}=\text{CH}_2$), 3.40 (d, $J = 8.7$ Hz, 2H, CH_2NH), 3.17 (br, 1H, NH), 2.92 (d, $J = 6.5$ Hz, 2H, CHCH_2), -0.03 (s, 9H, $\text{Si}(\text{CH}_3)_3$).

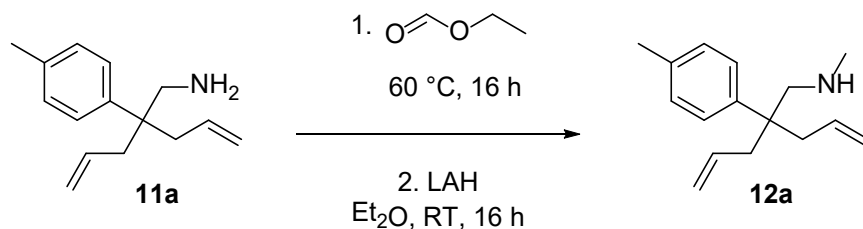
Synthesis of *N*-(2,2-diphenylpent-4-yn-1-yl)-1,1,1-trimethylsilanamine, **8a**



2,2-diphenylpent-4-yn-1-amine was synthesized following a published procedure.¹³⁹ Inside a nitrogen-filled glovebox, 0.136 g (0.58 mmol, 1 equiv.) of 2,2-diphenylpent-4-yn-1-amine was dissolved in DCM with 117 mg (1.16 mmol, 2 equiv.) of triethylamine to which a solution of TMSCl (69 mg, 0.64 mmol, 1.1 equiv.) in DCM was slowly added to. The reaction was stirred at room temperature overnight and the solvent was removed under a reduced pressure upon completion. The reaction mixture was extracted into hexanes and filtered through celite. The solvent was removed under a reduced pressure yielding colorless liquid as the product. $^1\text{H NMR}$

(C₆D₆, 300MHz, 298K): δ (ppm) = 7.12-7.10 (m, 10 H, ArH), 3.60 (d, J = 8.2 Hz, 2H, CH₂NH), 3.01 (dd, J = 2.7 Hz, 2H, CH≡CCH₂), 1.62 (t, J = 2.7 Hz, 1H, C≡CH), -0.03 (s, 9H, Si(CH₃)₃).

Synthesis of 2-allyl-*N*-methyl-2-(*p*-tolyl)pent-4-en-1-amine, 12a



2-allyl-2-(*p*-tolyl)pent-4-en-amine was synthesized according to a previously published procedure.¹⁴² 0.188 g (0.87 mmol) of 2-allyl-2-(*p*-tolyl)pent-4-en-amine was dissolved in 1 mL of ethyl formate in a Schlenk flask under an inert atmosphere. The reaction mixture was stirred at 60 °C for 16 h. Ethyl formate was removed under reduced pressure, and the residual was dissolved in diethyl ether. The mixture was added to a diethyl ether solution of LiAlH₄ (99 mg, 2.62 mmol, 3 equiv.) and then stirred for 16 h. The reaction was quenched by a 2 M NaOH solution at 0 °C. The product was extracted into diethyl ether and dried over MgSO₄. The volatiles were removed under reduced pressure yielding a light-yellow gel as the product, which was used without further purification. ¹H NMR (C₆D₆, 300MHz, 298K): δ (ppm) = 7.23 (d, 2H, J = 7.8 Hz, ArH), 7.13 (d, 2H, J = 7.8 Hz, ArH), 5.65 (m, 2H, CH₂=CH), 5.04 (m, 4H, CH₂=CH), 2.73 (s, 2H, NHCH₂), 2.51 (ddd, 4H, CH₂=CHCH₂), 2.33 (s, 3H, PhCH₃), 2.30 (s, 3H, NHCH₃) HRMS (ESI) calculated for C₁₆H₂₄N⁺ [M+H]⁺ = 230.1909, found 230.2273.

General procedure for hydroamination reactions catalyzed by Zr-1

(thiofan*)Zr(NEt₂)₂ (0.01 mmol, 10 mol%) was dissolved in C₆D₆ and added to a J-Young NMR tube. The substrate (0.1 mmol) was also dissolved in C₆D₆ and added to the J-Young tube. The tube was sealed and analyzed for a 0-hour ¹H NMR spectrum before being heated to 100 °C. Reactions were monitored by ¹H NMR spectroscopy.

General procedure for hydroamination reactions catalyzed by the oxidized state of Zr-1^{ox}

(thiolfan*)Zr(NEt₂)₂ (0.01 mmol, 10 mol%) was dissolved in C₆D₆ and added to a J-Young NMR tube. [^{Ac}Fc][BAr^F] (10.91 mg, 0.009 mmol, 9 mol%) was then added to the J-Young tube leading to a color change from yellow to brown. The tube was shaken until all solids dissolved. Then the substrate (0.1 mmol) was dissolved in C₆D₆ and added to the J-Young tube. The tube was then sealed and analyzed for a 0-hour ¹H NMR spectrum before being heated to 100 °C. Reactions were monitored by ¹H NMR spectroscopy.

General procedure for control experiments

[^{Ac}Fc][BAr^F] (0.01 mmol, 10 mol%) was dissolved in C₆D₆ and added to a J-Young NMR tube. The substrate (0.1 mmol) was dissolved in C₆D₆ and added to the J-Young tube. The tube was then sealed and analyzed for a 0-hour ¹H NMR spectrum before being heated to 100 °C. Reactions were monitored by ¹H NMR spectroscopy.

2.5 Appendix A

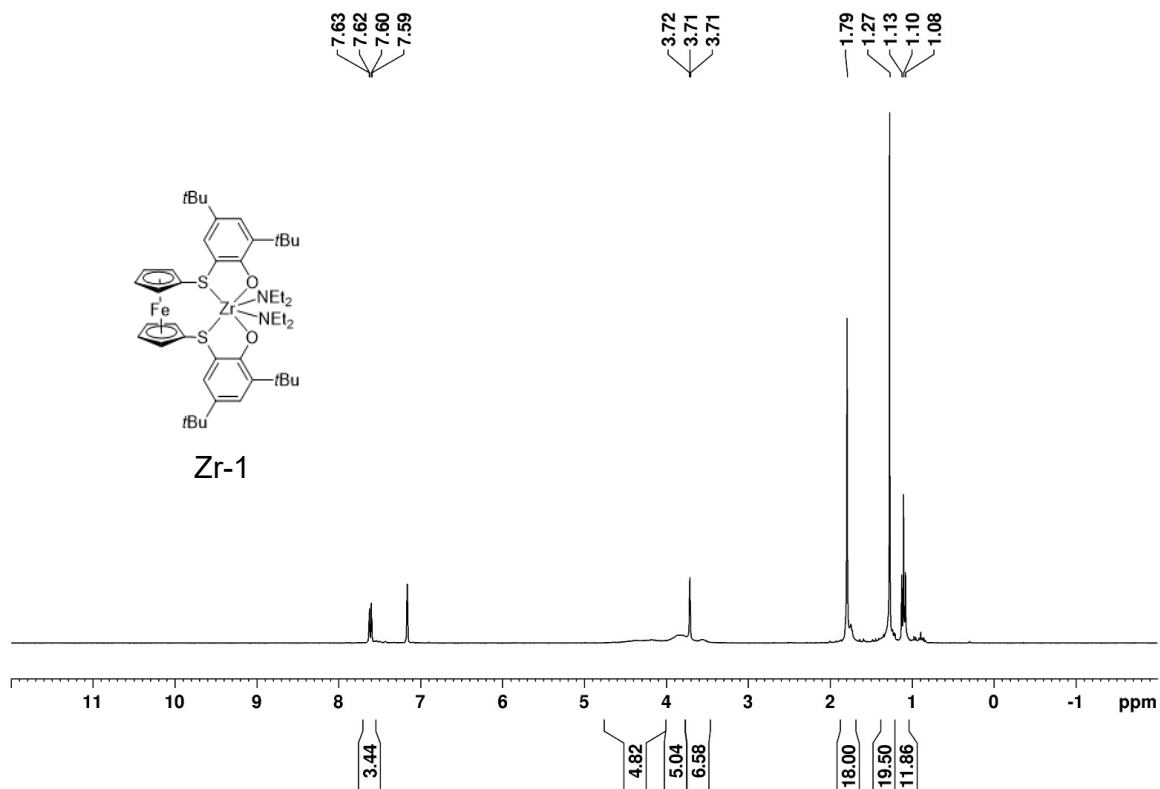


Figure A1: ¹H NMR (C₆D₆, 500 MHz, 298 K) spectrum of (thiolfan*)Zr(NEt₂)₂: δ (ppm) = 7.60 (d, 2H, ArH), 7.58 (d, 2H, ArH), 4.10 (br, 4H, Cp-H), 3.78 (br, 4H, Cp-H), 3.71 (s, 8H, NCH₂CH₃), 1.78 (s, 18H, C(CH₃)₃), 1.26 (s, 18H, C(CH₃)₃), 1.07 (t, 12H, NCH₂CH₃). The peak at 0.89 ppm is attributed to residual *n*-pentane.

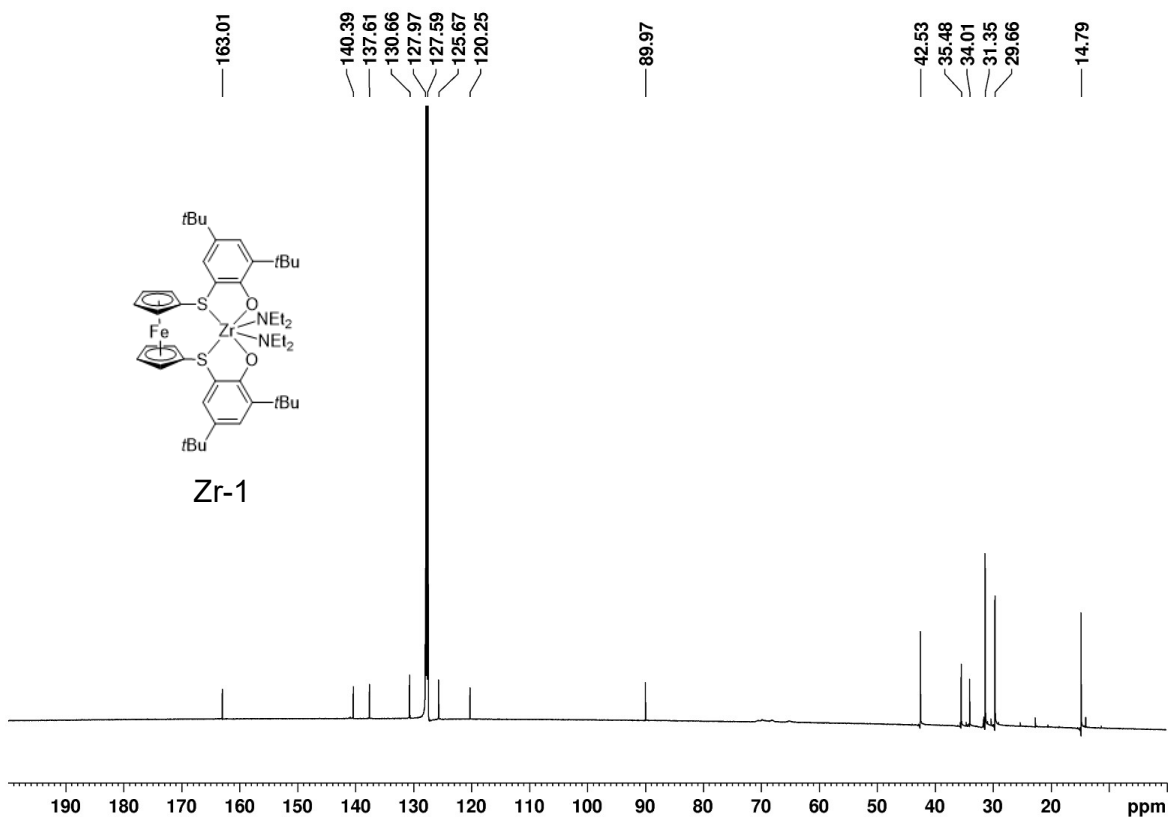


Figure A2: ^{13}C NMR (C_6D_6 , 125 MHz, 298 K) spectrum of (thiolfan*) $\text{Zr}(\text{NEt}_2)_2$: δ (ppm) = 163.0 (ArC), 140.3 (ArC), 137.6, (ArC), 130.6 (ArCH), 125.6 (ArCH), 120.2 (ArC), 89.97 (Cp), 70.5, 68.8, 65.1, 42.5 (NCH_2CH_3), 35.4($\text{C}(\text{CH}_3)_3$), 34.0 ($\text{C}(\text{CH}_3)_3$), 31.3 ($\text{C}(\text{CH}_3)_3$), 29.6 ($\text{C}(\text{CH}_3)_3$), 14.79 (NCH_2CH_3).

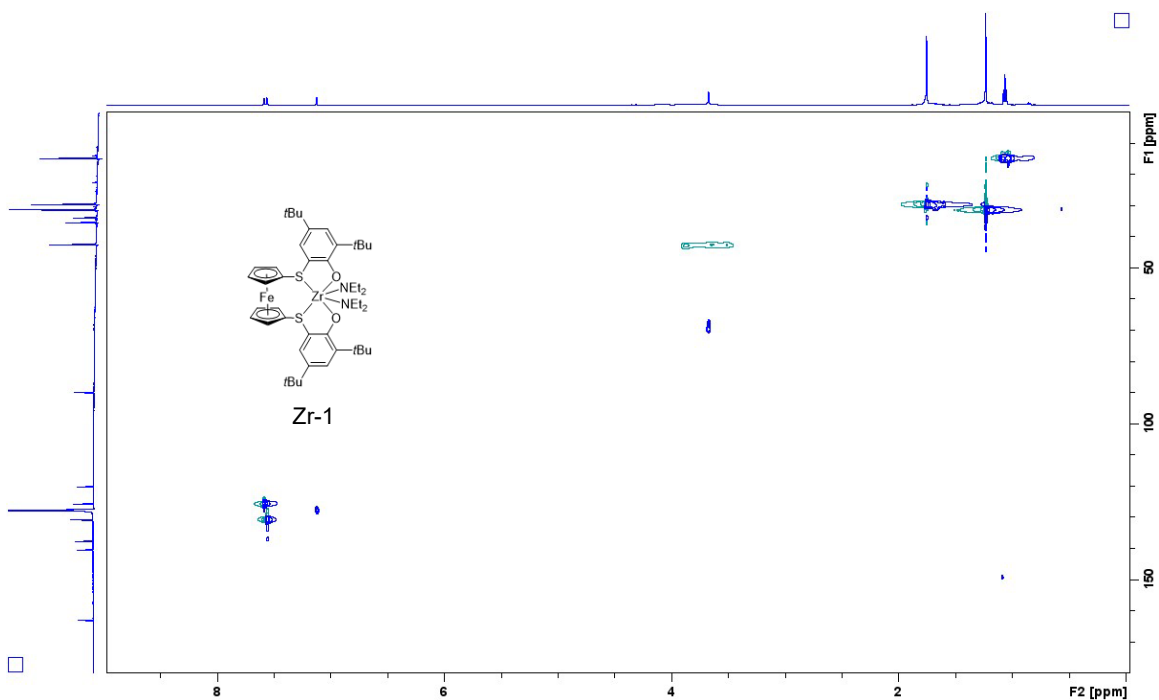


Figure A3. HSQC (C_6D_6 , 500 MHz, 298 K) spectrum of (thiolfan*) $Zr(NEt_2)_2$.

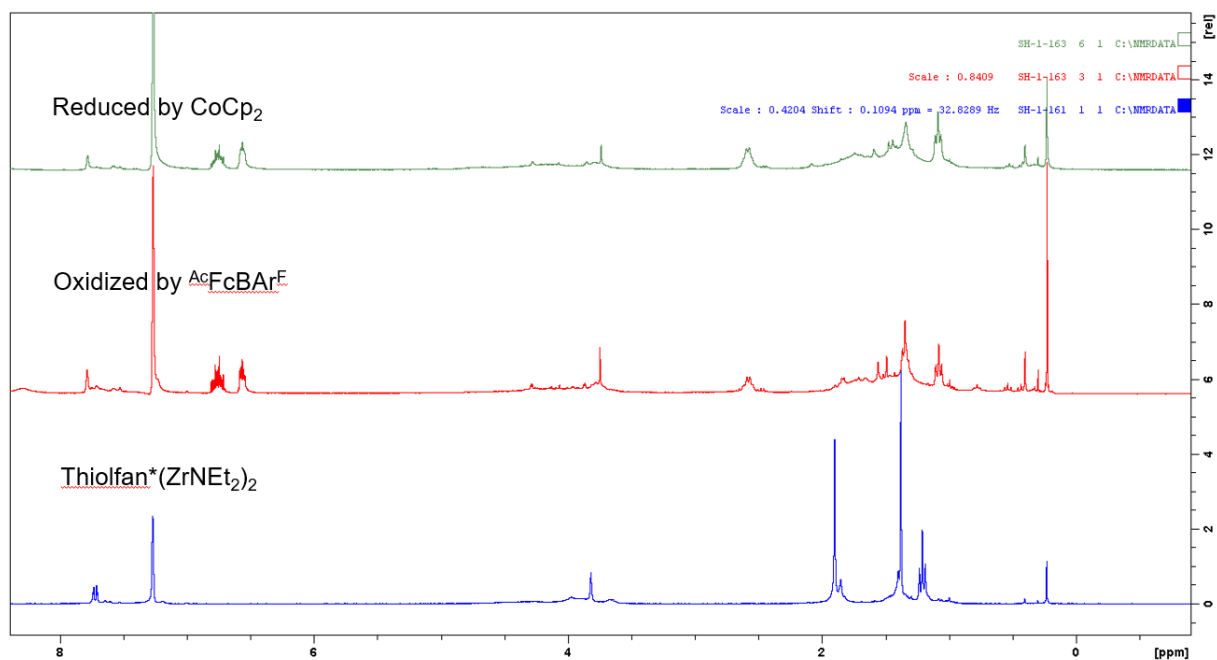


Figure A4: 1H NMR (C_6D_6 , 300 MHz, 298 K) spectrum of (thiolfan*) $Zr(NEt_2)_2$ chemical oxidation and reduction.

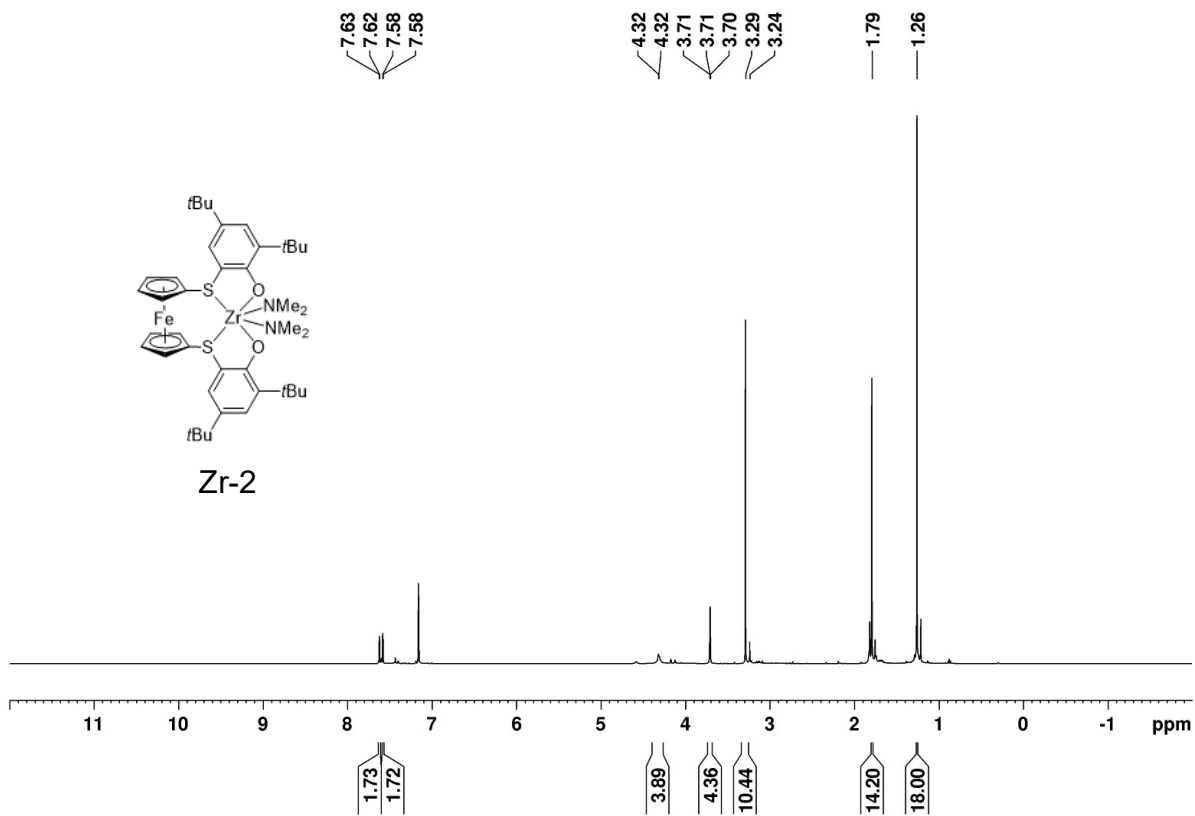


Figure A5. ^1H NMR (C_6D_6 , 500 MHz, 298K) spectrum of (thiolfan*) $\text{Zr}(\text{NMe}_2)_2$: δ (ppm) = 7.62 (d, 2H, ArH), 7.58 (d, 2H, ArH), 4.32 (s, 4H, CpH), 3.70 (t, 4H, CpH), 3.29 (s, 12H, NCH₃), 1.79 (s, 18H, C(CH₃)₃), 1.26 (s, 18H, C(CH₃)₃).

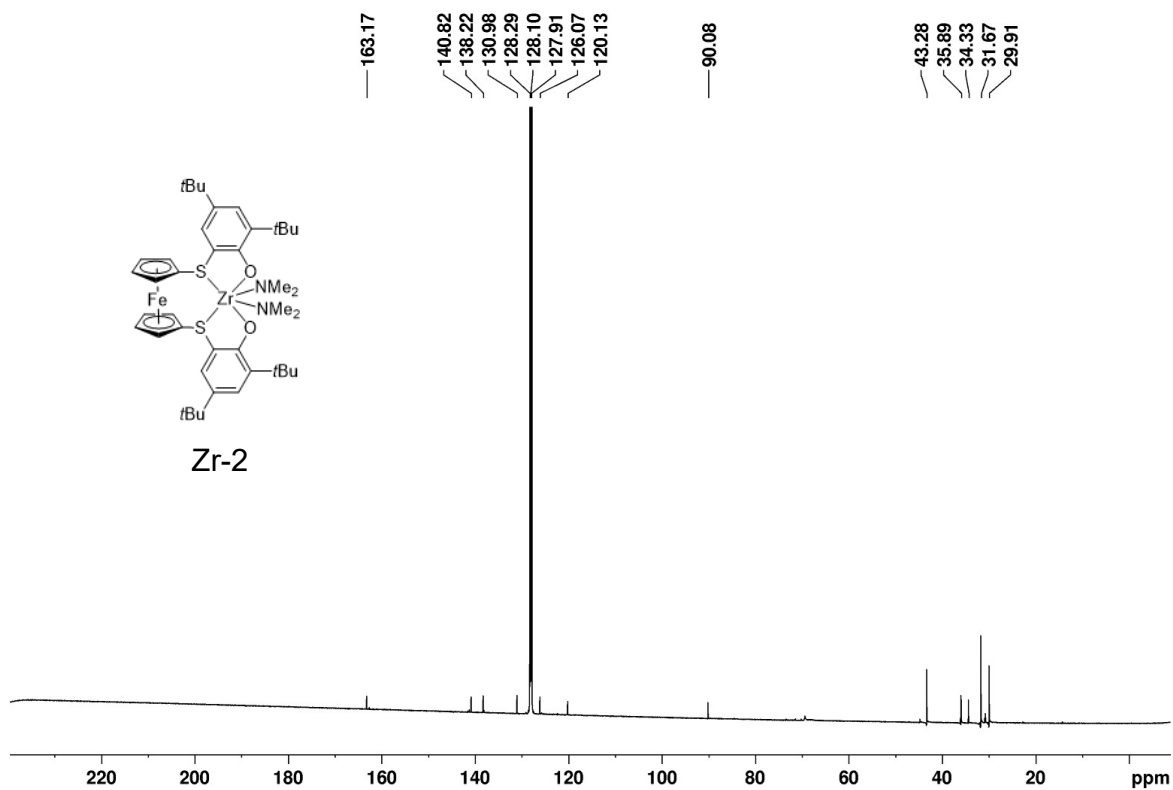


Figure A6. ^{13}C NMR (C_6D_6 , 125 MHz, 298K) spectrum of (thiolfan*) $\text{Zr}(\text{NMe}_2)_2$: δ (ppm) = 163.2 (ArC), 140.8 (ArC), 138.2, (ArC), 131.0 (ArCH), 126.1 (ArCH), 120.1 (ArC), 90.1 (Cp), 69.3(Cp), 43.3 (NCH₃), 35.9($\text{C}(\text{CH}_3)_3$), 34.3 ($\text{C}(\text{CH}_3)_3$), 31.7 ($\text{C}(\text{CH}_3)_3$), 29.9 ($\text{C}(\text{CH}_3)_3$).

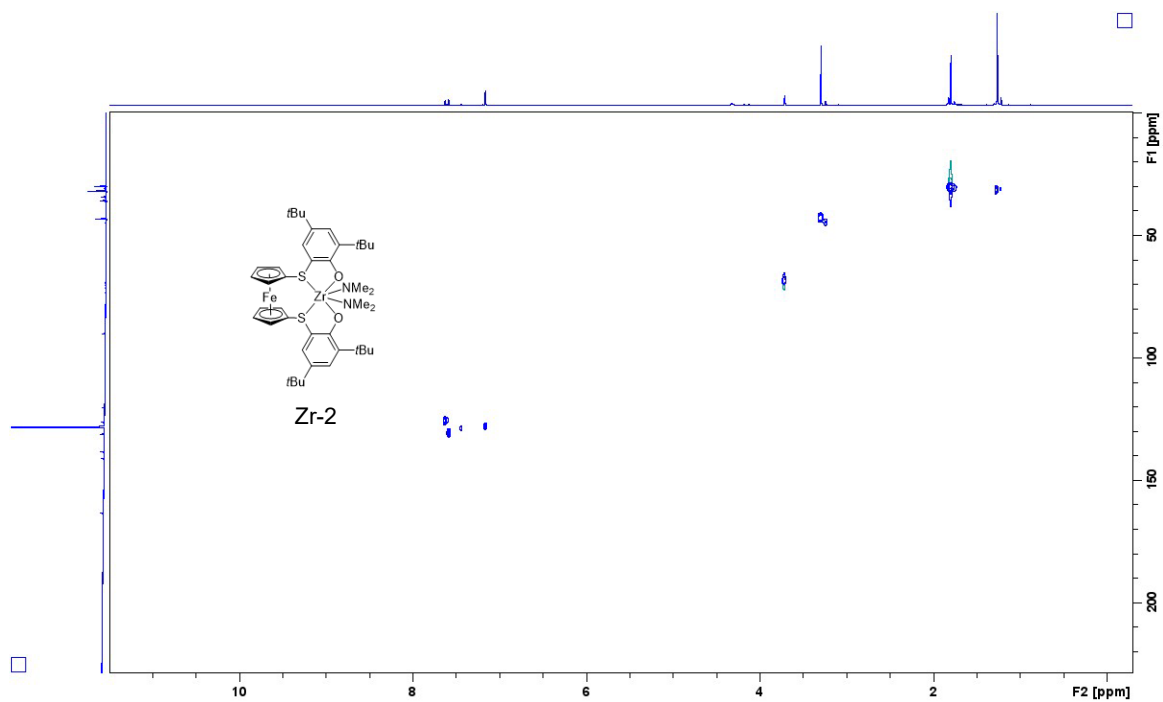


Figure A7: HSQC (C₆D₆, 500MHz, 298K) spectrum of (thiolfan*)Zr(NMe₂)₂.

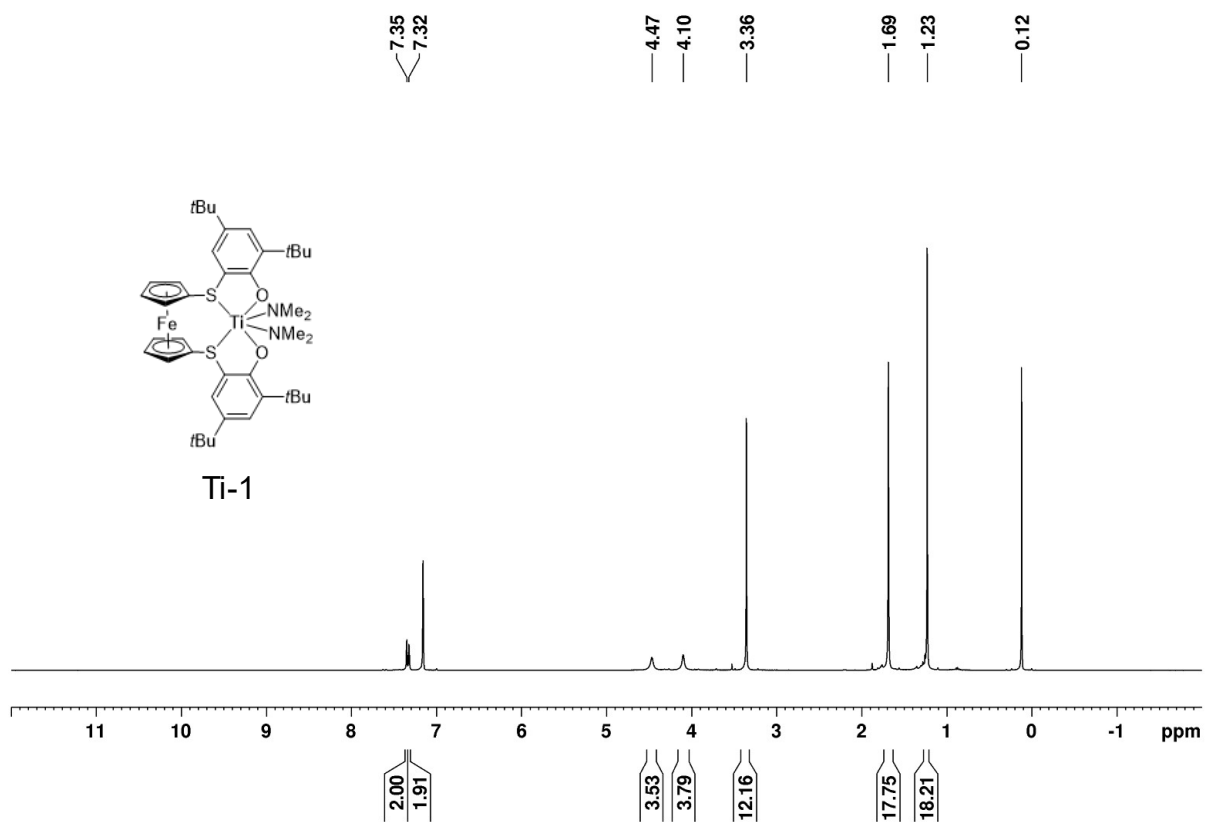


Figure A8. ^1H NMR (C_6D_6 , 300MHz, 298K) spectrum of (thiolfan*) $\text{Ti}(\text{NMe}_2)_2$: δ (ppm) = 7.35 (d, 2H ArH), 7.32 (d, 2H ArH), 4.47 (s, 4H CpH), 4.10 (t, 4H CpH), 3.36 (s, 12H, N CH_3), 1.69 (s, 18H, $\text{C}(\text{CH}_3)_3$), 1.23 (s, 18H, $\text{C}(\text{CH}_3)_3$). The peak at 0.12 ppm is attributed to the residual HMDSO.

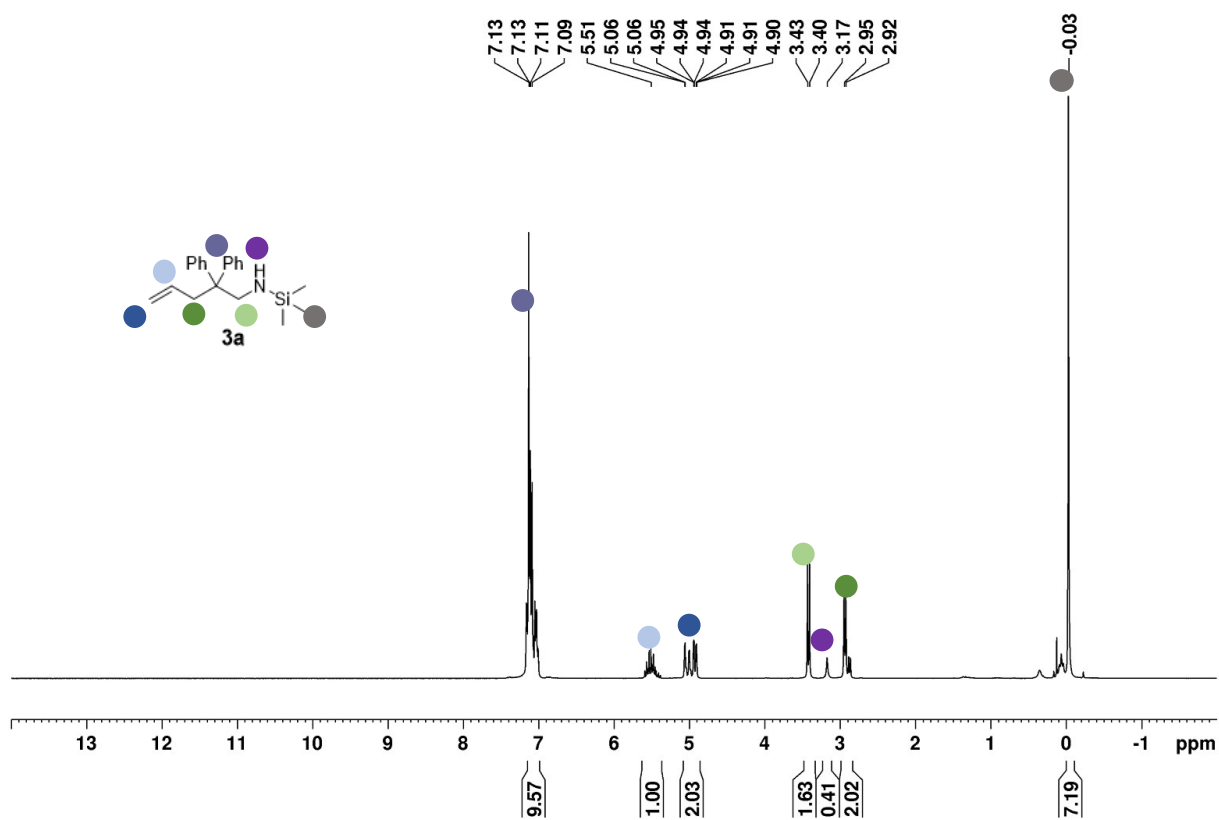


Figure A9. ^1H NMR (C_6D_6 , 300 MHz, 298 K) spectrum of **3a**: δ (ppm) = 7.13-7.09 (m, 10 H, ArH), 5.51-5.06 (m, 1H, $\text{CH}=\text{CH}_2$), 4.95-4.91 (dd, 2H, $\text{CH}=\text{CH}_2$), 3.40 (d, $J = 8.7$ Hz, 2H, CH_2NH), 3.17 (br, 1H, NH), 2.92 (d, $J = 6.5$ Hz, 2H, CHCH_2), -0.03 (s, 9H, $\text{Si}(\text{CH}_3)_3$).

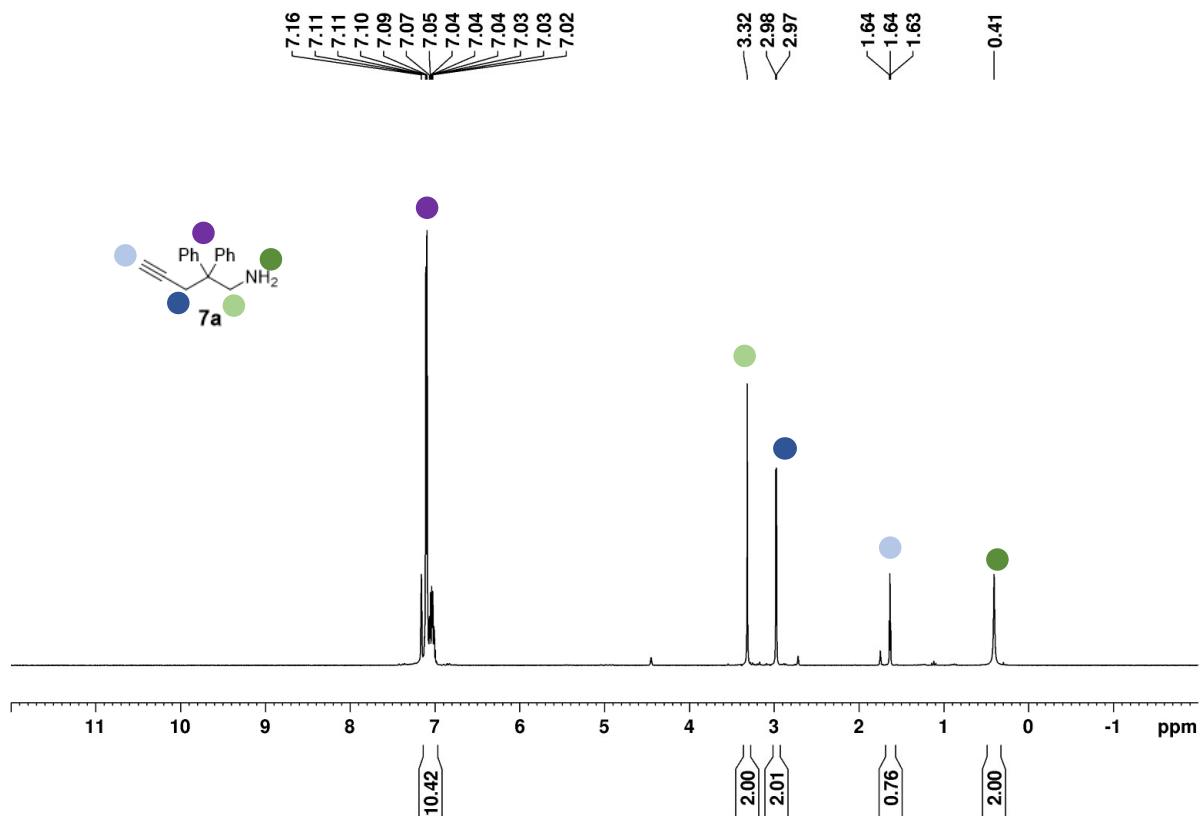


Figure A10. ¹H NMR (C₆D₆, 300MHz, 298K) spectrum of **7a**: δ (ppm) = 7.11-7.09 (m, 10 H, ArH), 3.32 (s, 2H, CH₂NH₂), 2.98 (d, 2H, *J* = 2.5 Hz, CH≡CCH₂), 1.63 (s, 1H, C≡CH), 0.41 (s, 2H, NH₂).

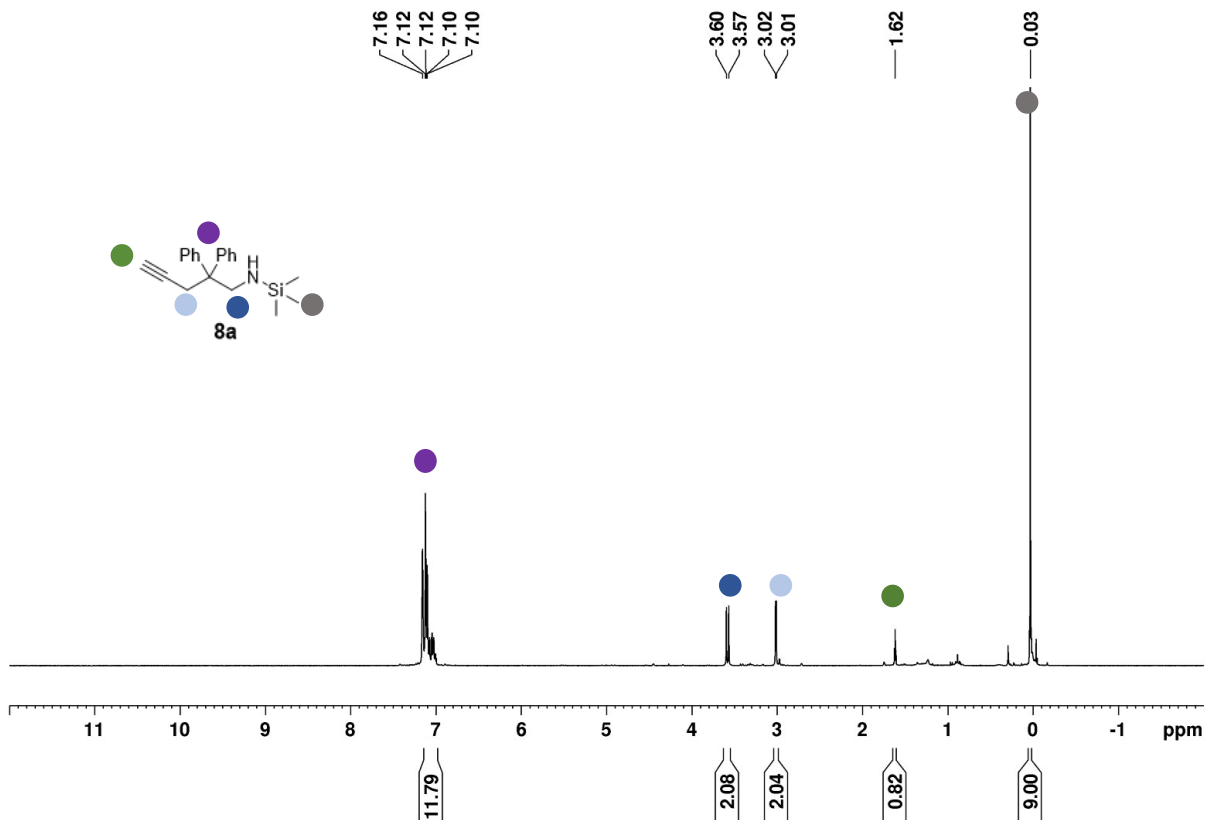


Figure A11. ^1H NMR (C_6D_6 , 300MHz, 298K) spectrum of **8a**: δ (ppm) = 7.12-7.10 (m, 10 H, ArH), 3.60 (d, $J = 8.2$ Hz, 2H, CH_2NH), 3.01 (dd, $J = 2.7$ Hz, 2H, $\text{CH}=\text{CCH}_2$), 1.62 (t, $J = 2.7$ Hz, 1H, $\text{C}\equiv\text{CH}$), -0.03 (s, 9H, $\text{Si}(\text{CH}_3)_3$).

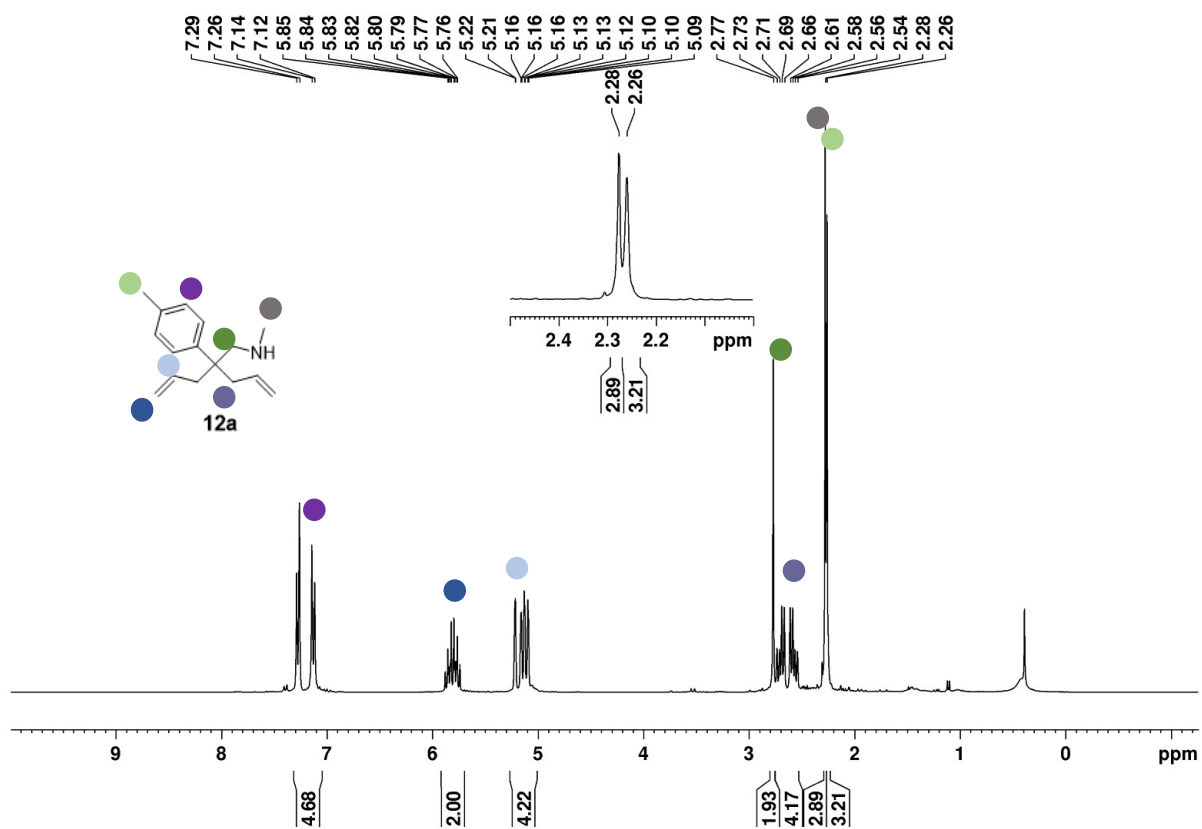


Figure A12. ^1H NMR (C_6D_6 , 300MHz, 298K) spectrum of **12a**: δ (ppm) = 7.23 (d, 2H, J = 7.8 Hz, ArH), 7.13 (d, 2H, J = 7.8 Hz, ArH), 5.65 (m, 2H, $\text{CH}_2=\text{CH}$), 5.04 (m, 4H, $\text{CH}_2=\text{CH}$), 2.73 (s, 2H, NHCH_2), 2.51 (ddd, 4H, $\text{CH}_2=\text{CHCH}_2$), 2.33 (s, 3H, PhCH_3), 2.30 (s, 3H, NHCH_3).

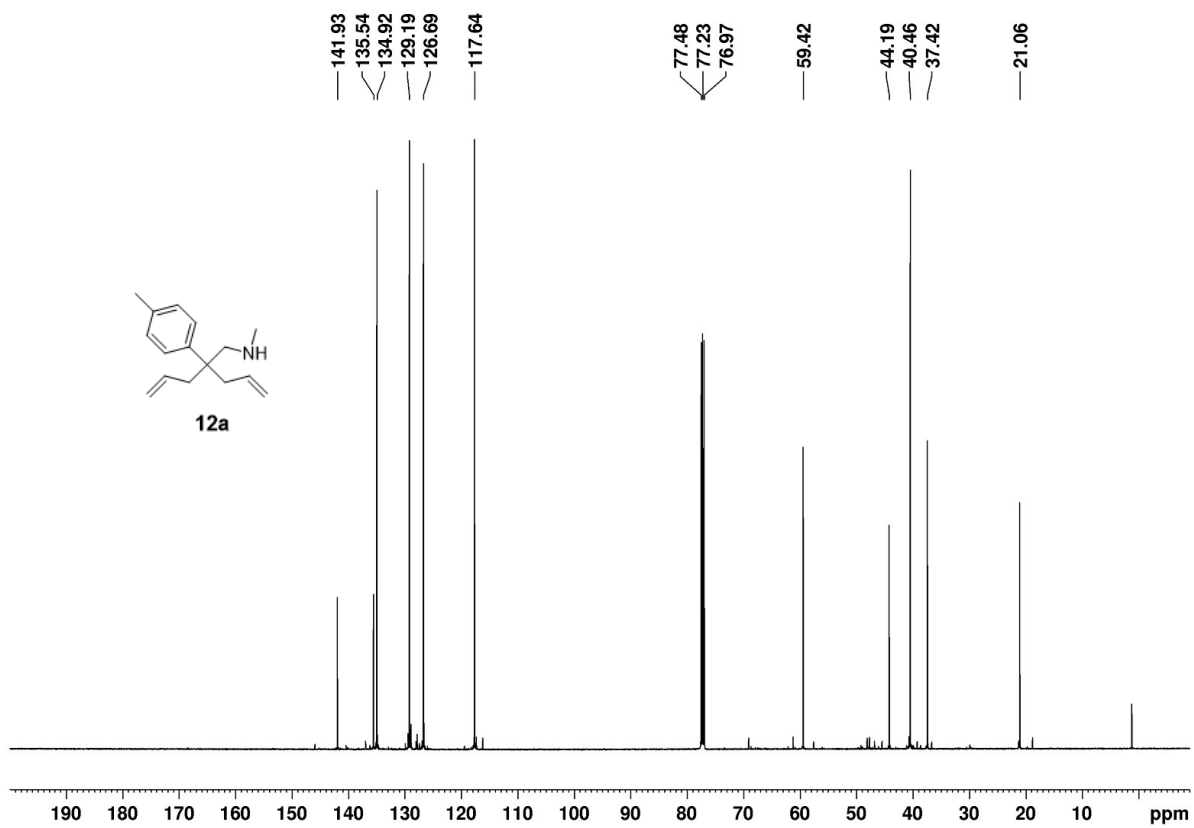


Figure A13. ^{13}C NMR (CDCl_3 , 125 MHz, 298K) spectrum of **12a**: δ (ppm) = 141.9, 135.5, 134.9, 129.2, 126.7, 117.6, 59.4, 44.2, 40.5, 37.4, 21.1.

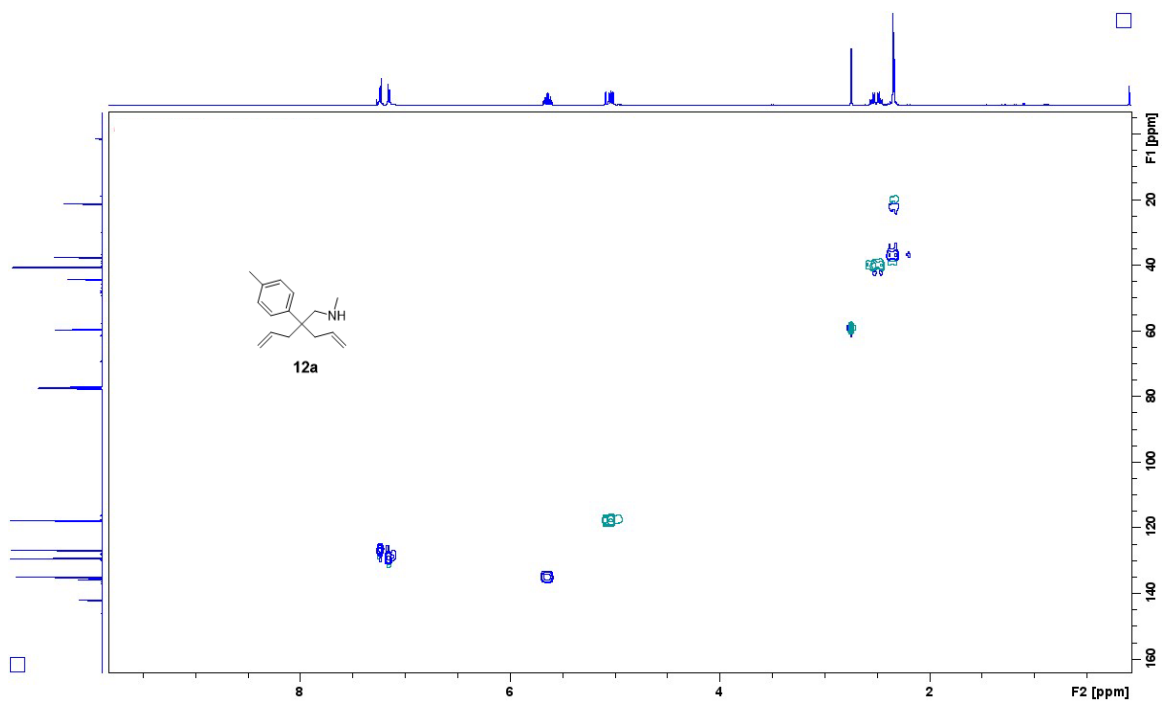


Figure A14. HSQC (C₆D₆, 500MHz, 298K) spectrum of **12a**.

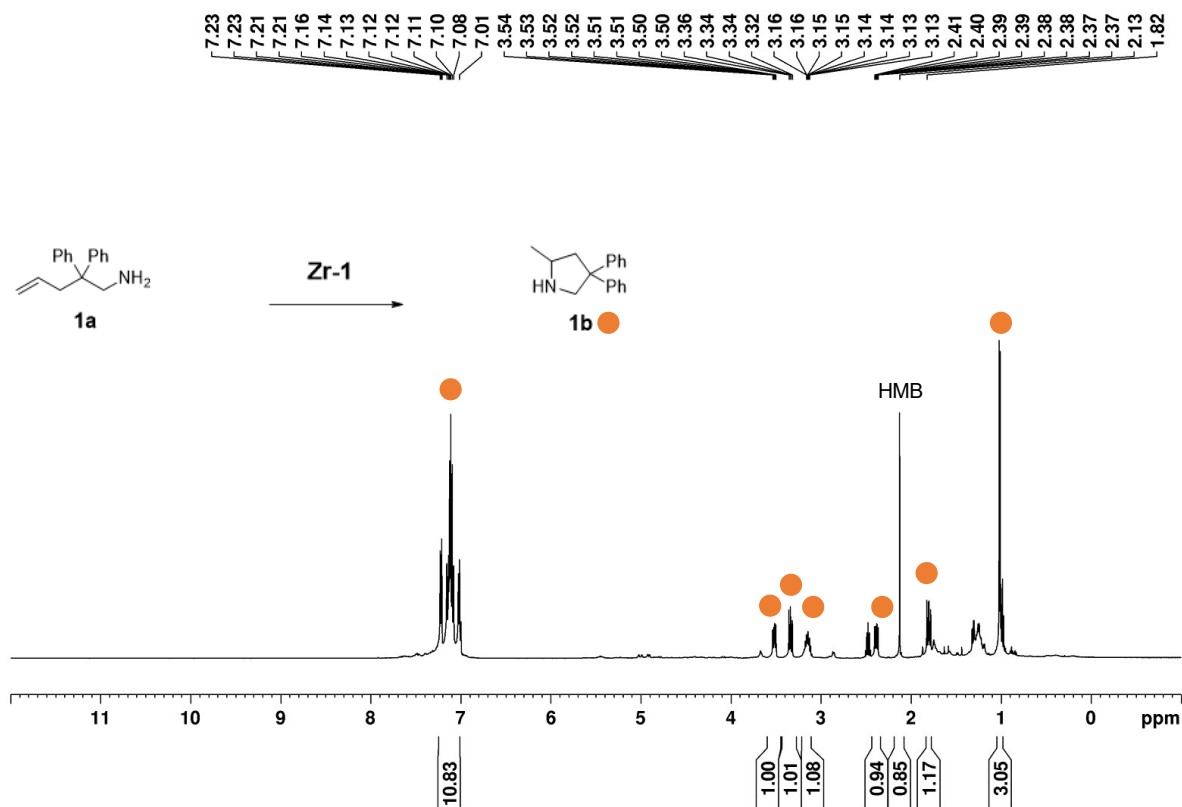


Figure A15. ¹H NMR spectrum (C₆D₆, 500 MHz, 298 K) of **1a** to **1b** catalyzed by **Zr-1** (Table 2.1, entry 1): δ (ppm) = 7.12 (m, 10H ArH), 3.53 (dd, 1H, NHCH₂), 3.35 (dd, 1H, NHCH₂), 3.14 (m, 1H, NHCHCH₃), 2.38 (dd, J = 8.1, 12.6 Hz, 1H, NCHCH₂), 1.82 (dd, J = 8.9, 12.4 Hz, 1H, NHCHCH₂), 1.02 (d, J = 6.2 Hz, 3H CHCH₃),

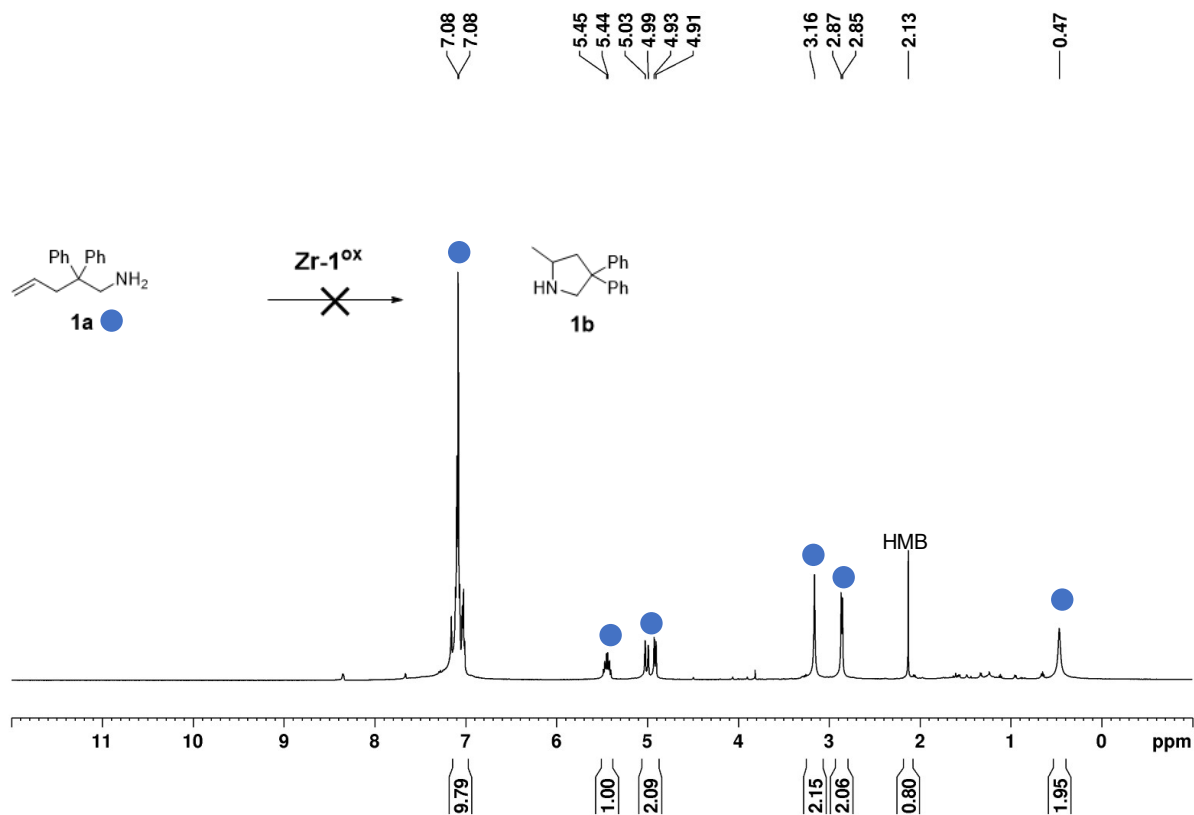


Figure A16. ^1H NMR spectrum (C_6D_6 , 500 MHz, 298 K) of **1a** catalyzed by **Zr-1^{ox}** (Table 2.1, entry 2): δ (ppm) = 7.08 (m, 10H, ArH), 5.45 (m, 1H, $\text{CH}_2=\text{CH}$), 5.02-4.91 (m, 2H, $\text{CH}_2=\text{CH}$), 3.16 (s, 2H, NH_2CH_2), 0.46 (s, 2H, NH_2), 2.88 (d, 2H, $J = 7.0$ Hz, CHCH_2),

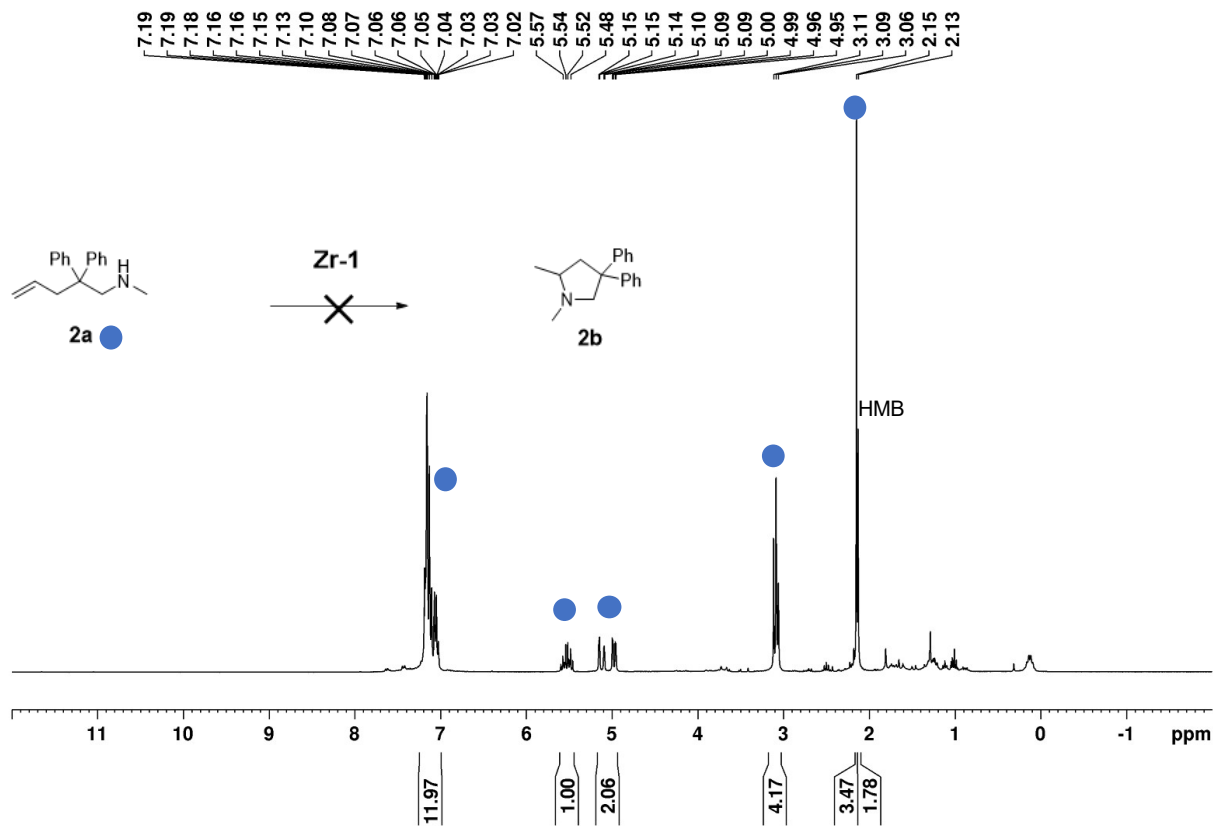


Figure A17. ¹H NMR spectrum (C₆D₆, 300 MHz, 298 K) of **2a** catalyzed by **Zr-1** (Table 2.1, entry 3): δ (ppm) = 7.19-7.02 (m, 10H, ArH), 5.57-5.48 (m, 1H, CH₂=CH), 4.99-4.95 (m, 2H, CH₂=CH), 3.11 (d, J = 7.3 Hz, 2H, CHCH₂), 3.06 (s, 2H, NHCH₂), 2.15 (s, 3H, NHCH₃).

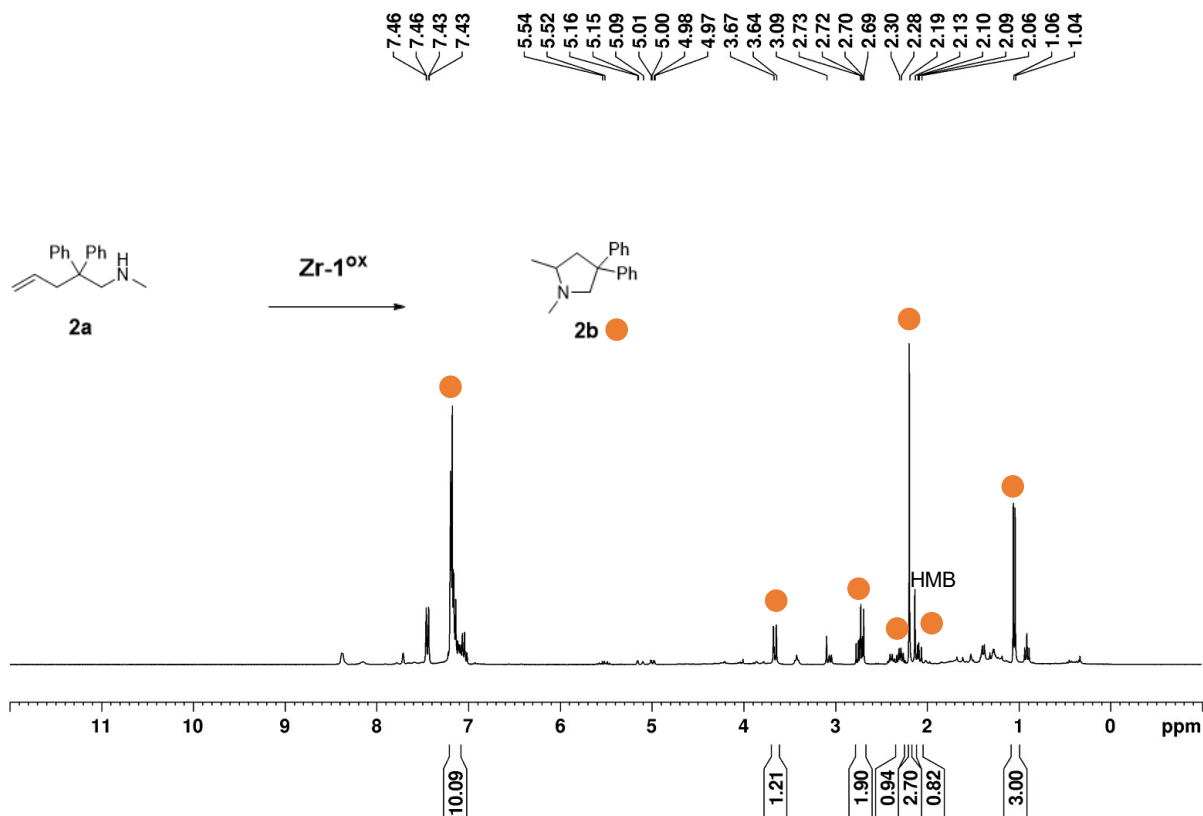


Figure A18. ^1H NMR spectrum (C_6D_6 , 300 MHz, 298 K) of **2a** to **2b** catalyzed by **Zr-1^{ox}** (Table 2.1, entry 4): δ (ppm) = 7.46-7.43 (m, 10H, ArH), 3.65 (d, 1H, $J = 9.5$ Hz, NCHCH₃), 2.71 (m, 2H, NCH₂C), 2.28 (m, 1H, CH₃CHCH₂), 2.08 (s, 3H, NCH₃), 2.06 (t, $J = 4.4$ Hz, 1H, CH₃CHCH₂), 1.04 (d, $J = 6.3$ Hz, 3H, CHCH₃).

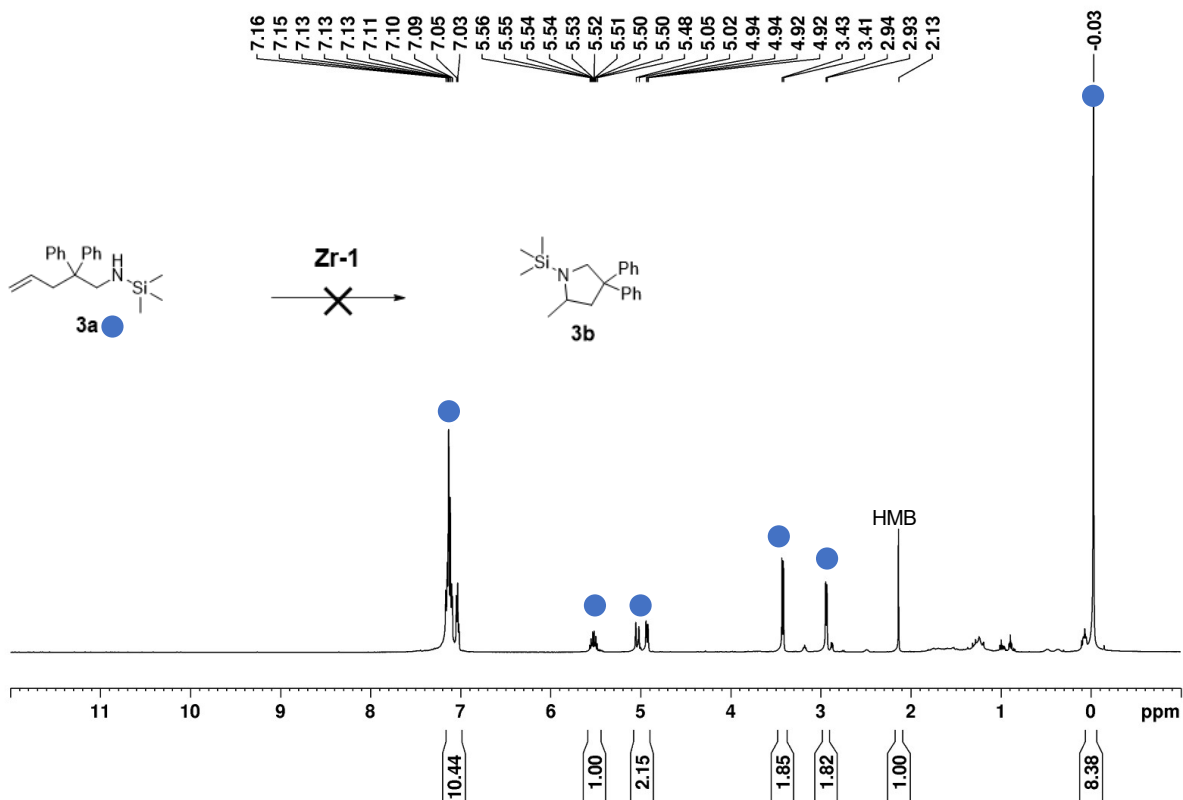


Figure A19. ¹H NMR spectrum (C₆D₆, 500 MHz, 298 K) of **3a** catalyzed by **Zr-1** (Table 2.1, entry 5): δ (ppm) = 7.16-7.03 (m, 10H, ArH), 5.56-5.48 (m, 1H, CH₂=CH), 5.05-4.92 (m, 2H, CH₂=CH), 3.42 (d, J = 7.4 Hz, 2H, NHCH₂), 2.94 (d, J = 7.2 Hz, 2H, CHCH₂), -0.03 (s, 9H, Si(CH₃)₃).

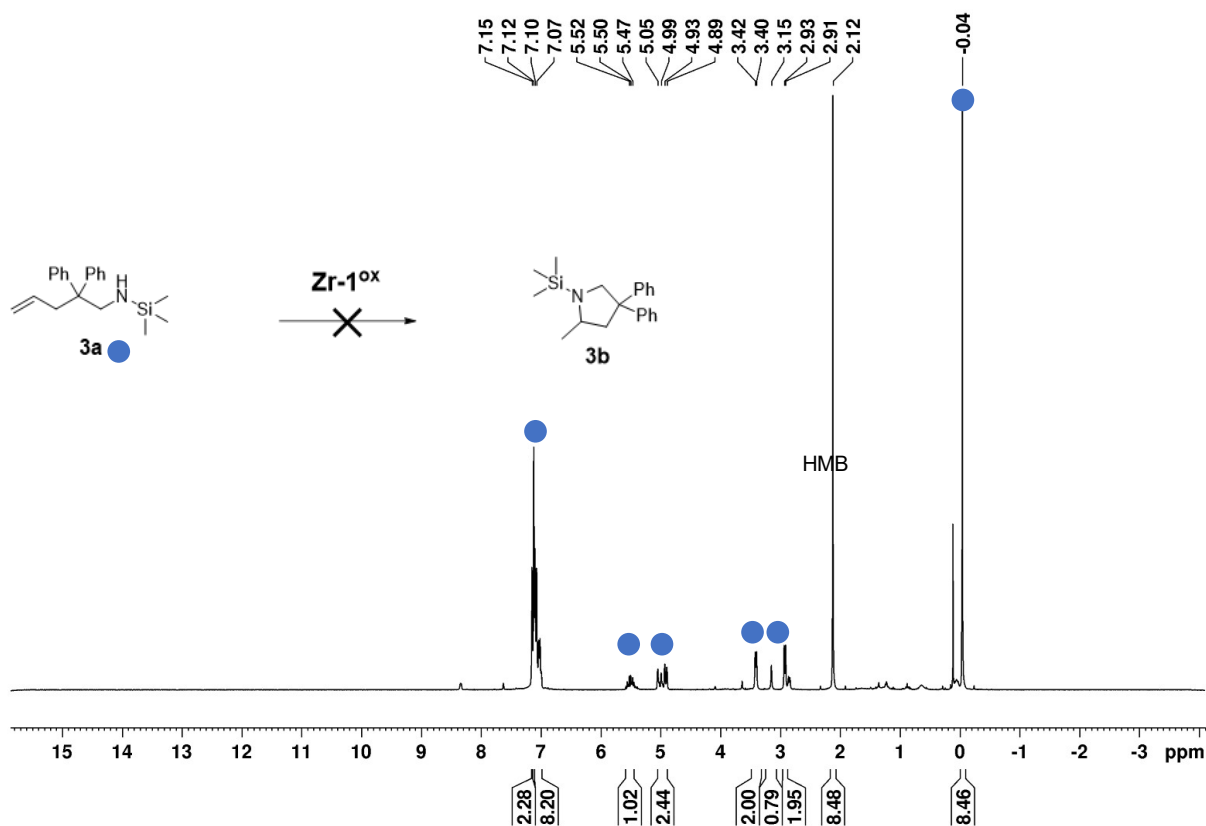


Figure A20. ¹H NMR spectrum (C₆D₆, 300 MHz, 298 K) of **3a** catalyzed by **Zr-1^{ox}** (Table 2.1, entry 6): δ (ppm) = 7.16-7.07 (m, 10H, ArH), 5.56-5.48 (m, 1H, CH₂=CH), 5.05-4.89 (m, 2H, CH₂=CH), 3.41 (d, *J* = 7.4 Hz, 2H, NHCH₂), 2.94 (d, *J* = 7.2 Hz, 2H, CHCH₂), -0.04 (s, 9H, Si(CH₃)₃).

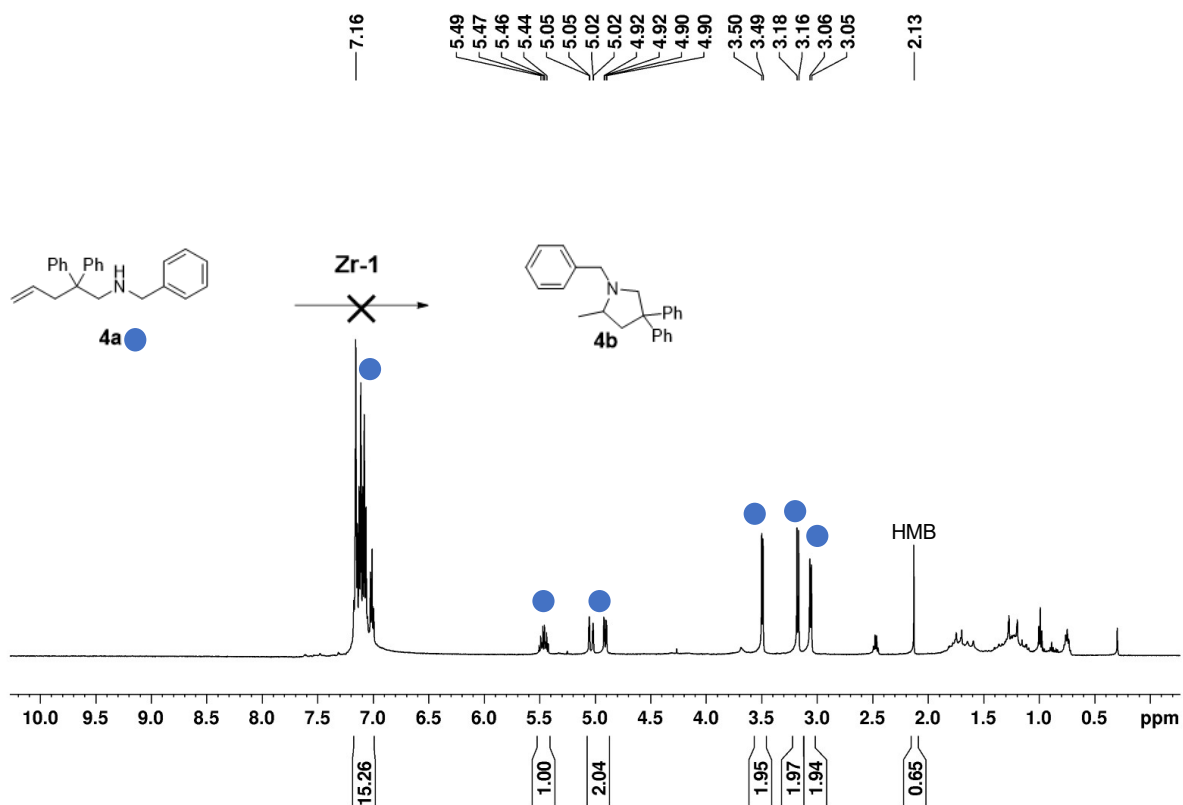


Figure A21. ¹H NMR spectrum (C₆D₆, 500 MHz, 298 K) of **4a** catalyzed by **Zr-1** (Table 2.1, entry 7): δ (ppm) = 7.16-7.03 (m, 15H, ArH), 5.49-5.44 (m, 1H, CH₂=CH), 5.05-4.90 (m, 2H, CH₂=CH), 3.49 (d, J = 6.5 Hz, 2H, NHCH₂Ph), 3.17 (d, J = 7.8 Hz, 2H, NHCH₂), 3.05 (d, J = 7.5 Hz, 2H, CHCH₂).

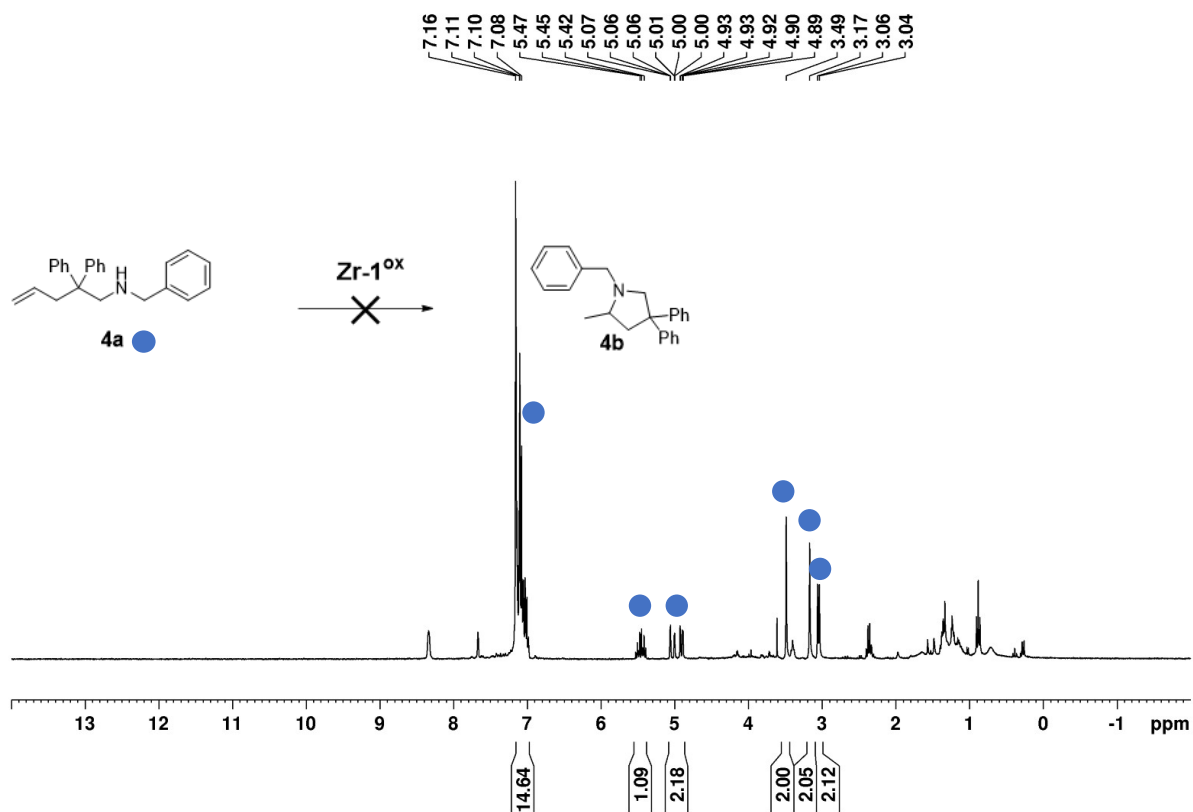


Figure A22. ¹H NMR spectrum (C₆D₆, 300 MHz, 298 K) of **4a** catalyzed by **Zr-1^{ox}** (Table 2.1, entry 8): δ (ppm) = 7.16-7.08 (m, 15H, ArH), 5.47-5.42 (m, 1H, CH₂=CH), 5.07-5.0 (m, 2H, CH₂=CH), 3.49 (, J = 6.5 Hz, 2H, NHCH₂Ph), 3.17 (d, J = 7.8 Hz, 2H, NHCH₂), 3.05 (d, J = 7.5 Hz, 2H, CHCH₂).

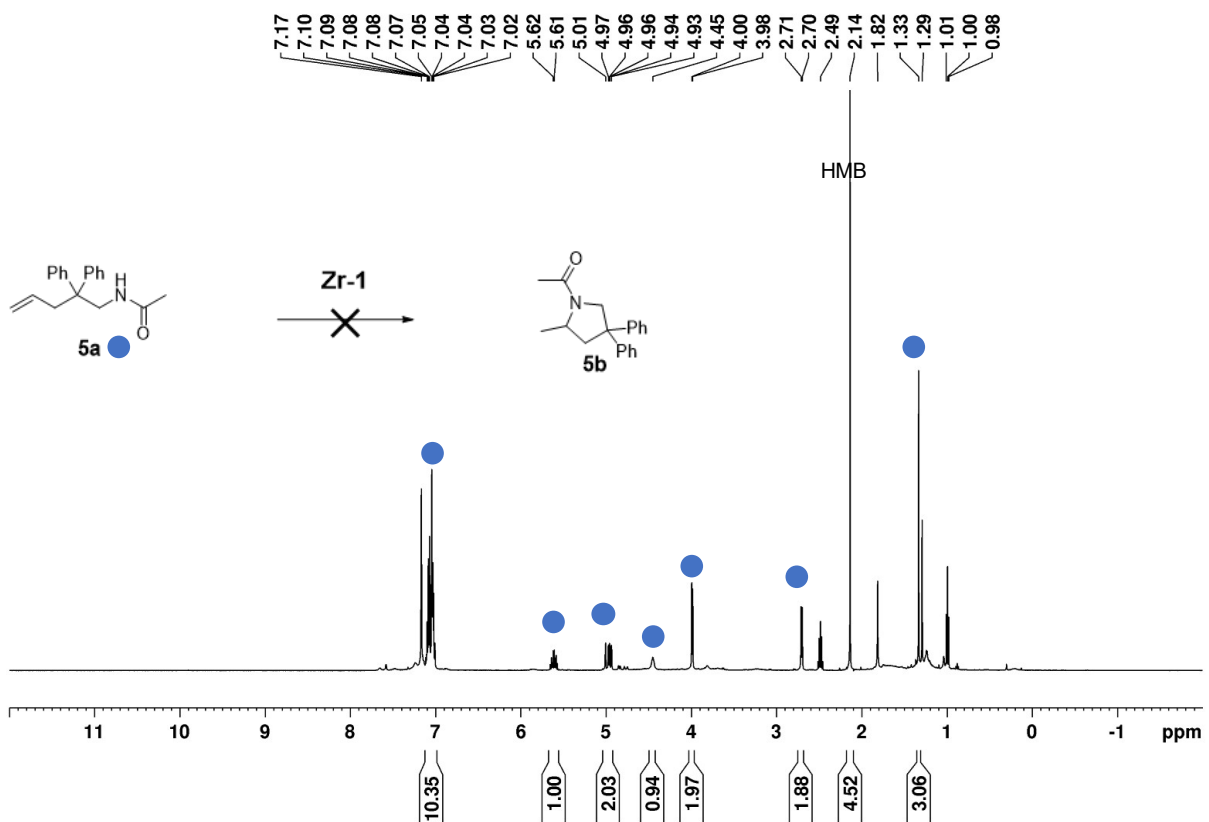


Figure A23. ^1H NMR spectrum (C_6D_6 , 500 MHz, 298 K) of **5a** catalyzed by **Zr-1** (Table 2.1, entry 9): δ (ppm) = 7.17-7.02 (m, 10H, ArH), 5.61 (m, 1H, $\text{CH}_2=\text{CH}$), 5.01-4.94 (m, 2H, $\text{CH}_2=\text{CH}$), 4.45 (br, 1H, NH), 3.99 (d, $J = 6.3$ Hz, 2H, NHCH_2), 2.71 (d, $J = 6.9$ Hz, 2H, CHCH_2), 1.33 (s, 3H, COCH_3). Peaks at 1.1 and 2.48 ppm are attributed to residual triethylamine.

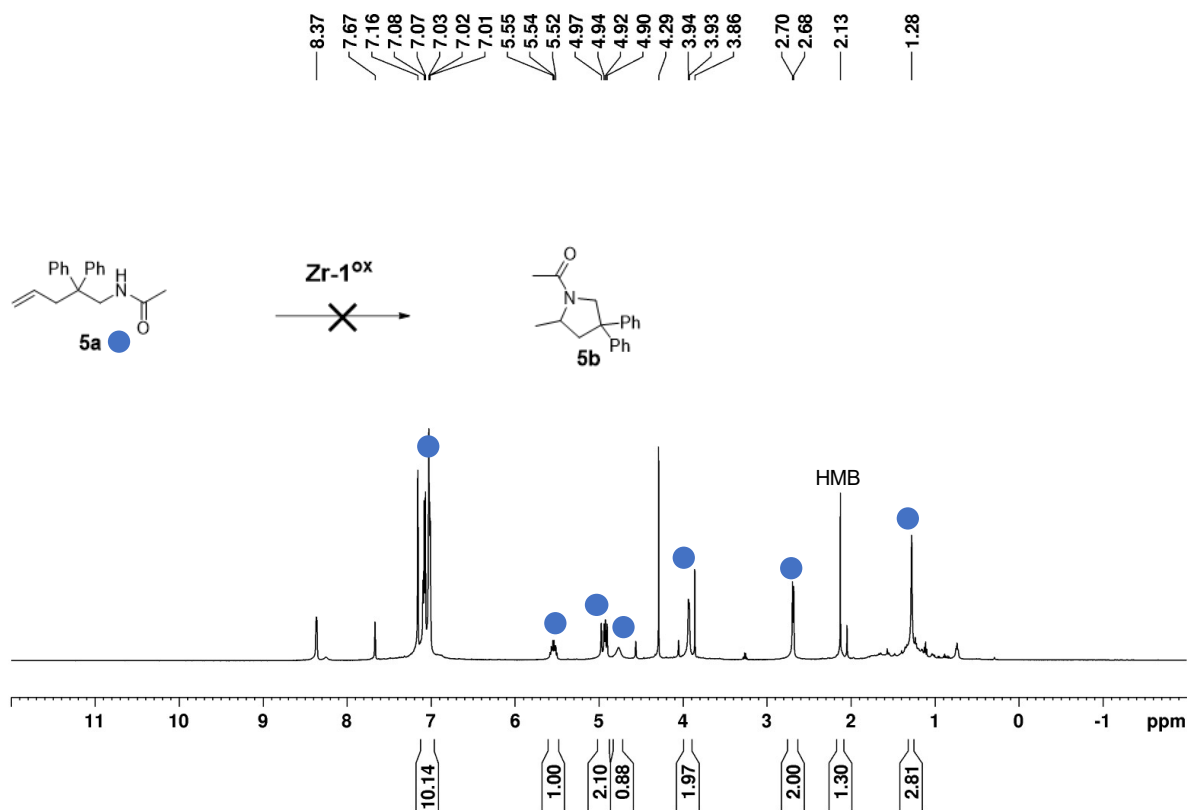


Figure A24. ¹H NMR spectrum (C₆D₆, 500 MHz, 298 K) of **5a** catalyzed by **Zr-1^{ox}** (Table 2.1, entry 10): δ (ppm) = 7.16-7.01 (m, 10H, ArH), 5.55-5.52 (m, 1H, CH₂=CH), 4.97-4.90 (m, 2H, CH₂=CH), 4.29 (br, 1H, NH), 3.94-3.86 (d, J = 6.3 Hz, 2H, NHCH₂), 2.69 (d, J = 6.9 Hz, 2H, CHCH₂), 1.28 (s, 3H, COCH₃). The peak at 4.29 ppm is attributed to residual dichloromethane.

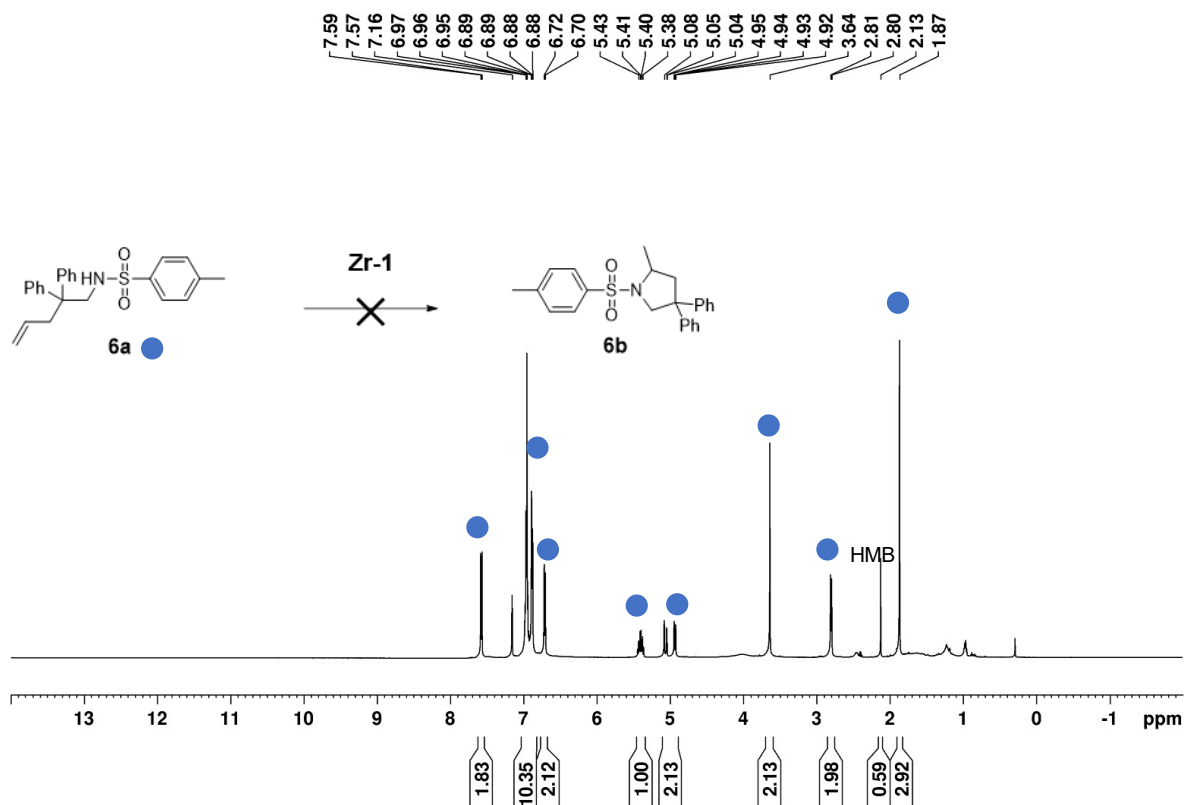


Figure A25. ^1H NMR spectrum (C_6D_6 , 500 MHz, 298 K) of **6a** catalyzed by **Zr-1** (Table 2.1, entry 11): δ (ppm) = 7.58 (d, J = 8.1 Hz, 2H, ArH), 7.16-6.88 (m, 10H, ArH), 6.71 (d, J = 8.1 Hz, 2H, ArH), 5.43-5.40 (m, 1H, $\text{CH}_2=\text{CH}$), 4.95-4.99 (m, 2H, $\text{CH}_2=\text{CH}$), 3.64 (s, 2H, NHCH_2), 2.80 (d, J = 7.4 Hz, 2H, CHCH_2), 1.87 (s, 3H, CCH_3).

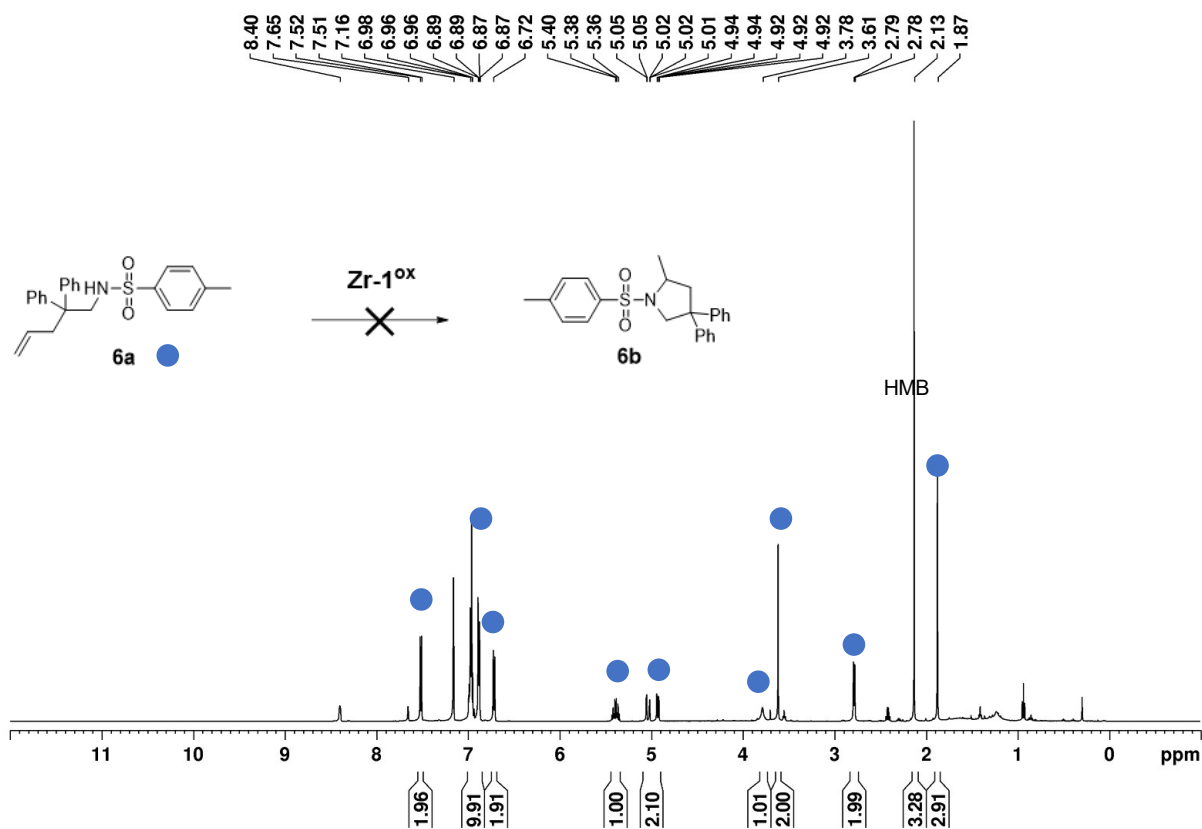


Figure A26. ¹H NMR spectrum (C₆D₆, 500 MHz, 298 K) of **6a** catalyzed by **Zr-1^{ox}** (Table 2.1, entry 12): δ (ppm) = 7.65 (d, *J* = 8.1 Hz, 2H, Ar*H*), 7.16-6.88 (m, 10H, Ar*H*), 6.71 (d, *J* = 8.1 Hz, 2H, Ar*H*), 5.40-5.36 (m, 1H, CH₂=CH), 5.05-4.92 (m, 2H, CH₂=CH), 3.78 (br, 1H, NH), 3.61 (s, 2H, NHCH₂), 2.78 (d, *J* = 7.4 Hz, 2H, CHCH₂), 1.87 (s, 3H, CCH₃).

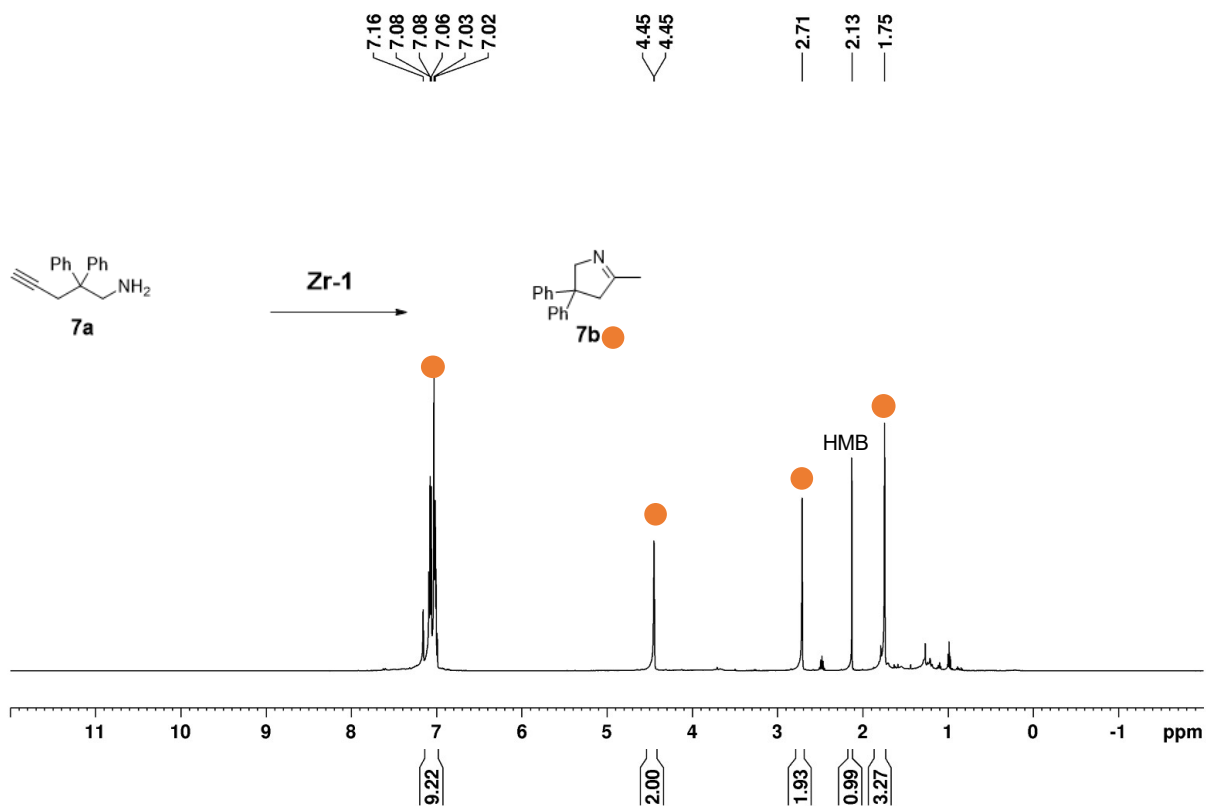


Figure A27. ¹H NMR spectrum (C₆D₆, 500 MHz, 298 K) of **7a** to **7b** catalyzed by **Zr-1** (Table 2.1, entry 13): δ (ppm) = 7.08-7.02 (m, 10H, ArH), 4.45 (s, 2H, NCH₂), 2.71 (s, 2H, CCH₂), 1.75 (s, 3H, CCH₃).

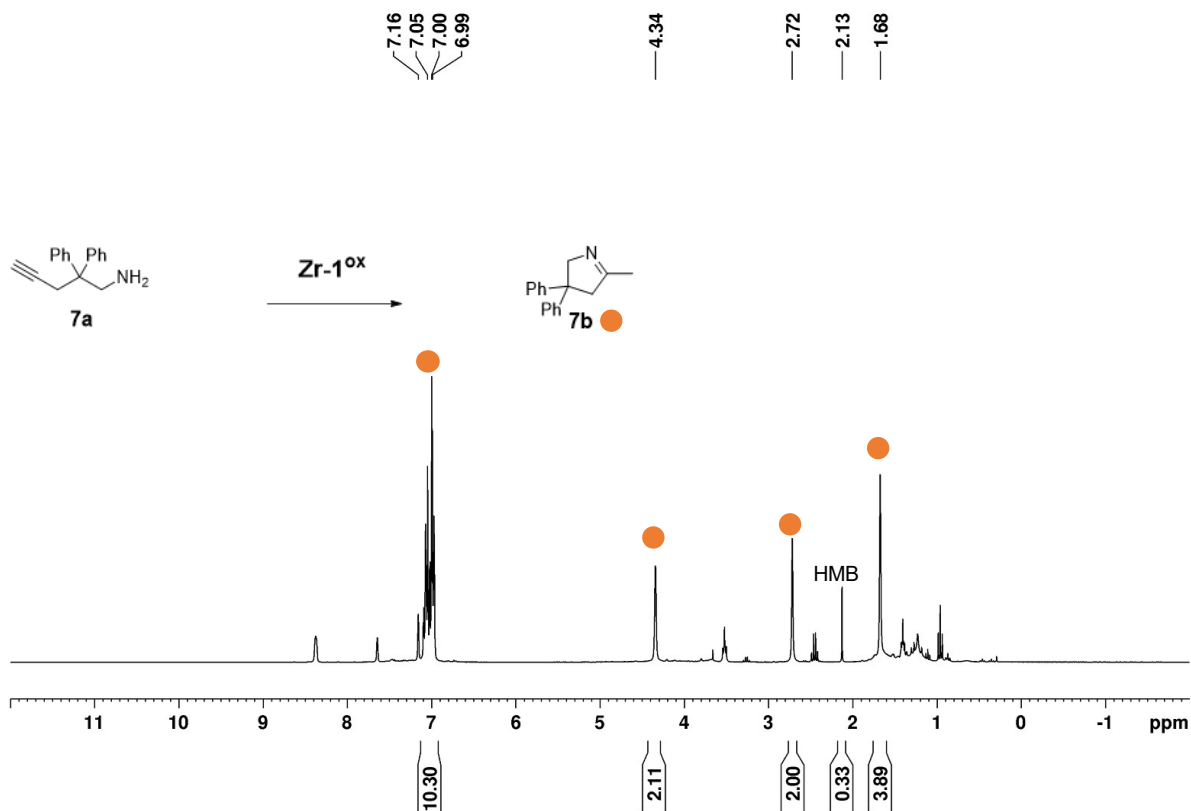


Figure A28. ¹H NMR spectrum (C₆D₆, 300 MHz, 298 K) of **7a** to **7b** catalyzed by **Zr-1^{ox}** (Table 2.1, entry 14): δ (ppm) = 7.05-6.99 (m, 10H, ArH), 4.34 (s, 2H, NCH₂), 2.72 (s, 2H, CCH₂), 1.68 (s, 3H, CCH₃).

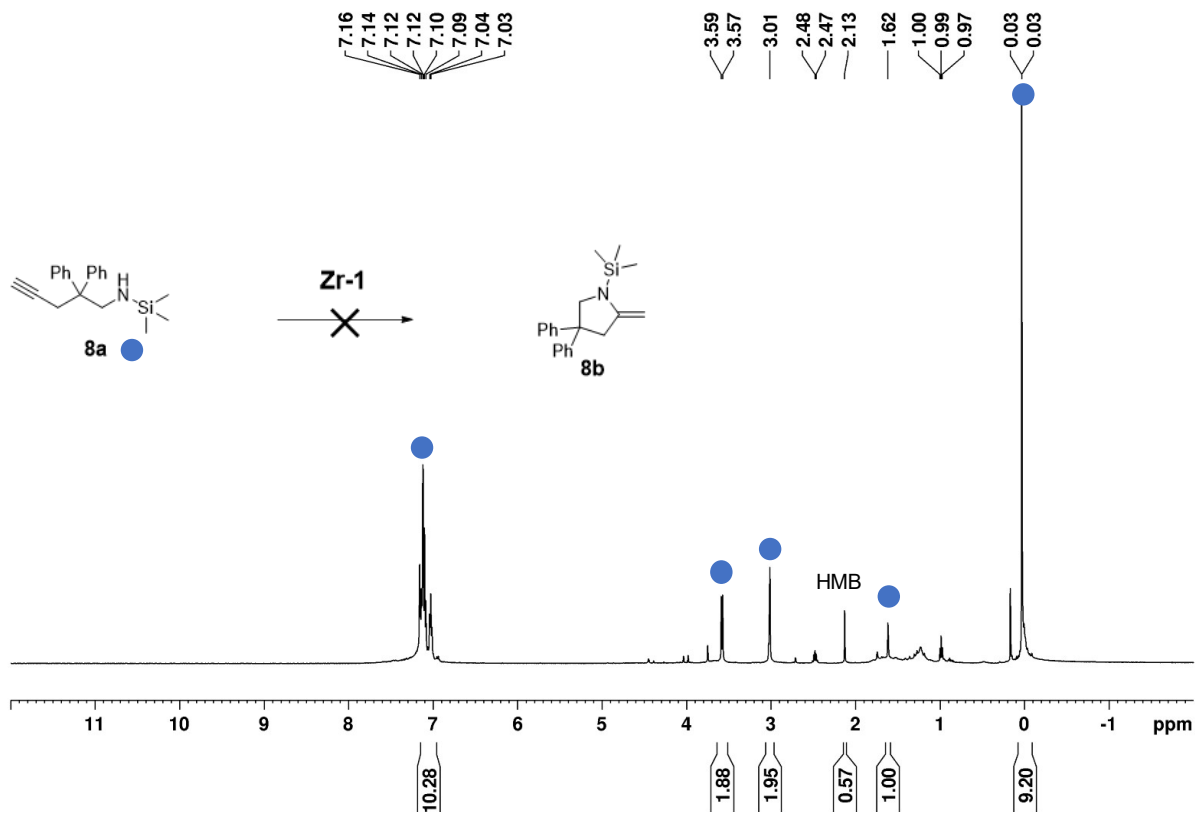


Figure A29. ¹H NMR spectrum (C₆D₆, 500 MHz, 298 K) of **8a** catalyzed by **Zr-1** (Table 2.1, entry 15): δ (ppm) = 7.14-7.03 (m, 10 H, ArH), 3.58 (d, *J* = 8.2 Hz, 2H, CH₂NH), 3.01 (dd, *J* = 2.7 Hz, 2H, CH=CCH₂), 1.62 (t, *J* = 2.7 Hz, 1H, C≡CH), 0.03 (s, 9H, Si(CH₃)₃).

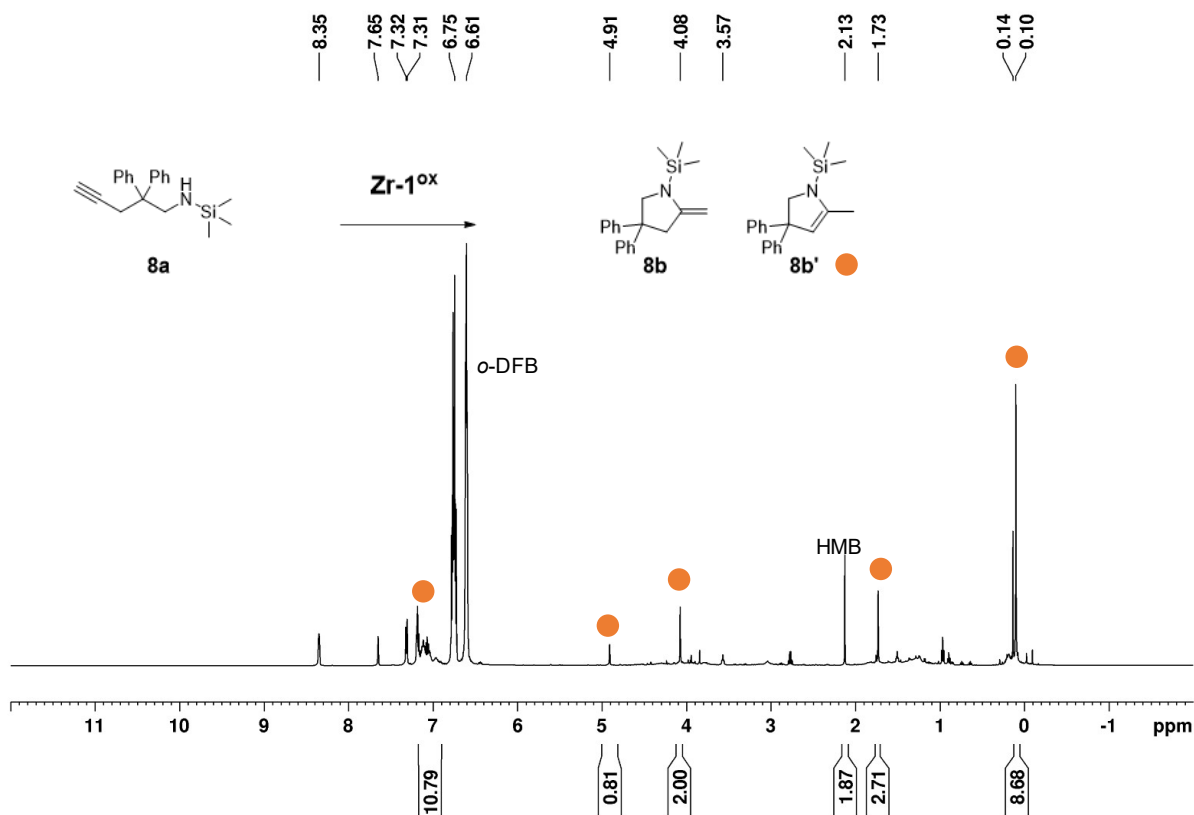


Figure A30. ¹H NMR spectrum (C₆D₆, 500 MHz, 298 K) of **8a** to **8b/8b'** catalyzed by **Zr-1^{ox}** (Table 2.1, entry 16): δ (ppm) = 7.31 (m, 10H, ArH), 4.90 (s, 1H, C=CH), 4.07 (s, 2H, NCH₂), 1.73 (s, 3H, CCH₃), 0.13 (s, 9H, Si(CH₃)₃).

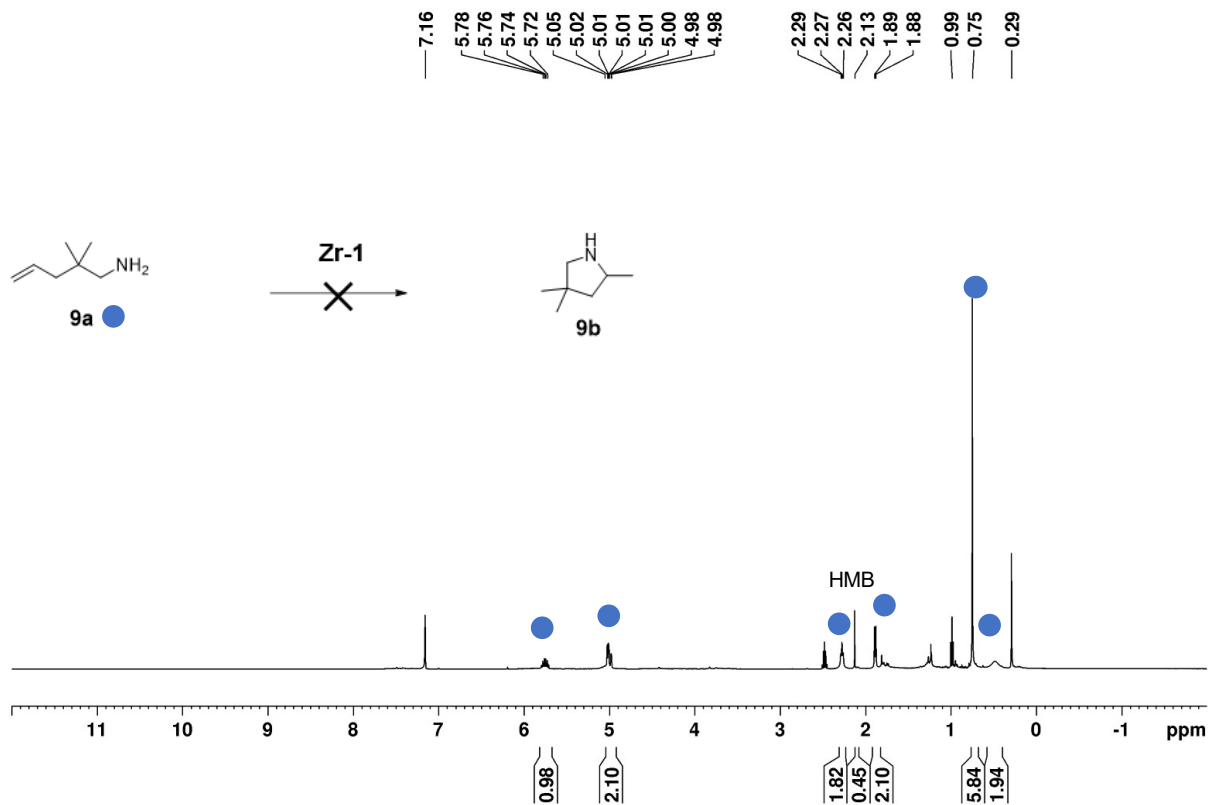


Figure A31. ¹H NMR spectrum (C₆D₆, 500 MHz, 298 K) of **9a** catalyzed by **Zr-1** (Table 2.1, entry 17): δ (ppm) = 5.78-5.72 (m, 1H, C=CH), 5.05-4.98 (m, 2H, C=CH₂), 2.29-2.26 (t, J = 6.6 Hz, 2H, CCH₃), 1.87 (d, J = 7.0 Hz, 2H, CHCH₂), 0.72 (s, 6H, C(CH₃)₂).

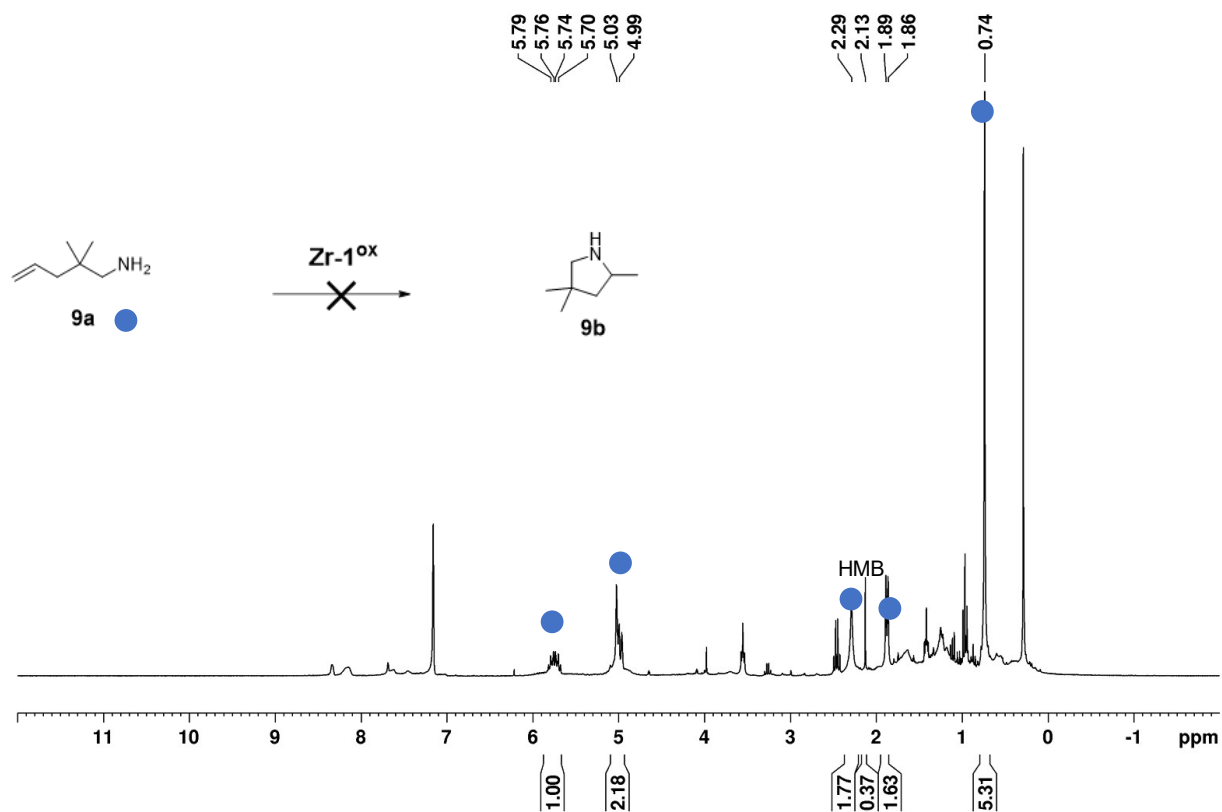


Figure A32. ^1H NMR spectrum (C_6D_6 , 300 MHz, 298 K) of **9a** catalyzed by Zr-1^{ox} (Table 2.1, entry 18): δ (ppm) = 5.78-5.70 (m, 1H, $\text{C}=\text{CH}$), 5.03-4.99 (m, 2H, $\text{C}=\text{CH}_2$), 2.29-2.26 (t, $J = 6.6$ Hz, 2H, NH_2CH_2), 1.87 (d, $J = 7.0$ Hz, 2H, CHCH_2), 0.74 (s, 6H, $\text{C}(\text{CH}_3)_2$).

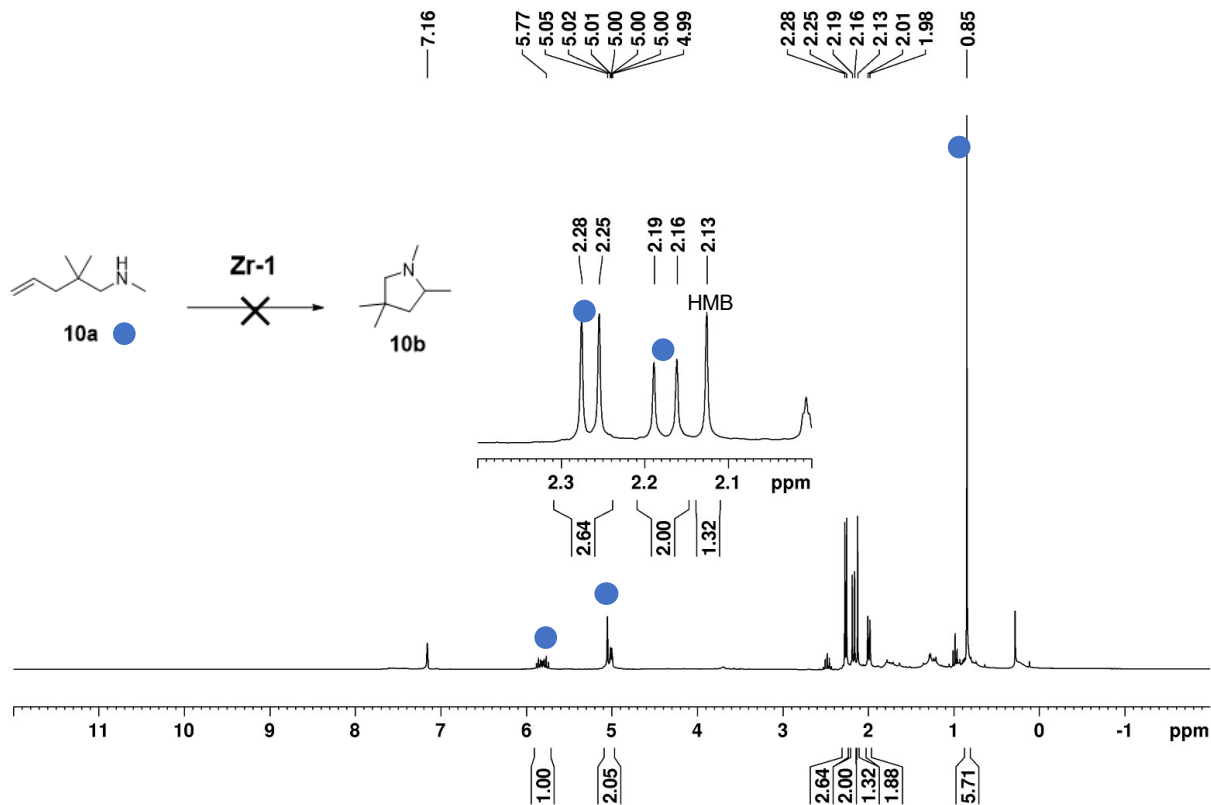


Figure A33. ¹H NMR spectrum (C₆D₆, 300 MHz, 298 K) of **10a** catalyzed by **Zr-1** (Table 2.1, entry 19): δ (ppm) = 5.75 (m, 1H, C=CH), 5.05-4.99 (m, 2H, C=CH₂), 2.28-2.25 (d, J = 6.6 Hz, 3H, NCH₃), 2.16-2.19 (d, J = 8.4 Hz, 2H, NHCH₂), 1.87 (d, J = 7.0 Hz, 2H, CHCH₂), 0.85 (s, 6H, C(CH₃)₂).

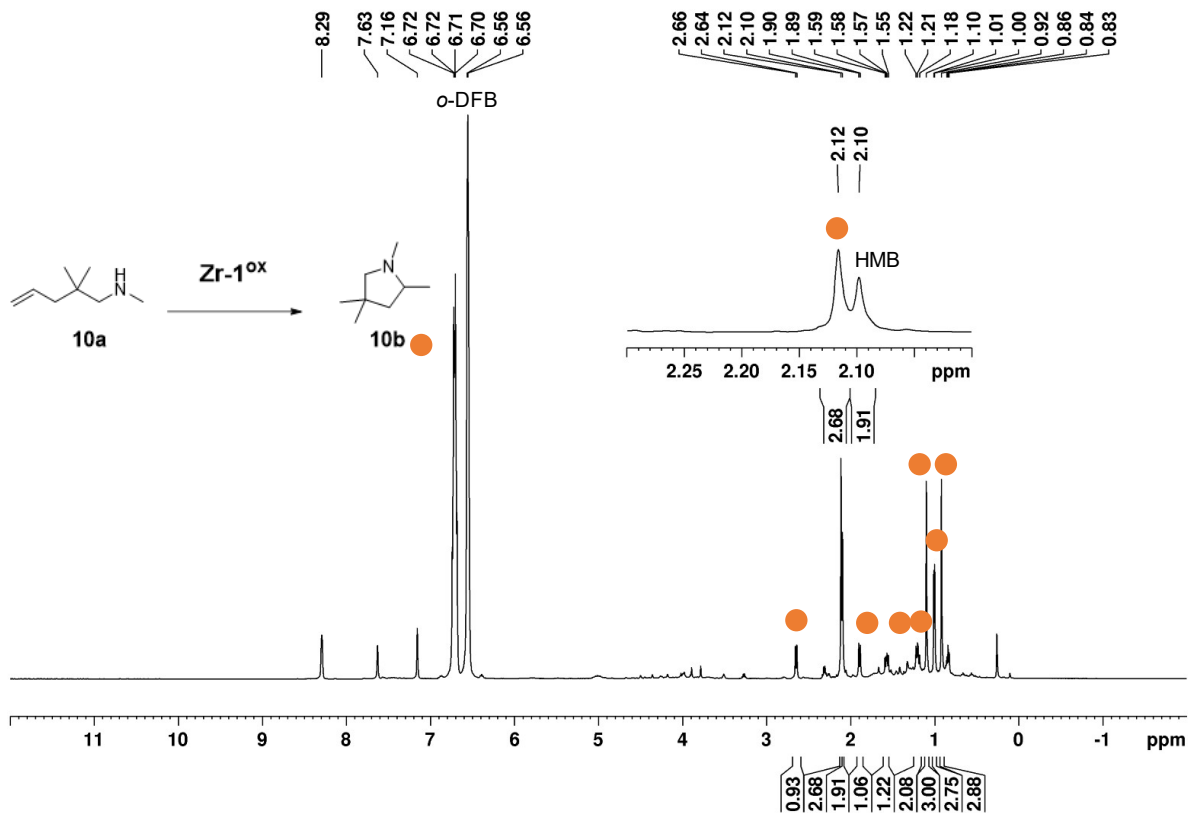


Figure A34. ¹H NMR spectrum (C₆D₆, 500 MHz, 298 K) of **10a** to **10b** catalyzed by **Zr-1^{ox}** (Table 2.1, entry 20): δ (ppm) = 2.65 (d, J = 9.1 Hz, 1H, NCH₂), 2.11 (s, 3H, NCH₃), 1.87 (d, J = 9.6 Hz, 1H, NCH₂), 1.59-1.55 (m, 1H, CCH₂CH), 1.22 (m, 2H, CCH₂CH), 1.10 (s, 3H, CCH₃), 1.01 (d, J = 6.3 Hz, 3H, CHCH₃), 0.92 (s, 3H, CCH₃).

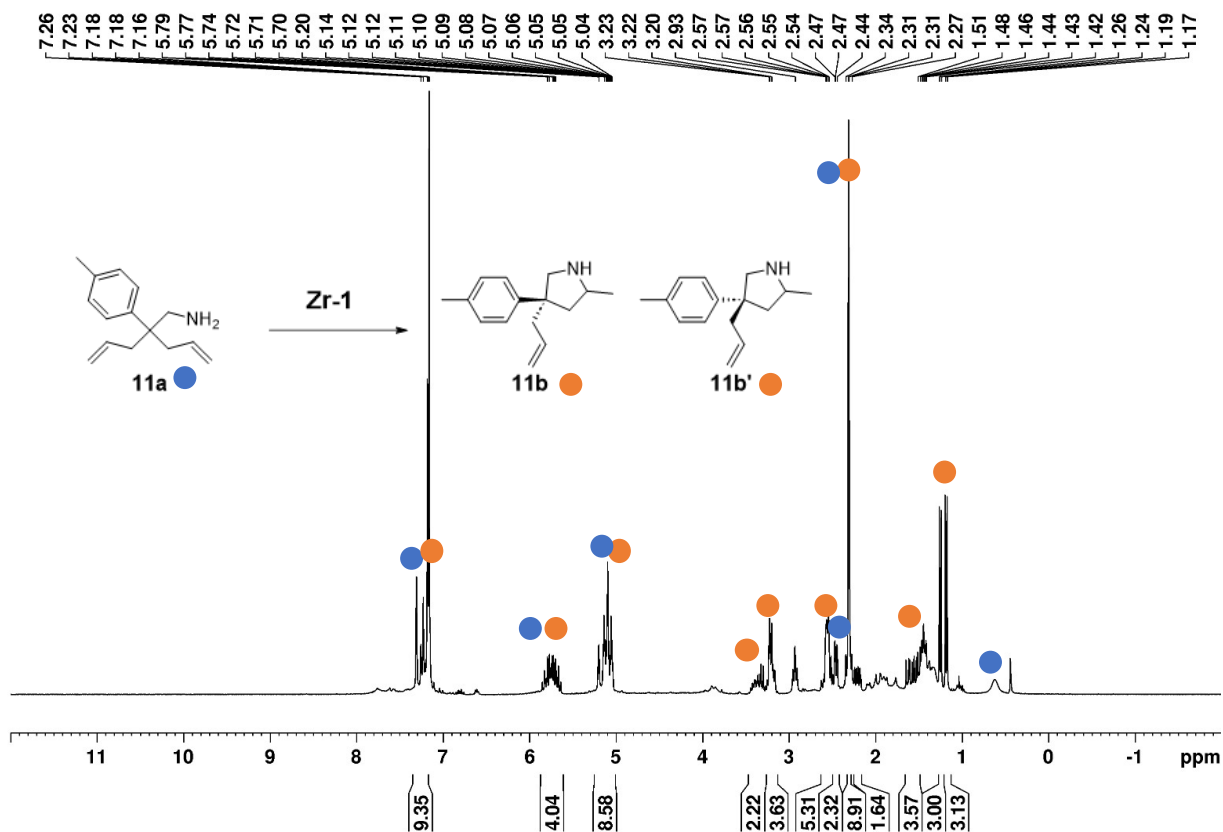


Figure A35. ¹H NMR spectrum (C₆D₆, 300 MHz, 298 K) of **11a** to **11b/11b'** (1:1 isomers) catalyzed by **Zr-1** (Table 2.1, entry 21): δ (ppm) = 7.26-7.18 (m, 10H, ArH), 5.69 (m, 2H, CH=CH₂), 5.07 (m, 4H, CH=CH₂), 3.32 (m, 2H, NHCHCH₃), 3.21 (m, 4H, NHCH₂), 2.47 (m, 4H, CCH₂), 2.10 (s, 6H, PhCH₃), 1.68-1.49 (m, 4H, CHCH₂), 1.05 (d, J = 6.2 Hz, 3H, CHCH₃), 0.97 (d, J = 6.2 Hz, 3H, CHCH₃).

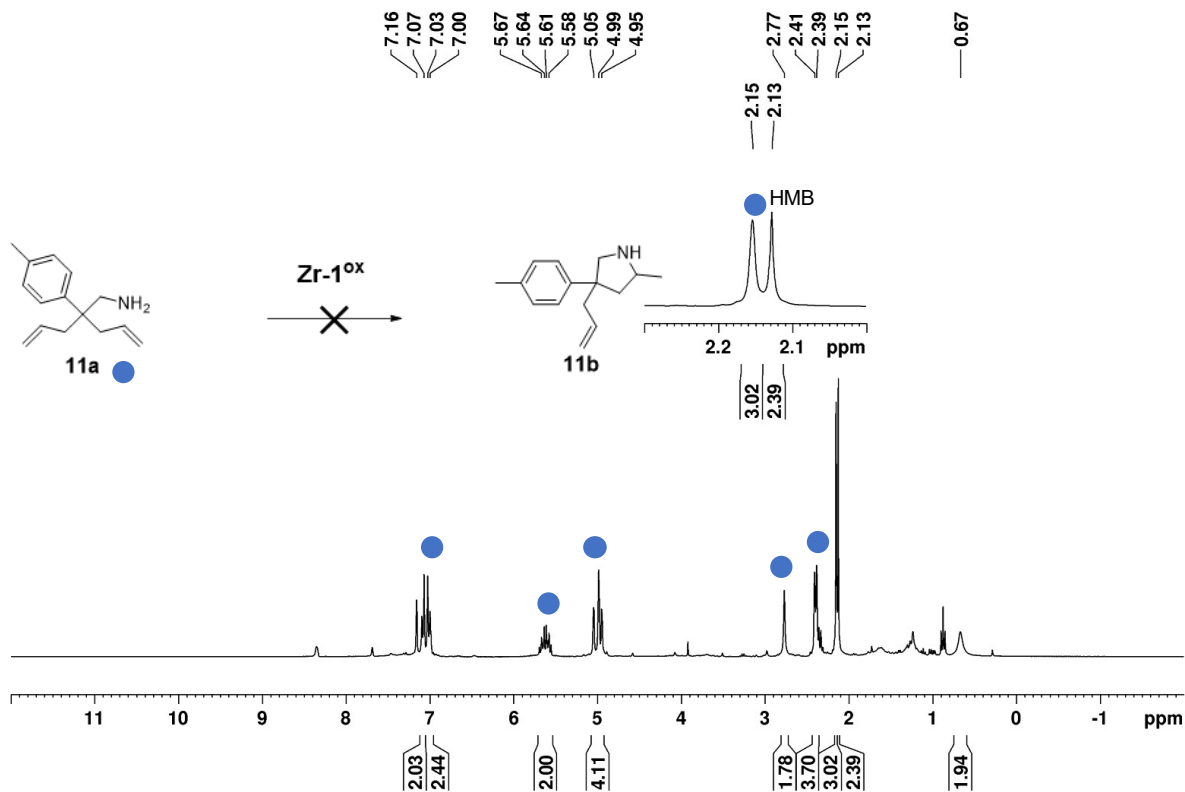


Figure A36. ^1H NMR spectrum (C_6D_6 , 300 MHz, 298 K) of **11a** catalyzed by Zr-1^{ox} (Table 2.1, entry 22): δ (ppm) = 7.06 (d, 2H, $J = 8.4$ Hz, ArH), 7.03 (d, 2H, $J = 8.4$ Hz, ArH), 5.65-5.58 (m, 2H, $\text{CH}_2=\text{CH}$), 5.05-4.95 (m, 4H, $\text{CH}_2=\text{CH}$), 2.77 (s, 2H, NHCH_2), 2.41-2.39 (m, 4H, $\text{CH}_2=\text{CHCH}_2$), 2.15 (s, 3H, PhCH_3), 0.67 (s, 2H, NH_2).

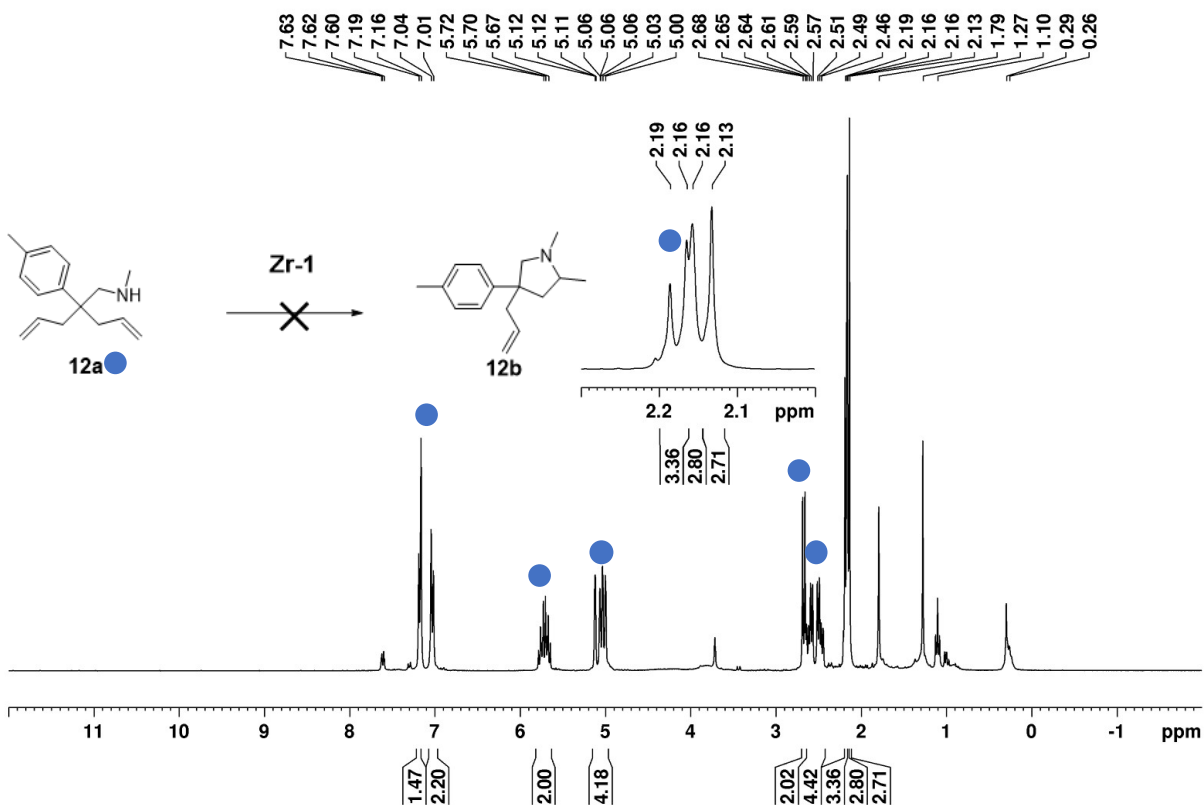


Figure A37. ¹H NMR spectrum (C₆D₆, 300 MHz, 298 K) of **12a** catalyzed by **Zr-1** (Table 2.1, entry 23): δ (ppm) = 7.19 (d, 2H, *J* = 7.8 Hz, Ar*H*), 7.03 (d, 2H, *J* = 7.8 Hz, Ar*H*), 5.72-5.67 (m, 2H, CH₂=CH), 5.12-5.0 (m, 4H, CH₂=CH), 2.68 (d, *J* = 7.8 Hz, 2H, NHCH₂), 2.6-2.45 (m, 4H, CH₂=CHCH₂), 2.19 (br, 3H, NHCH₃), 2.16 (s, 3H, PhCH₃). The peaks at 1.27, 1.78, and 7.62 ppm are attributed to **Zr-1**.

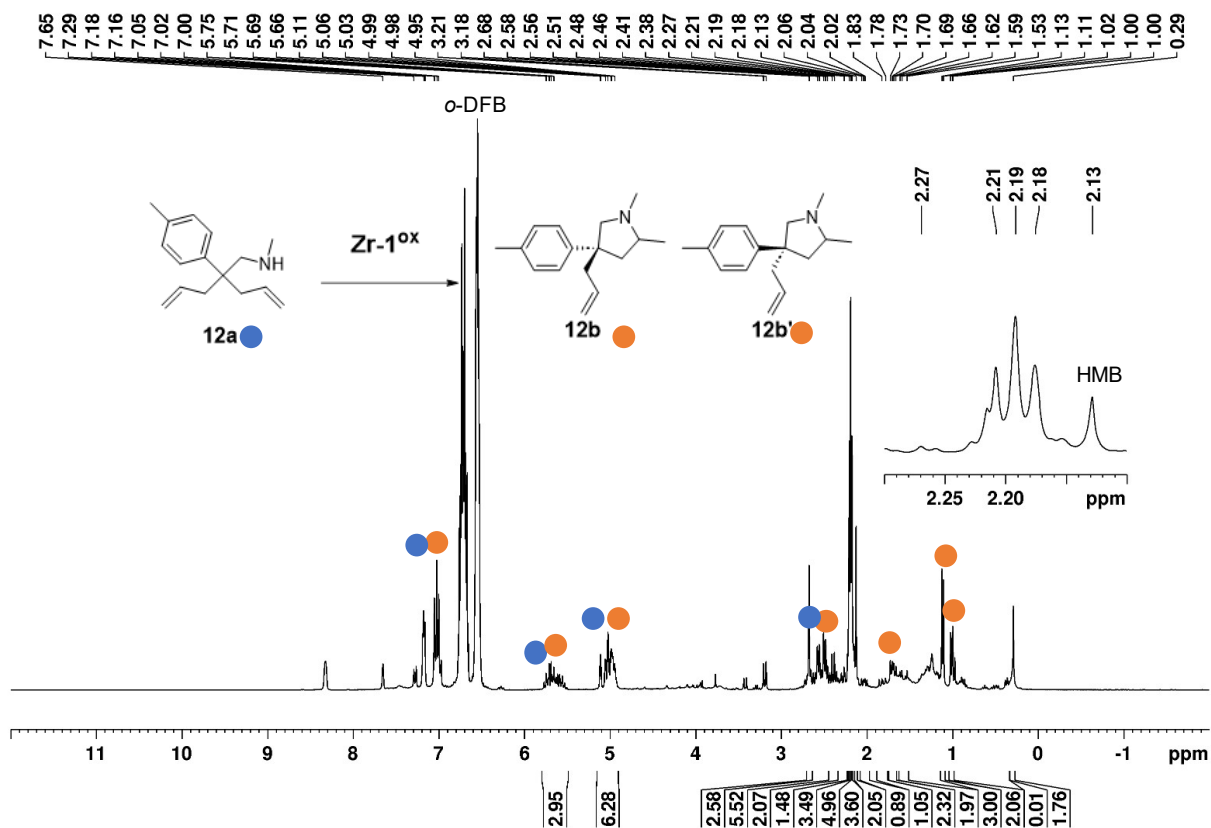


Figure A38. ^1H NMR spectrum (C_6D_6 , 300 MHz, 298 K) of **12a** to **12b/12b'** (3:2 isomers) catalyzed by **Zr-1** (Table 2.1, entry 24): δ (ppm) = 7.17-7.00 (m, 10H, ArH), 5.75-5.66 (m, 3H, $\text{CH}=\text{CH}_2$), 5.11-4.95 (m, 6H, $\text{CH}=\text{CH}_2$), 2.63-2.48 (m, 6H, NCH_3), 2.41-2.38 (m, 2H, NCH), 2.21 (br, 4H, NCH_2), 2.19 (s, 3H, PhCH_3), 2.18 (s, 3H, PhCH_3), 2.06-2.00 (m, 1H, $\text{CH}_2=\text{CHCH}_2$), 1.85-1.82 (m, 1H, $\text{CH}_2=\text{CHCH}_2$), 1.68-1.66 (m, 2H, CCH_2), 1.62-1.53 (m, 2H, CCH_2), 1.12 (d, $J = 5.9$ Hz, 3H, CHCH_3), 1.02 (d, $J = 6.2$ Hz, 2H, CHCH_3), 0.29 (br, 1H, NH).

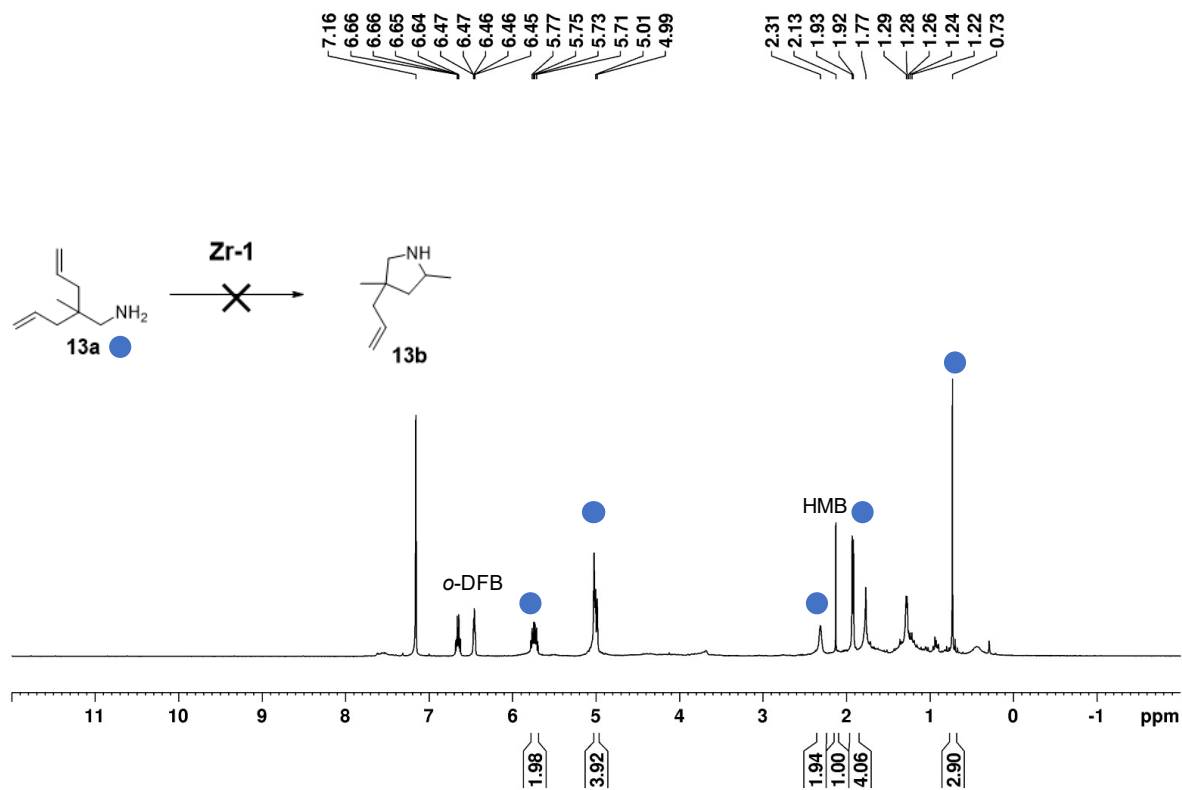


Figure A39. ¹H NMR spectrum (C₆D₆, 500 MHz, 298 K) of **13a** catalyzed by **Zr-1**: δ (ppm) = 5.77-5.73 (m, 2H, CH=CH₂), 5.01-4.99 (m, 4H, CH=CH₂), 2.31 (br, 2H, NH₂CH₂), 1.93 (d, J = 7.9 Hz, 4H, CHCH₂) 0.73 (s, 3H, CH₃), 0.43 (br, 2H, NH₂).

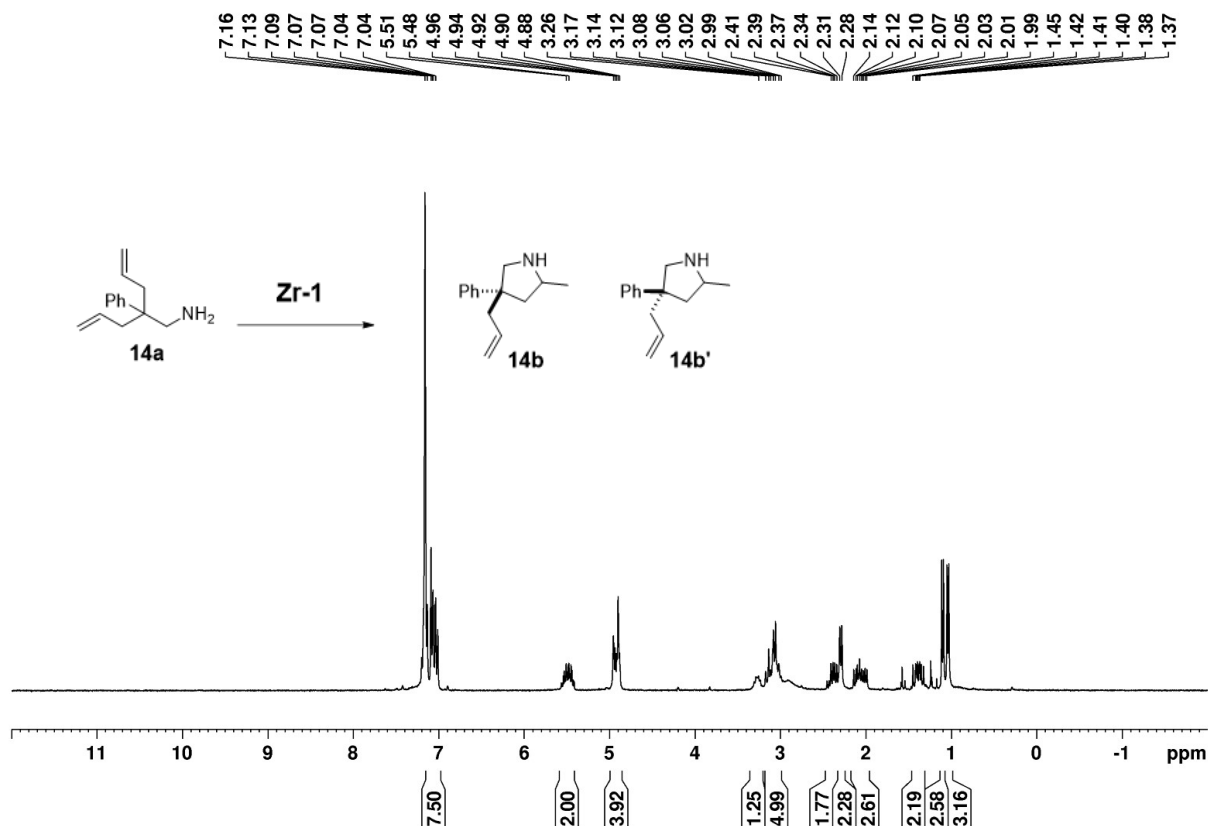


Figure A40. ¹H NMR spectrum (C₆D₆, 300 MHz, 298 K) of **14a** to **14b/14b'** catalyzed by **Zr-1** followed by organic aqueous extraction: δ (ppm) = 7.15-7.03 (m, 8H, ArH), 5.54-5.45 (m, 2H, CH=CH₂), 4.96-4.90 (m, 2H, CH=CH₂), 3.12-3.03 (m, 4H, NHCH₂), 2.46-2.30 (m, 2H, NHCHCH₂), 2.32-2.22 (m, 2H, CCH₂), 2.17-1.98 (m, 2H, CCH₂), 1.45-1.36 (m, 3H, CHCH₂), 1.11 (d, J = 5.4 Hz, 3H, CH₃) 1.05 (d, J = 6.1 Hz, 3H, CH₃).

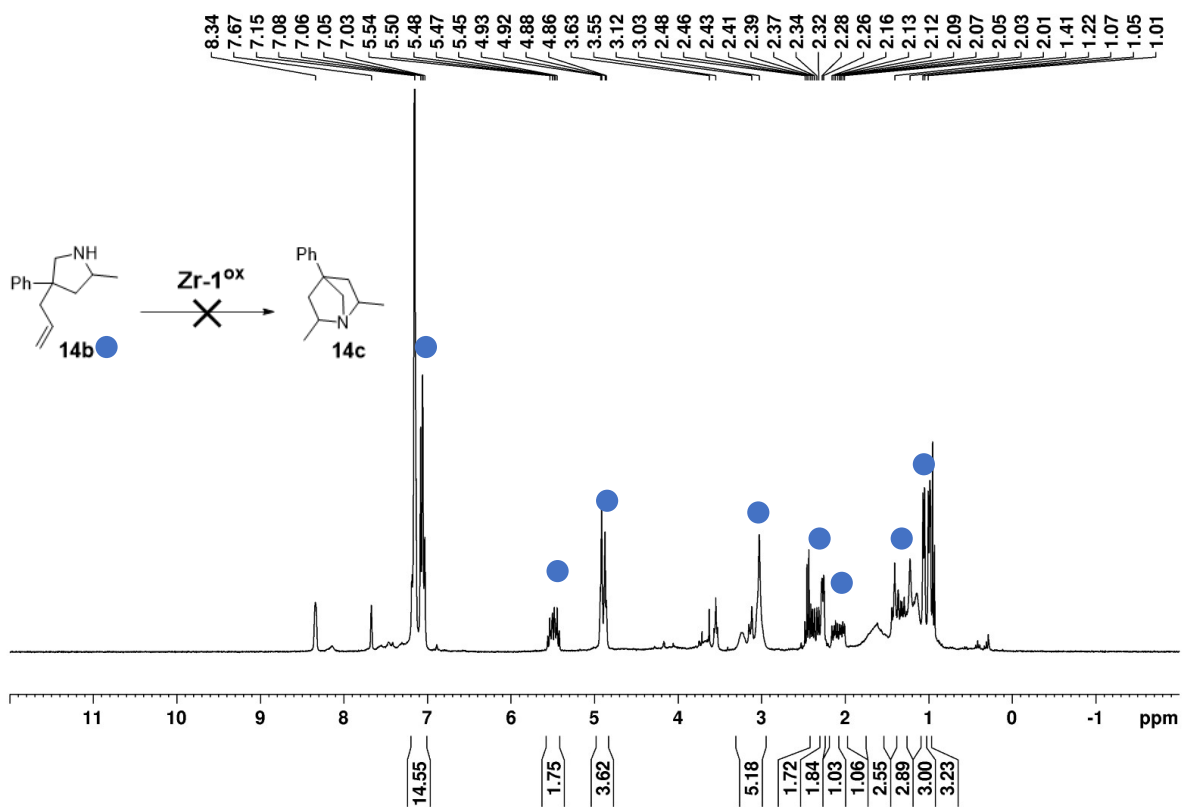


Figure A41. ¹H NMR spectrum (C₆D₆, 300 MHz, 298 K) of **14b** catalyzed by **Zr-1^{ox}**: δ (ppm) = 7.15-7.03 (m, 8H, ArH), 5.54-5.45 (m, 2H, CH=CH₂), 4.93-4.86 (m, 2H, CH=CH₂), 3.12-3.03 (m, 4H, NHCH₂), 2.40-2.30 (m, 2H, NHCHCH₂), 2.28-2.25 (m, 2H, CCH₂), 2.18-1.98 (m, 2H, CCH₂), 1.39-1.26 (m, 3H, CHCH₂), 1.07 (d, J = 5.4 Hz, 3H, CH₃) 1.00 (d, J = 6.1 Hz, 3H, CH₃).

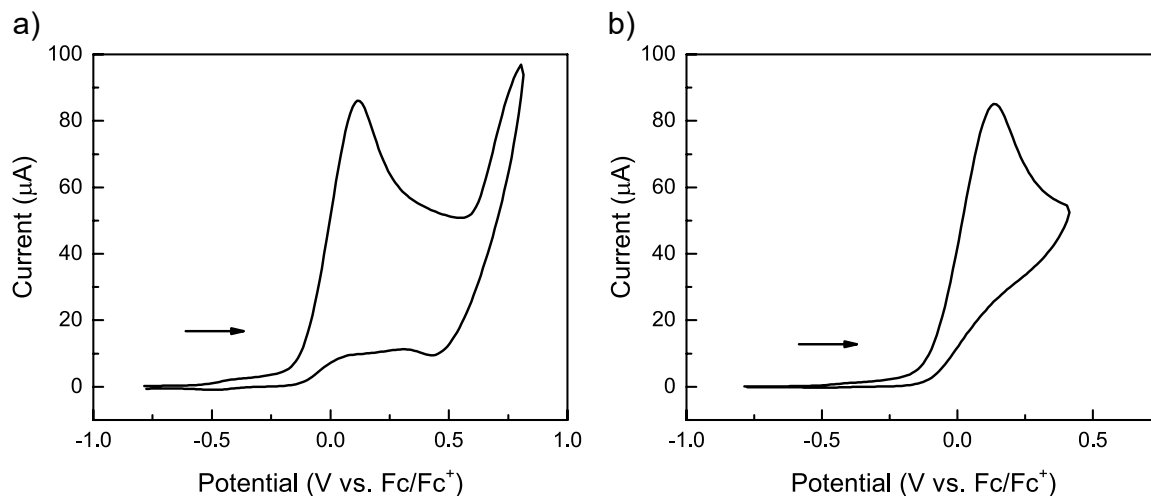


Figure A42. Cyclic voltammetry diagrams of **Zr-2** in *o*-DFB (scan rate: 100 mV/s, 100 mM TBAPF₆).

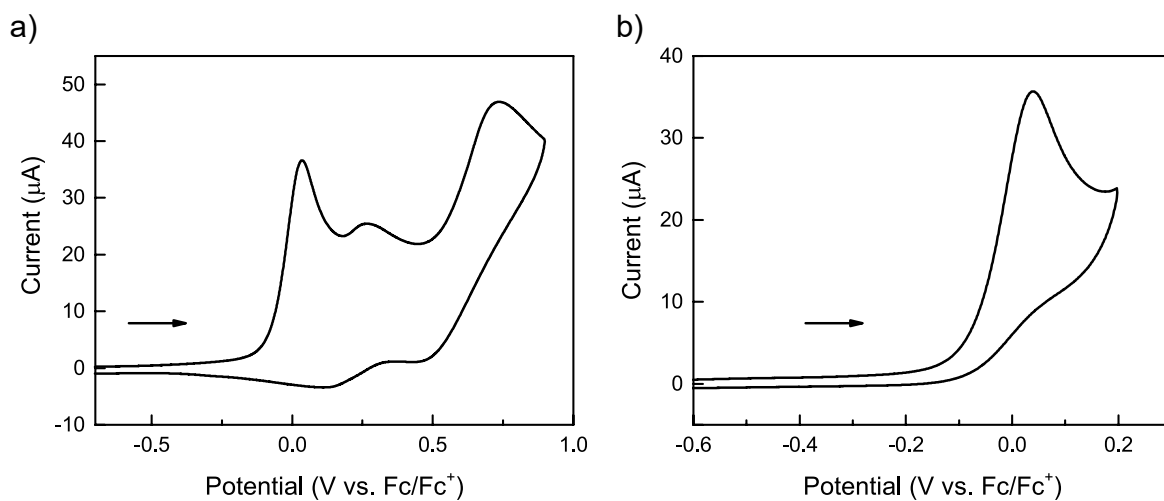


Figure A43. Cyclic voltammetry diagrams of **Ti-1** in *o*-DFB (scan rate: 100 mV/s, 100 mM TBAPF₆).

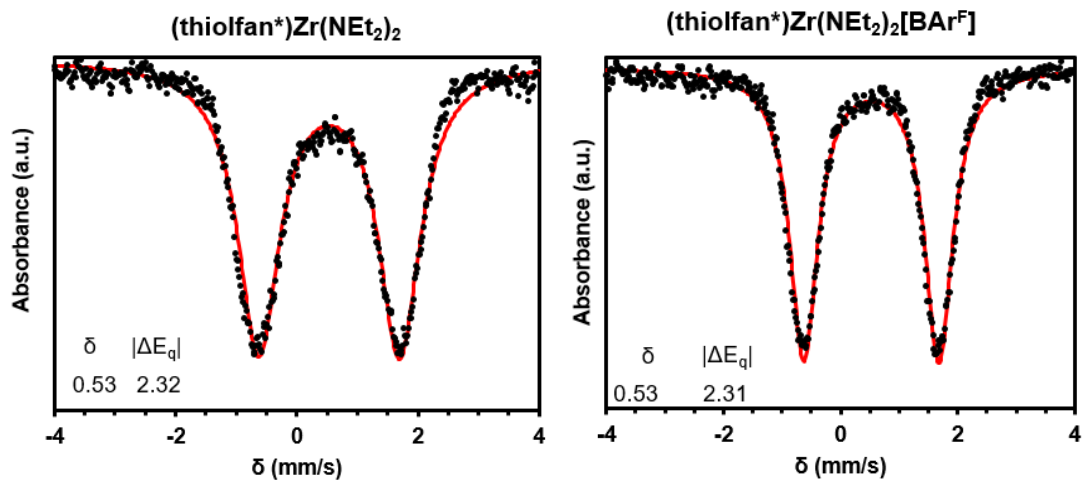


Figure A44. Zero-Field ^{57}Fe Mössbauer spectra of $(\text{thiofan}^*)\text{Zr}(\text{NEt}_2)_2$ (left) and $[(\text{thiofan}^*)\text{Zr}(\text{NEt}_2)_2][\text{BAr}^{\text{F}}]$ (right). Recorded as Solid Samples at 80 K.

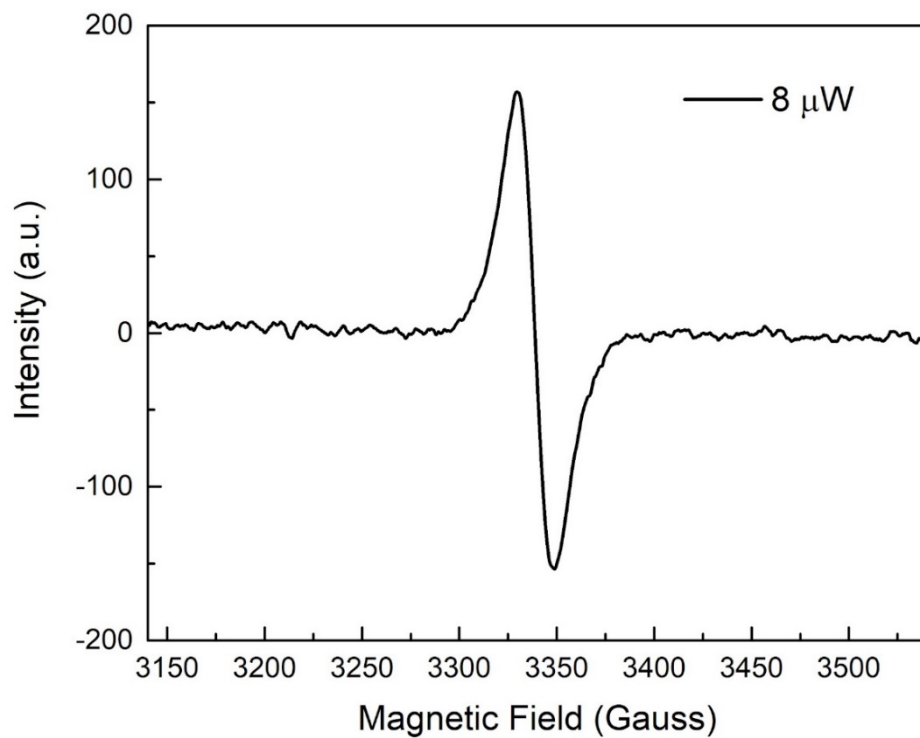


Figure A45. EPR spectrum of Zr-1^{ox} at 77 K in toluene.

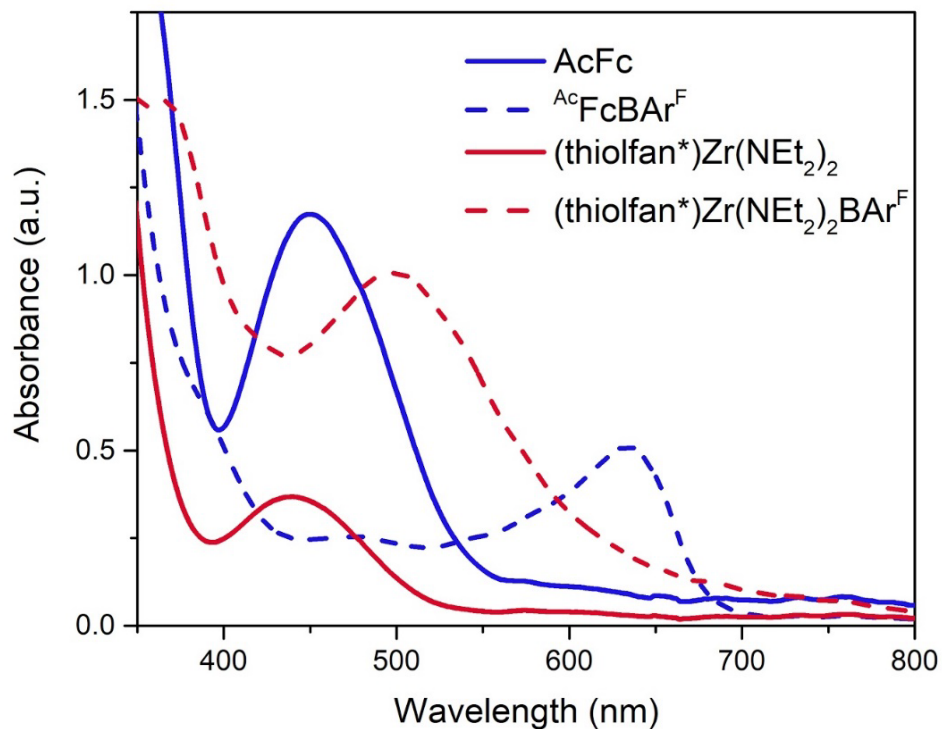
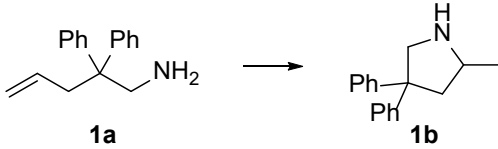
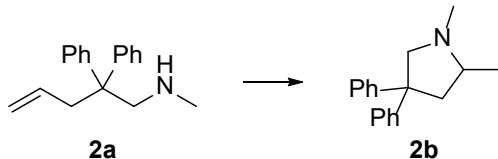
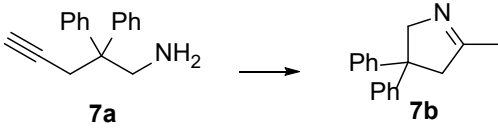
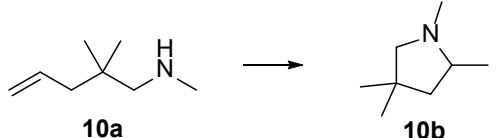


Figure A46. UV-Vis spectrum of $(\text{thiolfan}^*)\text{Zr}(\text{NEt}_2)_2$ (red solid line), $[(\text{thiolfan}^*)\text{Zr}(\text{NEt}_2)_2][\text{BAR}^{\text{F}}]$ (red dash line), acetyl ferrocene (blue solid line), and $[{}^{\text{Ac}}\text{Fc}][\text{BAR}^{\text{F}}]$ (blue dash line).

Table A1. Control experiments.

	Entry ^a	[Cat]	Conversion	Time
 <p>1a → 1b</p>	1	[^{Ac} Fc][BAR ^F]	0%	20 h
	2	FcPF ₆	0%	9 h
 <p>2a → 2b</p>	3	[^{Ac} Fc][BAR ^F]	100%	1 h
	4	^{Ac} Fc	0%	19 h
	5 ^b	NaBAR ^F	34%	2 h
	6 ^b	[Fc][BAR ^F]	100%	2 h
	7	FcPF ₆	0%	9 h
 <p>7a → 7b</p>	8	[^{Ac} Fc][BAR ^F]	100%	2 h
 <p>10a → 10b</p>	9	[^{Ac} Fc][BAR ^F]	100%	1 h

a. Reaction conditions: 10 mmol% catalyst, 0.5 mL C₆D₆, 100 °C. Conversions were calculated from the corresponding NMR spectra using hexamethylbenzene (HMB) as an internal standard.

b. Reactions were carried out in a 4 : 1 by volume C₆D₆ : *o*-C₆H₄F₂ solution.

Chapter 3. Synthesis of *N*-carboxyanhydrides from *ortho*-aromatic amino acids and CO₂

3.1 Introduction

The utilization of abundant chemical feedstocks to replace traditional fossil fuel-derived carbon sources presents an opportunity to establish a renewable and sustainable carbon economy.^{8, 153} Extensive research has been conducted on the use of CO₂ as a chemical feedstock, encompassing the formation of N-CO₂ bonds, fixation in biological and inorganic systems, electrochemical reduction, carboxylation of organic substrates, synthesis of carbonates, and polymerization processes.¹⁵³ Notably, prominent processes regarding CO₂ utilization intensively focus on the formation of carbonate and the production of bio-degradable copolymers.^{153, 154} Recently, the leverage of CO₂ in the formation of cyclic structures represented by *N*-carboxyanhydrides (NCAs) and their derivatives has become an area of growing interest. These compounds have emerged as valuable building blocks for the synthesis of polymers and high-complexity molecules.¹⁵⁵⁻¹⁵⁹ 5-membered NCAs are valuable monomers for polyamide synthesis towards diverse applications, including but not limited to drug delivery, peptide-based drugs, and surface coating, while 6-membered ring NCAs are important synthons in the preparation of poly(β -peptoids) (Figure 3.1).^{155, 160, 161}

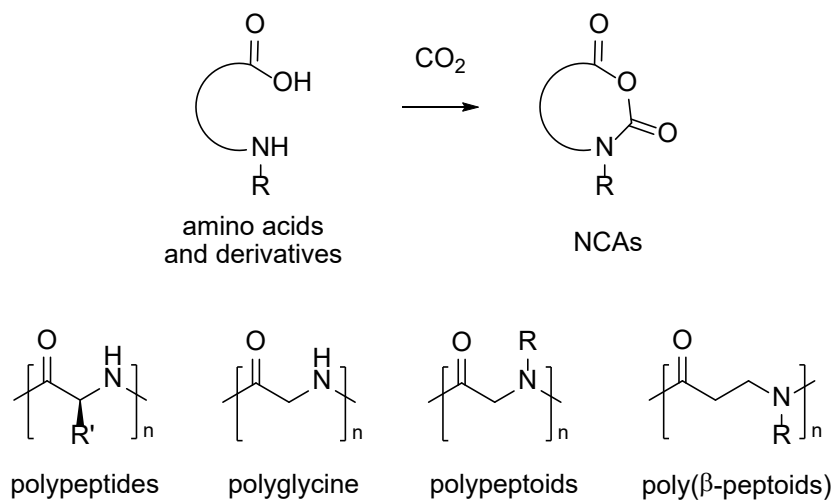
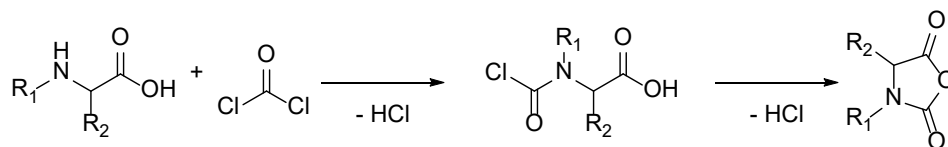


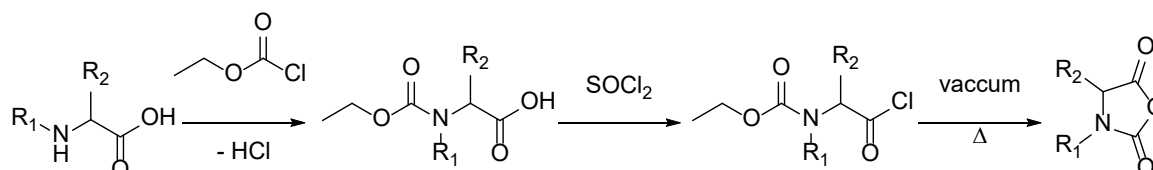
Figure 3.1. Synthesis of NCAs from CO₂ and polymers formed from ring-opening polymerization of NCAs.¹⁵⁵

A selection of methods for the synthesis of NCAs from amino acids and their derivatives are summarized in Figure 3.2. Among those conventional methods, for example, the Fuchs-Farthing reaction, the use of phosgene or its derivatives is inevitable, which raises significant concerns regarding safety and potential environmental pollution during the process.¹⁶² Alternative methods represented by the Leuchs method treat *N*-alkyloxycarbonyl amino acids with halogenating agents; *N*-alkyloxycarbonyl amino acids, the protected version of *N*-alkylated amino acid, involves the use of di-*tert*-butyl dicarbonate (Boc₂O), which is derived from phosgene.¹⁶³ Other reported methods either involve the release of harmful byproducts or employ other types of toxic reagents. Alternatively, the use of non-amino acid starting material only affords 6-membered ring NCAs, while multi-step synthesis is generally required to furnish the desired starting material.

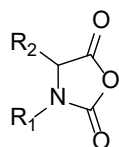
Fuchs-Farthing method



Leuchs's method



Wessely's method



Katchalski's method

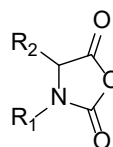
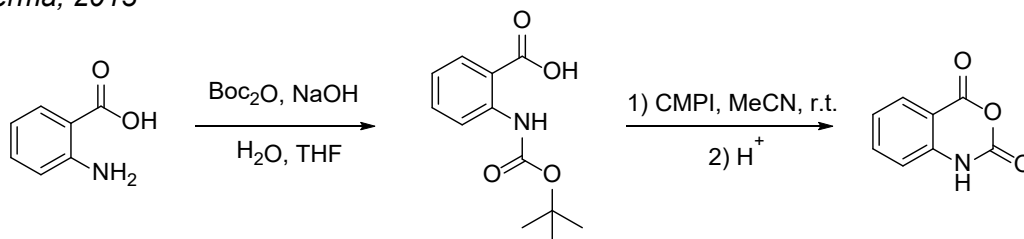


Figure 3.2. Common synthetic methods towards NCA formation.¹⁶⁴

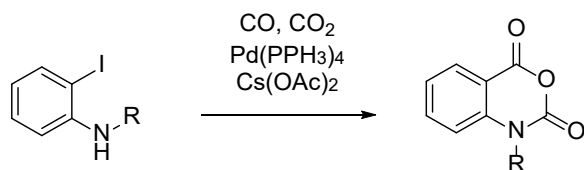
In response to the increasing demand for green and sustainable chemistry processes, the development of phosgene- and halogen-free methods under mild conditions garnered significant attention. Less toxic coupling agents such as Mukaiyama reagent, 2-chloro-1-methylpyridinium iodide (CMPI), and *n*-propylphosphonic anhydride (T3P) have been investigated.^{165, 166} In the meantime, the incorporation of simple C1 building blocks such as CO and CO₂ has been demonstrated.^{167, 168} Zhang, *et al.*, investigated the cyclization of *o*-iodoanilines from CO and CO₂ catalyzed by palladium catalyst, affording 6-membered ring NCAs with an aromatic backbone.¹⁶⁷ Endo, *et al.*, presented the cyclization of phenyl urethanes of amino acids into NCAs. The urethane derivatives of amino acid were generated from diphenyl carbonate which was obtained from CO₂ through phosgene-free conditions.¹⁶⁹ Most recently, T3P was found to

activate the Boc-protected amino acids to afford the corresponding NCA derivatives.¹⁶⁶ Inspired by these examples, we looked into incorporating CO₂ into the cyclization of amino acids in the presence of non-toxic coupling agents such as CMPI or T3P.

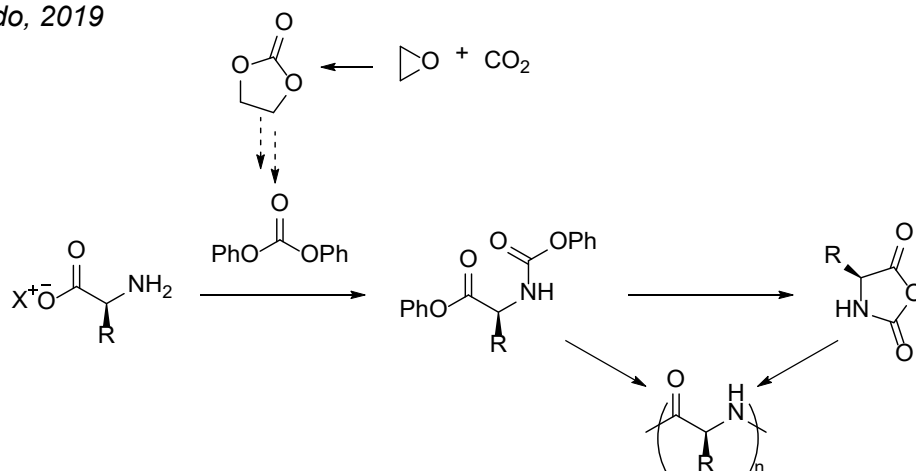
Verma, 2013



Zhang, 2017



Endo, 2019



Laconde, 2021

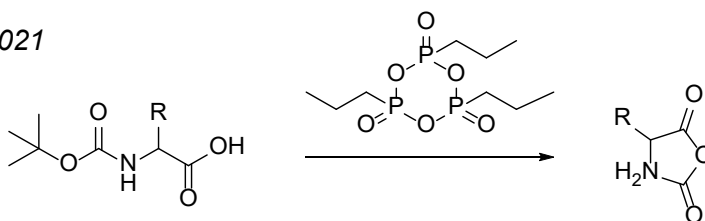


Figure 3.3. “Green” approaches towards 5 and 6-membered NCA derivatives.^{165-167, 169}

In addition to developing environmentally friendly conditions that utilize the easy-to-access C1 building block, CO₂, for NCA synthesis, we strive to explore the possibility of combining the synthesis and the ring-opening polymerization of NCAs. We envision a consecutive one-pot transformation of amino acids and CO₂ toward sustainable materials such as polypeptides and polyamides by integrating the abovementioned processes. Synthetic polypeptides, featuring the repeating amide bond in the polymer structure, are considered analogues of natural proteins. Naturally occurring polypeptides are obtained through highly selective and efficient biological processes which allow precise sequence control. On the other hand, synthetic polypeptides have been successfully synthesized from solid-state amino acid condensation or ring-opening polymerization of NCAs facilitated by the use of various catalysts and/or initiators (Figure 3.4). In comparison to the amino acid condensation method, ring-opening polymerization of NCAs introduces more chemical diversity of the side chains, allows large-scale synthesis without specific installation, and affords high molecular weight synthetic polypeptides and derivatives.

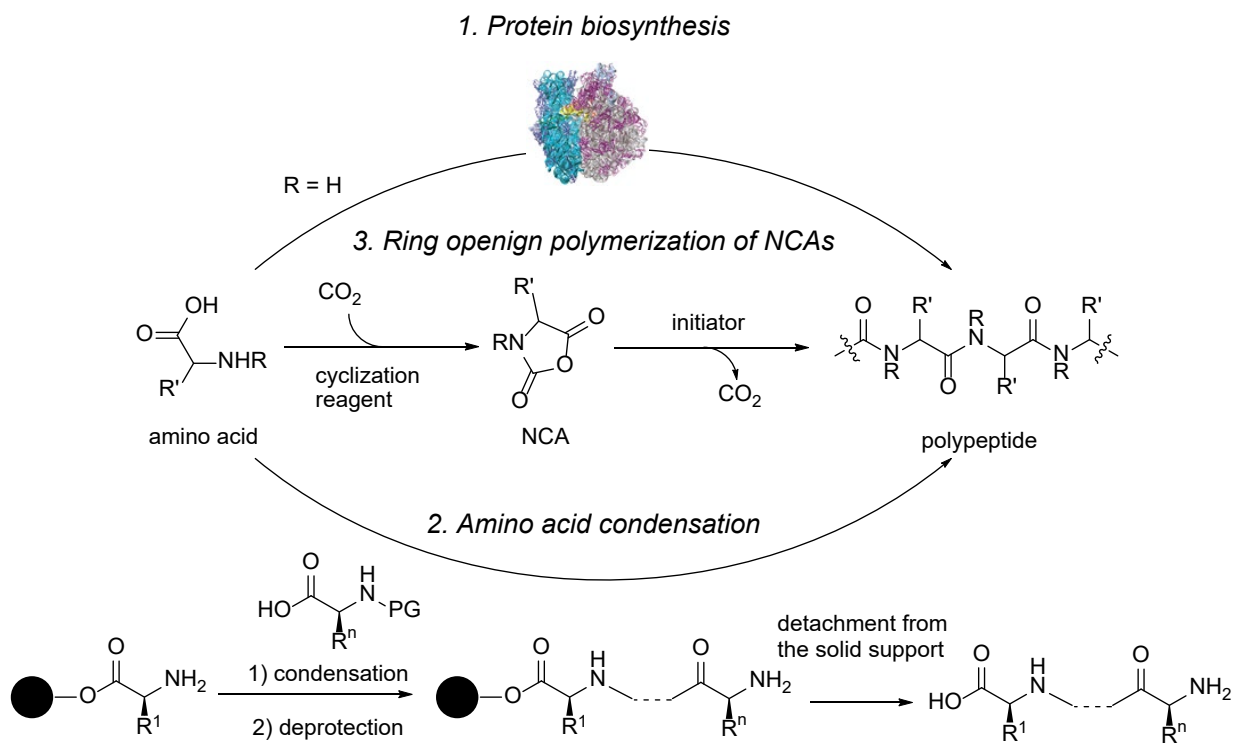


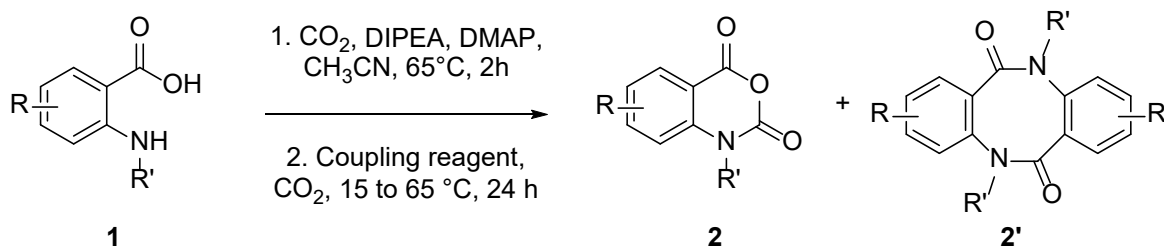
Figure 3.4. Naturally and synthetic approaches towards polypeptide and coupling NCA synthesis with subsequent polymerization.

Herein, we disclose the development and optimization of a green approach toward NCA synthesis, leveraging carbon dioxide as the building block. In addition, we introduce the preliminary results of a metal-catalyzed ring-opening polymerization of aromatic 6-membered ring NCAs. This chapter is a version of Tran, T. V.; **Shen, Y.**; Nguyen, H. D.; Deng, S.; Roshandel, H.; Cooper, M. D.; Waston, J. R.; J. Byers, J.; Diaconescu, P. L.; Do, L. H., ***N*-carboxyanhydrides directly from amino acids and carbon dioxide and their tandem reactions to therapeutic alkaloids**, *Green Chemistry*. **2022**, *24*, 9245-9252.

3.2 Results and discussion

Screening of reaction conditions

To circumvent the potential challenges of isolating the moisture-unstable 5-membered NCAs, we chose a specific group of *ortho*-aromatic amino acids, namely anthranilic acid and its derivatives to investigate. The reaction of these compounds with CO₂ in the presence of coupling reagents affords aromatic 6-membered ring NCAs that are easy to isolate and require minimum purification efforts (Scheme 3.1). Various amide coupling reagents were tested for the cyclization of *N*-substituted *ortho*-aromatic amino acid, 2-(*N*-benzylamino)benzoic acid (Table B1). Mukaiyama reagent (CMPI) and T3P exhibited general to great activity in the one-pot two-step synthesis, while acetonitrile turned out to be the optimal solvent (Table B1 and B2).

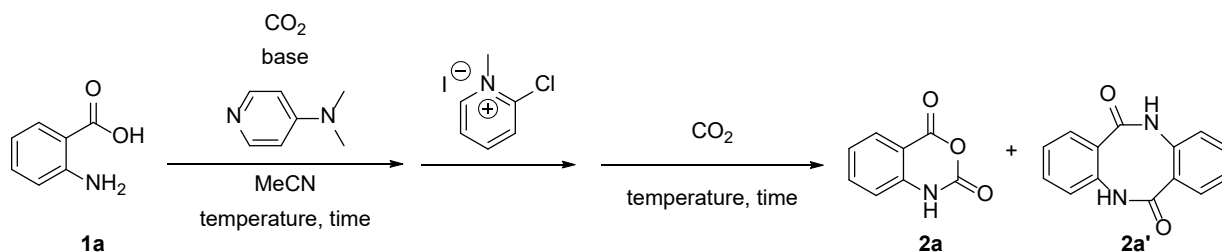


Scheme 3.1. Cyclization of *ortho*-aromatic amino acids to 6-membered ring NCAs.

We then looked into optimizing conditions for anthranilic acid **1a** using CMPI as the coupling reagent. The reactions were conducted in a one-pot two-step manner in a Parr reactor equipped with a stir bar unless otherwise noted. The anthranilic acid was activated with 4-dimethylaminopyridine (DMAP) and *N,N*-diisopropylethylamine (DIPEA) under CO₂ to form the corresponding carbamate. The coupling reagent was added after releasing pressure to promote ring-closing. The reactor was re-charged with CO₂ and heated up to the designated temperature for a period of time. It is important to note that besides the desired product, isatoic anhydride **2a**, dimeric structure **2a'** was also observed in a considerable amount. We noticed that decreasing the amount of coupling agent CMPI decreased the conversion of anthranilic acid and the yield of isatoic anhydride while increasing the amount of CMPI had small effects on the reaction (Table 3.1, entries 2 and 7). Interestingly, we noticed that CMPI reacted with DMAP and formed a yellow solid that could be isolated. The isolated solid was used to replace CMPI and DMAP and presented similar results (entries 7-9). Elongating reaction time from 20 to 40 hours was not beneficial to the reaction (entry 3). Replacing DIPEA with Et₃N with a longer reaction time and higher temperature did minimum effects on the reaction outcome (entries 4-6). We also tried to add all reagents at once in the beginning but the observed yield of isatoic anhydride was limited to a threshold of ~20-40%. In all attempts, we

observed a noticeable amount of the dimeric byproduct which encouraged us to explore better conditions. In the meantime, we observed unpredictable interactions between isatoic anhydride with the reaction reagent which might explain the low yield of the unsubstituted 6-membered ring NCAs.

Table 3.1. Two-step screening conditions for the synthesis of isatoic anhydride

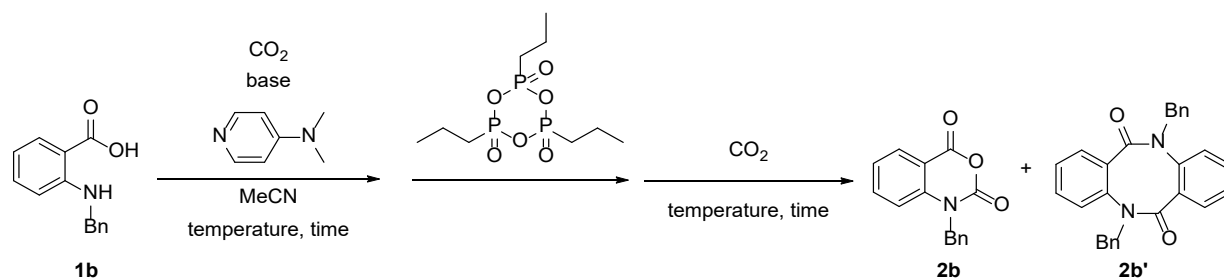


Entry ^a	Temp.	Time	CMPI	Base	Conversion (%) ^b	Yield (%) ^b	2a: 2a' ^c
	(°C)	(h)	(equiv.)				
1	50	20	1.4	DIPEA	91	40	N/A
2	50	20	1.05	DIPEA	81	27	1:1
3	50	40	1.4	DIPEA	80	18	100:80
4	50	20	1.4	Et ₃ N	98	28	100:75
5	50	12	1.4	Et ₃ N	94	41	100:102
6 ^d	70	20	1.4	Et ₃ N	98	24	100:56
7 ^e	50	20	1.8	DIPEA	98	25	100:56
8 ^e	70	20	1.8	DIPEA	99	34 ^c	100:35
9 ^e	70	20	1.8	Et ₃ N	>99	21 ^c	100:32

- a. Reaction conditions: 2-aminobenzoic acid (2.5 mmol), DMAP (varied), base (2.2 equiv.), CO₂ (300 psi), MeCN (50 mL). The reaction mixture was preheated at 50 °C for 2 h before adding CMPI as the activating reagent. The reactions were set up using **Method I** as described in the experimental section.
- b. Determined by GC-MS using a biphenyl internal standard.
- c. Calculated from ¹H NMR spectroscopy.
- d. The reaction mixture was preheated at 70 °C for 2 h before adding CMPI.
- e. Isolated solid from mixing CMPI with DMAP is used as the activating reagent without preheating in step 1. All reagents were combined at the beginning instead of adding stepwise.

In comparison, *N*-benzylisatoic anhydride **2b** was more stable than isatoic anhydride **2a**. No side reaction was observed between **2b** and reaction reagents. At the same time, we realized that compared to CMPI, T3P presented better selectivity towards the desired product over the dimer, therefore, we moved onto optimizing conditions for synthesizing *N*-benzylisatoic anhydride **2b** using T3P. We observed that both DMAP and DIPEA were necessary to obtain the *N*-benzylated NCA (Table 3.2, entries 1-3). Increasing the equivalent of DIPEA had ambiguous effects on the system while omitting CO₂ in either step was unbeneficial to the reaction (entries 4-6). Interestingly, when both the equivalent of T3P and DIPEA were increased, the reaction reached full conversion and the *N*-benzylisatoic anhydride **2b** could be isolated with high yield (entries 7-9).

Table 3.2. Two-step screening conditions for the synthesis of *N*-benzyl substituted 6-membered ring NCAs



Entry ^a	Temp. (°C)	Time (h)	T3P (equiv.)	DIPEA (equiv.)	Conversion (%) ^b	Yield (%) ^b	2b: 2b' ^b
1	70	20	1.5	2.2	100	30	100:80
2	70	20	1.5	2.2	64	5	100:60
3	70	20	1.5	0	78	0	N/A
4	70	20	1.5	4	95	24	100:66
5 ^c	70	20	1.5	4	100	11	100:169
6 ^{d, e}	65	20	1.5	4	90	6	100:30
7 ^e	65	20	1.5	4	100	34	100:21
8 ^e	65	20	3	4	100	77	100:2
9 ^f	65	20	3	4	100	71	100:5

a. Reaction conditions: 2-(*N*-benzylamino)benzoic acid (2.5 mmol), DMAP (varied), DIPEA (varied), CO₂ (300 psi), MeCN (50 mL). For step 1: preheat at 70 °C for 2 h before adding T3P (1.5 equiv.) as the activating reagent. The reactions were set up using **Method I** described in the experimental section.

- b.* Determined by ^1H NMR spectroscopy using ferrocene or 1,3,5-trimethoxybenzene as an internal standard.
- c.* No CO_2 after adding T3P.
- d.* No CO_2 before adding T3P.
- e.* The reaction was preheated at $60\text{ }^\circ\text{C}$ for 2 h.
- f.* The reaction was set up using **Method II** described in the experimental section (all reagents were combined in one-pot at the beginning of the reaction).

Substrate scope

With the developed method, we expanded our research onto a variety of *N*-substituted benzoic acid derivatives (Figure 3.5). Fluorination at the 4- and 5-positions on the aromatic part of the substrates formed the corresponding product **2c** and **2d** in 74% and 55% yield, respectively. While 5-methoxy substituted benzoic amino acid **1f** afforded product **2f** in 21% yield, the 4-methoxy substituted benzoic amino acid **1e** afforded product **2e** in 83% yield. The 5-methylated amino acid **1g** afforded product **2g** in a moderate yield of 42%. It is important to point out that the majority of the NCAs formed from our optimized conditions were isolated through a simple organic-aqueous workup circumventing the need for further purifications compared to other conventional methods.¹⁷⁰

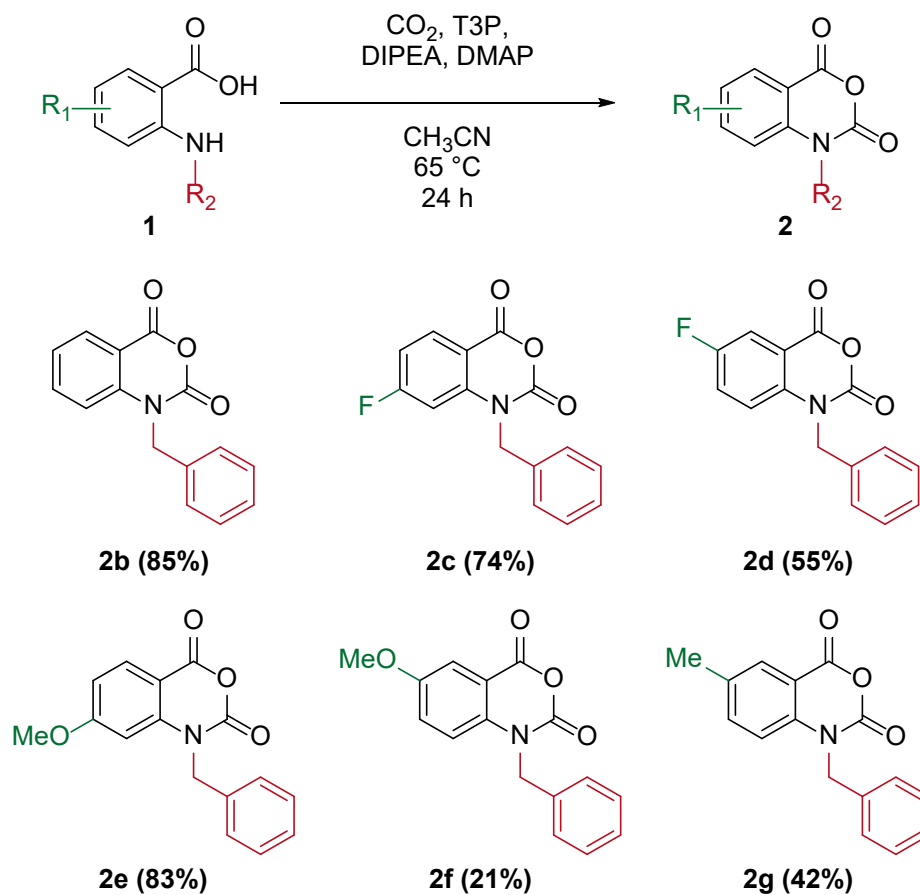


Figure 3.5. Exploring *N*-benzyl substituted 6-membered ring NCAs following **Method II** as described in the experimental section.

Due to the known instability of isatoic anhydride and conventional 5-membered NCAs, we decided to investigate milder conditions for the synthesis of unsubstituted and *N*-methylated 6-membered NCAs, as well as 5-membered NCAs. Encouraging, lowering reaction temperature, and removing DMAP from the reaction system afforded unstable 6-membered NCAs in moderate to good yields represented by **2a** 99%, **2h** 76%, and **2i** 77% (Figure 3.6). 5-membered NCAs were also prepared using the same conditions. Represented by 3-phenyloxazolidine-2,5-dione, 5-membered NCAs derived from α -amino acids could be isolated in moderate to good

yields. However, substrates with bulky or electro-withdrawing *N*-substituents were too sterically hindered or deactivated to afford the desired products. Unfortunately, non-substituted 5-membered NCAs could not be obtained via our developed methods.

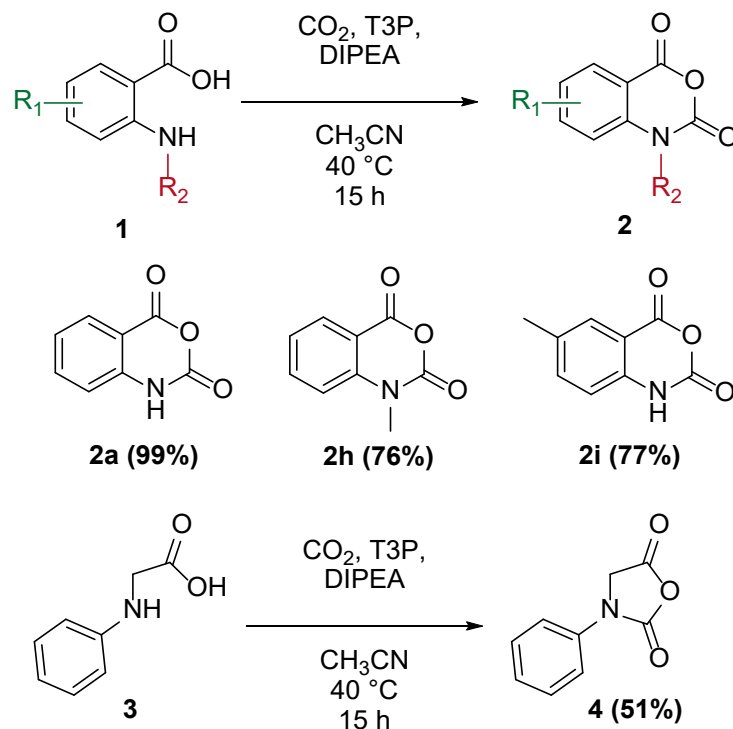


Figure 3.6. Synthesis of semi-stable NCAs under milder conditions following **Method III** as described in the experimental section.

Compatibility with polymerization

Furthermore, to integrate the synthesis and polymerization of *N*-carboxyanhydrides into a single reaction vessel and implement a one-pot tandem reaction sequence, we conducted the study on exploring conditions for the ring-opening polymerization of the aromatic 6-membered ring NCAs. The results of this investigation will be disclosed in the manuscript under revision: Deng, S.; **Shen, Y.**; Chantranuwathana, V.; Nguyen, H. D.; Tran, T. V.; Vasquez, K.; Byers, J.; Do, L. H.; Diaconescu, P. L., **ortho-Aromatic polyamides by ring-opening polymerization of *N*-**

carboxyanhydrides. In general, Schiff base metal complexes were active towards ring-opening polymerization of the 6-membered ring NCAs in the presence of co-catalyst PPNCI (Bis(triphenylphosphine)iminium chloride) (Figure 3.7). Polymeric products of **2b**, **2h**, and *N*-C₈H₁₇ substituted **2j** were isolated. However, the low solubility of the isolated polymers of **2b** and **2h** hampered our investigation of their molecular weights and other properties. Fortunately, longer alkyl substitution on nitrogen solved the problem. The polymers of **2j** (poly 6-NCA- C₈H₁₇) were characterized by SEC (see chapter 4 Figure C45-48 for SEC traces).

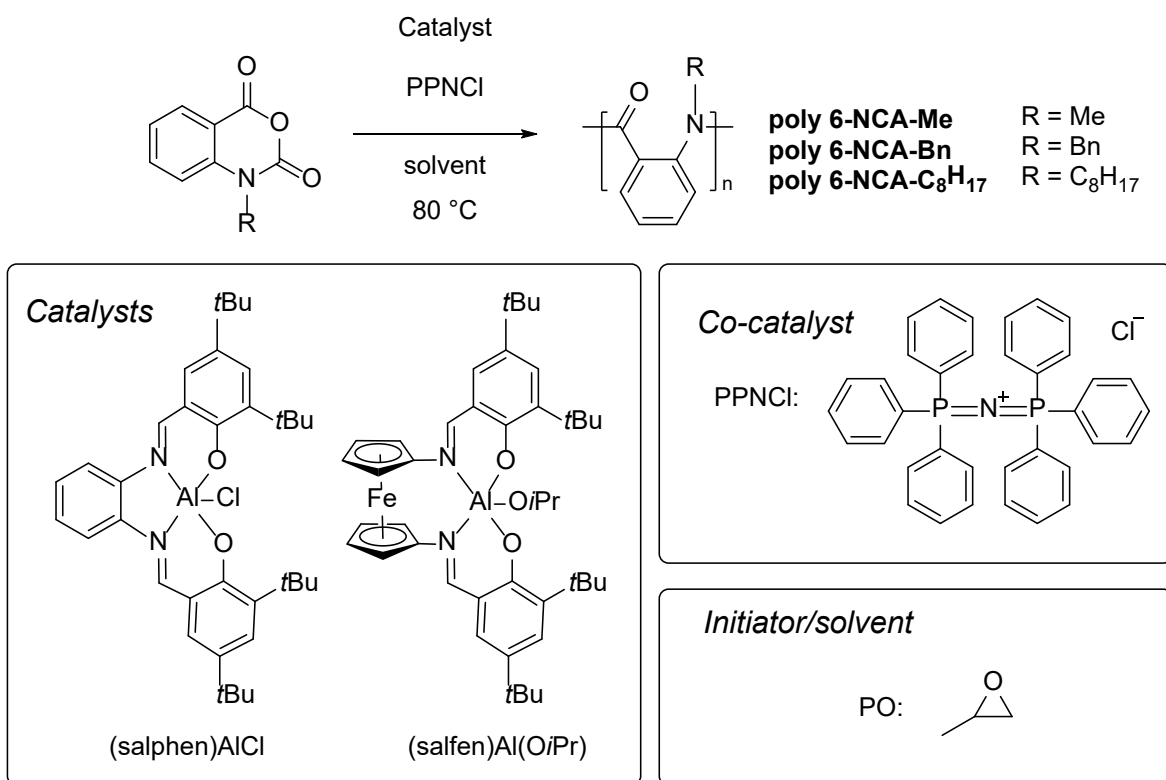


Figure 3.7. Polymerization conditions for 6-membered ring NCAs.

To combine the two processes into one reaction vessel, we first investigated different solvent combinations (Table B2). Besides MeCN which gave the best yield for the NCA synthesis, the combination of propylene carbonate and THF (3:7) also affords a good yield of **2a**

(Table B2, entry 5). The same combination was also effective in the polymerization of NCAs. However, the Schiff base aluminum compound catalyzed polymerization system was not compatible with other reagents in the presence of NCA synthesis as no polymer could be isolated in the presence of anthranilic acid derivatives or T3P. Therefore, a one-pot one-step implementation of NCA synthesis and subsequent polymerization was not feasible. While we are looking into integrating those two incompatible processes through a stepwise approach, we also envision spatially separating the two processes by immobilizing the key reagents for each step onto solid supports in one reaction vessel. Potential solid-phase coupling reagent for NCA synthesis to test includes but is not limited to P₂O₅ and polymer-supported Mukaiyama reagent.¹⁷¹

3.3 Conclusion and outlook

In summary, we have developed conditions to synthesize *N*-carboxyanhydrides (NCAs) from amino acids utilizing abundant CO₂ as a building block. We replaced extremely toxic reagents in our developed system and utilized conventional coupling reagents CMPI and T3P to facilitate the ring closing of NCAs. However, further investigation is required to explore the feasibility of a one-pot consecutive process for the formation of polypeptides/polypeptoids from amino acids through NCA synthesis and subsequent polymerization. It is important to mention that besides the aromatic 6-membered ring NCAs, which is the primary focus of the current study, our developed method demonstrated efficacy for the synthesis of *N*-substituted 5-membered NCAs. Unfortunately, we have not yet achieved satisfactory results with unsubstituted 5-membered NCAs due to their instability. While a few publications have demonstrated their approaches towards the versatile production of polypeptide/peptoids from

amino acids and derivatives, encompassing the formation of intermediate NCAs, they required multi-step synthesis and a tremendous amount of purification efforts.^{169, 172-174} Therefore, there is an urgent need on finding opportunities to convert the unstable unsubstituted 5-membered NCAs into polypeptides under controlled conditions.

3.4 Experimental section

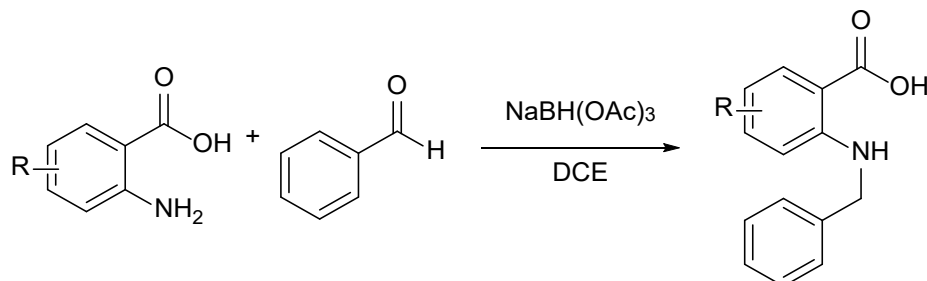
General considerations

4-(Dimethylamino)pyridine (DMAP), *n*-propylphosphonic anhydride (T3P), 2-chloro-1-methylpyridinium iodide (CMPI), 1,1'-carbonyldiimidazole (CDI), triethylamine (TEA), and *N,N*-diisopropylethylamine (DIPEA) were purchased from Sigma Aldrich or VWR and used as received. Carbon dioxide (USP grade) was purchased from Matheson Tri-Gas Inc. or Airgas Inc. and used as received. The other reagents were purchased from Ambeed Inc., Alfa Aesar, AK Scientific Inc., Matrix Scientific, TCI, and Sigma-Aldrich and used as received. Deuterated solvents were purchased from Cambridge Isotope Laboratories Inc. Acetonitrile was distilled over calcium hydride and stored over sieves prior to use.

NMR spectra were acquired using JEOL (ECA-300, 400, and 500), or Bruker (AV-300 and AV-500) at ambient temperature and referenced using residual solvent peaks. All ¹³C and ¹⁹F NMR spectra were proton decoupled. Gas chromatography-mass spectrometry (GC-MS) was performed using an Agilent 7890 GC/5977A MSD instrument equipped with an HP-5MS capillary column. DART-MS used a Thermo Exactive Plus MSD (Thermo Scientific) equipped with an ID-CUBE ion source and a Vapur Interface (IonSense). Both the source and MSD were controlled by Excalibur v. 3.0. The analyte was spotted on OpenSpot sampling cards (IonSense) using chloroform as the solvent. Ionization was accomplished using He plasma with no

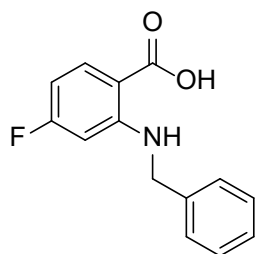
additional ionization agents. Mass calibration was carried out using Pierce LTQ Velos ESI (+) and (-) Ion calibration solutions (Thermo Fisher Scientific).

General procedure for the synthesis of 2-(N-Benzylamino)benzoic acids



Under N₂, 2-aminobenzoic acid derivative (1.0 equiv.) and benzaldehyde (1.0 equiv.) were dissolved in 1,2-dichloroethane in a 100 mL round-bottom flask with a magnetic stir bar. The mixture was stirred at ambient temperature for 2 h, which led to the formation of a slurry. Solid NaBH(OAc)₃ (1.4 equiv.) was added and the slurry was allowed to stir overnight under N₂. Upon completion, a saturated solution containing NaHCO₃ was added to quench the reaction. The mixture was extracted into ethyl acetate (3×100 mL) and the organic layer was separated, dried over MgSO₄, filtered, and evaporated to dryness. The benzylated products were obtained as solids and used in the next step without any further purification.

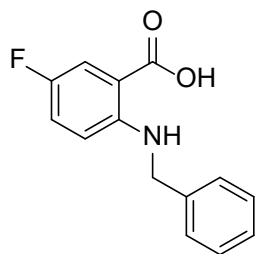
2-(N-Benzylamino)-4-fluorobenzoic acid (**1c**)



Compound **1c** was synthesized by following the above method. It was isolated as a white solid (1.83 g, 83%). This compound was reported previously.¹⁷⁵ ¹H NMR (300 MHz, 25 °C, DMSO-*d*₆):

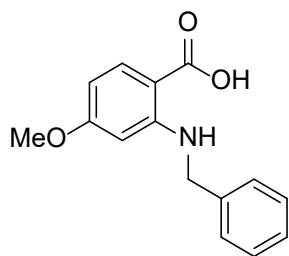
δ (ppm) = 8.48 (br, 1H, NH), 7.86 (dd, J = 8.8, 7.1 Hz, 1H, ArH), 7.34 (s, 4H, ArH), 7.31 – 7.28 (m, 1H, ArH), 6.45 (dd, J = 12.7, 2.5 Hz, 1H, ArH), 6.36 (td, J = 8.5, 2.5 Hz, 1H, ArH), 4.46 (s, 2H, NCH₂Ar). ¹³C NMR (125 MHz, 25 °C, DMSO-*d*₆): δ (ppm) = 169.3 (COOH), 166.3 (d, J = 248.0 Hz, CF), 152.9 (d, J = 12.7 Hz), 138.8, 134.6 (d, J = 11.9 Hz), 128.6, 127.1, 127.1, 107.3, 101.9 (d, J = 22.7 Hz), 97.8 (d, J = 25.8 Hz), 45.9 (NCH₂Ar). ¹⁹F NMR (282 MHz, 25 °C, DMSO-*d*₆): δ (ppm) = -104.40 (dt, J = 12.7, 7.7 Hz).

2-(*N*-Benzylamino)-5-fluorobenzoic acid (**1d**)



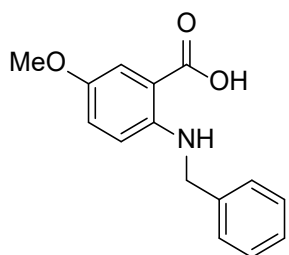
Compound **1d** was synthesized by following the above method. It was isolated as a white solid (1.54 g, 42%). This compound has been reported previously.¹⁷⁶ ¹H NMR (300 MHz, 25 °C, DMSO-*d*₆) of **1d**: δ (ppm) = δ 7.53 (dd, J = 9.8, 3.2 Hz, 1H, ArH), 7.34 (d, J = 4.4 Hz, 4H, ArH), 7.23 – 7.14 (m, 2H, ArH), 6.69 (dd, J = 9.3, 4.5 Hz, 1H, ArH), 4.45 (s, 2H, NCH₂Ar). ¹³C NMR (101 MHz, 25 °C, DMSO-*d*₆): δ (ppm) = 169.6 (d, J = 2.6 Hz, COOH), 152.8 (d, J = 231.2 Hz, CF), 148.2 (d, J = 0.5 Hz), 139.8, 129.1, 127.6, 127.5, 122.4 (d, J = 22.7 Hz), 117.1 (d, J = 22.7 Hz), 113.7 (d, J = 7.0 Hz), 110.8 (d, J = 6.3 Hz), 46.6 (NCH₂Ar). ¹⁹F NMR (376 MHz, 25 °C, DMSO-*d*₆): δ (ppm) = -130.1 (ddd, J = 9.8, 8.1, 4.5 Hz).

2-(*N*-Benzylamino)-4-methoxybenzoic acid (**1e**)



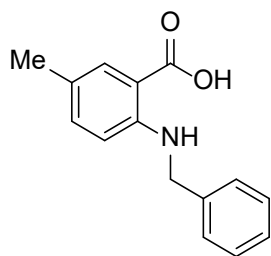
Compound **1e** was synthesized by following the above method. It was isolated as a brown solid (1.58 g, 41%). This compound was reported previously.¹⁷⁷ ¹H NMR (300 MHz, 25 °C, CDCl₃) of **1e**: δ (ppm) = 8.20 (br, 1H, COOH), 7.94 – 7.91 (d, $J = 7.0$ ppm, 1H, ArH), 7.36 (m, 5H, ArH), 6.22 (dd, $J = 9.1, 2.5$ Hz, 1H, ArH), 6.06 (d, $J = 2.5$ Hz, 1H, ArH), 4.46 (s, 2H, NCH₂Ar), 3.72 (s, 3H, CH₃OAr). ¹³C NMR (101 MHz, 25 °C, DMSO-*d*₆): δ (ppm) = 170.2 (COOH), 149.3, 146.2, 140.3, 129.0, 127.6, 127.4, 123.1, 115.0, 113.8, 110.8, 55.9 (CH₃OAr), 46.8 (NCH₂Ar).

2-(*N*-Benzylamino)-5-methoxybenzoic acid (**1f**)



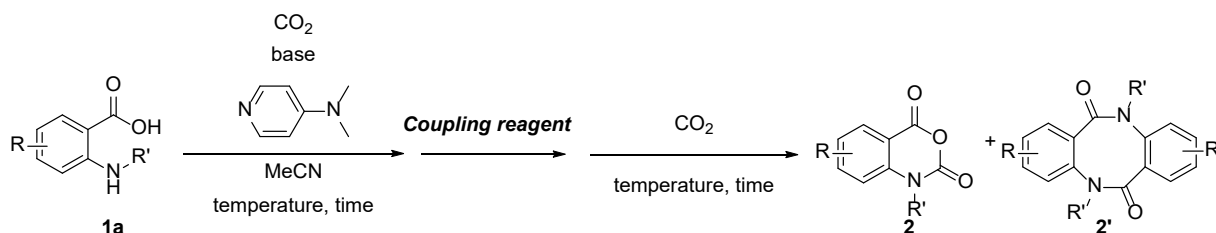
Compound **1f** was synthesized by following the above method. It was isolated as a yellow solid (2.50 g, 65%). This compound was reported previously.¹⁷⁵ ¹H NMR (300 MHz, 25 °C, CDCl₃) of **1f**: δ (ppm) = 7.50 (d, $J = 3.3$ Hz, 1H, ArH), 7.34 – 7.27 (m, 5H, ArH), 7.01 (dd, $J = 9.7, 3.3$ Hz, 1H, ArH), 6.63 (d, $J = 9.0$ Hz, 1H, ArH), 4.47 (s, 2H, NCH₂Ar), 3.76 (s, 3H, CH₃O). ¹³C NMR (101 MHz, 25 °C, DMSO-*d*₆): δ (ppm) = 170.2 (COOH), 164.7, 153.0, 139.8, 134.2, 129.1, 127.7, 127.5, 104.3, 102.3, 96.3, 55.5 (CH₃OAr), 46.5 (NCH₂Ar).

2-(*N*-Benzylamino)-5-methylbenzoic acid (**1g**)



Compound **1g** was synthesized by following the above method. It was isolated as a light-yellow solid (1.52 g, 70%). This compound was reported previously.¹⁷⁶ ¹H NMR (500 MHz, 25 °C, CDCl₃): δ (ppm) = 7.79 (s, 1H, ArH), 7.39 – 7.26 (m, 5H, ArH), 7.16 (d, *J* = 8.6 Hz, 1H, ArH), 6.57 (d, *J* = 8.6 Hz, 1H, ArH), 4.48 (s, 2H, NCH₂Ar), 2.23 (s, 3H, CH₃). ¹³C NMR (125 MHz, 25 °C, CDCl₃): δ (ppm) = 174.2 (COOH), 149.7, 139.0, 136.9, 132.4, 128.8, 127.2, 127.0, 124.3, 112.2, 109.0, 47.2 (NCH₂), 20.2 (ArCH₃).

General Procedure for the Synthesis of *N*-Carboxyanhydrides (NCA) from 2-Aminobenzoic Acids and CO₂



One-pot two-step, Method I: To a 350 mL stainless steel Parr reaction vessel equipped with a stir bar, 2-aminobenzoic acid derivative (2.5 mmol, 1 equiv.), 4-(dimethylamino)pyridine (1 equiv.), anhydrous acetonitrile (50 mL), and *N,N*-diisopropylethylamine (2.2 to 4 equiv.) were added. The reaction vessel was sealed and purged with CO₂ three times. The CO₂ pressure was increased to 300 psi and the system was heated to 65 °C and stirred for 2 h. The vessel was then cooled to RT and the CO₂ pressure was reduced to below 5 psi so that the coupling reagent (1.05

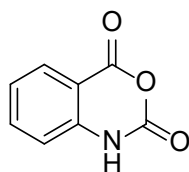
to 3 equiv.) could be injected into the reactor via syringe. The vessel was pressured with CO₂ to 300 psi and the contents were heated at 65 °C and stirred for another 24 h. To stop the reaction, the vessel was cooled to RT and slowly vented. The resulting mixture was then diluted with 250 mL of ethyl acetate, washed with a saturated solution of NaCl, and then washed again with cold water twice. The organic layer was collected, and dried over anhydrous MgSO₄, and the volatiles were removed under reduced pressure to afford the NCA product as a yellow/brown solid.

One-pot one-step, Method II: To a 350 mL stainless steel Parr reaction vessel equipped with a stir bar, 2-aminobenzoic acid derivative (2.5 mmol, 1 equiv.), 4-(dimethylamino)pyridine (1 equiv.), anhydrous acetonitrile (50 mL), *N,N*-diisopropylethylamine (0 to 4 equiv.), and *n*-propylphosphonic anhydride (4.5 mL - 50% wt in ethyl acetate, 1.5 to 3 equiv.) were added. The reaction vessel was sealed and purged with CO₂ three times. The CO₂ pressure was increased to 300 psi and the contents were heated to 65 °C and stirred for 24 h. To stop the reaction, the vessel was cooled to RT and vented. The resulting mixture was then diluted with 250 mL of ethyl acetate, washed with a saturated NaCl solution, and then washed again with cold water twice. The organic layer was collected and dried over anhydrous MgSO₄. The volatiles were removed under reduced pressure to afford the NCA product as a yellow/brown solid.

One-pot one-step, Method III: To a 350 mL stainless steel Parr reaction vessel equipped with a stir bar, 2-aminobenzoic acid derivative (2.5 mmol, 1 equiv.) and anhydrous acetonitrile (40 mL) were combined. The vessel was sealed, purged with CO₂ (300 psi), and stirred for 30 min at RT. After releasing the pressure, the temperature went down to below 5 °C. The vessel was then opened so that *N,N*-diisopropylethylamine (2 mL, 10 mmol, 4 equiv.), and *n*-propylphosphonic anhydride (4.5 mL, 7.5 mmol, 3 equiv.) could be injected into the reactor. The reaction vessel was quickly sealed and purged with CO₂ three times. The CO₂ pressure was increased to 300 psi

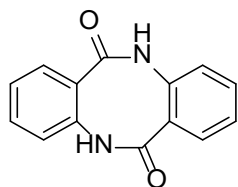
and the contents were heated to 40 °C and stirred for 15 h. To stop the reaction, the vessel was cooled to RT and vented. The resulting mixture was then diluted with 100 mL of ethyl acetate, washed with cold deionized water, and then washed again with a saturated NaCl solution. The organic layer was collected and dried over anhydrous MgSO₄. The volatiles were removed under reduced pressure to afford the NCA product as an off-white solid or brown oil.

3,1-Benzoxazine-2,4(1*H*)-dione (Isatoic anhydride, 2a)



Compound **2a** was synthesized by following **One-pot one-step, Method III**. It was obtained as an off-white solid (400 mg, 99%) without any further purification needed. This compound was reported previously.¹⁶⁶ ¹H NMR (300 MHz, 25 °C, DMSO-*d*₆): δ (ppm) = 11.71 (s, 1H, NH), 7.94 (dd, *J* = 7.9, 1.1 Hz, 1H, Ar*H*), 7.76 – 7.66 (m, 1H, Ar*H*), 7.29 (t, *J* = 7.4 Hz, 1H, Ar*H*), 7.17 (d, *J* = 8.2 Hz, 1H, Ar*H*). ¹³C NMR (101 MHz, 25 °C, DMSO-*d*₆): δ (ppm) = 160.4 (ArCOO), 147.7 (ArNCOO), 141.9, 137.5, 129.5, 124.1, 115.9, 110.8. GC-MS: calc. for C₈H₅NO₃ [M]⁺ = 163.0, found 163.0.

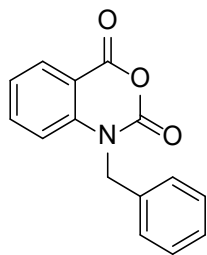
Dibenzo[*b,f*][1,5]diazocine-6,12(5*H*,11*H*)-dione (2a')



Compound **2a'** was synthesized by following the condition described in **Table B3**, entry 2. It was isolated as a yellow solid (190 mg, 64%) after purification by silica gel chromatography using

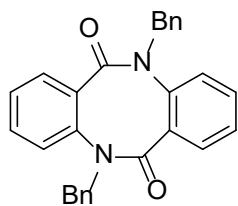
hexanes/ethyl acetate/diethyl ether (9/3/1) as the eluent. This compound was reported previously.¹⁷⁸ ¹H NMR (300 MHz, 25 °C, CDCl₃): δ (ppm) = 8.23 (dd, *J* = 7.9, 1.3 Hz, 1H, *ArH*), 8.11 (dd, *J* = 8.4, 1.5 Hz, 1H, *ArH*), 7.80 – 7.72 (m, 1H, *ArH*), 7.56 (d, *J* = 7.9 Hz, 1H, *ArH*), 7.49 – 7.41 (m, 1H, *ArH*), 7.32 – 7.26 (m, 1H, *ArH*), 6.75 (dt, *J* = 7.1, 3.4 Hz, 2H, *ArH*), 6.48 (br, 2H, *NH*). ¹³C NMR (101 MHz, 25 °C, CDCl₃): δ (ppm) = 159.4 (*ArCON*), 158.0, 149.8, 146.7, 136.6, 133.8, 129.7, 128.7, 127.8, 126.5, 116.9, 116.8, 116.6, 110.1. GC-MS: calc. for C₁₄H₁₀N₂O₂ [M]⁺ = 238.1, found 238.1.

1-Benzyl-3,1-benzoxazine-2,4-dione (2b)



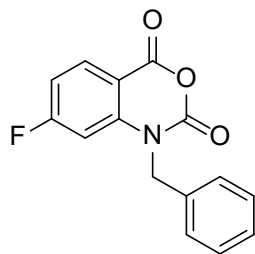
Compound **2b** was synthesized by following **One-pot one-step, Method II**. It was obtained as a light-yellow solid (487 mg, 77%) without any further purification needed. This compound was reported previously.¹⁶⁷ ¹H NMR (400 MHz, 25 °C, CDCl₃): δ (ppm) = 8.15 (dd, *J* = 7.9, 1.5 Hz, 1H, *ArH*), 7.63 (ddd, *J* = 8.7, 7.4, 1.6 Hz, 1H, *ArH*), 7.38 – 7.32 (m, 2H, *ArH*), 7.32 – 7.27 (m, 3H, *ArH*), 7.27 – 7.23 (m, 1H, *ArH*), 7.11 (d, *J* = 8.5 Hz, 1H, *ArH*), 5.30 (s, 2H, *NCH₂Ar*). ¹³C NMR (101 MHz, 25 °C, CDCl₃): δ (ppm) = 158.5 (*ArCOO*), 148.6 (*ArNCOO*), 141.5, 137.3, 134.5, 131.0, 129.3, 128.3, 126.7, 124.3, 114.8, 111.9, 48.6 (*NCH₂Ar*). GC-MS: calc. for C₁₅H₁₀NO₃ [M]⁺ = 253.1, found 253.1.

5,11-Bis(phenylmethyl)dibenzo[*b,f*][1,5]diazocine-6,12(5*H*,11*H*)-dione (2b')



Compound **2b'** was synthesized by following the condition described in **Table 3.1**, entry 5. It was isolated as an off-white solid (300 mg, 58%) after purification by silica gel chromatography using ethyl acetate/ hexanes (3/7) as the eluent. This compound was reported previously.¹⁷⁹ ¹H NMR (300 MHz, 25 °C, CDCl₃): δ (ppm) = 7.31 – 7.25 (m, 8H, ArH), 7.21 – 7.17 (m, 4H, ArH), 7.17 – 7.13 (m, 4H, ArH), 6.87 – 6.82 (m, 2H, ArH), 5.06 (d, *J* = 14.3 Hz, 2H, NCH₂Ar), 4.88 (d, *J* = 14.3 Hz, 2H, NCH₂Ar). ¹³C NMR (101 MHz, 25 °C, CDCl₃): δ (ppm) = 167.9 (ArCON), 139.1, 136.6, 135.3, 130.5, 129.1, 128.7, 128.5, 127.9, 127.9, 126.2, 53.0 (NCH₂Ar). GC-MS: calc. for C₂₈H₂₂N₂O₂ [M]⁺ = 418.2, found 418.2.

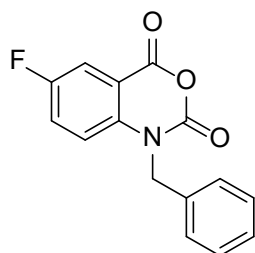
1-Benzyl-2H-6-fluorobenzo[*d*][1,3]oxazine-2,4-dione (**2c**)



Compound **2c** was synthesized by following **One-pot one-step, Method II**. It was obtained as a white-yellowish solid (502 mg, 74%) without any further purification needed. This compound was reported previously.¹⁸⁰ ¹H NMR (500 MHz, 25 °C, CDCl₃): δ (ppm) = 8.18 (dd, *J* = 8.8, 6.1 Hz, 1H, ArH), 7.38 (ddd, *J* = 7.6, 6.2, 1.3 Hz, 2H, ArH), 7.35 – 7.28 (m, 3H, ArH), 6.96 (ddd, *J* = 8.8, 7.8, 2.2 Hz, 1H, ArH), 6.81 (dd, *J* = 10.1, 2.2 Hz, 1H, ArH), 5.26 (s, 2H, NCH₂Ar). ¹³C NMR (125 MHz, 25 °C, CDCl₃): δ (ppm) = 168.1 (d, *J* = 259.0 Hz, CF), 157.5 (ArCOO), 148.5 (ArNCOO),

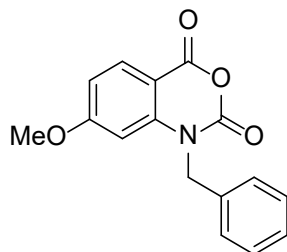
143.8 (d, $J = 12.3$ Hz), 133.9 (d, $J = 11.4$ Hz), 133.9, 129.4, 128.5, 126.7, 112.4 (d, $J = 22.9$ Hz), 108.4 (d, $J = 2.3$ Hz), 102.6 (d, $J = 28.1$ Hz), 49.0 (NCH₂Ar). GC-MS: calc. for C₁₅H₁₀NO₃F [M]⁺ = 271.1, found 271.1.

1-Benzyl-2*H*-7-fluorobenzo[*d*][1,3]oxazine-2,4-dione (2d)



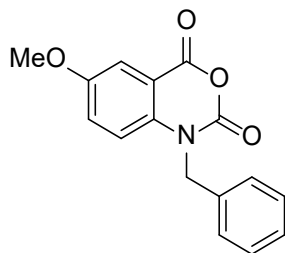
Compound **2d** was synthesized by following **One-pot one-step, Method II**. It was isolated as a light-yellow solid (404 mg, 55%) after purification by silica gel chromatography using ethyl acetate : hexanes (3:7) as the eluent, followed by recrystallization in CH₂Cl₂. This compound was reported previously.¹⁸¹ ¹H NMR (300 MHz, 25 °C, CDCl₃): δ (ppm) = 7.84 (dd, $J = 7.5, 3.0$ Hz, 1H, Ar*H*), 7.39 – 7.28 (m, 6H, Ar*H*), 7.09 (dd, $J = 9.2, 3.9$ Hz, 1H, Ar*H*), 5.30 (s, 2H, NCH₂Ar). ¹³C NMR (125 MHz, 25 °C, CDCl₃): δ (ppm) = 158.6 (d, $J = 247.5$ Hz, CF), 157.6 (d, $J = 3.0$ Hz, ArCOO), 148.2 (ArNCO), 137.9 (d, $J = 2.2$ Hz), 134.2, 129.4, 128.4, 126.6, 125.0 (d, $J = 23.7$ Hz), 117.0 (d, $J = 7.5$ Hz), 116.4 (d, $J = 24.3$ Hz), 113.3 (d, $J = 8.0$ Hz), 49.0 (NCH₂Ar). GC-MS: calc. for C₁₅H₁₀NO₃F [M]⁺ = 271.1, found 271.1.

1-Benzyl-2*H*-6-dimethoxybenzo[*d*][1,3]oxazine-2,4-dione (2e)



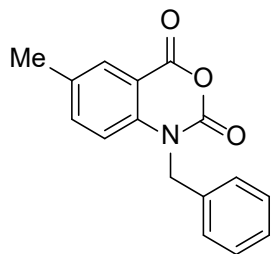
Compound **2e** was synthesized by following **One-pot one-step, Method II**. It was obtained as a yellow solid (587 mg, 83%) without any further purification needed. ^1H NMR (500 MHz, 25 °C, CDCl_3): δ (ppm) = 8.04 (d, J = 8.8 Hz, 1H, ArH), 7.39 – 7.25 (m, 5H, ArH), 6.75 (dd, J = 8.8, 1.8 Hz, 1H, ArH), 6.52 (s, 1H, ArH), 5.25 (s, 2H, NCH_2Ar), 3.78 (s, 3H, CH_3OAr). ^{13}C NMR (125 MHz, 25 °C, CDCl_3): δ (ppm) = 166.7 (ArCOO), 158.0 (ArNCOO), 149.1, 143.4, 134.6, 133.0, 129.2, 128.2, 126.8, 110.7, 104.5, 100.2, 56.0 (CH_3OAr), 48.7 (NCH_2Ar). ESI-MS (+): calc. for $\text{C}_{16}\text{H}_{13}\text{NO}_4$ $[\text{M}+\text{H}]^+ = 284.09173$, found 284.09251.

1-Benzyl-2H-7-dimethoxybenzo[*d*][1,3]oxazine-2,4-dione (2f)



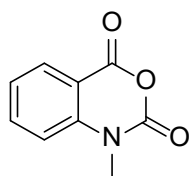
Compound **2f** was synthesized by following **One-pot one-step, Method II**. It was isolated as a white-yellowish solid (148 mg, 21%) after purification by silica gel chromatography using ethyl acetate : hexanes (3:7) as the eluent. ^1H NMR (500 MHz, 25 °C, CDCl_3): δ (ppm) = 7.57 (d, J = 3.0 Hz, 1H, ArH), 7.39 – 7.27 (m, 5H, ArH), 7.20 (dd, J = 9.1, 3.0 Hz, 1H, ArH), 7.03 (d, J = 9.2 Hz, 1H, ArH), 5.28 (s, 2H, NCH_2Ar), 3.84 (s, 3H, CH_3OAr). ^{13}C NMR (125 MHz, 25 °C, CDCl_3): δ (ppm) = 158.6 (ArCOO), 156.2 (ArNCOO), 148.5, 135.5, 134.7, 129.3, 128.2, 126.7, 126.0, 116.4, 112.6, 111.8, 56.1 (CH_3OAr), 48.7 (NCH_2Ar). GC-MS: calc. for $\text{C}_{16}\text{H}_{13}\text{NO}_4$ $[\text{M}]^+ = 283.1$, found 283.1. ESI-MS (+): calc. for $\text{C}_{16}\text{H}_{13}\text{NO}_4$ $[\text{M}+\text{H}]^+ = 284.09173$, found 284.09272.

1-Benzyl-2H-7-methylbenzo[*d*][1,3]oxazine-2,4-dione (2g)



Compound **2g** was synthesized by following **One-pot one-step, Method II**. It was isolated as a light-yellow solid (281 mg, 42%) after purification by silica gel chromatography using ethyl acetate : hexanes (3:7) as the eluent. This compound was reported previously.¹⁸¹ ¹H NMR (500 MHz, 25 °C, CDCl₃): δ (ppm) = 7.95 (d, *J* = 2.0 Hz, 1H, Ar*H*), 7.46 – 7.40 (m, 1H, Ar*H*), 7.39 – 7.27 (m, 5H, Ar*H*), 7.00 (d, *J* = 8.6 Hz, 1H, Ar*H*), 5.29 (s, 2H, NCH₂Ar), 2.37 (s, 3H, CH₃Ar). ¹³C NMR (125 MHz, 25 °C, CDCl₃) δ (ppm) = 158.6 (ArCOO), 148.6 (ArNCOO), 139.3, 138.3, 134.6, 134.3, 130.5, 129.2, 128.2, 126.7, 114.8, 111.7, 48.5 (NCH₂Ar), 20.5 (CH₃Ar). GC-MS: calc. for C₁₆H₁₃NO₃ [M]⁺ = 267.1, found 267.1.

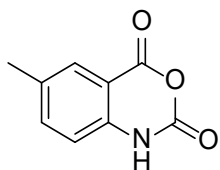
1-Methyl-2*H*-3,1-benzoxazine-2,4(1*H*)-dione (**2h**)



Compound **2h** was synthesized by following **One-pot one-step, Method III**. It was obtained as an off-white solid (335 mg, 76%) without any further purification needed. This compound was reported previously.¹⁶⁸ ¹H NMR (500 MHz, 25 °C, CDCl₃) of **2h**: δ (ppm) = 8.18 (dd, *J* = 7.8, 1.7 Hz, 1H, Ar*H*), 7.80 (dt, *J* = 8.9, 1.5 Hz, 1H, Ar*H*), 7.31 (dt, *J* = 7.9, 0.76 Hz, 1H, Ar*H*), 7.20 (d, *J* = 8.0 Hz, 1H, Ar*H*), 3.42 (s, 3H, CH₃N). ¹³C NMR (125 MHz, 25 °C, CDCl₃): δ (ppm) =

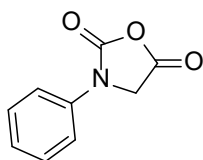
158.6 (ArCOO), 148.1 (ArNCOO), 142.1, 137.4, 130.9, 124.2, 113.9, 112.9, 32.0 (CH₃N). GC-MS: calc. for C₉H₇NO₃ [M]⁺ = 177.0, found 177.1.

6-Methyl-2*H*-3,1-benzoxazine-2,4(1*H*)-dione (2i)



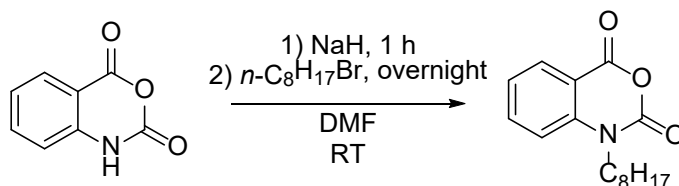
Compound **2i** was synthesized by following **One-pot one-step, Method III**. It was obtained as an off-white solid (341 mg, 77%) without any further purification needed. This compound was reported previously.¹⁸² ¹H NMR (500 MHz, 25 °C, DMSO-*d*₆): δ (ppm) = 11.65 (br, 1H, *NH*), 7.71 (s, 1H, *ArH*), 7.56 (dd, *J* = 8.3, 1.6 Hz, 1H, *ArH*), 7.06 (d, *J* = 8.3 Hz, 1H, *ArH*), 2.32 (s, 3H, CH₃Ar). ¹³C NMR (125 MHz, 25 °C, DMSO-*d*₆): δ (ppm) = 160.0 (ArCOO), 147.2 (ArNCOO), 139.3, 138.0, 133.0, 115.3, 110.0, 20.1 (CH₃Ar).

3-Phenyloxazolidine-2,5-dione (4)



Compound **4** was synthesized from *N*-phenylglycine by following **One-pot one-step, Method III**. It was obtained as an off-white solid (225 mg, 51%) after recrystallization in CHCl₃. This compound was reported previously.¹⁸³ ¹H NMR (300 MHz, 25 °C, CDCl₃): δ (ppm) = 7.51 (d, *J* = 7.9 Hz, 2H, *ArH*), 7.44 (t, *J* = 8.0 Hz, 2H, *ArH*), 7.25 (t, *J* = 7.2 Hz, 1H, *ArH*), 4.56 (s, 2H, NCH₂COO). ¹³C NMR (125 MHz, 25 °C, CDCl₃): δ (ppm) = 164.0 (CH₂COO), 149.1 (ArNCOO), 135.8, 129.8, 126.0, 118.9, 49.6 (NCH₂COO).

Synthesis of 1-octyl-2*H*-benzo[*d*][1,3]oxazine-2,4(1*H*)-dione (2j).



Compound **2j** was synthesized following a modified published procedure.¹⁸⁴ In a 100 mL round bottom flask, isatoic anhydride (1.7 g, 10.4 mmol, 1 equiv.) was added to 10 mL of DMF under nitrogen. To the stirring solution of isatoic anhydride, 0.38 g (15.6 mmol, 1.5 equiv.) of NaH was added in portions. The reaction was stirred for one hour at room temperature and to which 2.74 mL (15.6 mmol, 1.5 equiv.) of 1-bromooctane ($n\text{-C}_8\text{H}_{17}\text{Br}$) was added. The reaction was stirred overnight. Upon completion, the reaction mixture was added to 500 mL of ice water and extracted with ether three times. The combined organic layer was dried with MgSO_4 and filtered through celite. After the removal of the solvent, the crude was recrystallized from diethyl ether layered with hexanes to yield a white crystalline product (554 mg, 20%). ^1H NMR (500 MHz, 25 °C, CDCl_3) of **2j**: δ (ppm) = 8.18 (dd, $J = 8.0, 1.5$ Hz, 1H, ArH), 7.76 (dt, $J = 8.8, 1.6$ Hz, 1H, ArH), 7.29 (dt, $J = 8.8, 0.9$ Hz, 1H, ArH), 7.17 (d, $J = 8.5$ Hz, 1H, ArH), 7.15 (t, $J = 8$ Hz, 1H, ArH), 4.05 (t, $J = 8.0$ Hz, 2H, NCH_2), 1.75 (quintet, 2H NCH_2CH_2), 1.43-1.27 (m, $(\text{CH}_2)_5$), 0.88 (t, $J = 7.0$ Hz, 3H, CH_3).

3.5 Appendix B

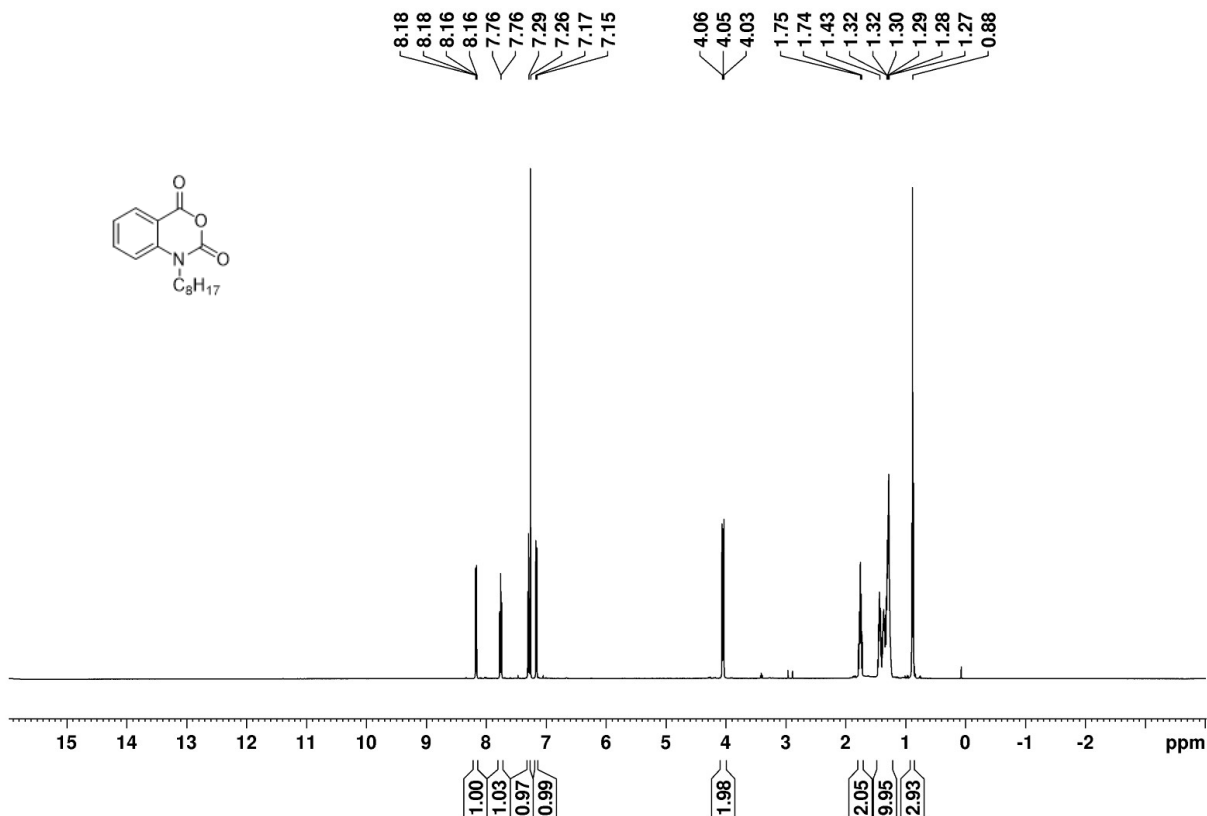
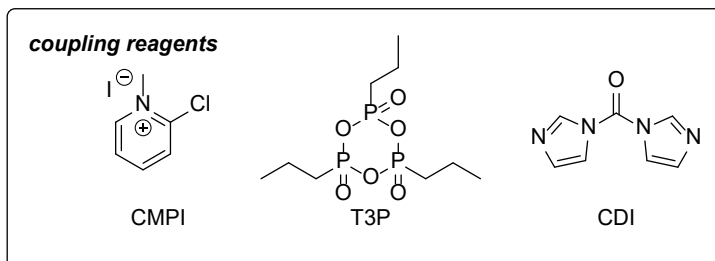
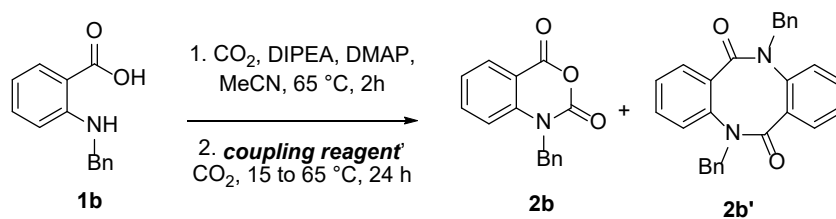


Figure B1. ¹H NMR (500 MHz, 25 °C, CDCl₃) of **2j**: δ (ppm) = 8.18 (dd, J = 8.0, 1.5 Hz, 1H, ArH), 7.76 (dt, J = 8.8, 1.6 Hz, 1H, ArH), 7.29 (dt, J = 8.8, 0.9 Hz, 1H, ArH), 7.17 (d, J = 8.5 Hz, 1H, ArH), 7.15 (t, J = 8 Hz, 1H, ArH), 4.05 (t, J = 8.0 Hz, 2H, NCH₂), 1.75 (quintet, 2H NCH₂CH₂), 1.43-1.27 (m, (CH₂)₅), 0.88 (t, J = 7.0 Hz, 3H, CH₃).

Table B1. Screening coupling reagents using the one-pot two-step method.

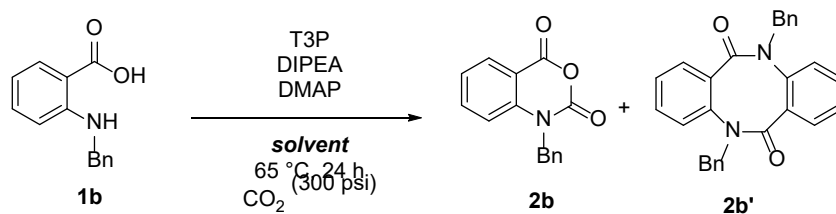


Entry ^a	Coupling reagent	Conversion ^b	Isolated yield	2b: 2b' ^b
	(equiv.)	(%)	(%)	
1	T3P (1.5)	100	80	100:8
2	T3P (3)	100	82	100:1
3	CMPI (1.5)	100	54	100:20
4	CDI (1.5)	100	0	-

a. Reaction conditions: 2-(*N*-benzylamino)benzoic acid (2.5 mmol), DMAP (1 equiv.), DIPEA (4 equiv.), MeCN (50 mL). The reactions were set up using **Method I** described in the experimental section.

b. Determined by ¹H NMR spectroscopy using 1,3,5-trimethoxybenzene as an internal standard.

Table B2. One-pot synthesis of *N*-benzyl substituted six-membered NCAs in different solvents.

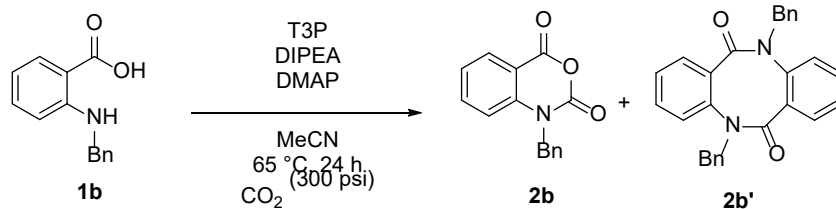


Entry ^a	Solvent	Conversion ^b	Yield ^b	2b: 2b' ^b
		(%)	(%)	
1	THF	100	-	100:40
2	MeCN	100	85	100:0
3	Ethylene carbonate	100	-	100:0
4	Propylene carbonate	100	27	100:0
5	Propylene carbonate: THF (3:7)	100	73	100:0
6	Propylene oxide	100	-	-

a. Reaction conditions: 2-(*N*-benzylamino)benzoic acid (2.5 mmol), DMAP (1 equiv), DIPEA (4 equiv.), T3P (3 equiv.), CO₂ (300 psi), solvent (50 mL). The reactions were set up using **Method II** described in the experimental section.

b. Determined by ¹H NMR spectroscopy using 1,3,5-trimethoxybenzene as an internal standard.

Table B3. Studying the effect of different reagents and reactants.



Entry ^a	Experiment	Conversion ^b (%)	Yield of 2b ^b (%)	Yield of	
				2b ^{rb} (%)	2b : 2b' ^b
1	Omitting CO ₂	100	0	68	0:100
2	Omitting DIPEA	90	2.5	-	1: 16
3	Omitting DMAP	63	10	-	100: 37.5
4	Omitting T3P	42.5	0	0	0:0
5	T3P (1.5 equiv.)	95	56	-	100: 11
6	T3P (3 equiv.)	100	85	-	100:0

a. Reaction conditions: 2-(N-benzylamino)benzoic acid (2.5 mmol), DMAP (1 equiv.), DIPEA (4 equiv.), T3P (3 equiv.), CO₂ (300 psi), CH₃CN (50 mL). The reactions were set up using **Method II** described in the experimental section.

b. Determined by ¹H NMR spectroscopy using 1,3,5-trimethoxybenzene as internal standard.

Chapter 4. Surface immobilization of ferrocene-based compounds

4.1 Introduction

Harnessing easily tunable and well-defined organometallic catalysts with robust and recyclable solid supports has garnered significant attention.⁵⁴ Various strategies have been pursued to heterogenize homogeneous organometallic catalysts onto solid support in order to combine the advantages from both realms. The resulting hybrid catalysts often exhibit enhanced catalytic performance in comparison to their homogeneous analogue. Reports on surface-immobilization of Schiff base compounds, represented by salen and salphen, have been shown to improve catalytic activities, prolong catalyst lifetimes, and facilitate catalyst recycling.¹⁸⁵⁻¹⁹¹ It is important to emphasize the immense potential of attaching metal complexes onto conducting or semiconducting solid surfaces. The immobilization of metal complexes onto electrically addressable surfaces potentially enables efficient electron transfers between the interfaces, therefore expanding the capability of the hybrid material in electrochemical applications.¹⁹² A growing number of applications based on the surface-anchored metal complexes based on pyridine or porphyrin have been reported for energy storage- and conversion-related reactions.¹⁹³ However, fewer investigations were focused on salen derivatives regardless of their superior catalytic behavior in a wide range of organic transformations.^{188-190, 194, 195} There remains a gap in combining the superior molecular catalytic activities of salen derivatives with the outstanding electronic communication capability of the solid surfaces. It is important to realize that the conductive/semiconductive surface holds unrealizing potentials beyond chemically or electrochemically inert support.^{196, 197} In addition, integrating redox-active transition metal complexes on electrically addressable surfaces may provide temporal control over a catalytic process through electrochemically induced redox events.⁵² The utilization of surface-bounded

compounds also allows the investigation of spatial control by confining the catalytic active species on the surface.

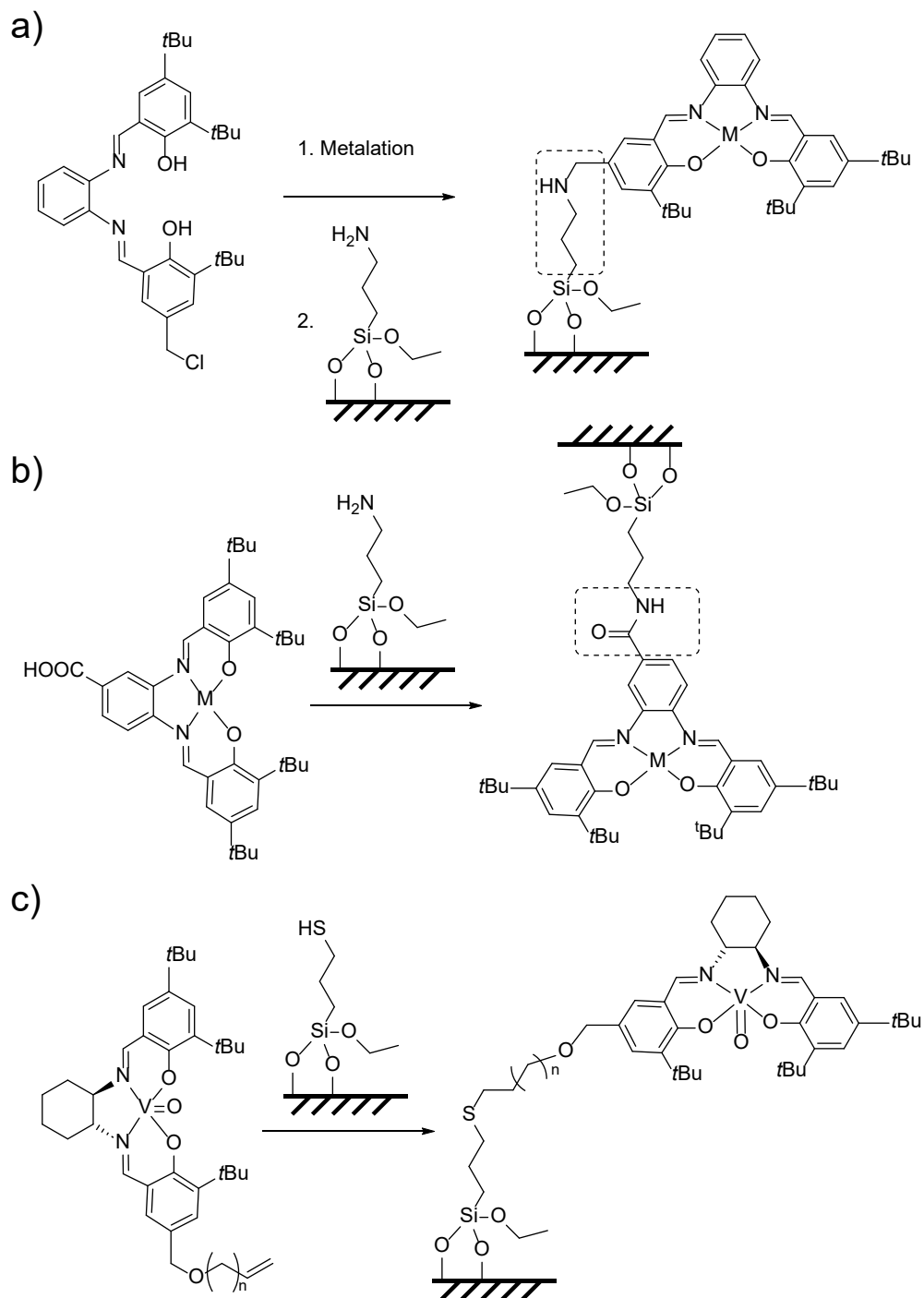


Figure 4.1. Selection of examples of surface-immobilized Schiff base derivatives through a) substitution of alkyl chloride with amine; b) amide bond formation; c) radical addition of alkene

with thiol.^{186, 189, 191, 198}

Metal oxides have garnered significant attention as solid supports for surface immobilization of molecular compounds owing to their inherent stability and versatility. Surface functionalization onto metal oxides can be accessed through a diverse range of anchoring groups including carboxylic acids, phosphonic acids, silanes, etc.^{199, 200} A selection of methods to immobilize salen-supported metal complexes is shown in Figure 4.1, while more strategies have been developed based on different solid surfaces through manifold linkages.^{186, 189, 191, 198} In the previous chapter, we briefly discussed the ring-opening polymerization of 6-membered ring NCAs catalyzed by salenAl complexes and the attempts towards integrating the synthesis of NCAs with their subsequent polymerization process. However, owing to the incompatibility of the reaction conditions between NCA synthesis and polymerization steps, integration of the two processes in one pot without compartmentalization was unfeasible. In order to potentially achieve a separation of the active reagent involved in the two steps, our approach involves the immobilization of the polymerization catalyst onto a solid support. Meanwhile, our collaborators are exploring potential compartmentalization for the active reagents involved in NCA synthesis.

More importantly, inspired by a study on surface-initiated redox switchable polymerization achieved by anchoring an iron catalyst to TiO₂ nanoparticles,⁵² we became interested in extending the study of redox-switchable ring-opening polymerization to the solid state by immobilizing the ferrocene derivative onto a conducting surface (Figure 4.2). The immobilization of redox-active metal complexes onto a conducting surface provides a viable platform to explore surface-initiated polymerizations. Such a hybrid system holds the potential of synthesizing distinct polymer blocks through the selective application of an electrical stimulus.

Compared to the homogeneous electrochemically controlled redox switchable system, spatially confining the catalyst on the electrode potentially reduces the distance from the electrode to the redox mediator by adjusting the length of the linkage, thereby circumventing mass transport limitations. Furthermore, the investigations disclosed in this chapter provide invaluable insights for the further development of a hybrid catalyst through the heterogenization of a homogeneous catalyst on a functional surface.

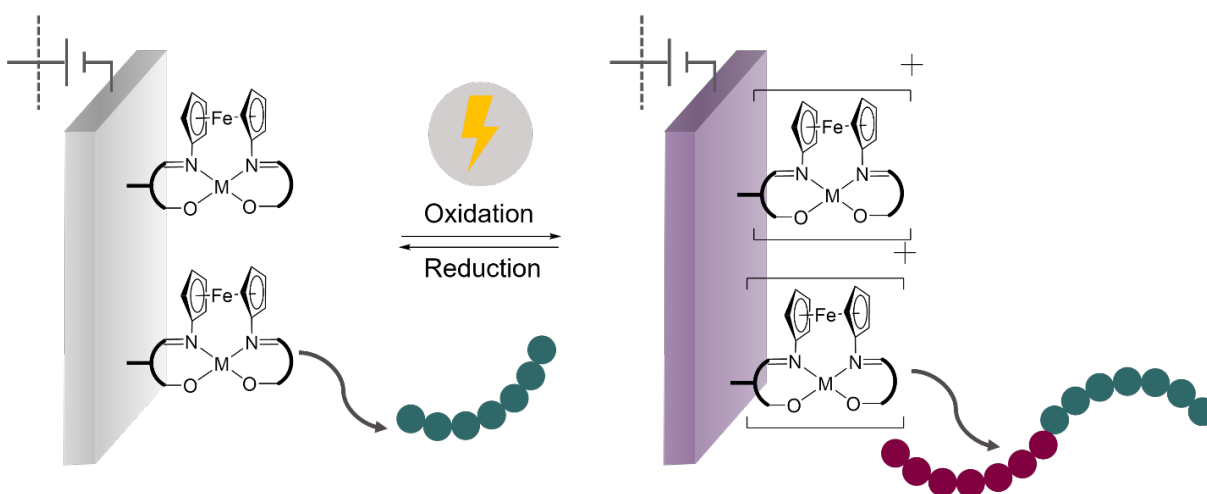


Figure 4.2. Immobilization of the redox-responsive catalyst onto the electrode for spatiotemporal control over polymerization reactions.

4.2 Results and discussion

Synthesis of salfen-derived compounds with anchoring handles (salfen-CH₂X, salfen-COOR, and salfen-C≡CH)

Inspired by the successful anchoring of the Schiff base compounds onto solid support via alkyl chloride linkages, we decided to first attempt to synthesize a salfen derivative with alkyl chloride appended (salfen = *N,N'*-bis(2,4-di-*tert*-butylphenoxy)-1,1'-ferrocenediimine).^{189, 201-203} We proposed that with a self-assembled monolayer of aminosilane, 3-(trimethoxysilyl)propan-

1-amine for example, a Salfen-based metal complex modified with alkyl chloride could be potentially attached to a solid surface (Figure 4.3). Our initial approaches to synthesizing salfen-CH₂Cl, **A1**, under different conditions, did not yield the desired product. In fact, the reaction of 1 equivalent of 1,1'-diaminoferrocene with 2 equivalents of 3-(*tert*-butyl)-5-(chloromethyl)-2-hydroxybenzaldehyde in methanol provided 3-(*tert*-butyl)-5-(methoxymethyl)-2-hydroxybenzaldehyde as the product; and activating the aldehyde using anhydrous HCl (2 M in ether) in methanol provide a salfen-derived compound, **A2**, as observed in NMR spectroscopy (Figure C10-14). Unfortunately, the reaction did not work in non-alcoholic solvents (Table C1). We postulated that the substitution of the reactive alkyl chloride is faster than the amine-aldehyde condensation reaction in methanol. The substitution of Cl⁻ with MeO⁻ from methanol occurs instantly before the imine formation started, therefore yielding **A2** as the product (Scheme 4.1).

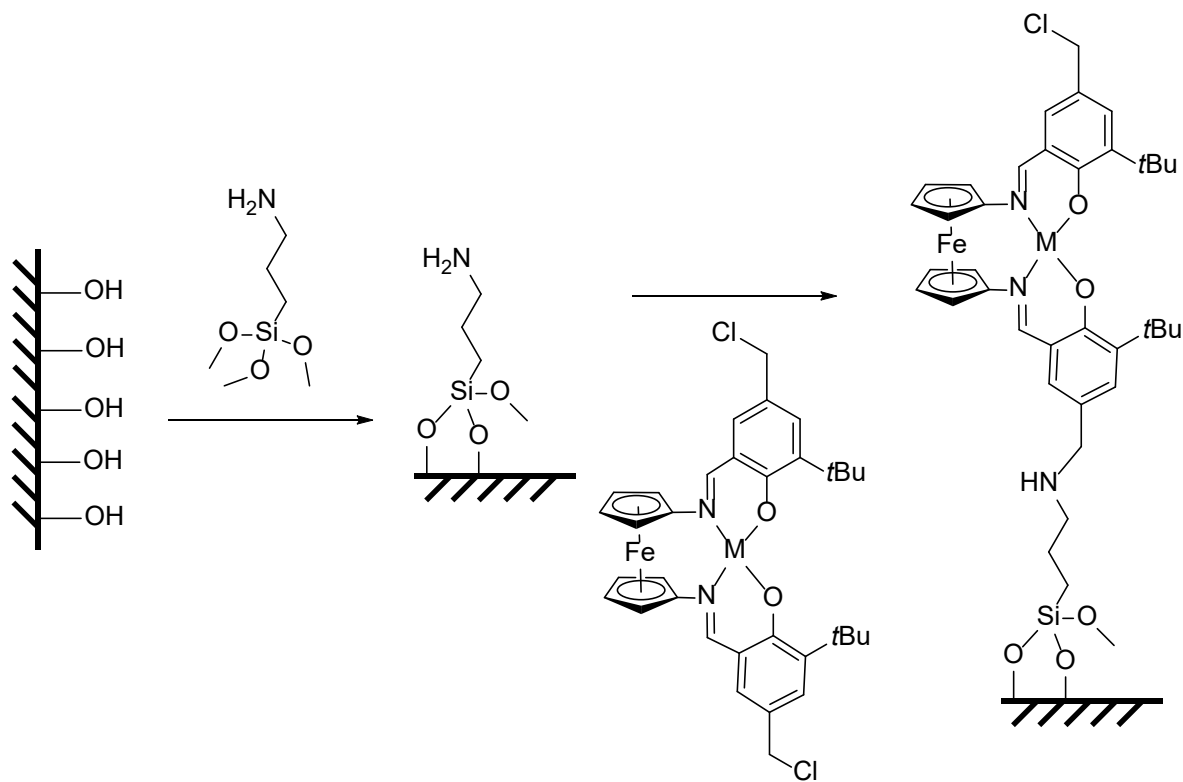
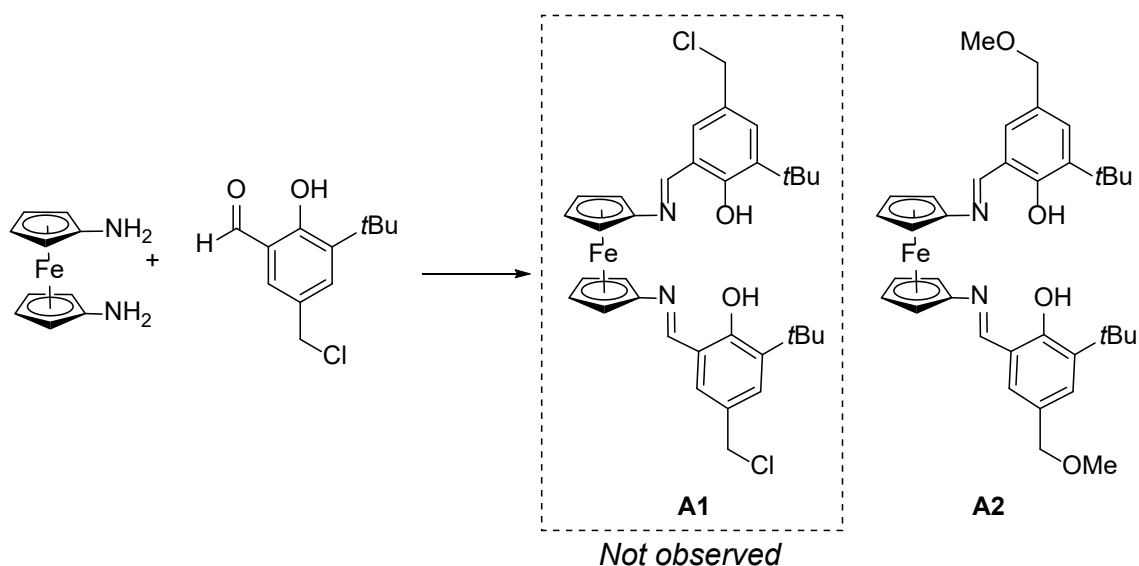


Figure 4.3. Proposed anchoring strategy for metal complex supported by salfen derivative with alkyl chloride.



Scheme 4.1. Attempt to synthesize salfen derivative with alkyl chloride.

We next looked into salfen compounds with carboxylic substitution on the phenoxy ring of salfen for ease of modification compared to the modification on the ferrocene backbone.²⁰⁴⁻²⁰⁶ L1-L4 with methyl ester substitutions were synthesized and isolated from methanol in the form of solid precipitation (Figure 4.4). The compounds were characterized by NMR spectroscopy. However, attempts to synthesize the carboxylic derivative of Salfen instead of esters following similar procedures were not successful.^{204, 207, 208} The reaction of 3-(*tert*-butyl)-5-formyl-4-hydroxybenzoic acid with 1,1'-diaminoferrocene in THF did not precipitate. Solid was isolated after removing THF under reduced pressure, which was purified by re-dissolving into methanol and layered with hexanes. However, the isolated solid from methanol had low solubility in common solvents. Nonetheless, an ¹H NMR spectrum in CDCl₃ was acquired and compared with the starting aldehyde indicating the disappearance of the aldehyde and the formation of an imine

(Figure C31). The same reaction was conducted in methanol; however, the result could not be further improved. Deprotecting the methyl ester derivative **L4** in the presence of a base led to a complete decomposition of the compound.

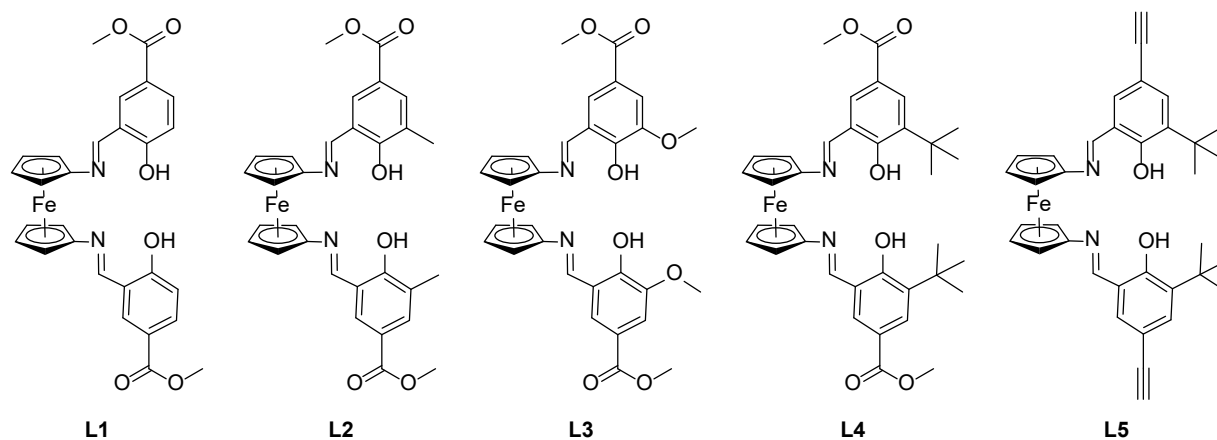


Figure 4.4. Representations of **L1-5**.

Meanwhile, inspired by the robust linkage established through the azide-alkyne “click” reaction, we attempted to synthesize an alkyne-substituted salphen derivative.²⁰⁹ The triazole linkage from the “click” reaction offers a unique platform for comprehensive characterization via several spectroscopy techniques.^{210,211} Encouraged by the promising results demonstrated in the published literature concerning the success of “click” chemistry in cross-linking of polymeric networks,^{211,212} formations of nanocomposites,²¹³ and immobilization of molecular compounds onto solid supports,^{214,215} we embarked on synthesizing, salphen incorporating alkyne substitution, **L5**, to facilitate “click” reactions (Figure 4.5).^{216,217} The condensation of 1,1'-diaminoferrocene and 3-(*tert*-butyl)-5-ethynyl-2-hydroxybenzaldehyde was carried out in methanol, yielding orange-red precipitation after overnight stirring at room temperature, which was isolated on top of a medium frit and characterized by NMR spectroscopy (Figure C32-35).

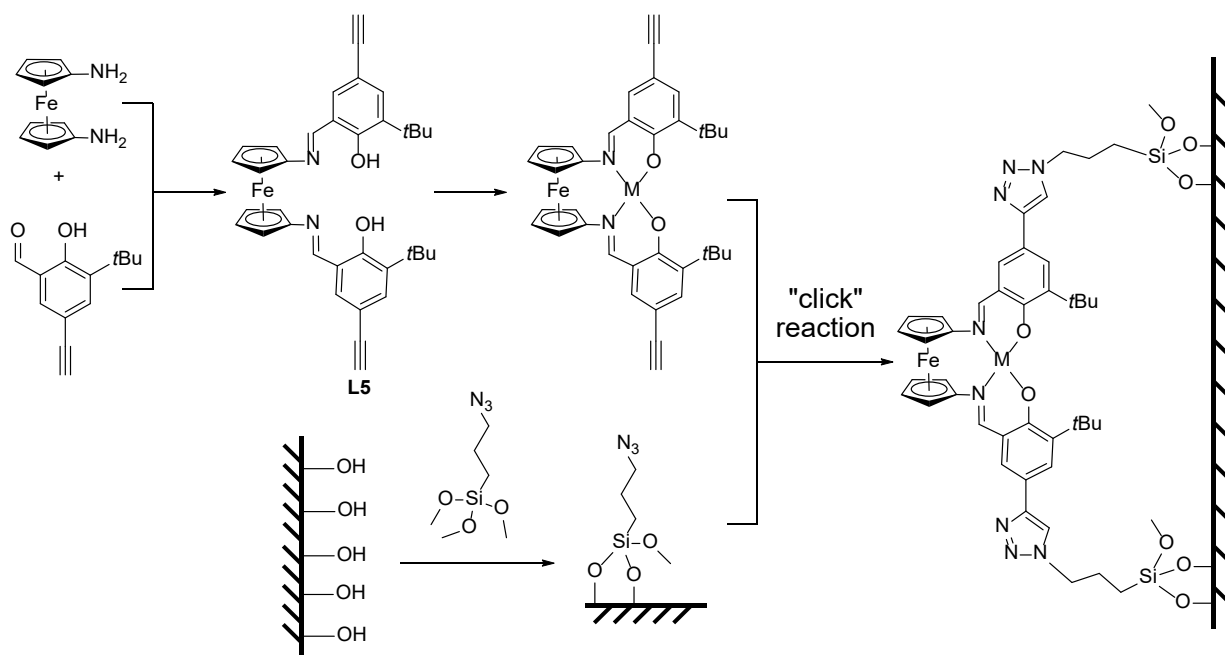


Figure 4.5. The proposed anchoring strategy of the alkyne-derived salphen-supported metal complex via azide-alkyne “click” reaction.

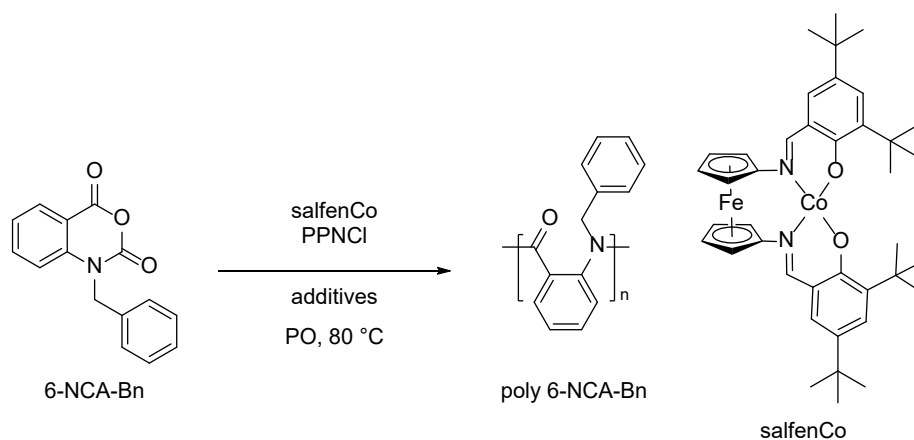
Synthesis of metal complexes supported by L1-L5

The low solubility of the salphen derivatives hampered the synthesis of a metal complex. From the preliminary results, aluminum complexes supported by salphen and salphen ligands were proven to be active catalysts for 6-membered ring NCA polymerization. Efforts toward synthesizing an aluminum complex from **L1-L3**, unfortunately, were fruitless. Following the published synthetic procedure of (salphen)Al(O*i*Pr)₃, we attempted to react Al(O*i*Pr)₃ with **L1-L3** under similar conditions.⁸⁶ Reactions of Al(O*i*Pr)₃ with **L1** in toluene or the combination of toluene and DCM at room temperature or elevated temperature exhibited substantial complexity that precluded unambiguous interpretation through NMR spectroscopy (Table C2, entries 1-4). Reactions of Al(O*i*Pr)₃ with **L3** in different solvent combinations at room temperature showed no reaction over a designated period of time and became messy at elevated temperatures (entries

5-10, 13). Similar results have been observed for **L2** as well (entries 14-16). The low solubility of compound **L1-3** in commonly used solvents at ambient conditions and the observed uncontrollable reaction kinetics at elevated temperatures led to unpredictable reaction outcomes.

Owing to the challenges encountered during the synthesis of an aluminum complex, our investigation was redirected toward the utilization of cobalt and chromium. A preliminary study of (salfen)Co demonstrated it as an active catalyst towards 6-membered ring NCA polymerization. However, similar to (salfen)Al(OiPr), (salfen)Co was inactive in the presence of the coupling reagents and starting amino acids (Table 4.1). Nonetheless, **L4** with the highest solubility among the ester-substituted salfen compounds, and **L5** with alkyne substitution were employed to synthesize cobalt and chromium complexes based on published procedures.^{89, 218}

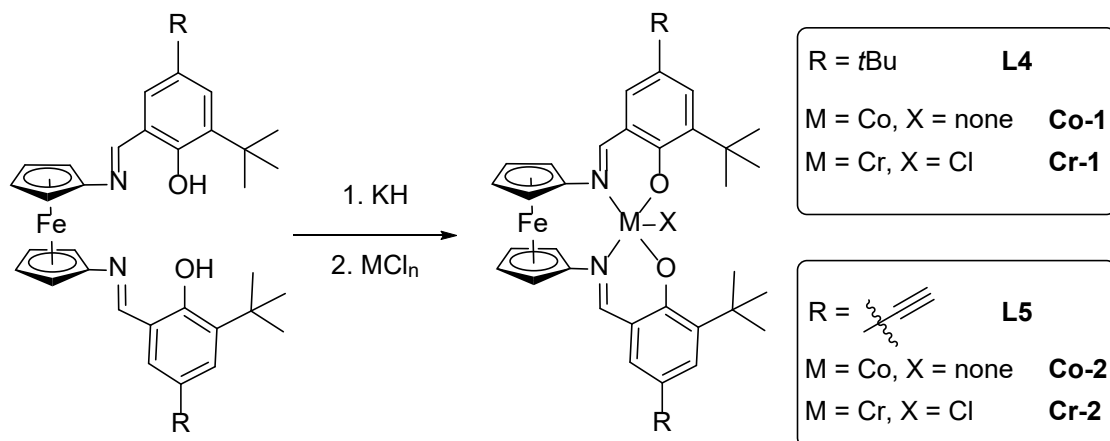
Table 4.1. Compatibility of (salfen)Co for 6-membered ring NCA polymerization



	N-benzyl anthranilic acid	6-NCA- Bn	T3P	P₂O₅	DIPEA	DMAP
Yield	N/A	80%	N/A	N/A	78%	N/A

Standard conditions: (salphen)Co (0.004 mmol, 1 equiv.), PPNC1 (0.008 mmol, 2 equiv.), and 6-NCA-Bn (0.2 mmol, 50 equiv.) were added to a 25 mL Schlenk tube with 0.7 mL PO in total with or without additives. The reaction was heated at 80 °C for 2 hours. The reaction was then quenched with methanol to isolate any precipitation. Due to the insoluble nature of the polymer of 6-NCA-Bn, no NMR spectrum assignment was available. The yield was calculated based on the mass of the isolated precipitation after washing with methanol and DCM followed by centrifugation and overnight drying under vacuum.

To synthesize a cobalt complex supported by salphen derivatives with anchoring handles, **L4** and **L5** were employed following the published procedure of (salphen)Co.⁸⁹ 1 equivalent of **L4** or **L5** were deprotonated by 2 to 2.2 equivalents of potassium hydride in THF. Cobalt complexes **Co-1** and **Co-2** were prepared by salt metathesis between the potassium salt of **L4** and **L5** and CoCl₂, respectively (Scheme 4.2). Both cobalt complexes are paramagnetic, as expected for cobalt(II). Chromium complexes **Cr-1** and **Cr-2** were prepared following a similar procedure, replacing CoCl₂ with CrCl₃.²¹⁸ The chromium complexes were NMR silent due to their paramagnetic nature.



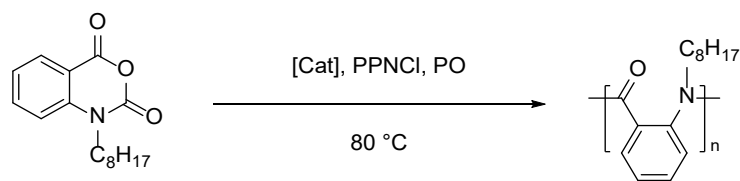
Scheme 4.2. Synthesis of **Co-1**, **Co-2**, **Cr-1**, and **Cr-2**.

In addition to ^1H NMR spectroscopy, high-resolution mass spectrometry (HRMS) was employed to confirm the formation of the compounds. HRMS (ES+) of **Co-1** and **Co-2** were found for $[\text{M}+\text{H}]^+$. In the case of chromium, HRMS (ES+) were found after the loss of the chloride for the positively charged complexes ($[\text{M}-\text{Cl}]^+$). All four compounds were characterized by UV-Vis spectroscopy in comparison to their corresponding pro-ligands. **L4** and **L5** had similar absorption spectra in THF in the range of 300-500 nm while coordination to cobalt or chromium caused a shift in the spectra. **Co-1** featured in 382 nm and **Co-2** featured in 406 nm while **C2-1** featured in 403 nm and **Cr-2** featured in 426 nm (Figure C43-44).^{89, 219} Those absorbance bands indicate successful coordination of the corresponding transition metal with **L4** or **L5**.

Homogenous polymerization of 6-membered ring NCA catalyzed by Co and Cr complexes

To ascertain the efficacy of the cobalt and chromium complexes supported by the modified salphen derivatives **L4** and **L5**, we conducted an initial assessment of their activity in the polymerization of 6-membered ring NCAs. Delightfully, all four newly synthesized complexes were able to polymerize N-substituted 6-membered ring NCAs, namely 6-NCA-C₈H₁₇ in the presence of co-catalyst PPnCl with remarkable isolated yield (Table 4.2). Owing to the higher solubility of the long alkyl substitution on the 6-membered ring NCA, the isolated polymers from Table 5.2 were characterized by ^1H NMR spectroscopy and SEC (Figure C42, C45-48).

Table 4.2. Polymerization of 6-NCA-C₈H₁₇ catalyzed by homogenous cobalt and chromium complexes supported by **L4** and **L5**



Entry ^a	Catalyst	Yield ^b	M_n (kDa) ^c	M_n (theo, kDa) ^d	Dispersity ^c	dn/dc ^c
1	Co-1	92%	16.8	10.7	1.33	0.116
2	Co-2	99%	24.4	12.2	1.48	0.136
3	Cr-1	85%	29.2	10.2	1.45	0.129
4	Cr-2	96%	24.7	11.4	1.56	0.138

- a. All experiments were conducted in 0.7 mL of PO with 0.004 mmol of catalyst, 0.008 mmol (2 equiv.) of PPNCI, and 0.2 mmol (50 equiv.) of 6-NCA-C₈H₁₇ in duplicates.
- b. Polymers were isolated by adding MeOH to precipitate and washed with DCM/MeOH, centrifuged, and dried under a vacuum overnight. The yields were determined gravimetrically. Determined by SEC measurements.
- c. $M_{n,theo} = ([6-NCA-R]_0/[Cat]) \times (MW \text{ of } 6-NCA-R - MW \text{ of } CO_2) \times \text{polymer yield}$.

Surface immobilization of salfen-COOMe, salfen-C≡CH, and their supported complex

Inspired by the pioneering work done by Qi *et al.*, we aimed to immobilize a metal complex with redox-responsive ligand onto an electro-addressable surface to enable future electrochemical control over the reaction process.⁵² P25 TiO₂ nanoparticle-coated FTO plates were selected based on its superior results on surface-initiated electrochemically controlled ring-opening polymerization reactions. We employed P25 TiO₂ nanoparticles for the initial

investigation of the surface anchoring strategies. We have prepared the ester-substituted salfen compounds **L1-L4**, along with metal complexes **Co-1** and **Cr-1** supported by **L4**. Our initial scientific investigation revolved around the immobilization of **L1** onto P25 TiO₂ nanoparticles through transesterification. Following an unpublished experimental procedure developed by the Byers group, **L1** was mixed with pre-treated P25 TiO₂ nanoparticles. The resulting nanoparticles were washed several times followed by centrifugation until the supernatant was colorless, dried under a reduced pressure, and analyzed by IR spectroscopy and ICP-MS.

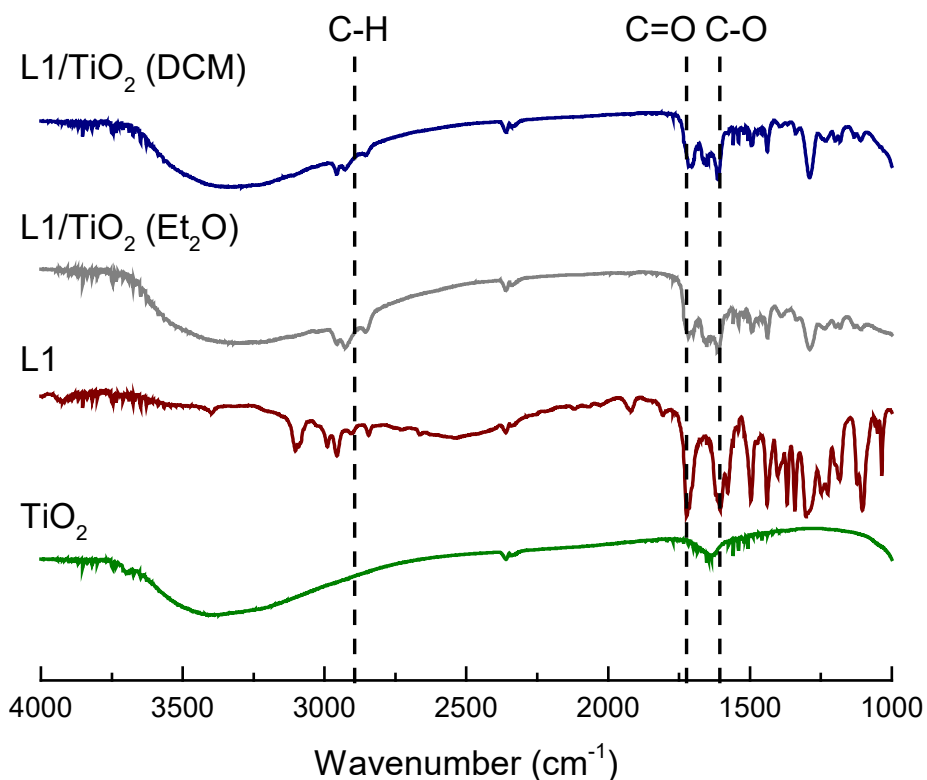


Figure 4.6. Overlay of IR spectra of TiO₂ nanoparticles (green), **L1** (brown), and **L1** immobilized TiO₂ nanoparticles using diethyl ether as solvent (gray), and DCM as solvent (gray).

Based on IR analysis (Figure 4.6), in comparison with the untreated P25 TiO₂

nanoparticles, the treated TiO₂ nanoparticles using either DCM or diethyl ether as solvent displayed C-H stretching at 2800-3000 cm⁻¹, C=O stretching at 1650-1750 cm⁻¹, and C-O stretching at 1250-1300 cm⁻¹ with low intensity. These bands were identifiable for **L1**, while slight shifting of the C=O and C-O stretching was observed for **L1/TiO₂** due to immobilization. However, the low intensity and the ambiguous shift for the ester peaks were insufficient to confirm the formation of the ester linkage from the surface OH with **L1**. We postulate that tethering of **L1** onto the surface could be achieved potentially through the formation of ester linkage while acknowledging the possibility of physical adsorption. Nonetheless, **Co-1/TiO₂** and **Cr-1/TiO₂** were prepared following a similar procedure.

To assess the effectiveness of surface immobilization through the proposed mechanism, we compared the ICP-MS analysis results of **L1/TiO₂**, **Co-1/TiO₂**, and **Cr-1/TiO₂** with several control experiments (Table C4). Salfen without ester substitution as anchoring handle revealed 0.277 wt% surface loading on average with respect to plain TiO₂ nanoparticles while salfen-supported complexes (Al and Co) revealed much lower surface loadings (Table C4, entries 1-3). **L1/TiO₂** was tested twice for different reaction solvents, revealing 0.331-0.418 wt% on average (entries 4-7). However, **Co-1/TiO₂** and **Cr-1/TiO₂** again showed much lower surface loading compared to the ligand, and a possible decomposition of the complex upon immobilization could be attributed to the higher concentration of Co and Cr compared to the detected Fe concentration as the ligand might be washed off upon decomposition, leaving the Co and Cr on the surface (entries 8-9). Overall, we postulate that the immobilization of compounds and complexes supported by ester-substituted salfen onto TiO₂ nanoparticles could be potentially achieved via a combined mechanism of transesterification, physical adsorption, and axial coordination to the metal center.²²⁰ Unfortunately, we lack direct evidence of confirming the primary interaction

between the surface and the anchored species. Further investigation and optimization of the anchoring conditions are needed to improve the surface loading and draw a conclusion.

In the meantime, we investigated conditions to establish triazole linkage between the surface with the self-assembled monolayer of azide with the alkyne-functionalized salfen derivatives.^{211, 221, 222} Compared to the ambiguous assignments of the ester linkage in the previous case, the triazole bond established from the azide-alkyne “click” reaction provides a characteristic platform to be analyzed by NMR spectroscopy in homogeneous reactions.^{211, 221-225} In the context of solid-phase reactions, the determination of the progress of “click” reactions can be achieved through IR and Raman spectroscopy. For efficient and effective investigations on the “click” reaction, **L5** was chosen for the initial screening of reaction conditions. (3-azidopropyl)trimethoxysilane (APTMS), the azidosilane used to form the self-assembled monolayer, was employed as the azide starting material. The obtained results were analyzed by NMR spectroscopy and summarized in Table C3. Reactions between **L5** and APTMS in THF catalyzed by Cu(I) in the presence of bases revealed no reaction at room temperature overnight. At elevated temperatures, a mixture of mono-cyclized and di-cyclized products was observed. In addition, the reaction could be initiated by Cu(II) in the presence of reductant sodium ascorbate. However, to ensure the solubility of **L5**, a polar aprotic organic solvent such as DCM was needed (Table C3, entry 4). The formation of triazole was confirmed by the sharp peak at 7.68 ppm observed for Table C3 entries 1-2 and 4-5 in the ¹H NMR spectra obtained in CDCl₃ (Figure 4.7). The singlet at 7.68 ppm for all the successful trials was assigned to the triazole C=CH. However, all trials presented more than one product which is possibly due to the uncontrolled cyclization of one or two terminal alkynes on **L5**. Therefore, the integration of the protons for each peak might not reflect the real number of protons corresponding to the structure

subjected to analysis. In order to facilitate the subsequent surface functionalization step, DCM was deliberately selected as the reaction solvent due to its compatibility and the ability of the reaction to proceed at room temperature. Cu(I) was utilized to circumvent the need for water which might destroy the immobilization system.

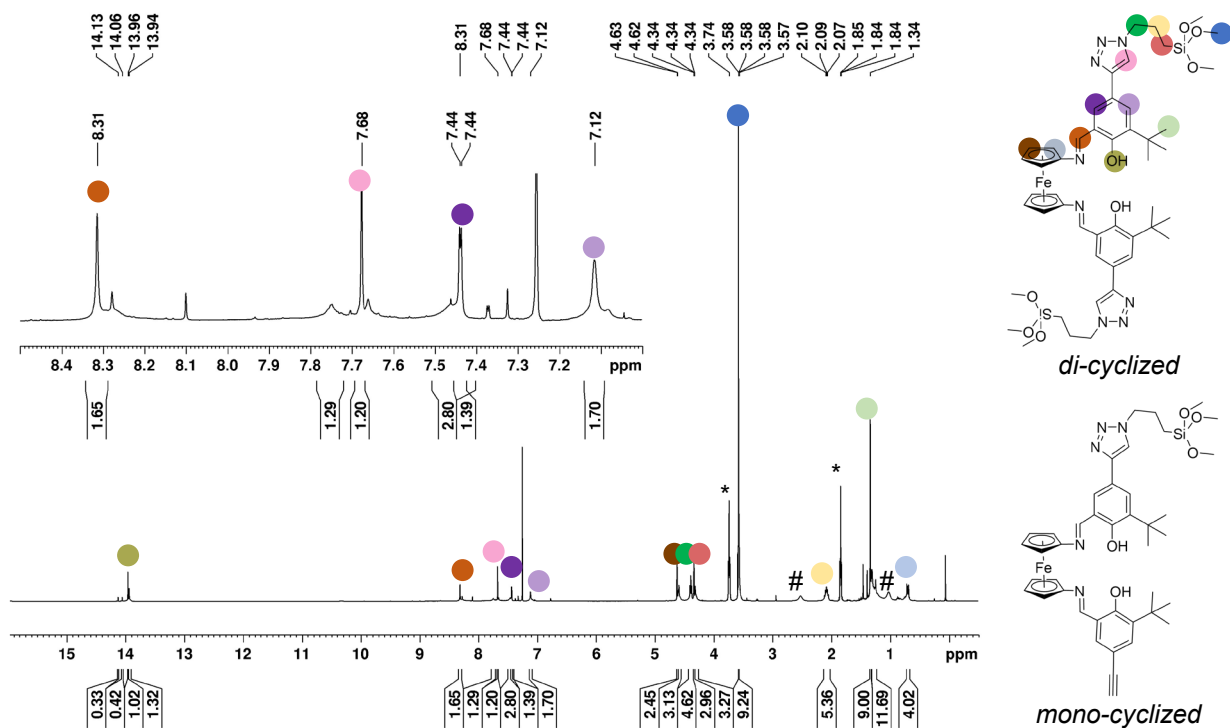


Figure 4.7. ¹H NMR spectrum analysis for Table C3, entry 2 (500 MHz, CDCl₃, 25 °C). * is residual THF and # is residual Et₃N.

With a set of conditions for “click” reactions in hand, we moved on to investigating surface functionalization of P25 TiO₂ nanoparticles and TiO₂ coated fluorine doped tin oxide (FTO) plates (TiO₂/FTO) modified with a self-assembled monolayer of APTMS using **L5**. Surface modification with functional silane such as APTMS to TiO₂ nanoparticles or TiO₂/FTO was accomplished following published procedures, which enables stable surface binding of alkyl

azide for subsequent reactions.^{214, 221} The azide-terminated silane-treated nanostructured surfaces were analyzed by IR spectroscopy (Figure C50). The presence of the alkyl azide vibrational band around 2100 cm^{-1} confirmed the successful surface modification via APTMS monolayer.²¹⁴ X-ray photoelectron spectroscopy (XPS) further verified the presence of surface-attached azide. The high-resolution N 1s XPS spectrum has resonances at 400 and 404 eV from the azide groups which is in accordance with the literature (Figure C54b).²²¹

The azide-treated surfaces **azide/TiO₂** and **azide/TiO₂/FTO** were then subjected to the previously developed Cu(I)-catalyzed azide-alkyne cycloaddition (CuAAC) reactions with alkyne-terminated **L5**. Specifically, **L5** was attached to the azide-modified surface by CuAAC click reactions in DCM using the condition developed previously. After the reaction was completed, it was washed by DCM following centrifugation until the supernatant became colorless. However, the ICP-MS analysis revealed a high concentration of leftover Cu (Table C4, entry 10), which was also observed in the survey scan in XPS (Figure C55a). The trial was repeated with more efficient washes for ICP analysis confirming the minimum amount of Cu left on the sample (Table C4, entry 11). The XPS spectrum after the coupling of **L5** onto the azide-treated surface revealed a change in N 1s: two overlapping peaks at 399 and 401 eV in accordance with the literature.²²¹ Fe 2p resonances at 708 and 724 eV was also observed verifying the presence of surface-bounded **L5**. IR spectra collected before and after immobilizing **L5** were compared to the IR spectra of **L5** (Figure C51). The IR spectrum of **L5/TiO₂** displayed C-H stretching at $2800\text{-}3000\text{ cm}^{-1}$, C=N stretching around 1600 cm^{-1} , and aromatic C-C stretching around 1400 cm^{-1} inherited from **L5**. However, the alkyne C≡C resonance and azide resonance overlapped at 2100 cm^{-1} . The residual band at 2100 cm^{-1} observed for **L5/TiO₂** was possibly due to either leftover azide or unreacted C≡C bond on **L5**. However, no band was

observed around the same region in Raman spectra indicating the residual band at 2100 cm^{-1} may be attributed to leftover azide (Figure C53).²²⁶ Residual azide remained after CuAAC “click” reaction on the surface has been reported before, which could be reasoned by some azide sites were blocked by the immobilized complex.²¹⁴ Interestingly, the intensity of the peak at 2100 cm^{-1} was significantly reduced when **L5** was attached to the **azide/TiO₂/FTO** surface, while other characteristics were maintained (Figure C52). Additionally, the disappearance of the alkyne C-H stretching for **L5** at 3300 cm^{-1} indicated the successful reaction between the alkyne-terminated **L5** with the surface azide (Figure 4.8). However, the expected triazole peaks around 1400 to 1500 cm^{-1} were not well resolved due to the overlap with the aromatic C=C.²²³ **Cr-2** was attached to P25 TiO₂ nanoparticles and TiO₂/FTO plates via a similar method. However, the XPS spectrum of **Cr-2/TiO₂** revealed N 1s resonance at 400 and 404 eV, likely due to the residual azide but barely any Cr 2p was observed (Figure C55b). ICP-MS analysis indicated that the surface loading of **Cr-2** on the TiO₂ surface was higher than **Co-1** and **Cr-1** from the other method (0.271 wt%) but still considerably low for an effective surface functionalization (Table C4, entry 12).⁵²

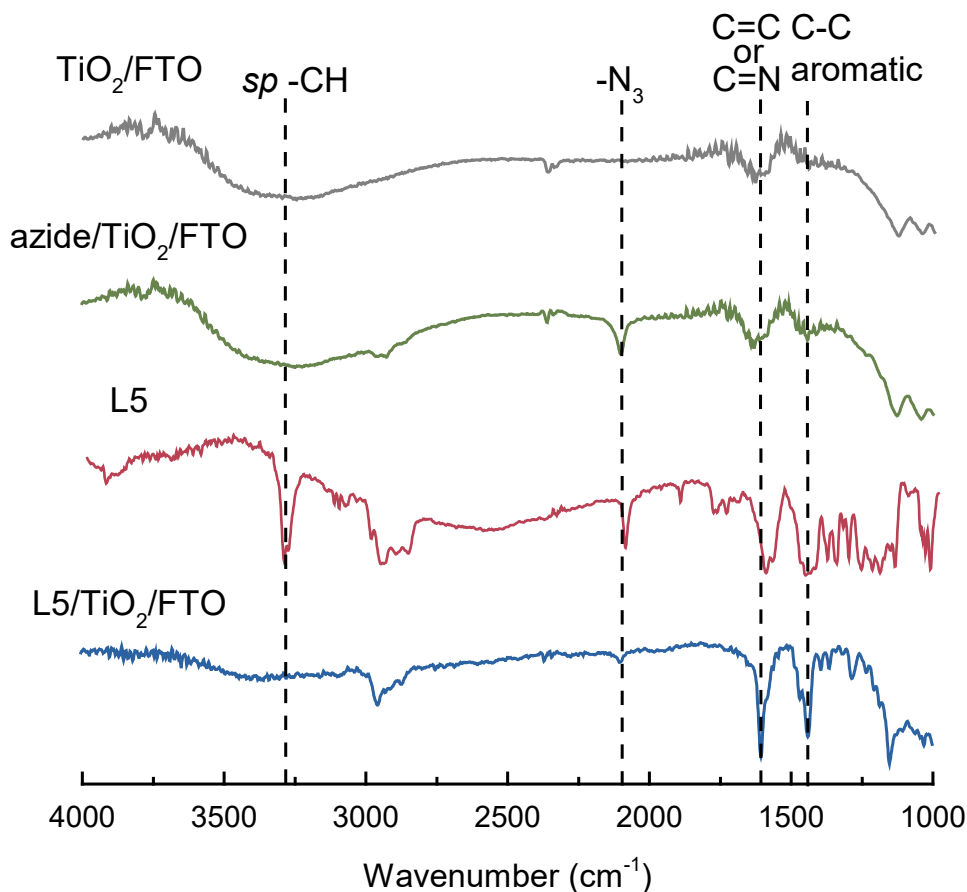


Figure 4.8. Overlay of IR spectra of TiO₂/FTO (gray), **azide**/TiO₂/FTO (green), **L5** (red), and **azide**/TiO₂/FTO (blue).

Cyclic voltammetry measurements of the **L5**-modified TiO₂/FTO surface (**L5**/TiO₂/FTO) were compared with that of the homogeneous compound **L5** in the same electrolyte (100 mM TBAPF₆, *o*-DFB). Pt wire was used as the counter electrode and non-aqueous Ag/Ag⁺ was used as the reference electrode. For the homogeneous compound measurements, TiO₂/FTO plate was used as the working electrode while functionalized plate **L5**/TiO₂/FTO was used as the working electrode for the investigation of the “click” anchoring strategy. Figure 4.9a demonstrated the cyclic voltammograms (CVs) of **L5** measured at sweep

rates from 10 mV/s to 200 mV/s. A reversible redox event was observed centering at $E_{1/2} = 0.182$ V vs Fc/Fc⁺ at 100 mV/s scan rate. In the case of the surface attached **L5** (**L5/TiO₂/FTO**), the redox event corresponds to the Fe in the ferrocene moiety became irreversible at high scan rates and quasi-reversible at low scan rates (Figure 4.9b). Owing to the interference with the background TiO₂, the measurements could not be investigated further at lower potentials (Figure C56-57). The maintenance of a similar redox feature compared to the homogeneous compound **L5** after immobilization suggested the presence of **L5** on the anchored surface. The alkyl linkage between the redox active ferrocene backbone to the surface allowed **L5** with only one side of the compound attached to the surface to orient flexibly in the electrolyte. The solvent *o*-DFB is a good solvent to solubilize **L5**, therefore, the surface-confined **L5** was found “molecularly” behaved.²²⁷ The quasi-reversibility of the observed electron transfer process for **L5/TiO₂/FTO** may be attributed to several reasons: 1) the flexibility of the linkage between the ferrocene moiety and the surface allowed different orientations of the surface attachment to be present at the same time. 2) the relatively long distance caused inefficient electron transfer from the surface to the surface-confined **L5** increased the peak-to-peak separation upon increasing the scan rate.²¹⁴ It is important to note that after the CV measurements, the **L5/TiO₂/FTO** plate remains the same color. However, the peak current versus scan rate reflected a non-perfect linear relationship which implied further investigation is needed to confirm the surface-confined redox process (Figure C58).^{214, 228}

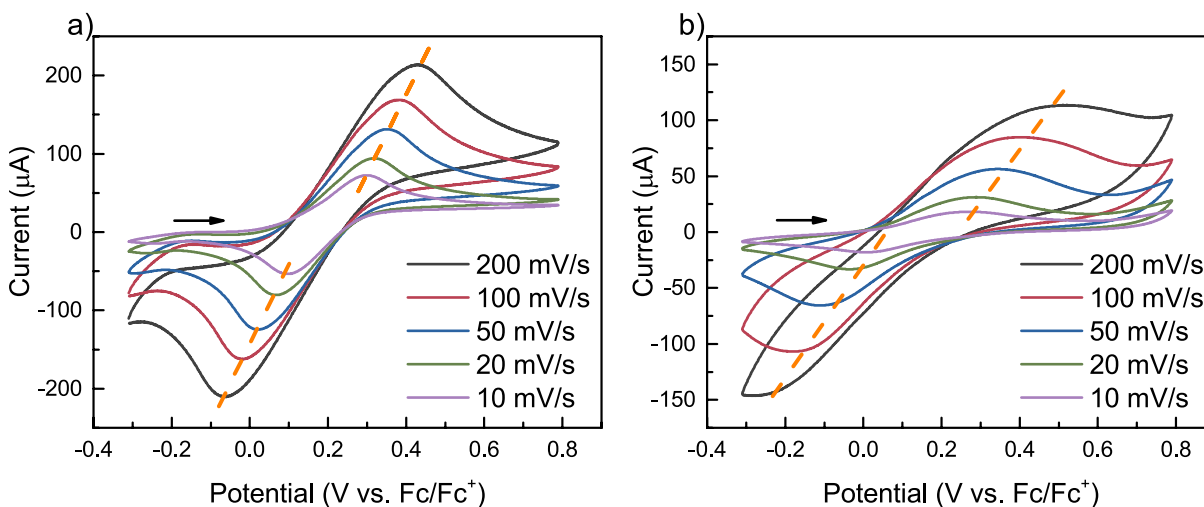


Figure 4.9. a) Cyclic voltammograms of L5 using TiO₂/FTO as the working electrode at various scan rates; b) Cyclic voltammograms of L5/TiO₂/FTO as the working electrode at various scan rates.

4.3 Conclusion and outlook

In summary, we developed a series of salfen-derivatives modified with anchoring handles, ester, and terminal alkyne, for surface immobilization onto semiconducting surfaces. In the meantime, we synthesized cobalt and chromium complexes supported by those modified salfen derivatives and investigated their activity in the polymerization of 6-membered NCAs. The surface immobilization of salfen derivatives with terminal alkyne was investigated for CuAAC “click” reactions and found to provide a reliable platform to achieve surface immobilization. However, further study is needed on improving the surface coverage, testing the heterogenous catalysis activity, and integrating the incompatible processes of NCA synthesis with its polymerization. We also envision incorporating redox switching through the semiconducting solid support to access multiple states of the surface-bounded catalysts electrochemically. Therefore, *in situ* switching between the reactivities toward different

monomers may be achieved. Such an approach holds the potential on enabling temporal control over the process of co-polymerization of a variety of monomers (Figure 4.10).

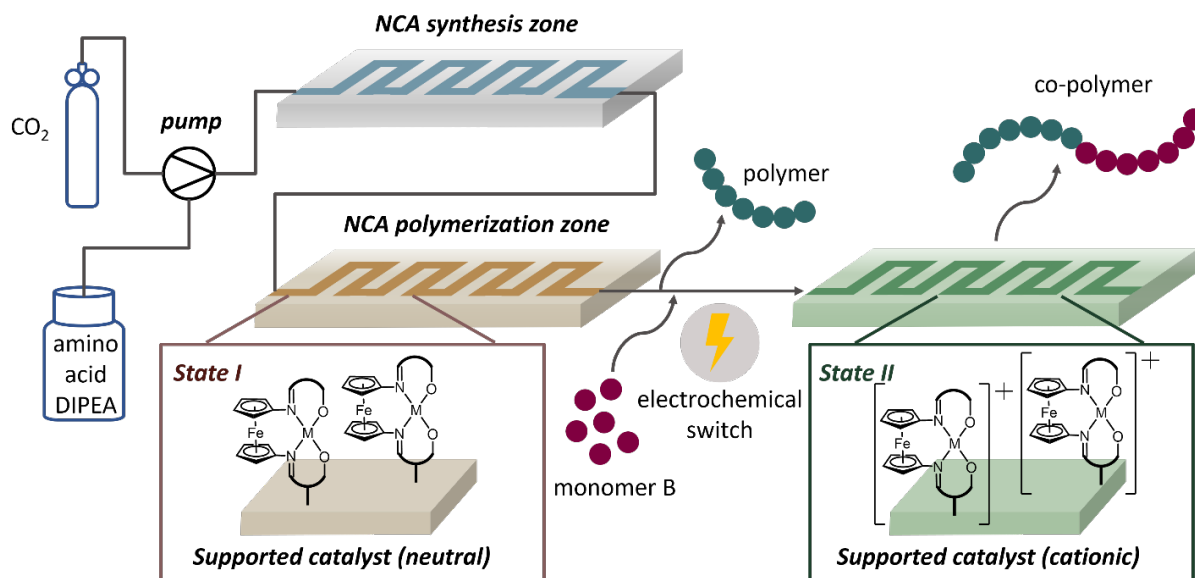


Figure 4.10. Perspective work on incorporating incompatible NCA synthesis and its ring-opening polymerization in serial and enabling switchable co-polymerization of NCA with another type of monomer to produce sustainable materials.

4.4 Experimental section

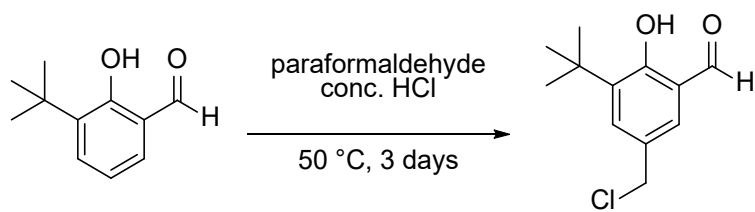
General Considerations

Unless stated otherwise, all reactions were carried out under a dry nitrogen atmosphere using standard Schlenk techniques or an MBraun inert-gas glovebox. Solvents were purified using a two-column solid-state purification system by the method of Grubbs and transferred to the glovebox without exposure to air.¹³⁶ Propylene oxide (PO), methanol, and triethyl amine (Et_3N) were distilled according to the recommended methods under nitrogen.²²⁹ All solvents were stored on activated molecular sieves and/or sodium for at least a day prior to use. NMR solvents were obtained from Cambridge Isotope Laboratories, degassed, and stored over

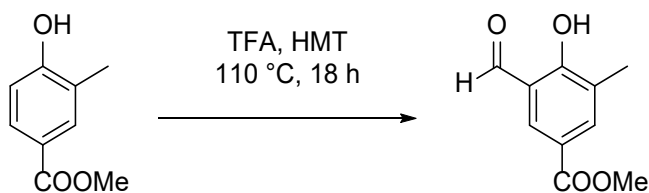
activated molecular sieves prior to use. Titania P25 nanoparticles were purchased from Sigma-Aldrich and dried under vacuum for 3 days at 125 °C before use. TiO₂/FTO Plates were prepared according to a published procedure and dried under vacuum for 3 days at 125 °C before use.⁵² 1,1'-diaminoferrocene was synthesized according to a published procedure.⁸⁰ 4-bromo-2-(*tert*-butyl)phenol was either purchased from Sigma-Aldrich or synthesized following a published procedure.²¹⁶ 5-bromo-3-(*tert*-butyl)-2-hydroxybenzaldehyde was either purchased from VWR or synthesized following a published procedure.²³⁰ Anhydrous *N,N*-dimethylformamide, *N,N*-diisopropylethylamine (DIPEA), *n*-propylphosphonic anhydride (T3P, 50 wt% ethyl acetate), trifluoroacetic acid, tetra-*n*-butylammonium fluoride (TBAF, 1 M solution in THF), ethynyltrimethylsilane, tetrabutylammonium tribromide (TBABr₃), 3-(*tert*-butyl)-2-hydroxybenzaldehyde, 2-(*tert*-butyl)phenol, methyl 3-formyl-4-hydroxybenzoate, methyl 4-hydroxy-3-methylbenzoate, methyl 4-hydroxy-3-methoxybenzoate, (3-chloropropyl)trimethoxysilane were purchased from Fisher or VWR and used without further purification. Bis(triphenylphosphine)iminium chloride (PPNCl) was purchased from Sigma Aldrich. All other reagents were purchased from Fisher or VWR unless otherwise specified. The syntheses of **A3**, **L1-L5** were followed by a published procedure with minor modifications.⁸⁰ Nuclear magnetic resonance spectra were recorded on Bruker AV300, Bruker DRX500, and Bruker AV500 spectrometers at 25 °C in C₆D₆, and CDCl₃ unless otherwise specified. Chemical shifts are reported with respect to solvent residual peaks (C₆D₆ at 7.16 ppm and CDCl₃ at 7.26 ppm). IR spectra were measured on an Agilent Technologies Cary 620 Fourier transform infrared spectrometer (FTIR) fitted with a Cary 600 Series FTIR Microscope. Ultraviolet-visible (UV-Vis) spectra were collected on Agilent Cary 60 UV-Vis spectrophotometer. X-ray photoelectron spectroscopy (XPS) was measured on a Krotos AXIS Supra photoelectron spectrometer. High-

resolution mass spectroscopy measurements were conducted on an electrospray mass spectrometer, Waters LCT-Premier XE Time of Flight Instrument, controlled by MassLynx 4.1 software (Waters Corporation, Milford MA). The instrument was equipped with the Multi-Mode Ionization source operated in the electrospray mode. A solution of Leucine Enkephalin (Sigma Chemical, L9133) was used in the Lock-Spray to obtain accurate mass measurements. Samples were infused using direct loop injection on a Waters Acquity UPLC system. Raman spectrum was collected on LabRAM HR Evolution Raman spectrometer with a 633 nm laser. Inductively coupled plasma mass spectrometry (ICP-MS, NexION 2000, PerkinElmer) analysis was performed to detect Fe, Al, Co, Cu, and Cr in the provided samples. All samples were used as received without further purification or modification. The calibration curve was established using a standard solution while the dwell time was 50 ms with thirty sweeps and three replicates with background correction. Molar masses of polymers were determined by size exclusion chromatography using a SEC-MALS instrument at UCLA. SEC-MALS uses a Shimadzu Prominence-i LC 2030C 3D equipped with an autosampler, two MZ Analysentechnik MZ-Gel SDplus LS 5 μm , 300 \times 8 mm linear columns, a Wyatt DAWN HELEOS-II, and a Wyatt Optilab T-rEX. The column temperature was set at 40 $^{\circ}\text{C}$. A flow rate of 0.70 mL/min was used and samples were dissolved in THF. The number of average molar mass and molecular weight distribution values were determined using the dn/dc values which were calculated by 100% mass recovery method from the RI signal. Cyclic voltammograms were acquired with a CH Instruments CHI630D potentiostat and recorded with CH Instruments software (version 13.04). All potentials are given with respect to the ferrocene-ferrocenium couple.

Synthesis of aldehyde compounds

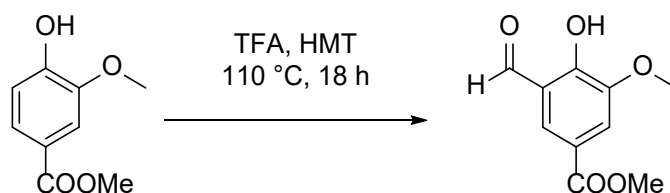


3-(*tert*-butyl)-5-(chloromethyl)-2-hydroxybenzaldehyde was synthesized following the published procedures with minor modifications.^{201, 231} In a 50 mL Schlenk flask, 7.3 mL concentrated HCl was cooled to 5 °C under nitrogen. Under nitrogen, 1.78 g (10 mmol, 1 equiv.) of 3-(*tert*-butyl)-2-hydroxybenzaldehyde and 0.67 g (22 mmol, 2.2 equiv.) of paraformaldehyde was added. The reaction was stirred at 50 °C for three days. After cooling to room temperature, the reaction mixture was extracted with diethyl ether three times. The combined organic layer was washed with saturated NaHCO₃ solution and brine. The organic layer was separated, dried with MgSO₄, filtered through celite and evaporated to dryness, giving the product as pale yellow oil, which turned to pale yellow solid after drying under reduced pressure and used in the next step without further purification (2.19 g, 96%). ¹H NMR (500 MHz, CDCl₃, 25 °C) δ , ppm: 11.86 (s, 1H, OH), 9.87 (s, 1H, O=CH), 7.53 (d, 1H, ArH), 7.44 (d, 1H, ArH), 4.59 (s, 1H, CH₂Cl), 1.42, (s, 9H, C(CH₃)₃).

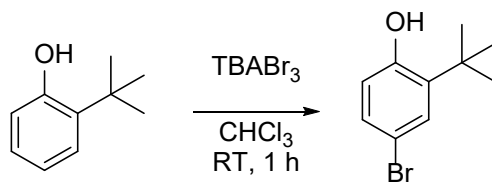


Methyl 3-formyl-4-hydroxy-5-methylbenzoate was synthesized following the published procedure with minor modifications.²³² In a 50 mL Schlenk flask, 460 mg (2.77 mmol, 1 equiv.) of methyl 4-hydroxy-3-methylbenzoate was mixed with 194 mg (1.138 mmol, 0.5 equiv.) of hexamethylenetetramine (HMT) in 5 mL TFA under nitrogen. The reaction was heated to reflux overnight. After cooling to room temperature, the reaction was diluted with water and extracted

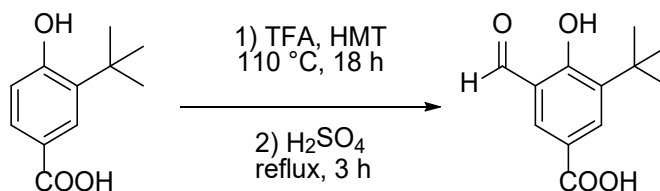
with ethyl acetate. The organic layer was separated and washed with water and brine. The combined organic layer was dried with MgSO_4 , filtered through celite, and evaporated to dryness. The crude product was purified by recrystallization in ethyl acetate layered with hexanes at room temperature. The white crystalline solid was filtered out, the mother liquor was concentrated and purified by silica gel chromatography using ethyl acetate/hexanes (1/5) as the eluent, giving a yellow crystalline product (261 mg, 49%). ^1H NMR (300 MHz, CDCl_3 , 25 °C) δ , ppm: 11.64 (s, 1H, OH), 9.92 (s, 1H, O=CH), 8.16 (d, 1H, ArH), 8.06 (d, 1H, ArH), 3.92 (s, 3H, OCH₃), 1.42, (s, 3H CH₃).



Methyl 3-formyl-4-hydroxy-5-methoxybenzoate was synthesized following the published procedure with minor modifications.²³² In a 50 mL Schlenk flask, 517 mg (2.83 mmol, 1 equiv.) of methyl 4-hydroxy-3-methoxybenzoate was mixed with 200 mg (1.43 mmol, 0.5 equiv.) of HMT in 5.2 mL TFA under nitrogen. The reaction was heated to reflux overnight. After cooling to room temperature, the reaction was diluted with water and extracted with ethyl acetate. The organic layer was separated and washed with water and brine. The combined organic layer was dried with MgSO_4 , filtered through celite, and evaporated to dryness. The crude product was purified by recrystallization in ethyl acetate layered with hexanes at room temperature, giving a yellow crystalline product (459 mg, 77%). ^1H NMR (300 MHz, CDCl_3 , 25 °C) δ , ppm: 11.54 (s, 1H, OH), 9.96 (s, 1H, O=CH), 7.98 (d, 1H, ArH), 7.75 (d, 1H, ArH), 3.98 (s, 3H, OCH₃), 3.94, (s, 3H O=COCH₃).

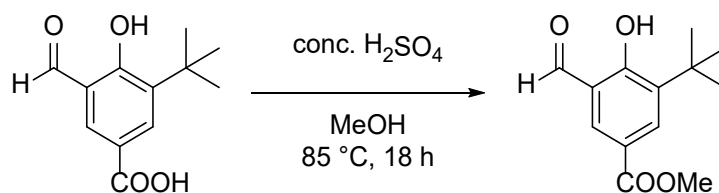


4-bromo-2-(*tert*-butyl)phenol was synthesized following the published procedure with minor modifications.²¹⁶ In a 250 mL round bottom flask, 8 mL (52.5 mmol, 1 equiv.) was dissolved in 150 mL of chloroform under nitrogen. 25.2 g (52.2 mmol, 1 equiv.) of tetrabutylammonium tribromide (TBABr₃) was added to the stirring solution portion-wise. The reaction was monitored by TLC and upon completion, the reaction was hydrolyzed with 150 mL of saturated Na₂S₂O₃ solution and extracted with DCM. The combined organic phase was washed with water and dried with MgSO₄, filtered through celite, and evaporated to dryness. The crude was redissolved in diethyl ether and washed with brine. The combined organic phase was dried with MgSO₄, filtered through celite, and evaporated to dryness giving the product as brown oil and used in the next steps without further purification (8.55 g, 71%). The product is also commercially available.

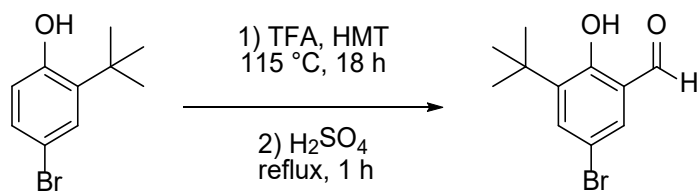


3-(*tert*-butyl)-4-hydroxybenzoic acid was synthesized according to the published procedure.²⁰⁷ 3-(*tert*-butyl)-5-formyl-4-hydroxybenzoic acid was synthesized following the published procedure with minor modifications.²⁰⁷ To a 100 mL Schlenk flask, 3-(*tert*-butyl)-4-hydroxybenzoic acid (0.5 g, 2.57 mmol, 1equiv.) and 730 mg (5.21 mmol, 2 equiv.) of HMT were mixed in 20 mL of trifluoroacetic acid (TFA) under nitrogen. The reaction was heated to reflux overnight. After 18 hours, 14 mL of 33% H₂SO₄ was added to the mixture and the reaction

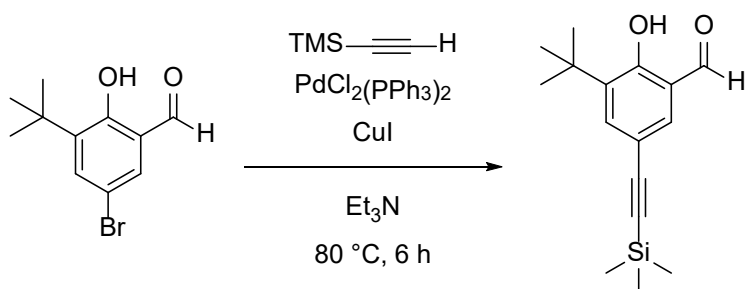
was refluxed for another 3 hours. After cooling to room temperature, the reaction was diluted with diethyl ether and washed with brine twice, the organic layer was dried with MgSO₄ and filtered through celite. The solution was concentrated under reduced pressure. To the resulting oil 2 M NaOH (aq) was added and the mixture was poured into an ice/HCl mixture. Beige solids were collected on top of filter paper. If no precipitation formed after pouring into an ice/HCl mixture, the mixture was extracted with chloroform and the combined organic layer was dried with MgSO₄, filtered through celite, and evaporated to dryness giving solid which is used in the next steps without further purification (405 mg, 71%). ¹H NMR (300 MHz, CDCl₃, 25 °C) δ, ppm: 12.30 (s, 1H, OH), 9.96 (s, 1H, O=CH), 8.26 (s, 2H, ArH), 1.45, (s, 9H C(CH₃)₃).



Methyl 3-(*tert*-butyl)-5-formyl-4-hydroxybenzoate was synthesized following the published procedure with minor modifications.²⁰⁵ 1.66 mg (7.5 mmol, 1 equiv.) of 3-(*tert*-butyl)-4-hydroxybenzoic acid was dissolved in 60 mL of methanol, to which drops of concentrated sulfuric acid were added. The reaction was refluxed overnight. After 18 hours, the reaction was cooled to room temperature and neutralized with a saturated NaHCO₃ solution. The volatiles were removed under reduced pressure. The crude mixture was extracted with ethyl acetate and washed with water three times. The organic layer was dried with MgSO₄, filtered through celite, and evaporated to dryness. The product was purified by silica gel chromatography using ethyl acetate/hexanes (1/10) as the eluent. The purified product was obtained as yellow solids (800 mg, 45%). ¹H NMR (500 MHz, CDCl₃, 25 °C) δ, ppm: 12.20 (s, 1H, OH), 9.93 (s, 1H, O=CH), 8.20 (d, 1H, ArH), 8.17 (d, 1H, ArH), 3.93, (s, 3H OCH₃), 1.44, (s, 9H C(CH₃)₃).

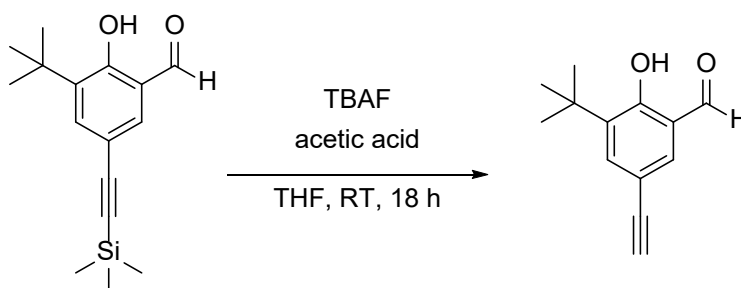


5-bromo-3-(*tert*-butyl)-2-hydroxybenzaldehyde was synthesized following the published procedure with minor modifications.²³⁰ To a 50 mL Schlenk flask, 1.8 g (8.7 mmol, 1 equiv.) of 4-bromo-2-*tert*-butylphenol, 2.45 g (17.5 mmol, 2 equiv.) of HMT were mixed in 8 mL of TFA and refluxed at 115 °C overnight. After 18 hours, 4 mL of 33% H₂SO₄ was added and the reaction was refluxed for another hour. After cooling to room temperature, the reaction mixture was extracted with diethyl ether three times. The combined organic layer was washed with water three times followed by washing with saturated NaHCO₃, water, and brine one time each. The organic layer was separated, dried with MgSO₄, filtered through celite, and evaporated to dryness. The crude product was obtained as brown oil with yellow solids crushed out of the oil and purified by silica gel chromatography using ethyl acetate/hexanes (1/10) as the eluent. The purified product was obtained as yellow solids (1.11 g, 54%). ¹H NMR (300 MHz, CDCl₃, 25 °C) δ, ppm: 11.72 (s, 1H, OH), 9.81 (s, 1H, O=CH), 7.58 (d, 1H, ArH), 7.51 (d, 1H, ArH), 1.40, (s, 9H C(CH₃)₃).



3-(*tert*-butyl)-2-hydroxy-5-((trimethylsilyl)ethynyl)benzaldehyde was synthesized following the published procedures with minor modifications.^{216, 230} Under nitrogen atmosphere, in a dry two-necked flask, 5-bromo-2-hydroxybenzaldehyde (213.5 mg, 0.83 mmol, 1 equiv.),

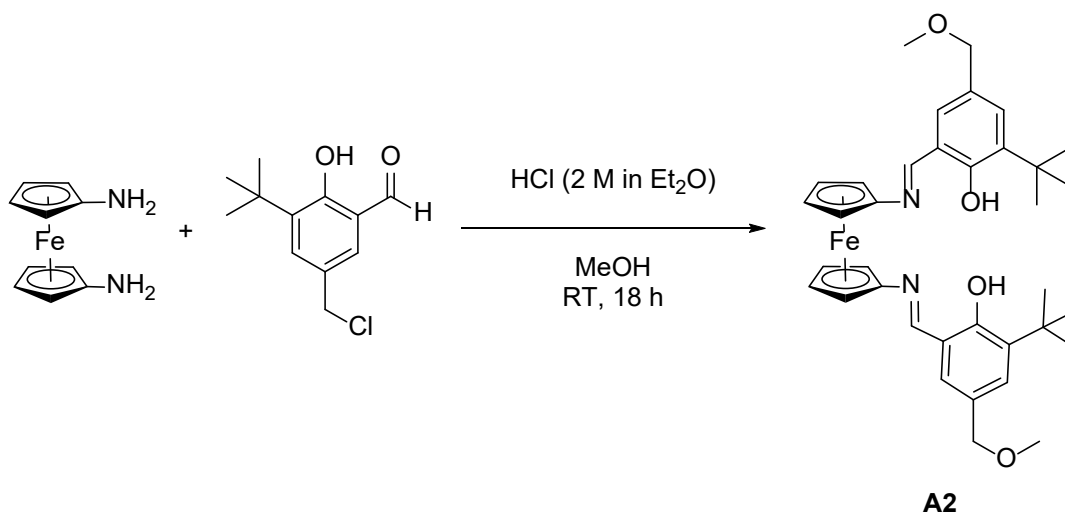
[PdCl₂(PPh₃)₂] (18.5 mg, 0.026 mmol, 3 mol%) and CuI (6.2 mg, 0.033 mmol, 4 mol%) were mixed in 5 mL of triethylamine. 0.18 ml (1.25 mmol, 1.5 equiv.) of ethynyltrimethylsilane was added. The reaction was heated to 80°C for 6 h. After cooling to room temperature, the mixture was filtered through celite and the flask was washed with DCM. After removing the solvent under reduced pressure, the crude product was obtained as a black gel which was dissolved in hexanes and purified by silica gel chromatography using hexanes as the elute. The purified product was obtained as brown oil (200 mg, 88%). ¹H NMR (300 MHz, CDCl₃, 25 °C) δ, ppm: 11.90 (s, 1H, OH), 9.83 (s, 1H, O=CH), 7.59 (d, 1H, ArH), 7.56 (d, 1H, ArH), 1.41, (s, 9H C(CH₃)₃), 0.25, (s, 9H Si(CH₃)₃).



3-(*tert*-butyl)-5-ethynyl-2-hydroxybenzaldehyde was synthesized following the published procedures with minor modifications.^{216, 230} In a 20 mL vial, 0.8 mL (0.8 mmol, 1.1 equiv.) TBAF (1 M in THF) was added to a stirring solution of 3-(*tert*-butyl)-2-hydroxy-5-((trimethylsilyl)ethynyl)benzaldehyde (200 mg, 0.73 mmol, 1 equiv.) in THF along with 41 μL acetic acid. The reaction was stirred at room temperature and monitored by TLC. Upon completion, the reaction mixture was diluted with DCM and washed with water until pH = 7 of the aqueous phase. The organic phase was dried with MgSO₄, filtered through celite, and evaporated to dryness. The crude product was obtained as purple gel and purified by silica gel chromatography using hexanes as the eluent. The purified product was obtained as yellow oil (105 mg, 71%) ¹H NMR (300 MHz, CDCl₃, 25 °C) δ, ppm: 11.93 (s, 1H, OH), 9.84 (s, 1H,

O=CH), 7.62 (d, 1H, ArH), 7.58 (d, 1H, ArH), 3.02 (s, 1H, CCH), 1.41, (s, 9H C(CH₃)₃).

Synthesis of A2.



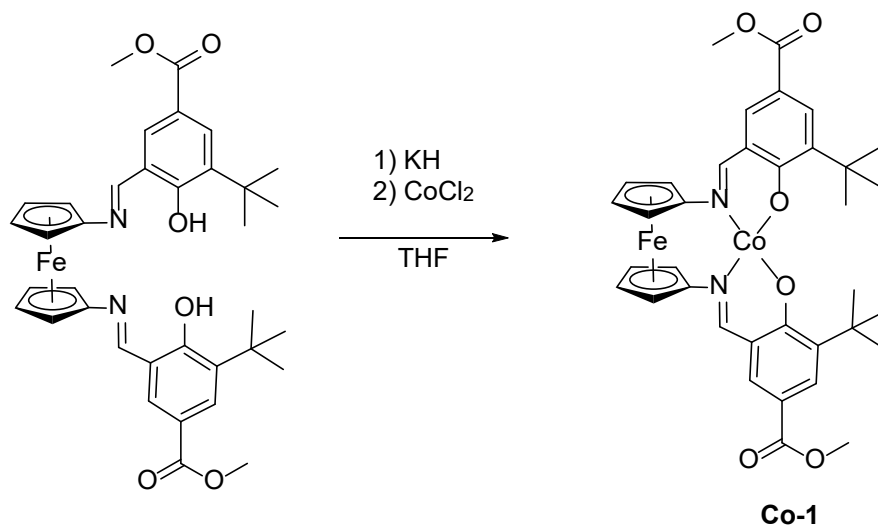
To a stirring solution of 3-(*tert*-butyl)-5-(chloromethyl)-2-hydroxybenzaldehyde (2 equiv.) in methanol, HCl (0.8 equiv., 2M in diethyl ether) was added dropwise. The solution became dark, to which 1,1'-diaminiferrocene (1 equiv.) in methanol was added dropwise. The solution became dark red right away. Red precipitation formed after an hour. The reaction was stirred at room temperature overnight. The red precipitation was collected on top of a medium frit and the residual volatiles were removed under a reduced pressure yielding **A2** as a dark red solid in quantitative yield. ¹H NMR (300 MHz, CDCl₃, 25 °C) spectrum of **A2**. δ, ppm: 13.85 (s, 2H, OH), 8.45 (s, 2H, N=CH), 7.26 (s, 1H, ArH), 6.89 (s, 1H, ArH), 4.56 (s, 4H, OCH₂), 4.32 (t, 4H, C₅H₄), 4.28 (t, 4H, C₅H₄), 3.37 (s, 6H, OCH₃), 1.47, (s, 18H, C(CH₃)₃). ¹³C NMR (125 MHz, C₆D₆, 25 °C) δ, ppm: 161.2 (N=C), 159.8 (COH), 137.2, 129.2, 129.0, 128.1, 119.2, 102.6, 74.3 (OCH₂), 69.0 (C₅H₄), 64.4 (C₅H₄), 57.4 (OCH₃), 34.8 (C(CH₃)₃), 29.4 (C(CH₃)₃).

General procedure for the synthesis of A3, L1-L5

To a stirring solution of 2-hydroxybenzaldehyde (2 equiv.) in methanol, 1,1'-diaminiferrocene (1 equiv.) in methanol was added dropwise. The reaction was stirred at room

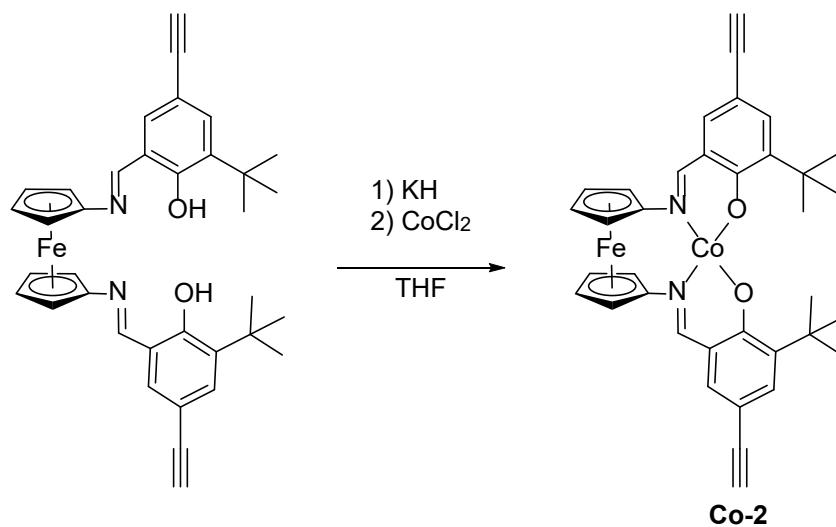
temperature overnight. The precipitation was collected on top of a medium frit and the residual volatiles were removed under reduced pressure. Compounds **A3**, **L1-L5** are characterized by NMR spectroscopy.

Synthesis of Co-1



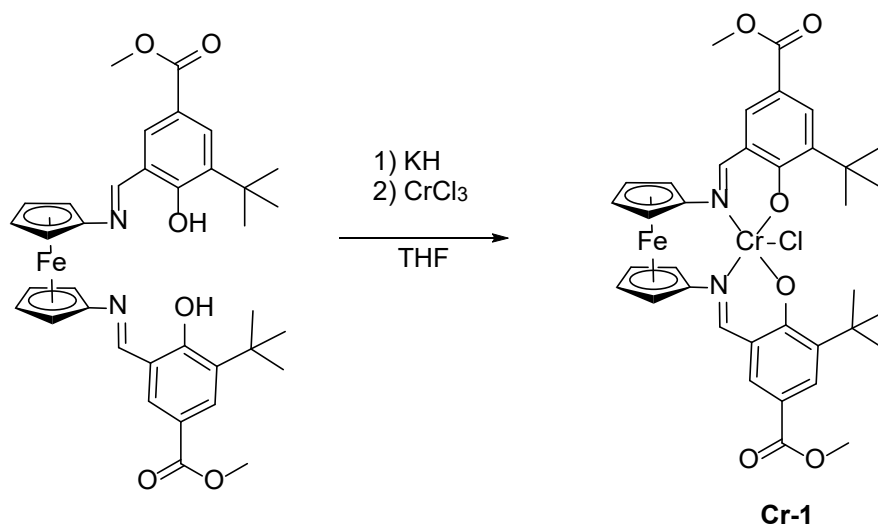
In a nitrogen-filled glovebox, 114.4 mg (0.175 mmol) of pro-ligand **L4** in 6 mL of THF was added to a stirring THF solution of KH (14.4 mg, 0.36 mmol, 2.1 equiv.) in 2 mL THF. The reaction was stirred overnight yielding an orange slurry, to which CoCl_2 was added (25 mg, 0.19 mmol, 1.1 equiv.). The reaction turned to dark red after 10 min and was stirred at room temperature for 4 hours. The solution became clear red-brown and was filtered through celite. The volatiles were removed under reduced pressure. The product was recrystallized in THF layered with hexanes yielding dark red solid collected on top of a medium frit (107 mg, 87 %). HRMS (ES^+) of $\text{C}_{36}\text{H}_{38}\text{CoFeN}_2\text{O}_6$: Found 710.1511 Da $[\text{M}+\text{H}]^+$, calculated 710.1490 Da. ^1H NMR spectrum (500 MHz, CDCl_3 , 25 °C) δ (ppm): 62.97 (s, ArH), 52.73 (s, ArH), 18.94 (s, C_5H_4), 10.62 (s, C_5H_4), -3.26 (s, N=CH), -4.57 (s, $\text{C}(\text{CH}_3)_3$), -6.85 (s, OCH_3).

Synthesis of Co-2



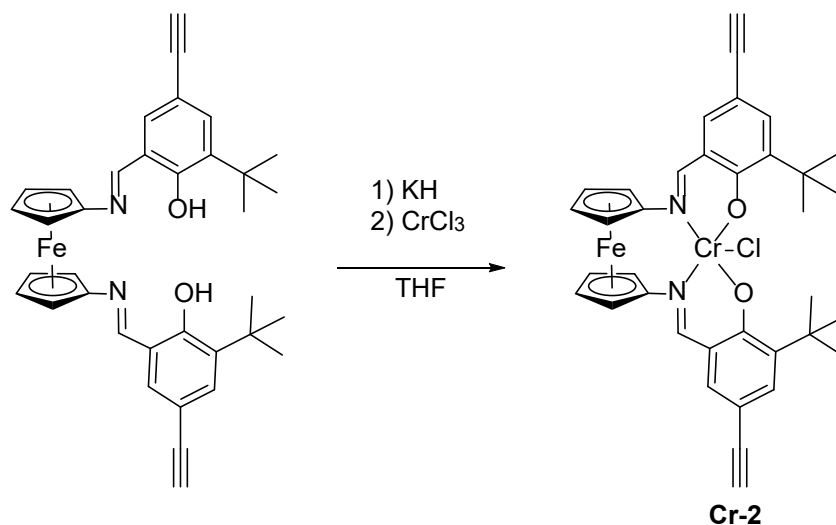
In a nitrogen-filled glovebox, 101.1 mg (0.173 mmol) of pro-ligand **L5** in 4 mL of THF was added to a stirring THF solution of KH (15.2 mg, 0.38 mmol, 1.1 equiv.). The reaction was stirred at room temperature for 4 hours and then filtered through celite. The filtrate was added to a CoCl₂ suspension (24.7 mg, 0.19 mmol, 1.1 equiv.) in THF. The reaction was stirred at room temperature overnight and became dark red. The volatiles were removed under reduced pressure. The solid was redissolved in toluene and filtered through celite. The volatiles were removed under reduced pressure. The product was recrystallized in toluene layered with hexanes yielding red/brown solid (101 mg, 90%). HRMS (ES⁺) of C₃₆H₃₄CoFeN₂O₂: Found 642.1392 Da [M+H]⁺, calculated 642.1381 Da. ¹H NMR (500 MHz, CDCl₃, 25 °C) δ, ppm: 61.68 (s, ArH), 53.78 (s, ArH), 18.22 (s, C₅H₄), -2.74 (s, C₅H₄), -3.11 (s, C(CH₃)₃), -4.21 (s, C(CH₃)₃), -5.36 (s, CCH), -7.58 (s, N=CH).

Synthesis of Cr-1



In a nitrogen-filled glovebox, 101.8 mg (0.156 mmol) of pro-ligand in 5 mL of THF was added to a stirring THF solution of KH (14 mg, 0.343 mmol, 2.2 equiv.). The reaction was stirred overnight and filtered through celite. The filtrate was added to a suspension of CrCl₃ in THF (27 mg, 0.172 mmol, 1.1 equiv.) and stirred at room temperature for 2 days. The solution became brown and was filtered through celite. The volatiles were removed under a reduced pressure and the solid was redissolved in toluene and filtered through celite. The product was recrystallized in toluene layered with hexanes yielding a dark brown product (97 mg, 84%). Due to the paramagnetic nature of the complex, no peak was observed in the ¹H NMR spectrum. HRMS (ES⁺) of C₃₆H₃₈CrFeN₂O₆⁺: Found 702.1472 Da, calculated 702.1486 Da.

Synthesis of Cr-2



In a nitrogen-filled glovebox, 109.5 mg (0.187 mmol) of pro-ligand **L5** in 4 mL of THF was added to a stirring THF solution of KH (16.7 mg, 0.412 mmol, 2.2 equiv.). The reaction was stirred at room temperature for 3 hours and then filtered through celite. The filtrate was added to a CrCl₃ (32.5 mg, 0.206 mmol, 1.1 equiv.) suspension in THF. The reaction was stirred at room temperature for two days and became dark brown. The reaction was filtered through celite and the volatiles were removed under a reduced pressure. The solid was redissolved in toluene and filtered through celite again. The solvent was concentrated, and the product was recrystallized in toluene layered with hexanes yielding dark brown solid (117 mg, 93%). Due to the paramagnetic nature of the complex, no peak was observed in the ¹H NMR spectrum. HRMS (ES⁺) of C₃₆H₃₄CrFeN₂O₂⁺: Found 634.1395 Da, calculated 634.1376 Da.

Synthesis of (3-azidopropyl)trimethoxysilane (APTMS)

(3-azidopropyl)trimethoxysilane was synthesized following published procedures with slight modifications.²³³ In the dark, in a 200 mL round bottom flask, 3 mL (14 mmol, 1 equiv.) of (3-chloropropyl)trimethoxysilane was mixed with 2.3 g (35 mmol, 2.5 equiv.) of sodium azide in

40 mL anhydrous DMF under nitrogen. The reaction was heated to 50 °C for two days. The reaction was cooled to room temperature upon completion and diluted with ether. The reaction was washed with water and the organic layer was separated. The combined aqueous layer was washed again with diethyl ether which was combined with the organic layer from the first wash and washed with water again. The combined organic layer was dried with MgSO₄ and filtered through celite. The solvent was removed under reduced pressure yielding a clear liquid product that is used without further purification (3 g, quantitative yield). ¹H NMR (500 MHz, CDCl₃, 25 °C) δ, ppm: 3.57 (s, 9H, Si(OCH₃)₃), 3.27 (t, 2H, SiCH₂CH₂CH₂N₃), 1.72 (m, 2H, SiCH₂CH₂CH₂N₃), 0.71 (m, 2H, SiCH₂CH₂CH₂N₃).

General procedure for the polymerization of 6-membered NCA

In a nitrogen-filled glovebox, polymerization catalyst (0.004 mmol, 1 equiv.), PPNC1 (0.008 mmol, 2 equiv.), and 6-NCA-C₈H₁₇ (0.2 mmol, 50 equiv.) were added to a 25 mL Schlenk tube with 0.7 mL PO in total. The Schlenk Tube was then sealed and taken out of the glovebox and heated at 80 °C for a designated period of time. Upon completion, the reaction was cooled to room temperature, and the product was precipitated with methanol and washed with a small amount of DCM and excess MeOH three times. The polymer was collected after centrifugation and dried under reduced pressure before further characterization.

Anchoring L1 onto P25 TiO₂ powder (L1/TiO₂)

P25 TiO₂ powder was heated under reduced pressure at 125 °C for three days to remove the surface-bound water prior to bringing it into a nitrogen-filled glovebox. 130 mg of P25 TiO₂ powder was mixed with 35 mg of L1 in either diethyl ether or DCM. The slurry was slowly stirred at room temperature for 3-5 days. The mixture was centrifuged to collect the powder which was then washed with the reaction solvent four to five times followed by centrifugation

after each wash until the supernatant was colorless. The resulting powder was dried under reduced pressure and appeared to be orange/yellow. Anchoring of **Co-1**, **Cr-1**, salfen, (salfen)Al(OiPr), and (salfen)Co followed a similar procedure.

Preparation of azide self-assembled monolayers on P25 TiO₂ powder (azide/TiO₂) or P25 TiO₂ coated FTO plate (azide/TiO₂/FTO)

The anchoring of APTMS was adapted from a published procedure.²¹⁴ P25 TiO₂ powder and P25 TiO₂ coated FTO plate **TiO₂/FTO** were heated under reduced pressure at 125 °C for three days to remove the surface-bound water before bringing it into a nitrogen-filled glovebox. 200 mg P25 TiO₂ powder or 5 slides of **TiO₂/FTO** plate were immersed in 10 mL of toluene with 100 µL of APTMS for 3-4 days in the dark. **Azide/TiO₂** powder was isolated and then washed with toluene 3 times followed by centrifugation after each wash. The powder was sat in toluene overnight and centrifuged one more time. The solid was collected, dried under reduced pressure, and stored in the dark at -30 °C. **Azide/TiO₂/FTO** plates were removed from the solution after soaking with APTMS solution and rinsed with toluene and methanol. The plates were immersed in toluene overnight, dried under reduced pressure, and stored in the dark at -30 °C.

Anchoring L5 onto P25 TiO₂ powder (L5/TiO₂)

In a nitrogen-filled glovebox, 65 mg of **azide/TiO₂** was added to a mixture of 20 mg **L5**, 1 mg CuI, and 10 µL of triethyl amine in DCM. The slurry was stirred at room temperature for 3 days in the dark. The mixture was centrifuged to collect the powder which was then washed with DCM four to five times followed by centrifugation after each wash until the supernatant was colorless. The resulting powder was dried under reduced pressure and appeared to be orange/yellow. **Cr-2** was anchored following a similar procedure, giving yellow powder.

Anchoring L5 onto P25 TiO₂ coated FTO plate (L5/TiO₂/FTO)

In a nitrogen-filled glovebox, 2 slides of **azide/TiO₂/FTO** plates were soaked into a solution of 18 mg **L5**, 1 mg CuI, and 10 μ L of triethyl amine in DCM in the dark with gentle stirring for 3 days. The reaction solution was removed from the reaction vessel. The plates were rinsed with methanol once followed by DCM twice then soaked in toluene overnight. The plates were dried under reduced pressure and stored at -30 °C. **Cr-2** was anchored following a similar procedure.

Procedure for CV measurements

In a nitrogen-filled glovebox, cyclic voltammogram experiments of homogenous compound **L5** and **L5** anchored P25 TiO₂ coated FTO plate (**L5/TiO₂/FTO**) were conducted using a three-electrode configuration, where **TiO₂/FTO** was used as the working electrode for the CV measurements for the homogenous compounds **L5**; and **L5/TiO₂/FTO** was used as the working electrode for the CV measurements for the functionalized system. For all experiments, Pt wire was used as the counter electrode, and non-aqueous Ag/Ag⁺ was used as the reference electrode. A 100 mM solution of tetrabutylammonium hexafluorophosphate (TBAPF₆) in *o*-DFB was used as the electrolyte. The scan rate was varied (10 mV/s to 200 mV/s) to study the diffusion process on the electrode.

4.5 Appendix C

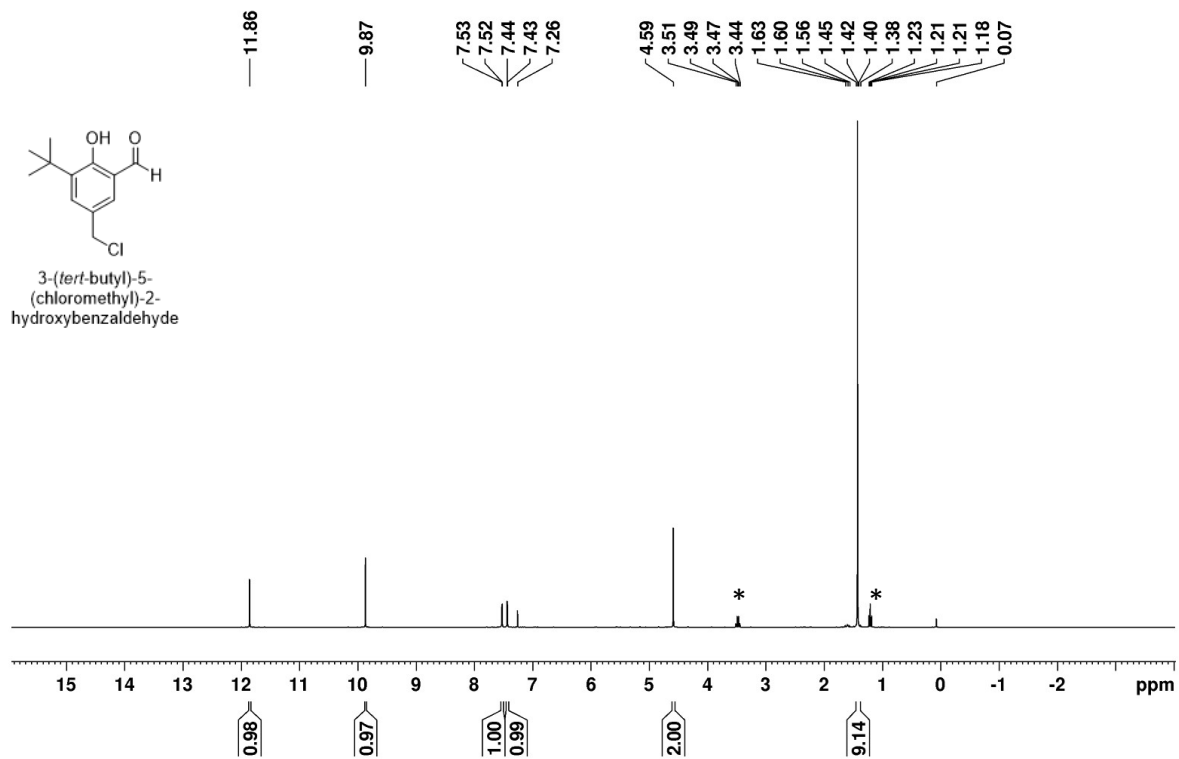


Figure C1. ^1H NMR (500 MHz, CDCl_3 , 25 °C) spectrum of 3-(*tert*-butyl)-5-(chloromethyl)-2-hydroxybenzaldehyde. δ , ppm: 11.86 (s, 1H, OH), 9.87 (s, 1H, O=CH), 7.53 (d, 1H, ArH), 7.44 (d, 1H, ArH), 4.59 (s, 1H, CH_2Cl), 1.42, (s, 9H $\text{C}(\text{CH}_3)_3$). *residual ether.

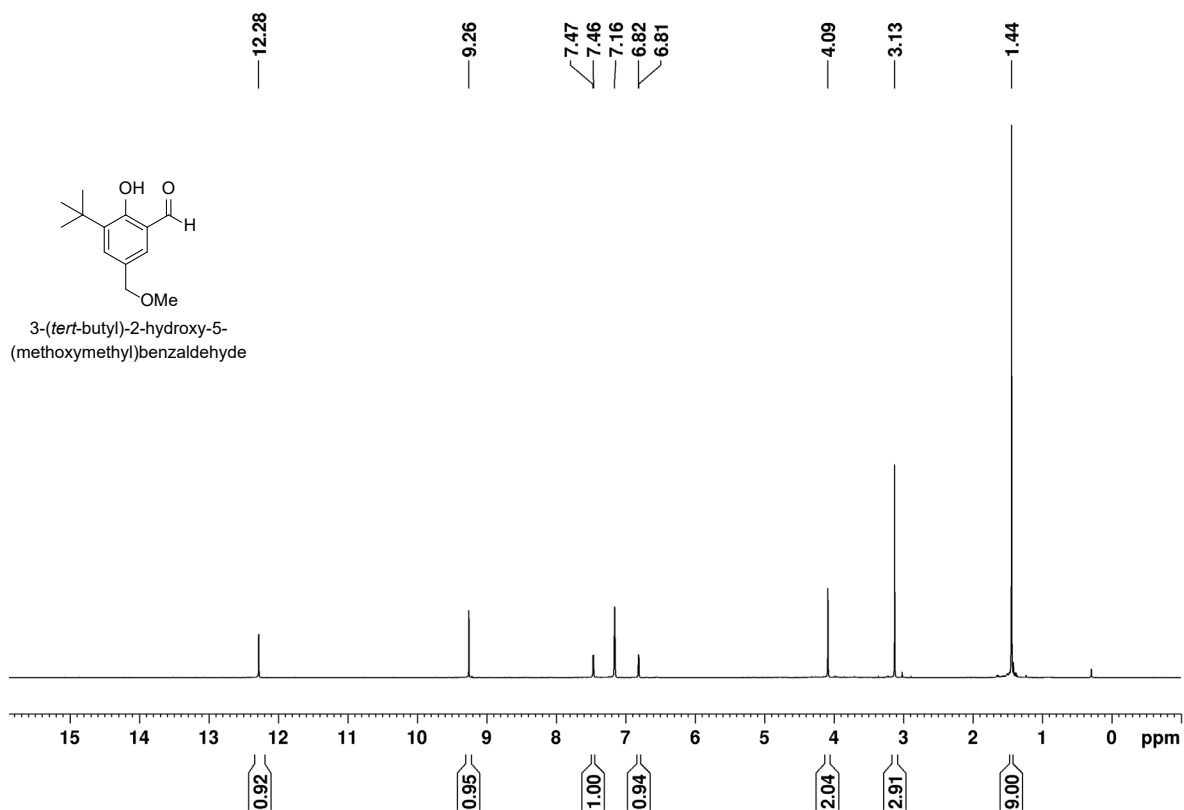


Figure C2. $^1\text{H NMR}$ (300 MHz, C_6D_6 , 25 °C) spectrum of 3-(*tert*-butyl)-5-(methoxymethyl)-2-hydroxybenzaldehyde. δ , ppm: 12.28 (s, 1H, OH), 9.26 (s, 1H, O=CH), 7.47 (d, 1H, ArH), 6.81 (d, 1H, ArH), 4.09 (s, 1H, CH_2O), 3.13 (s, 3H, OCH_3), 1.44 (s, 9H $\text{C}(\text{CH}_3)_3$).

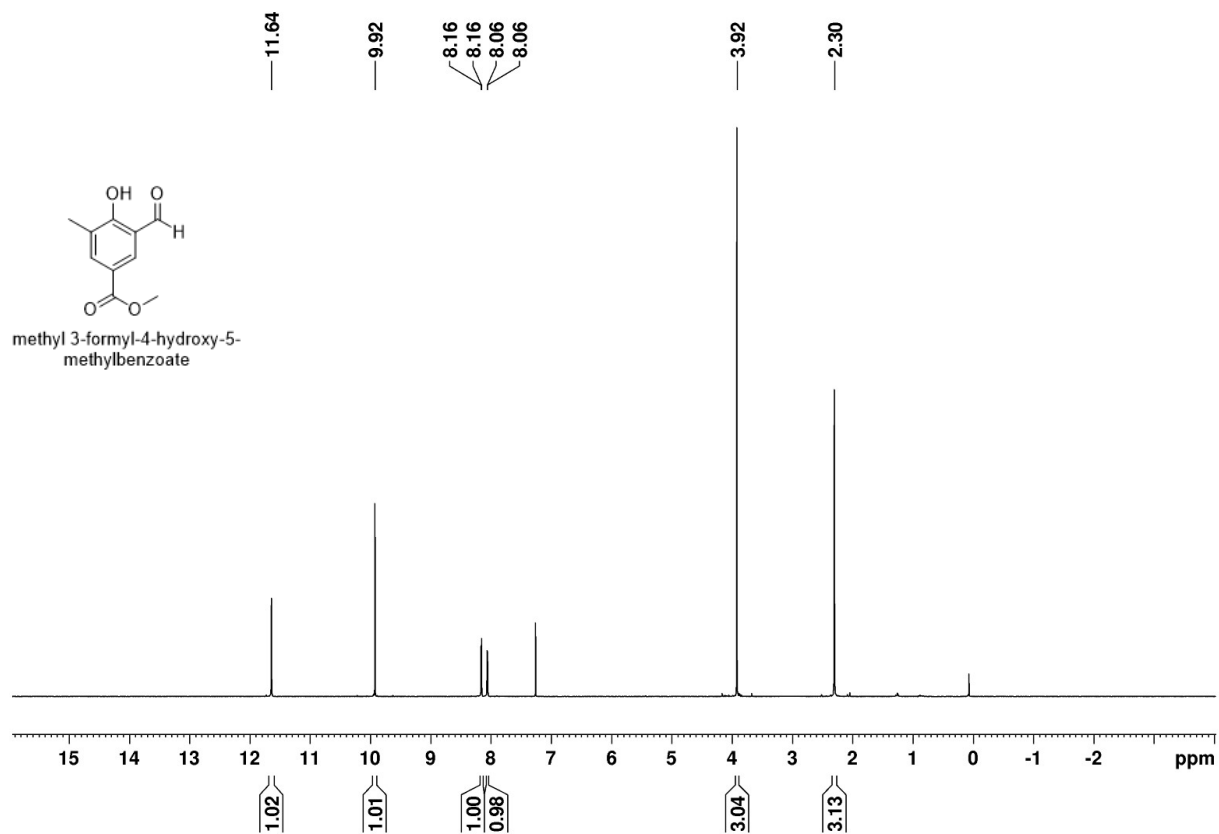


Figure C3. ¹H NMR (300 MHz, CDCl₃, 25 °C) spectrum of methyl 3-formyl-4-hydroxy-5-methylbenzoate. δ, ppm: 11.64 (s, 1H, OH), 9.92 (s, 1H, O=CH), 8.16 (d, 1H, ArH), 8.06 (d, 1H, ArH), 3.92 (s, 3H, OCH₃), 1.42 (s, 3H CH₃).

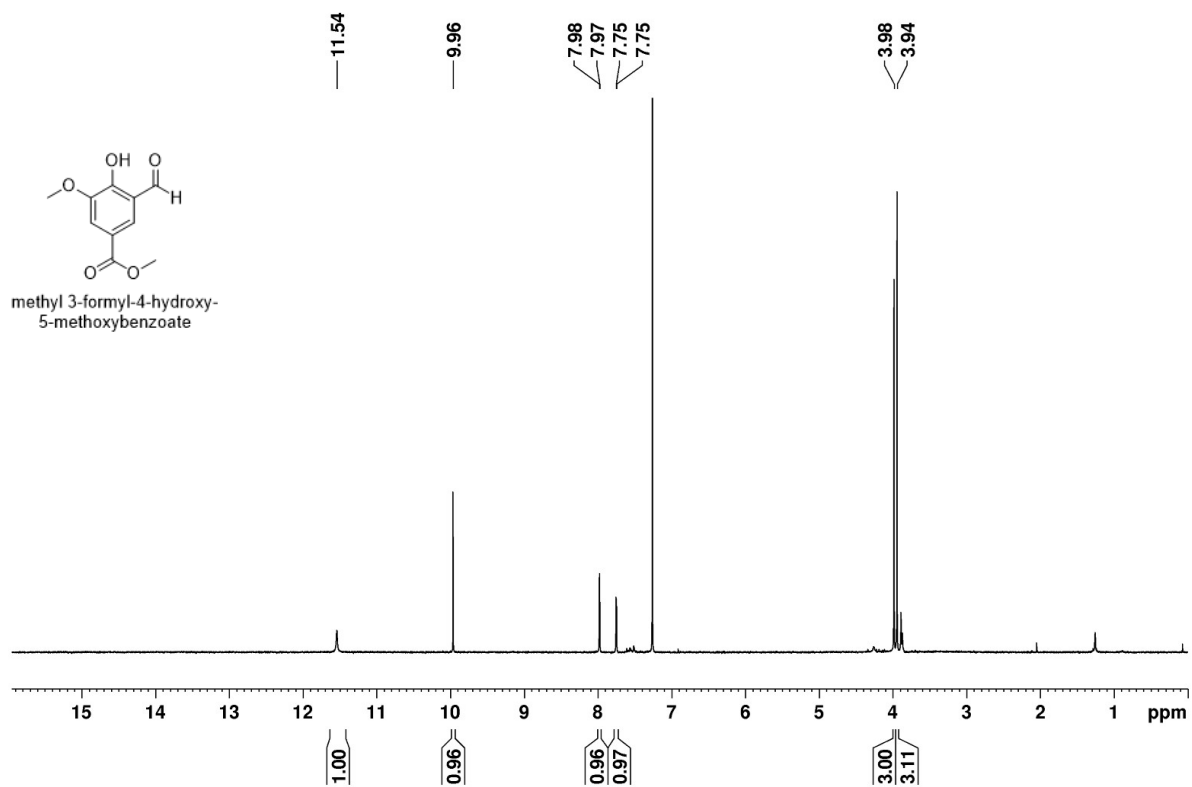


Figure C4. ¹H NMR (300 MHz, CDCl₃, 25 °C) spectrum of methyl 3-formyl-4-hydroxy-5-methoxybenzoate. δ, ppm: 11.54 (s, 1H, OH), 9.96 (s, 1H, O=CH), 7.98 (d, 1H, ArH), 7.75 (d, 1H, ArH), 3.98 (s, 3H, OCH₃), 3.94 (s, 3H O=COCH₃).

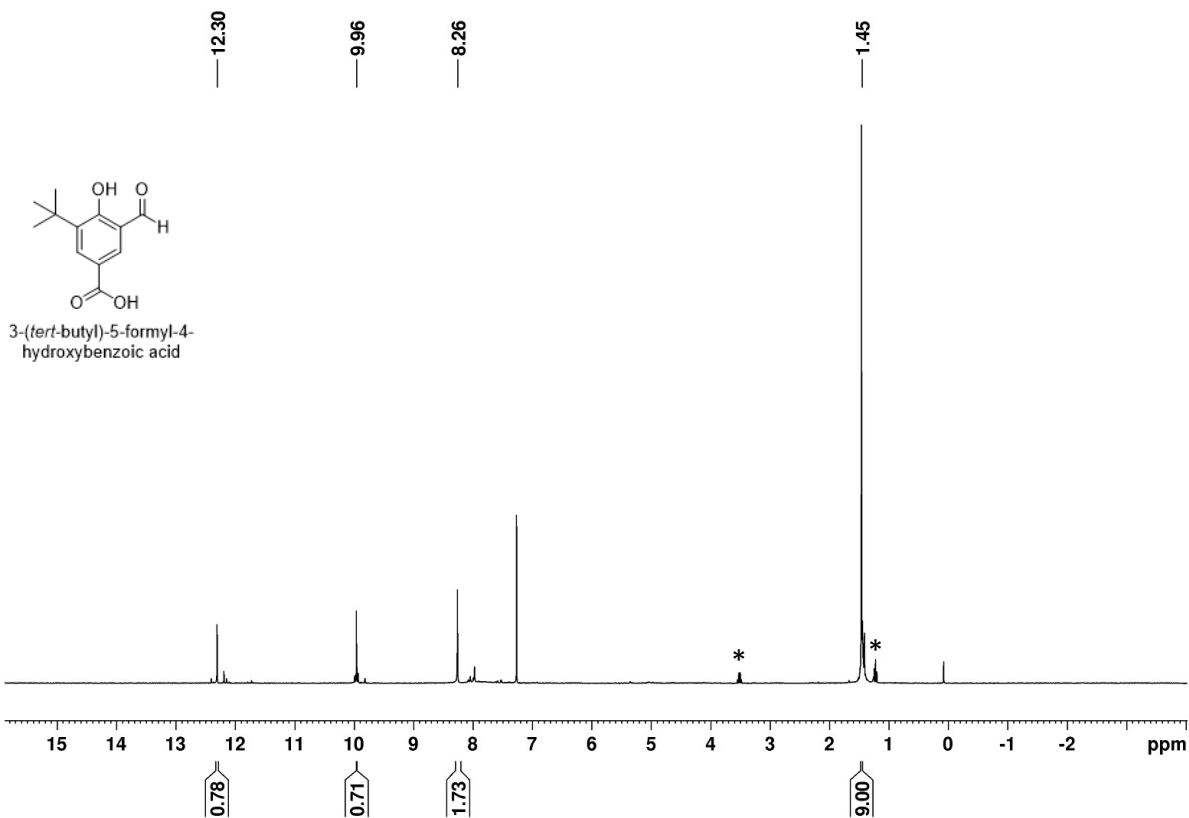


Figure C5. ^1H NMR (300 MHz, CDCl_3 , 25 °C) spectrum of 3-(*tert*-butyl)-5-formyl-4-hydroxybenzoic acid. δ , ppm: 12.30 (s, 1H, OH), 9.96 (s, 1H, O=CH), 8.26 (s, 2H, ArH), 1.45, (s, 9H $\text{C}(\text{CH}_3)_3$). *residual diethyl ether.

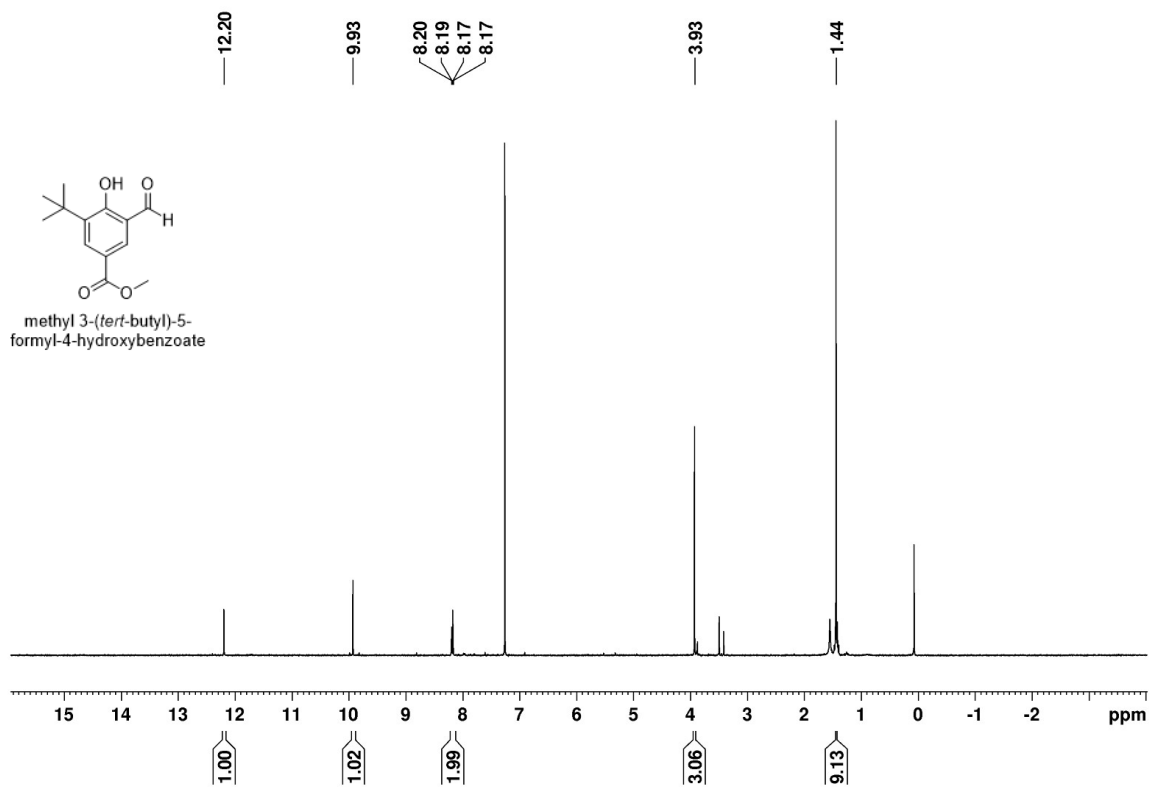


Figure C6. ¹H NMR (500 MHz, CDCl₃, 25 °C) spectrum of methyl 3-(*tert*-butyl)-5-formyl-4-hydroxybenzoate. δ, ppm: 12.20 (s, 1H, OH), 9.93 (s, 1H, O=CH), 8.20 (d, 1H, ArH), 8.17 (d, 1H, ArH), 3.93, (s, 3H OCH₃), 1.44, (s, 9H C(CH₃)₃).

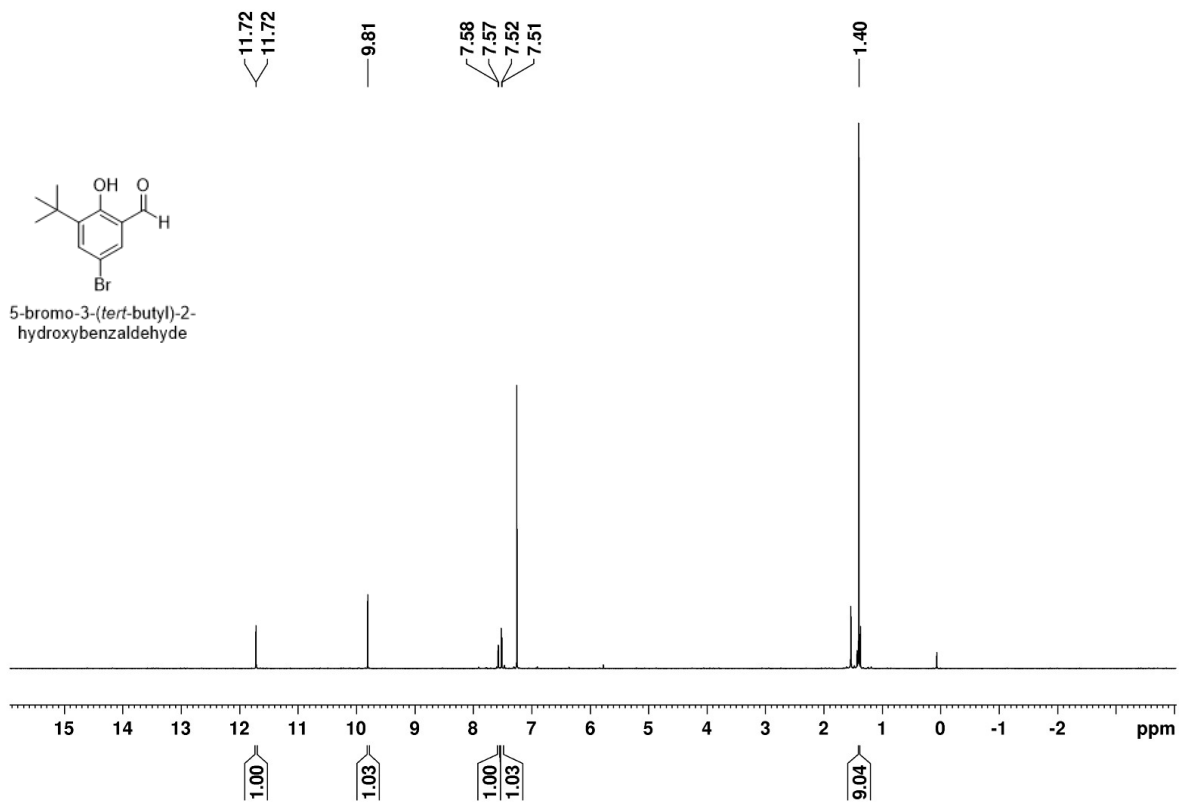


Figure C7. ^1H NMR (300 MHz, CDCl_3 , 25 $^\circ\text{C}$) spectrum of 5-bromo-3-(*tert*-butyl)-2-hydroxybenzaldehyde. δ , ppm: 11.72 (s, 1H, OH), 9.81 (s, 1H, O=CH), 7.58 (d, 1H, ArH), 7.51 (d, 1H, ArH), 1.40, (s, 9H C(CH₃)₃).

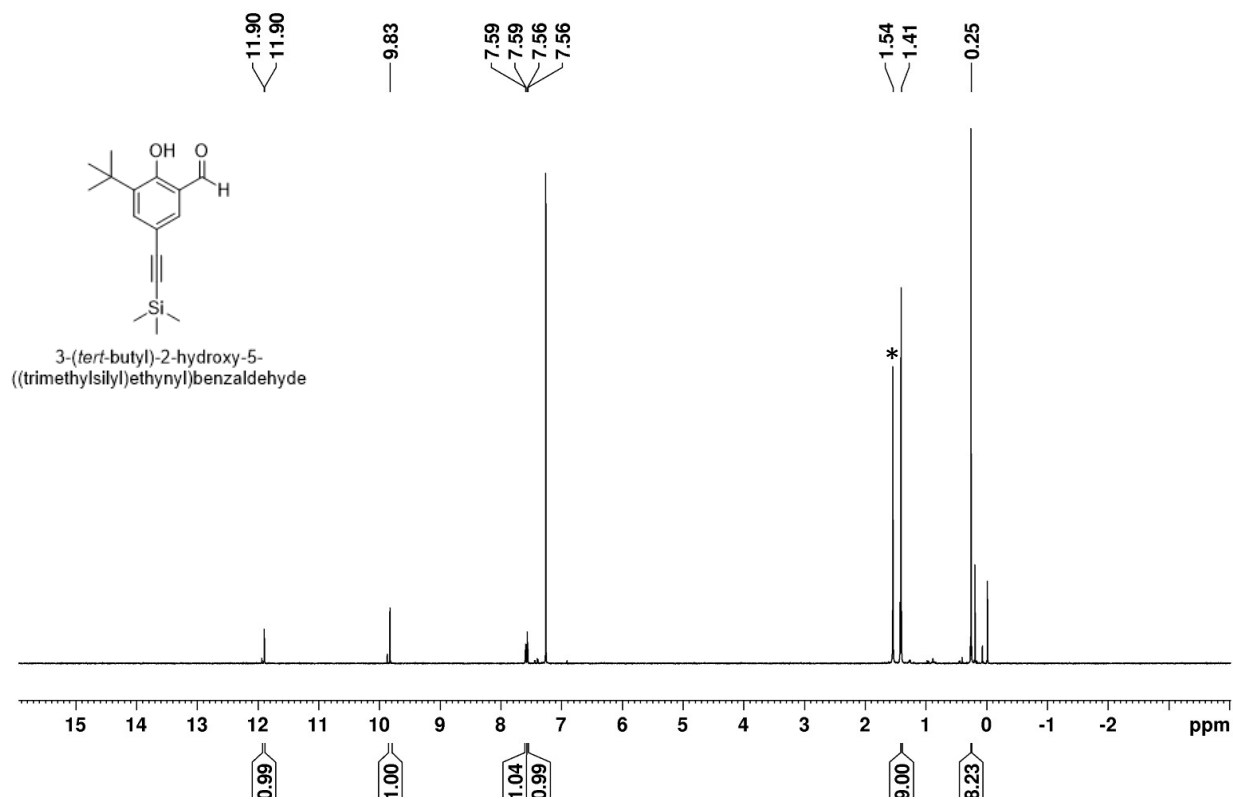


Figure C8. ^1H NMR (300 MHz, CDCl_3 , 25 °C) spectrum of 3-(*tert*-butyl)-2-hydroxy-5-((trimethylsilyl)ethynyl)benzaldehyde. δ , ppm: 11.90 (s, 1H, OH), 9.83 (s, 1H, O=CH), 7.59 (d, 1H, ArH), 7.56 (d, 1H, ArH), 1.41, (s, 9H $\text{C}(\text{CH}_3)_3$), 0.25, (s, 9H $\text{Si}(\text{CH}_3)_3$). *residual water in the deuterated solvent.

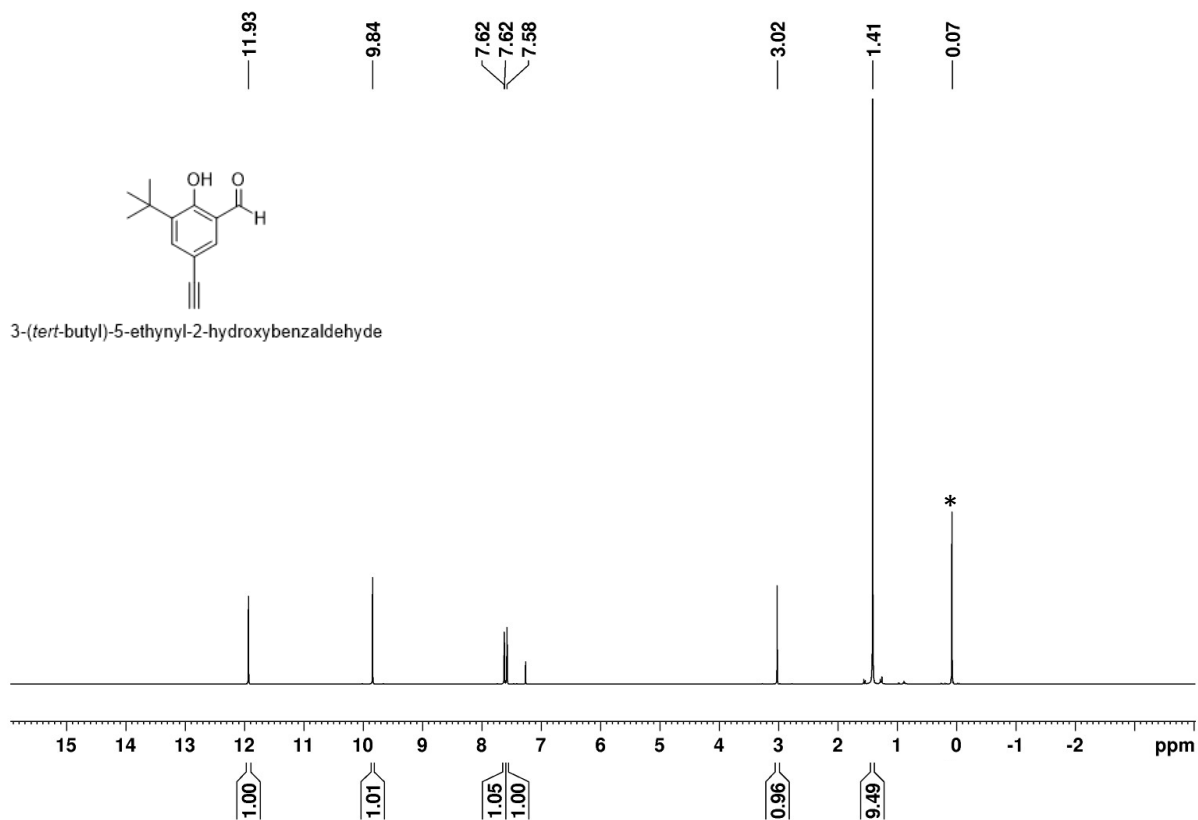


Figure C9. ^1H NMR (300 MHz, CDCl_3 , 25 $^\circ\text{C}$) spectrum of 3-(*tert*-butyl)-5-ethynyl-2-hydroxybenzaldehyde. δ , ppm: 11.93 (s, 1H, OH), 9.84 (s, 1H, O=CH), 7.62 (d, 1H, ArH), 7.58 (d, 1H, ArH), 3.02 (s, 1H, CCH), 1.41, (s, 9H C(CH₃)₃). *residual grease.

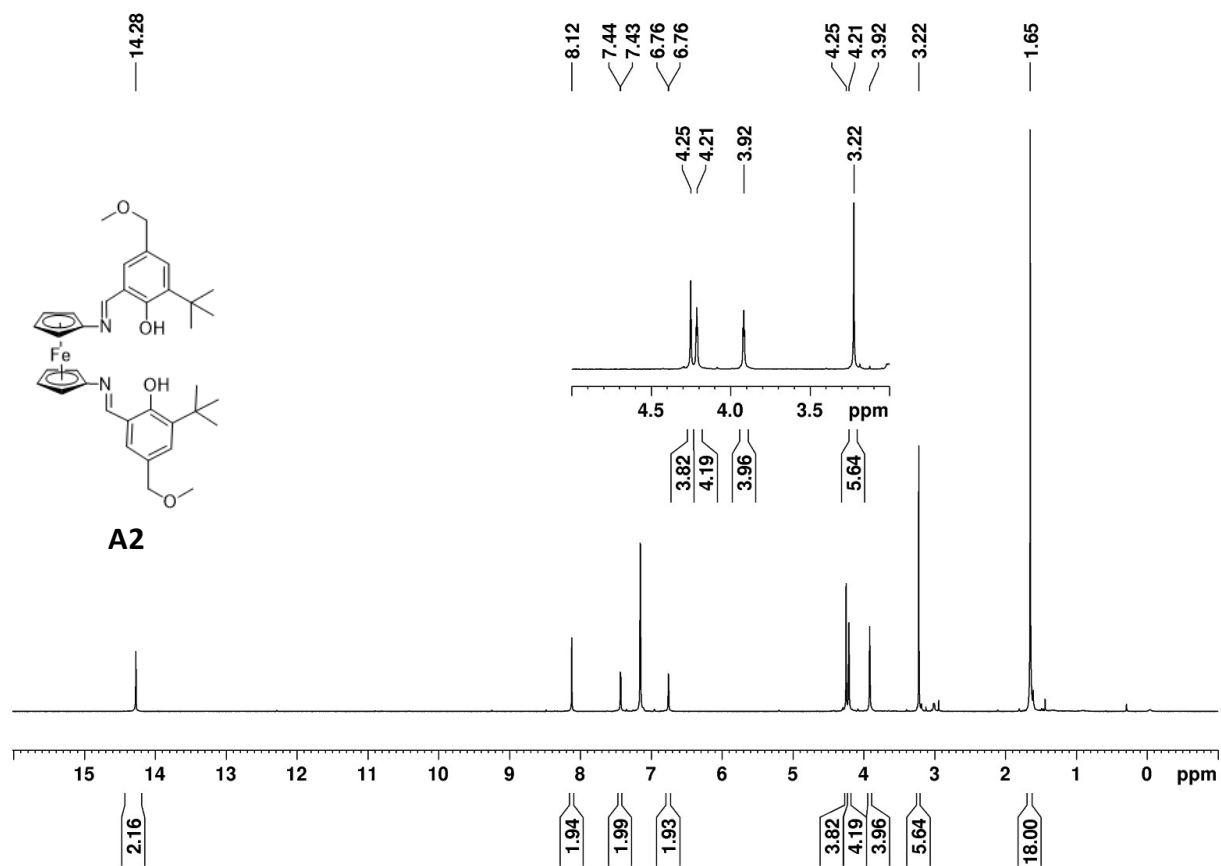


Figure C10. $^1\text{H NMR}$ (300 MHz, C_6D_6 , 25 $^\circ\text{C}$) spectrum of **A2**. δ , ppm: 14.28 (s, 2H, OH), 8.12 (s, 2H, N=CH), 7.44 (s, 2H, ArH), 6.76 (s, 2H, ArH), 4.25 (s, 4H, OCH₂), 4.21 (t, 4H, C₅H₄), 3.92 (t, 4H, C₅H₄), 3.22 (s, 6H, OCH₃), 1.65, (s, 18H C(CH₃)₃).

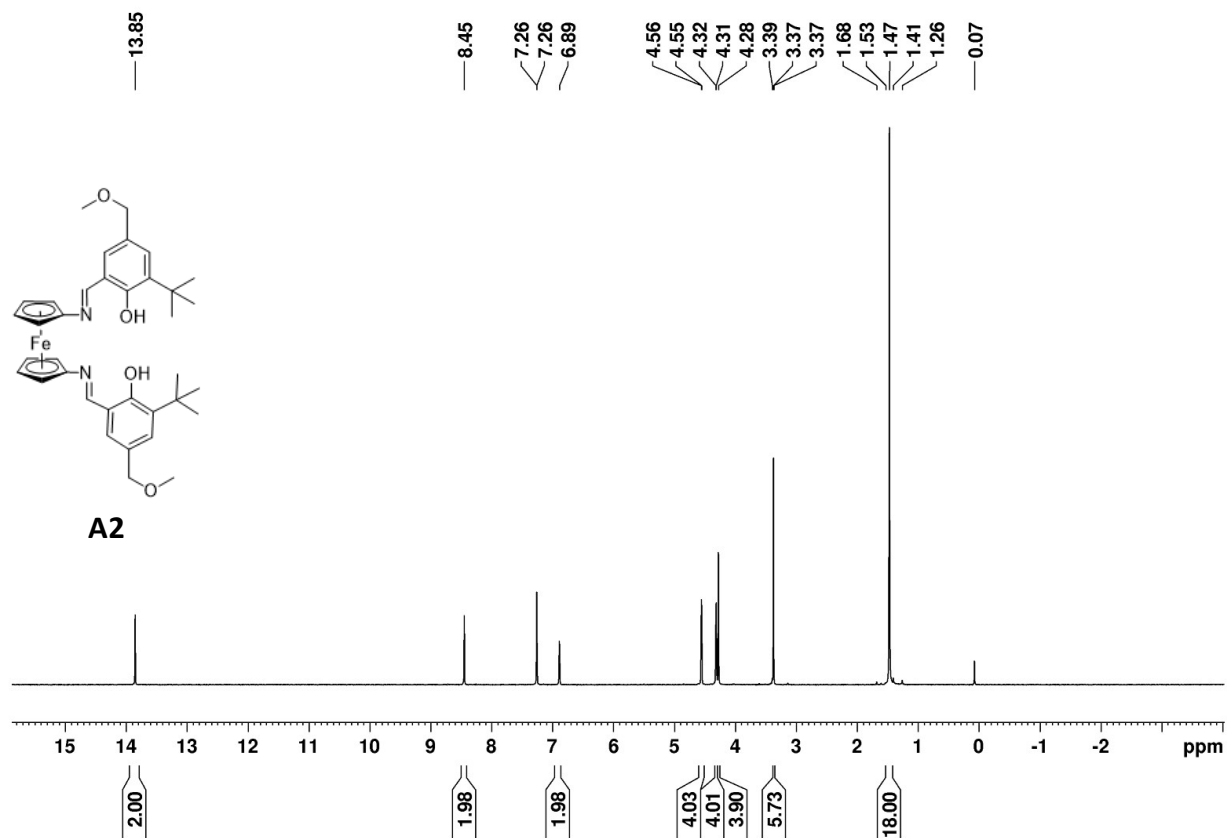


Figure C11. ¹H NMR (300 MHz, CDCl₃, 25 °C) spectrum of **A2**. δ, ppm: 13.85 (s, 2H, OH), 8.45 (s, 2H, N=CH), 7.26 (s, 1H, ArH), 6.89 (s, 1H, ArH), 4.56 (s, 4H, OCH₂), 4.32 (t, 4H, C₅H₄), 4.28 (t, 4H, C₅H₄), 3.37 (s, 6H, OCH₃), 1.47, (s, 18H, C(CH₃)₃).

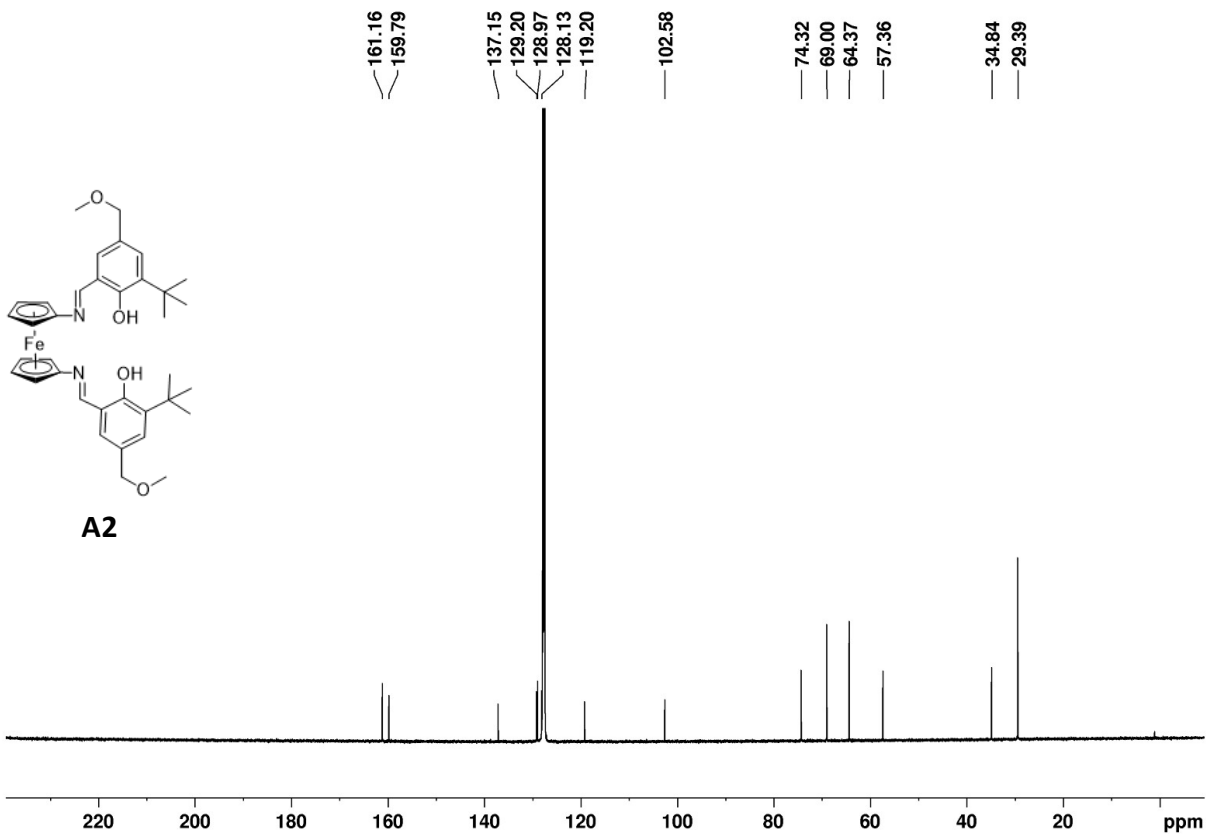


Figure C12. ^{13}C NMR (125 MHz, C_6D_6 , 25 °C) spectrum of **A2**. δ , ppm: 161.2 (N=C), 159.8 (COH), 137.2, 129.2, 129.0, 128.1, 119.2, 102.6, 74.3 (OCH₂), 69.0 (C₅H₄), 64.4 (C₅H₄), 57.4 (OCH₃), 34.8 (C(CH₃)₃), 29.4 (C(CH₃)₃).

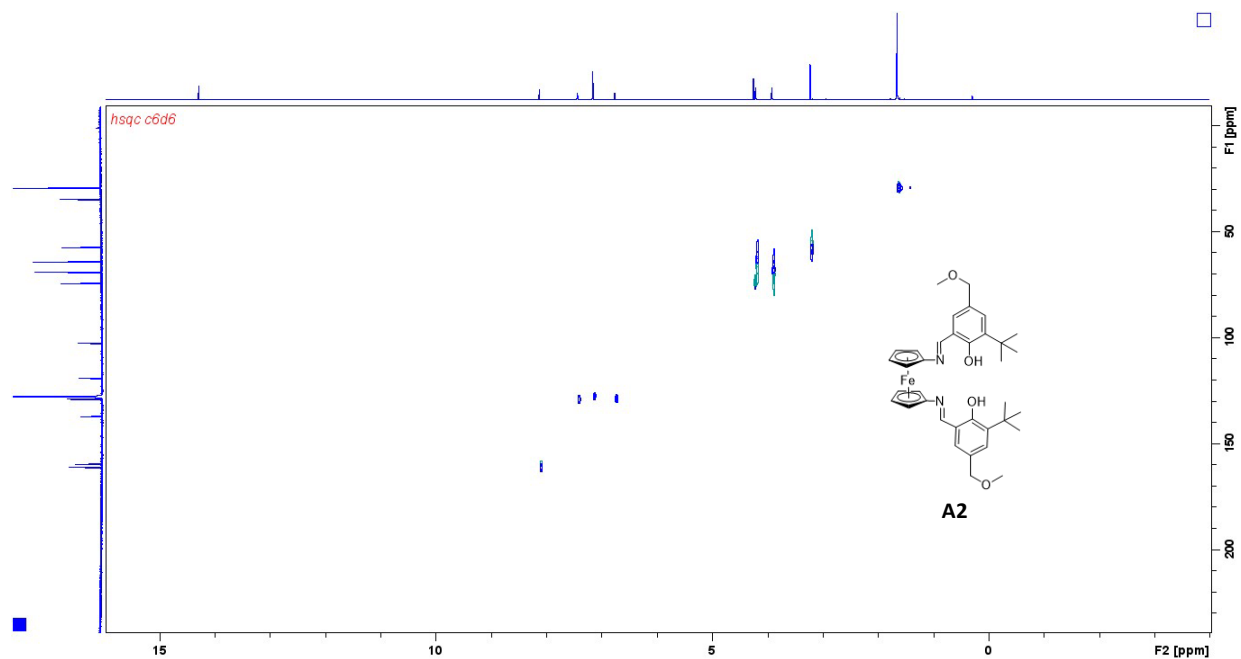


Figure C13. 2D HSQC NMR (500 MHz, C₆D₆, 25 °C) spectrum of **A2**.

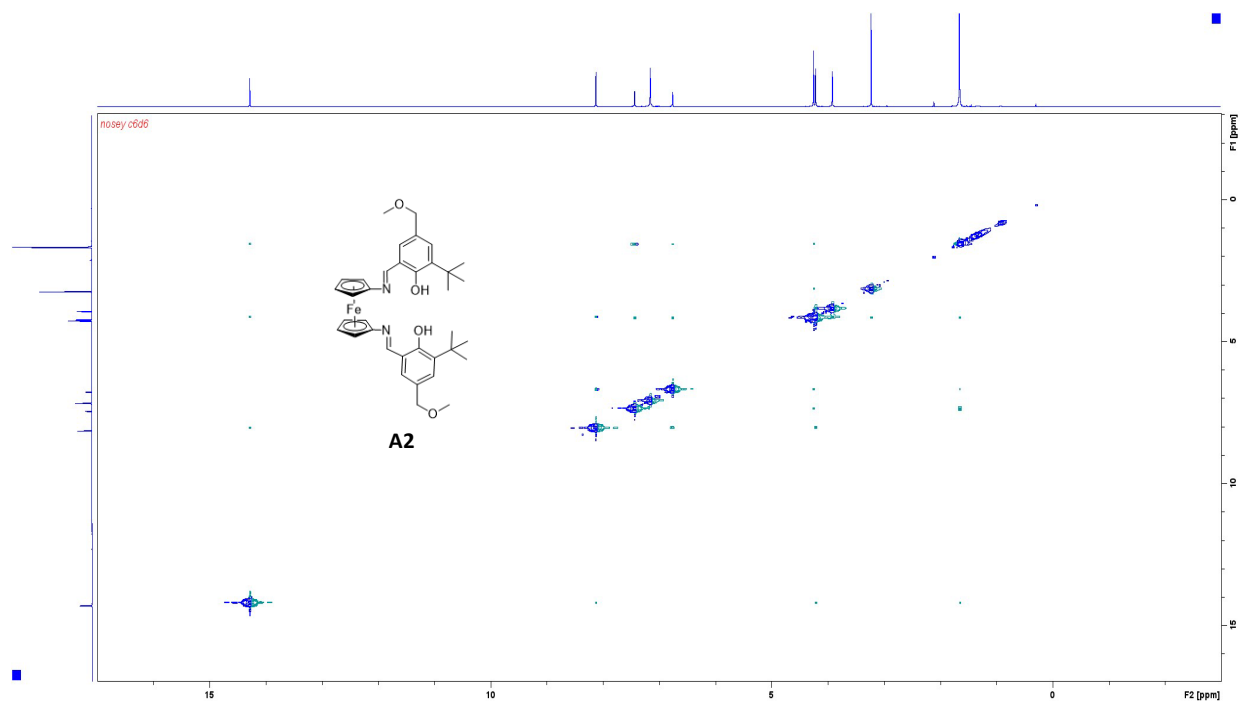


Figure C14. 2D NOESY NMR (500 MHz, C₆D₆, 25 °C) spectrum of **A2**.

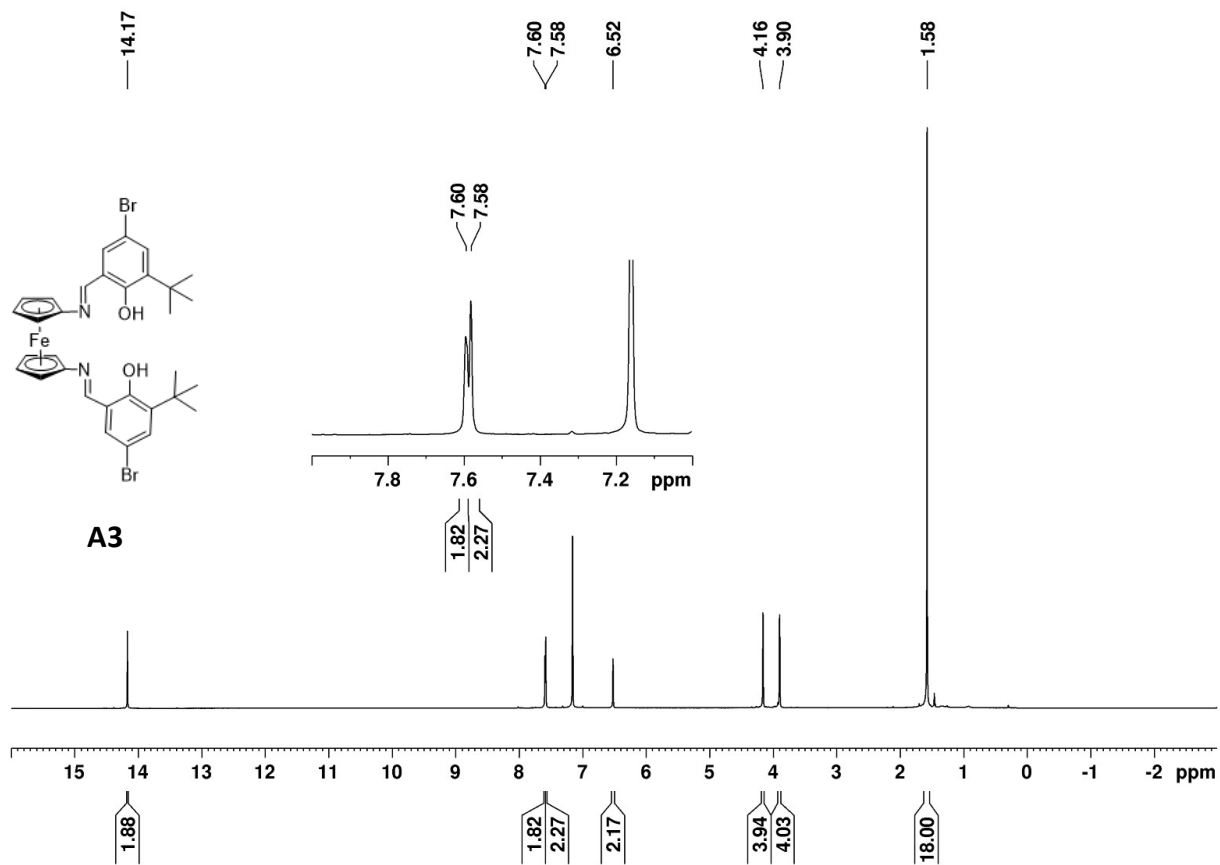


Figure C15. ^1H NMR (500 MHz, C_6D_6 , 25 °C) spectrum of **A3**. δ , ppm: 14.17 (s, 2H, OH), 7.60 (s, 2H, N=CH), 7.58 (s, 2H, ArH), 6.52 (s, 2H, ArH), 4.16 (t, 4H, C_5H_4), 3.90 (t, 4H, C_5H_4), 1.58, (s, 18H, $\text{C}(\text{CH}_3)_3$).

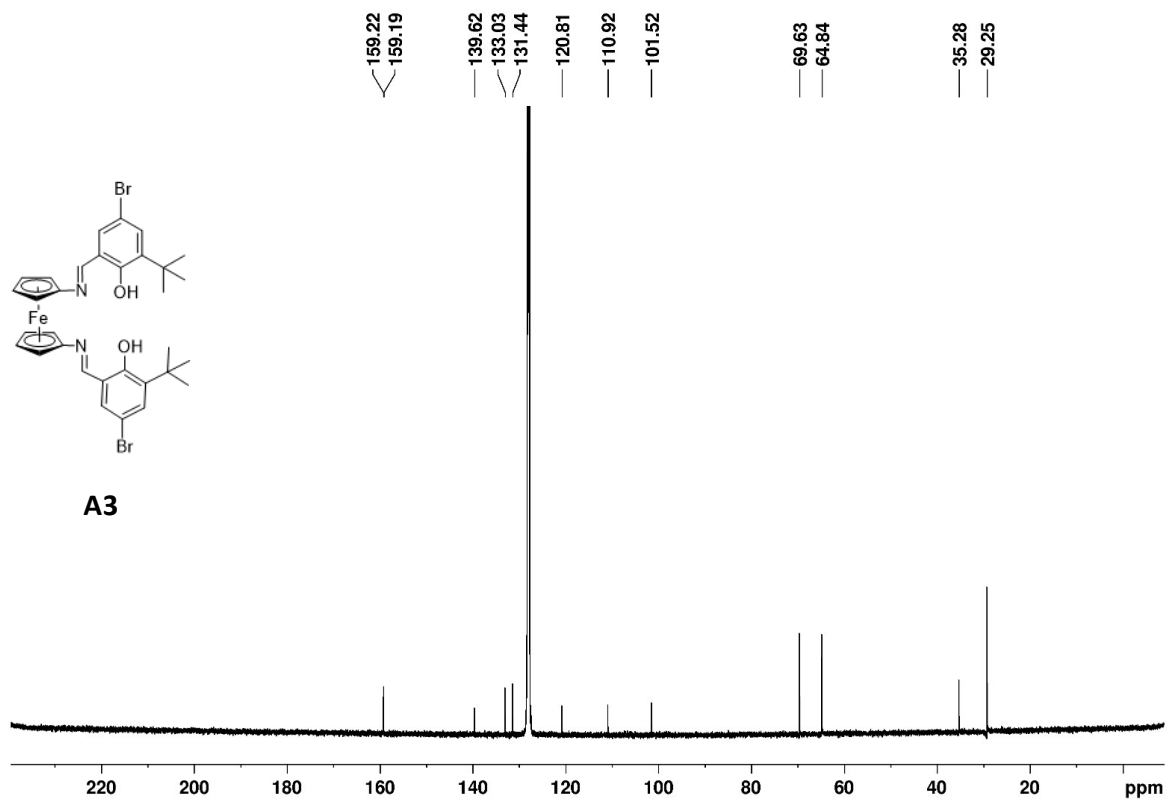


Figure C16. ^{13}C NMR (125 MHz, C_6D_6 , 25 °C) spectrum of **A3**. δ , ppm: 159.22 (N=C), 159.19(COH), 137.6, 133.0, 131.4, 120.8, 110.9, 101.5, 69.6 (C_5H_4), 64.8 (C_5H_4), 35.3 ($\text{C}(\text{CH}_3)_3$), 29.3 ($\text{C}(\text{CH}_3)_3$).

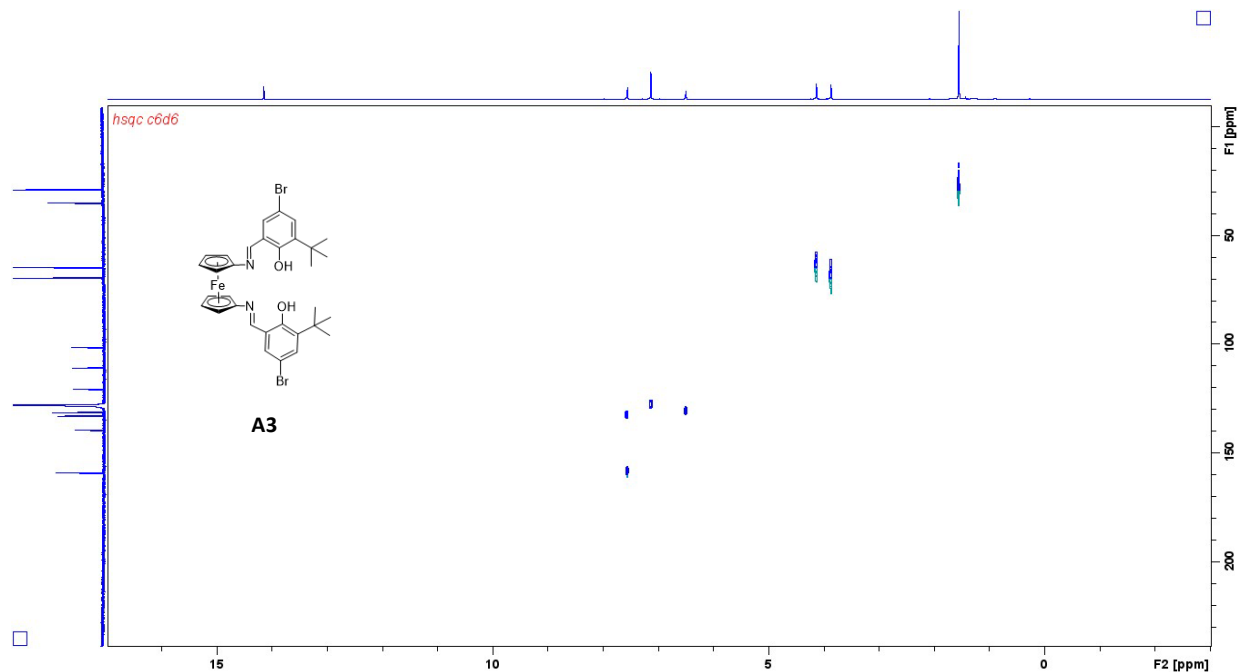


Figure C17. 2D HSQC NMR (500 MHz, C₆D₆, 25 °C) spectrum of **A3**.

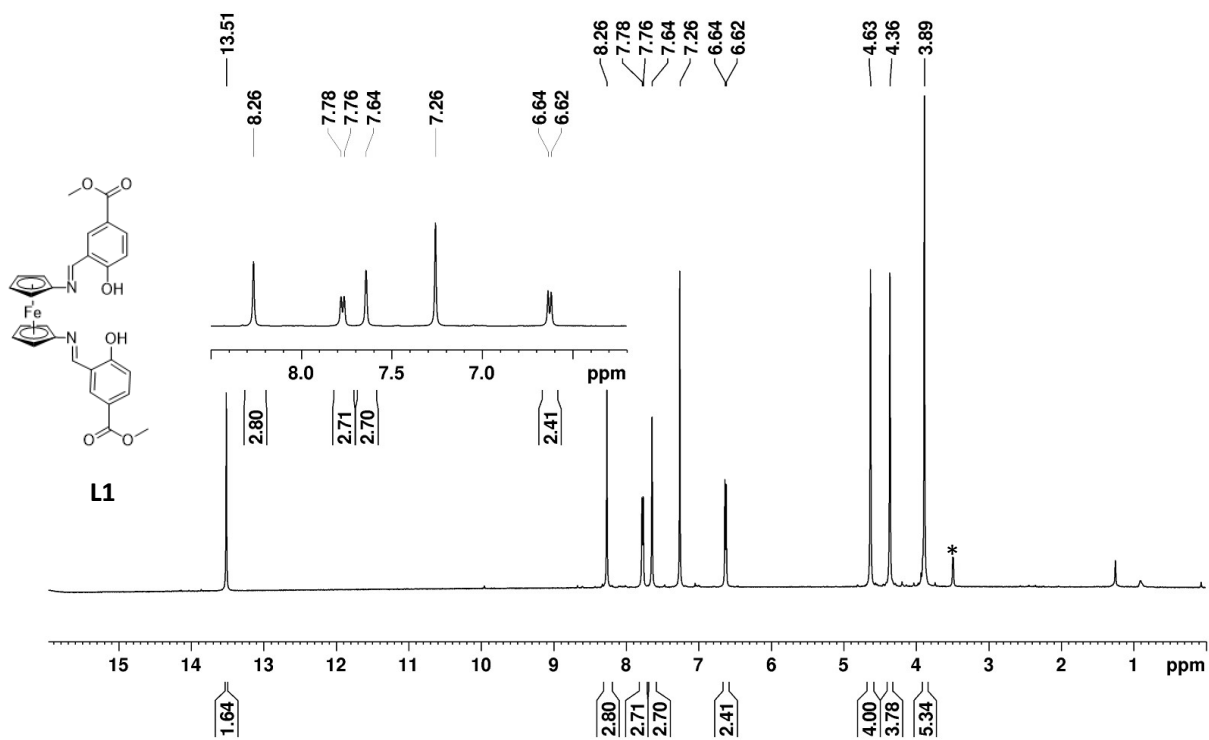


Figure C18. ¹H NMR (500 MHz, CDCl₃, 25 °C) spectrum of **L1**. δ, ppm: 13.51 (s, 2H, OH),

8.26 (s, 2H, N=CH), 7.78 (s, 2H, ArH), 7.64 (s, 2H, ArH), 6.52 (d, 2H, ArH), 4.63 (t, 4H, C₅H₄), 4.36 (t, 4H, C₅H₄), 3.89 (s, 6H, OCH₃). *residual methanol.

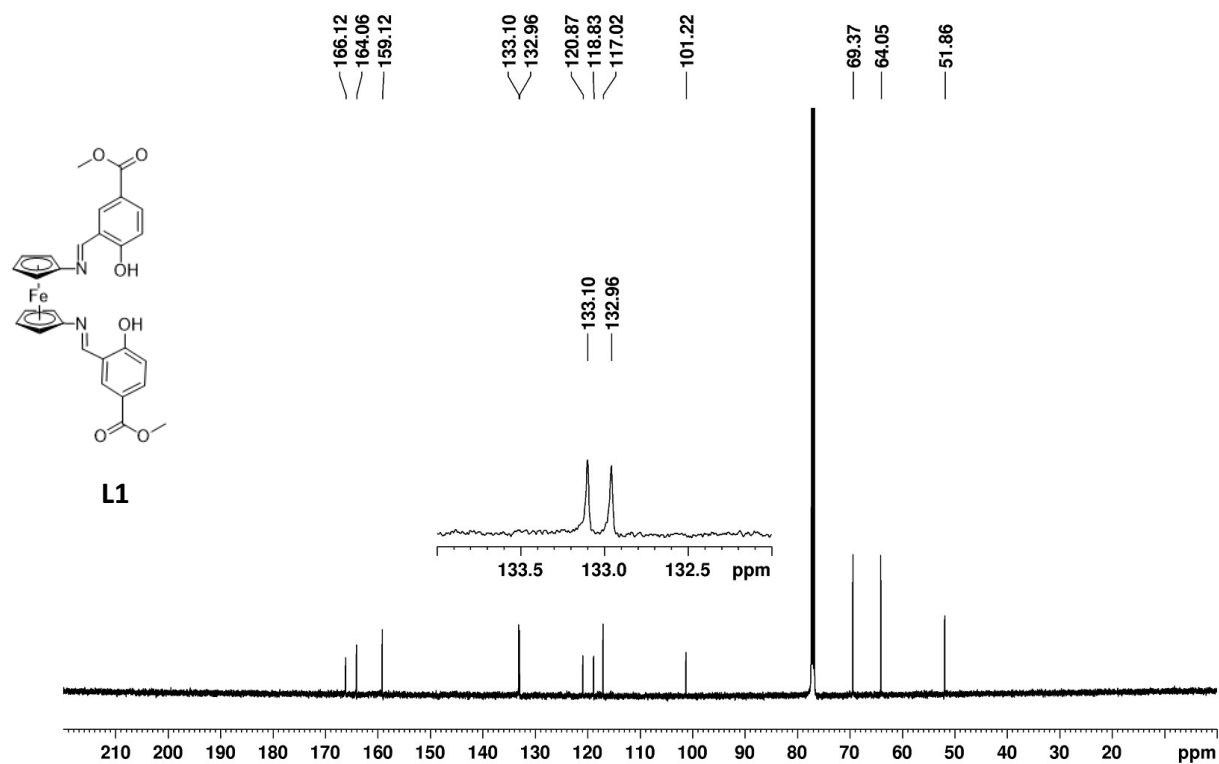


Figure C19. ¹³C NMR (125 MHz, CDCl₃, 25 °C) spectrum of L1. δ, ppm: 166.1 (C=O), 164.1 (COH) 159.1 (N=C), 133.1, 132.9, 120.9, 118.8, 117.0, 101.2, 69.3 (C₅H₄), 64.0 (C₅H₄), 51.9 (OCH₃), 34.8 (C(CH₃)₃), 29.4 (C(CH₃)₃).

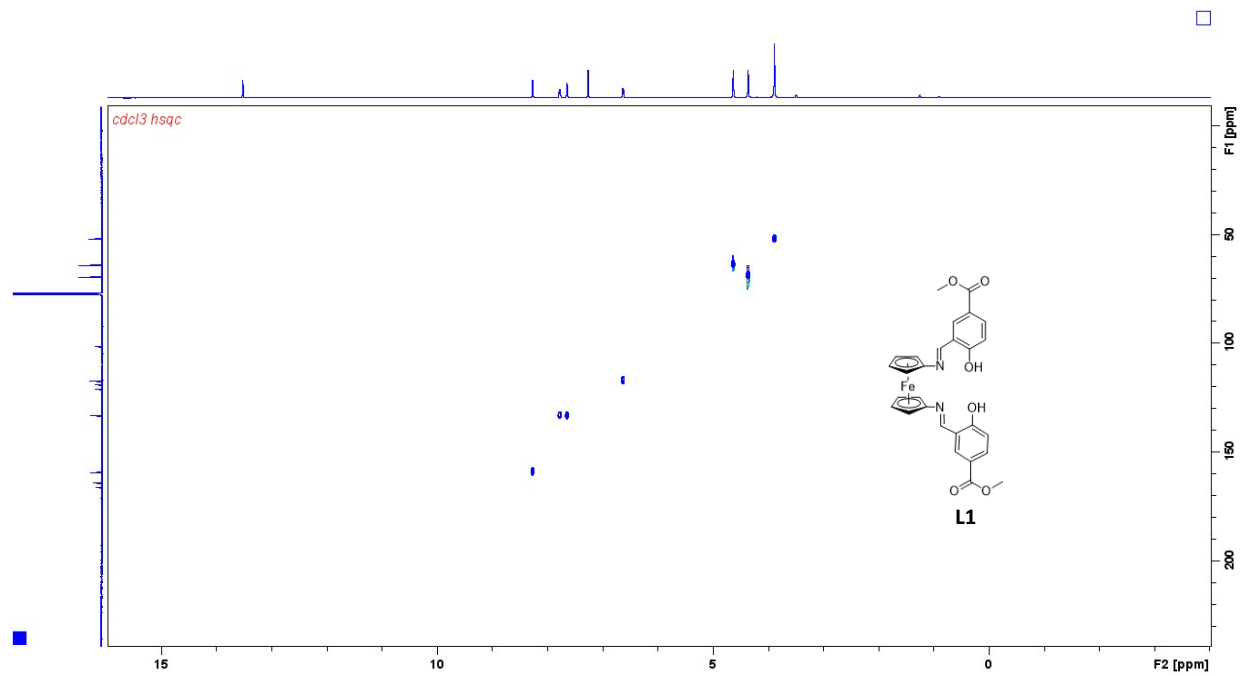


Figure C20. 2D HSQC NMR (500 MHz, CDCl₃, 25 °C) spectrum of **L1**.

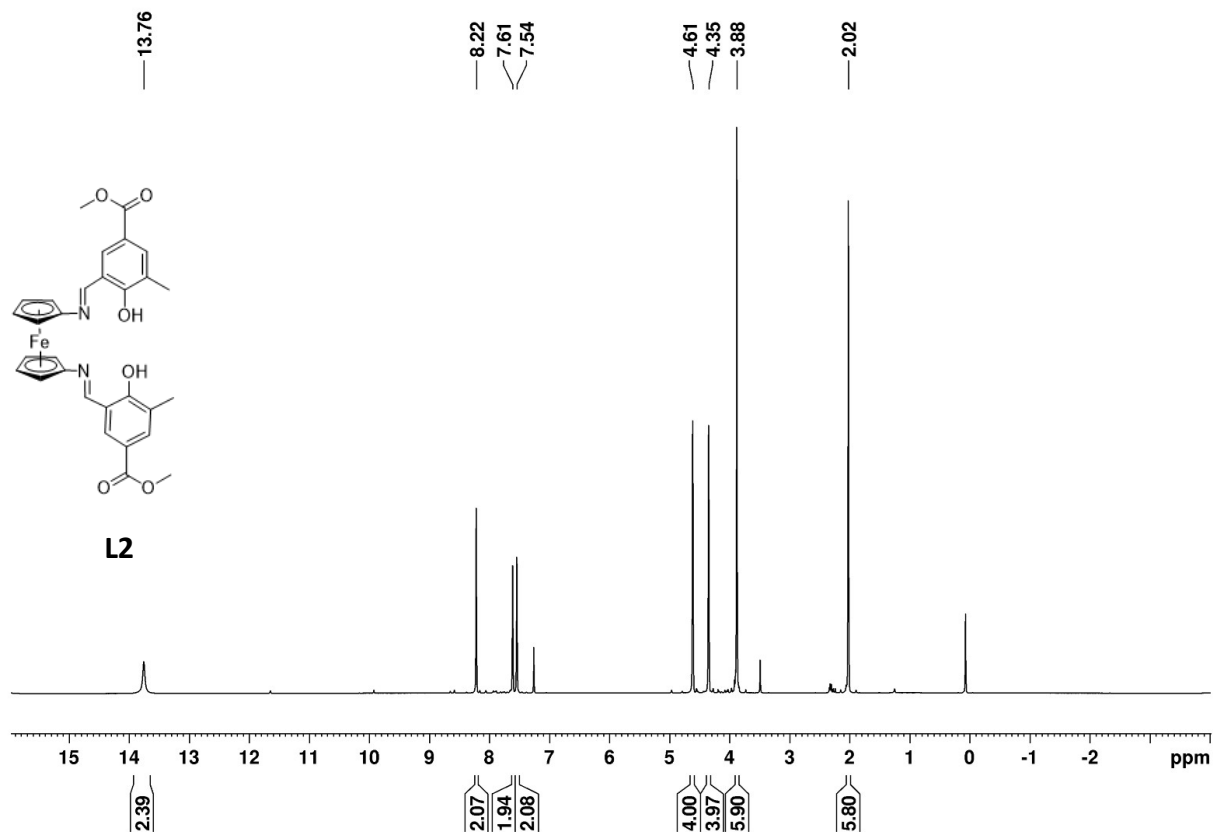


Figure C21. $^1\text{H NMR}$ (500 MHz, CDCl_3 , 25 °C) spectrum of **L2**. δ , ppm: 13.76 (s, 2H, OH), 8.22 (s, 2H, N=CH), 7.61 (s, 2H, ArH), 7.54 (s, 2H, ArH), 4.61 (t, 4H, C_5H_4), 4.35 (t, 4H, C_5H_4), 3.88 (s, 6H, OCH_3), 2.02 (s, 6H, CCH_3).

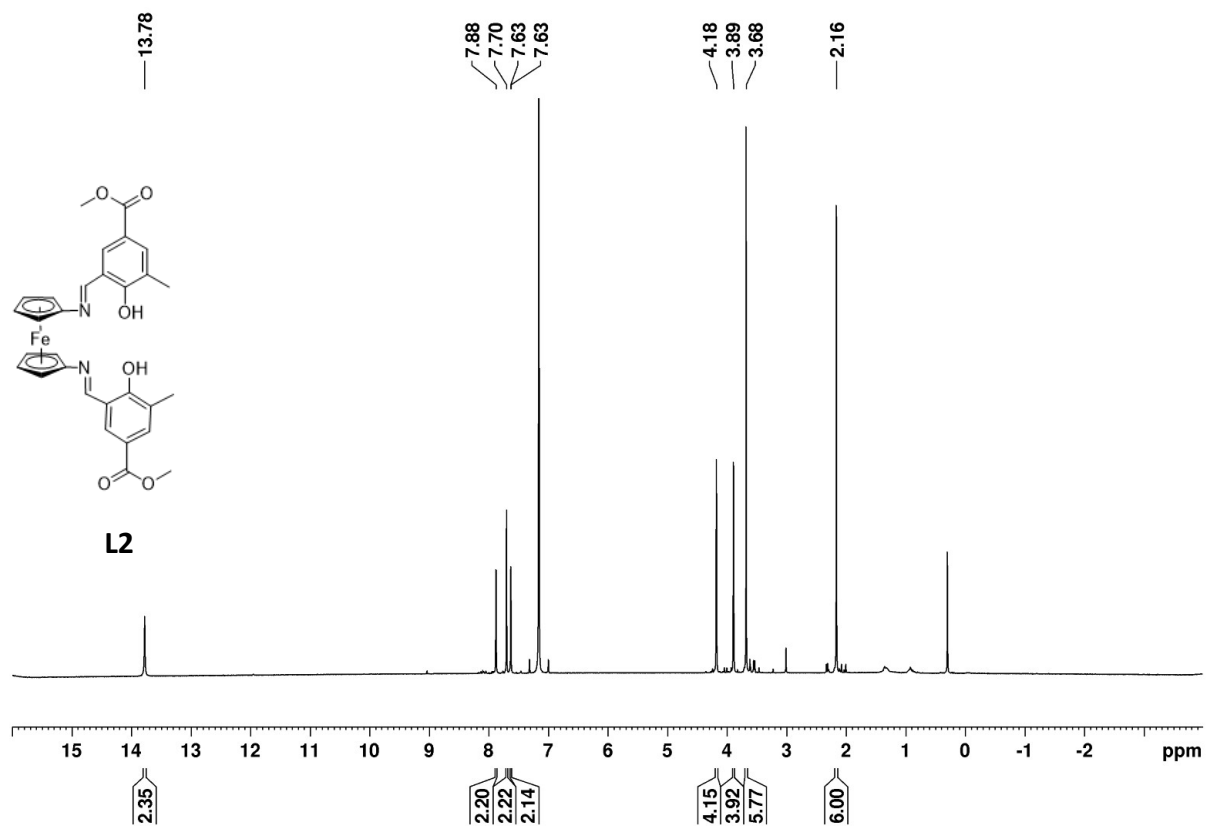


Figure C22. $^1\text{H NMR}$ (500 MHz, C_6D_6 , 25 $^\circ\text{C}$) spectrum of **L2**. δ , ppm: 13.78 (s, 2H, OH), 7.88 (s, 2H, N=CH), 7.70 (s, 2H, ArH), 7.63 (s, 2H, ArH), 4.18 (t, 4H, C_5H_4), 3.89 (t, 4H, C_5H_4), 3.68 (s, 6H, OCH_3), 2.16 (s, 6H, CCH_3).

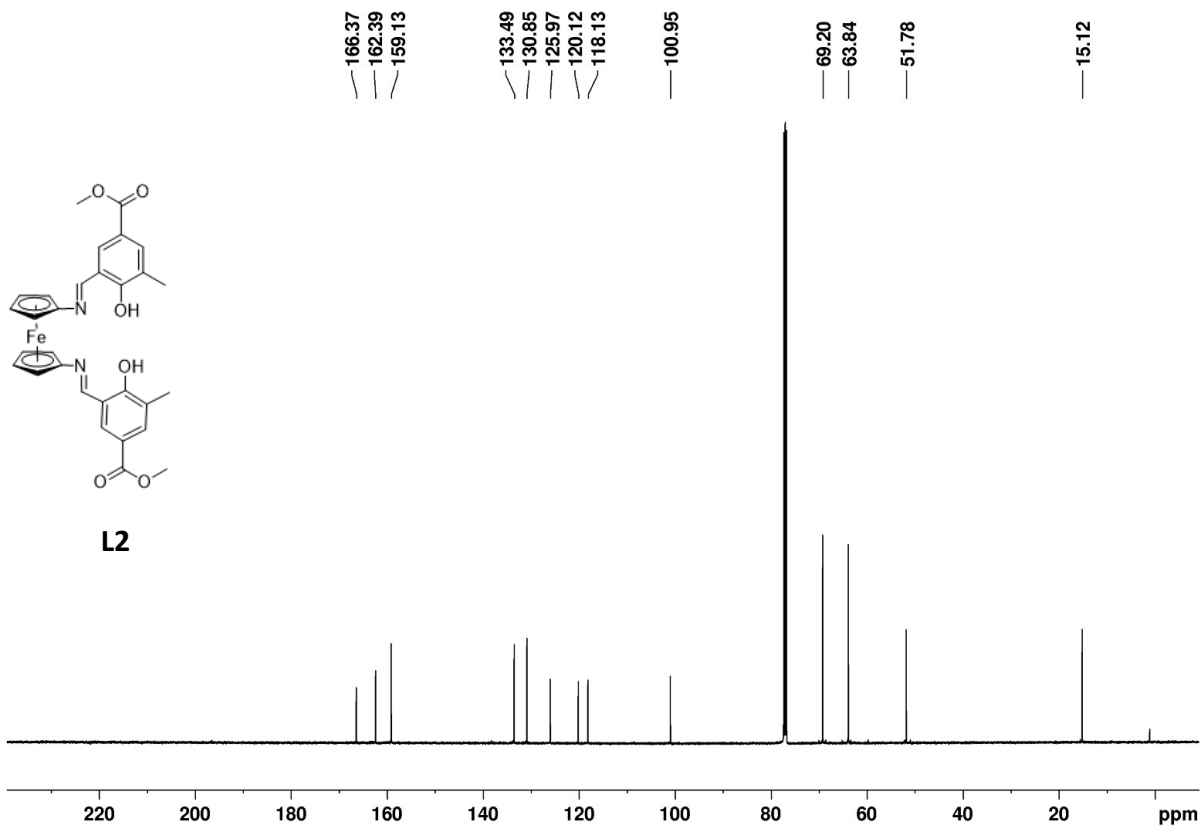


Figure C23. ^{13}C NMR (125 MHz, CDCl_3 , 25 °C) spectrum of **L2**. δ , ppm: 166.4 ($\text{C}=\text{O}$), 162.4 (COH), 159.8 ($\text{N}=\text{C}$), 133.5, 130.9, 126.0, 120.1, 118.1, 100.9, 69.2 (C_5H_4), 63.8 (C_5H_4), 51.8 (OCH_3), 15.1 (CCH_3).

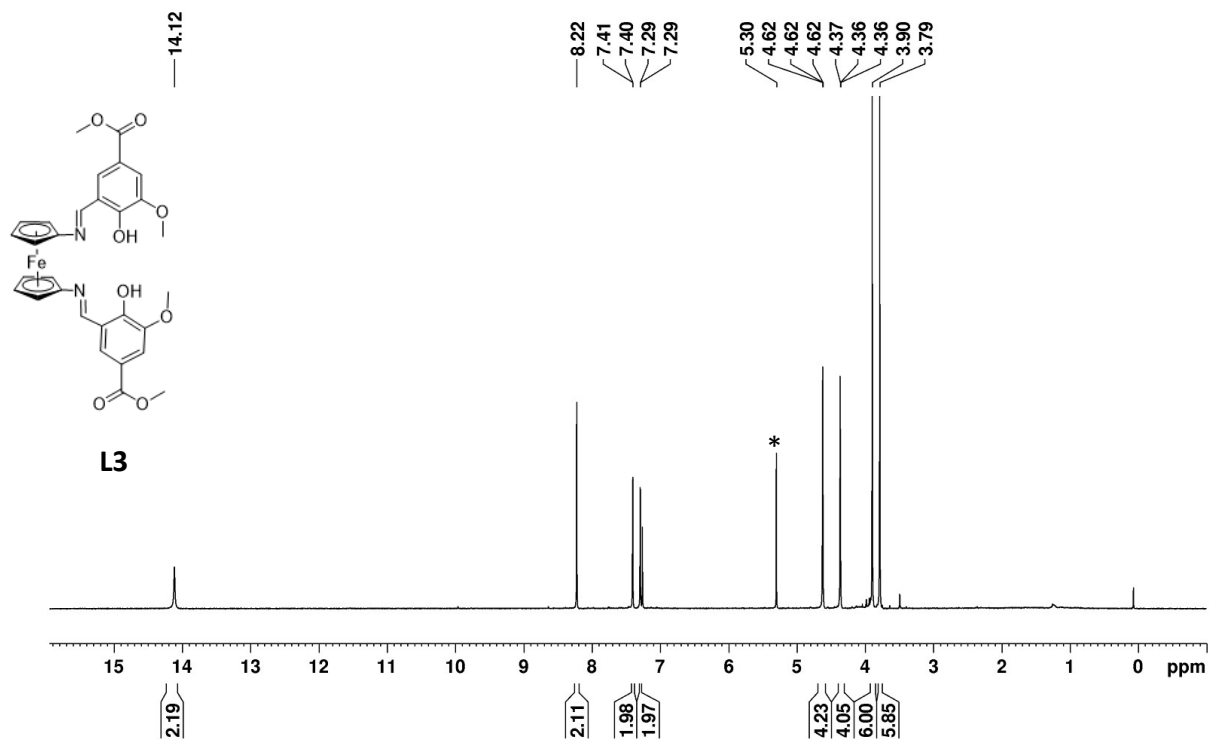


Figure C24. $^1\text{H NMR}$ (500 MHz, CDCl_3 , 25 °C) spectrum of L3. δ , ppm: 14.12 (s, 2H, OH), 8.22 (s, 2H, N=CH), 7.40 (d, 2H, ArH), 7.29 (d, 2H, ArH), 4.62 (t, 4H, C_5H_4), 4.37 (t, 4H, C_5H_4), 3.90 (s, 6H, O=COCH₃), 3.79 (s, 6H, OCH₃). * is residual DCM.

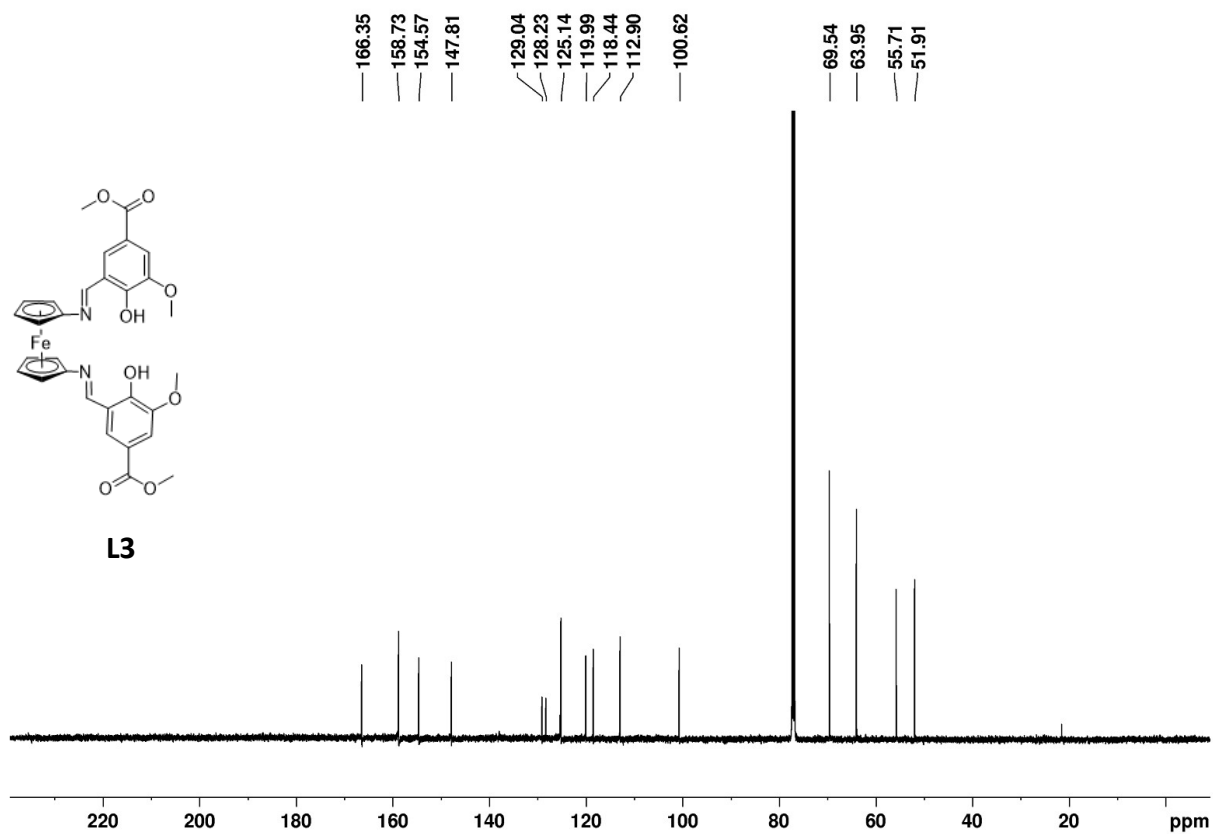


Figure C25. ^{13}C NMR (125 MHz, CDCl_3 , 25 °C) spectrum of **L3**. δ , ppm: 166.4 (C=O), 158.7 (N=C), 154.6 (COH), 147.8 (COCH₃), 129.0, 128.2, 125.1, 120.0, 118.4, 112.9, 100.6, 69.5 (C₅H₄), 63.9 (C₅H₄), 55.7 (OCH₃), 51.9 (O=COCH₃).

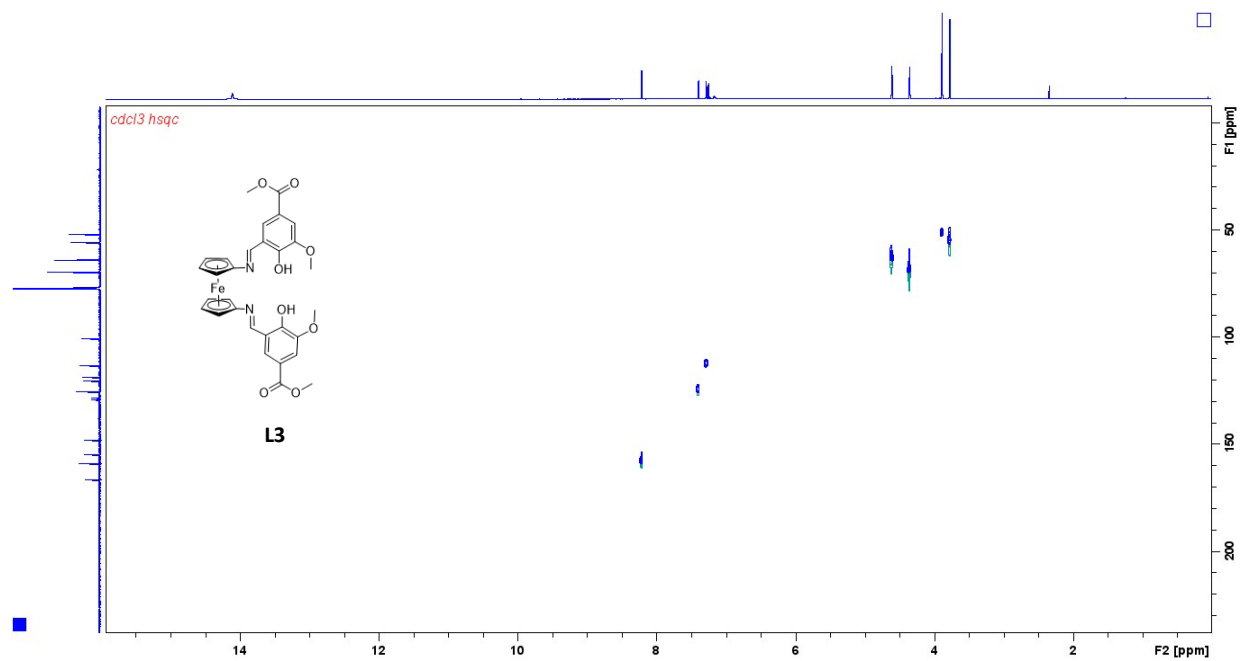


Figure C26. 2D HSQC NMR (500 MHz, CDCl_3 , 25 °C) spectrum of **L3**.

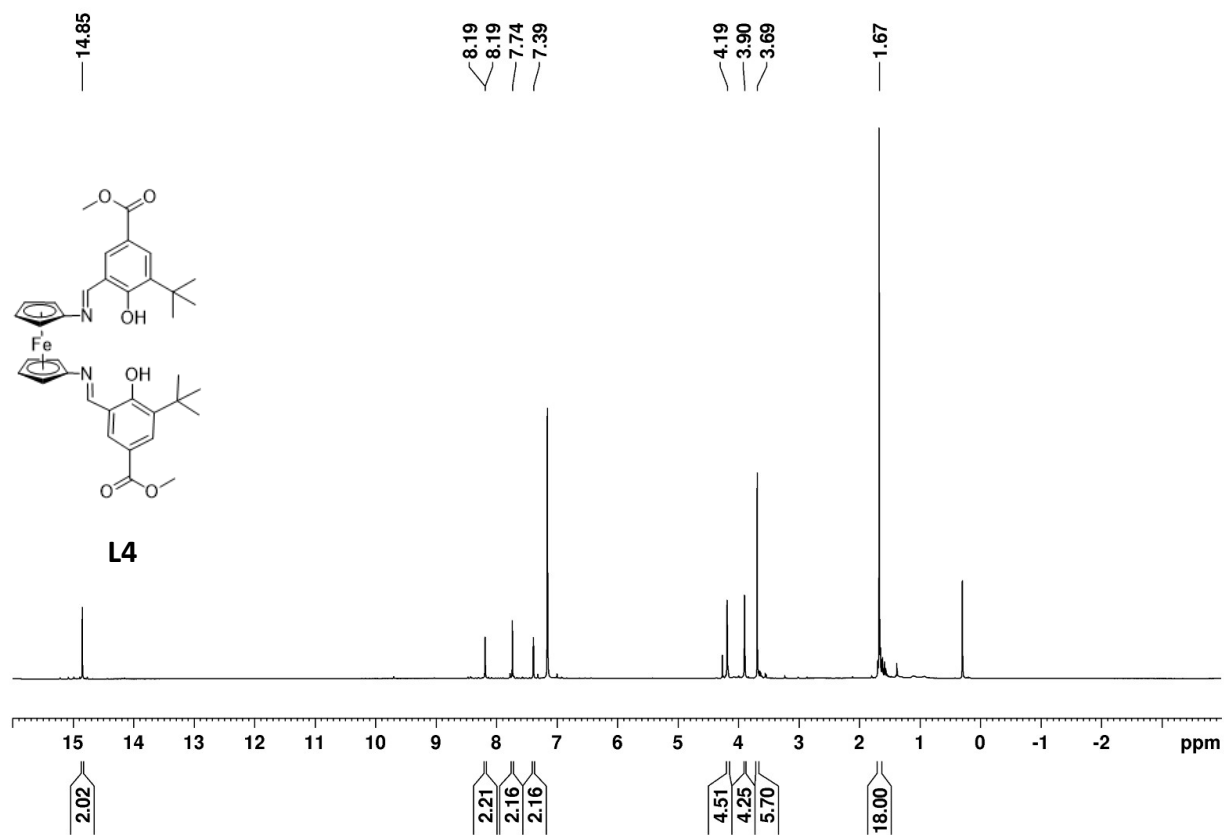


Figure C27. ^1H NMR (500 MHz, C_6D_6 , 25 $^\circ\text{C}$) spectrum of **L4**. δ , ppm: 14.85 (s, 2H, OH), 8.19 (s, 2H, N=CH), 7.74 (d, 2H, ArH), 7.39 (d, 2H, ArH), 4.19 (t, 4H, C_5H_4), 3.90 (t, 4H, C_5H_4), 3.69 (s, 6H, OCH_3), 1.67 (s, 18H, $\text{C}(\text{CH}_3)_3$).

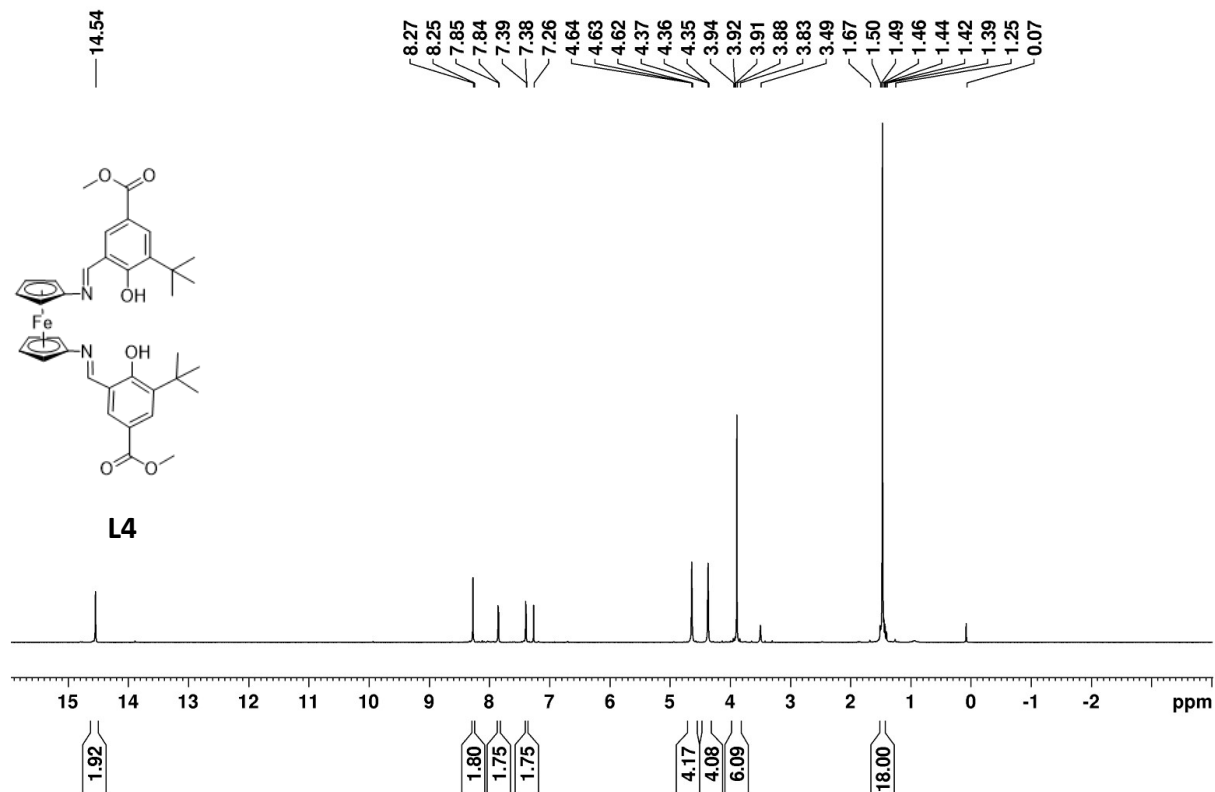


Figure C28. ^1H NMR (300 MHz, CDCl_3 , 25 $^\circ\text{C}$) spectrum of **L4**. δ , ppm: 14.54 (s, 2H, OH), 8.27 (s, 2H, N=CH), 7.85 (d, 2H, ArH), 7.39 (d, 2H, ArH), 4.64 (t, 4H, C_5H_4), 4.37 (t, 4H, C_5H_4), 3.94 (s, 6H, OCH_3), 1.46 (s, 18H, $\text{C}(\text{CH}_3)_3$). 3.49 ppm is attributed to residual methanol and 0.07 ppm is attributed to residual grease.

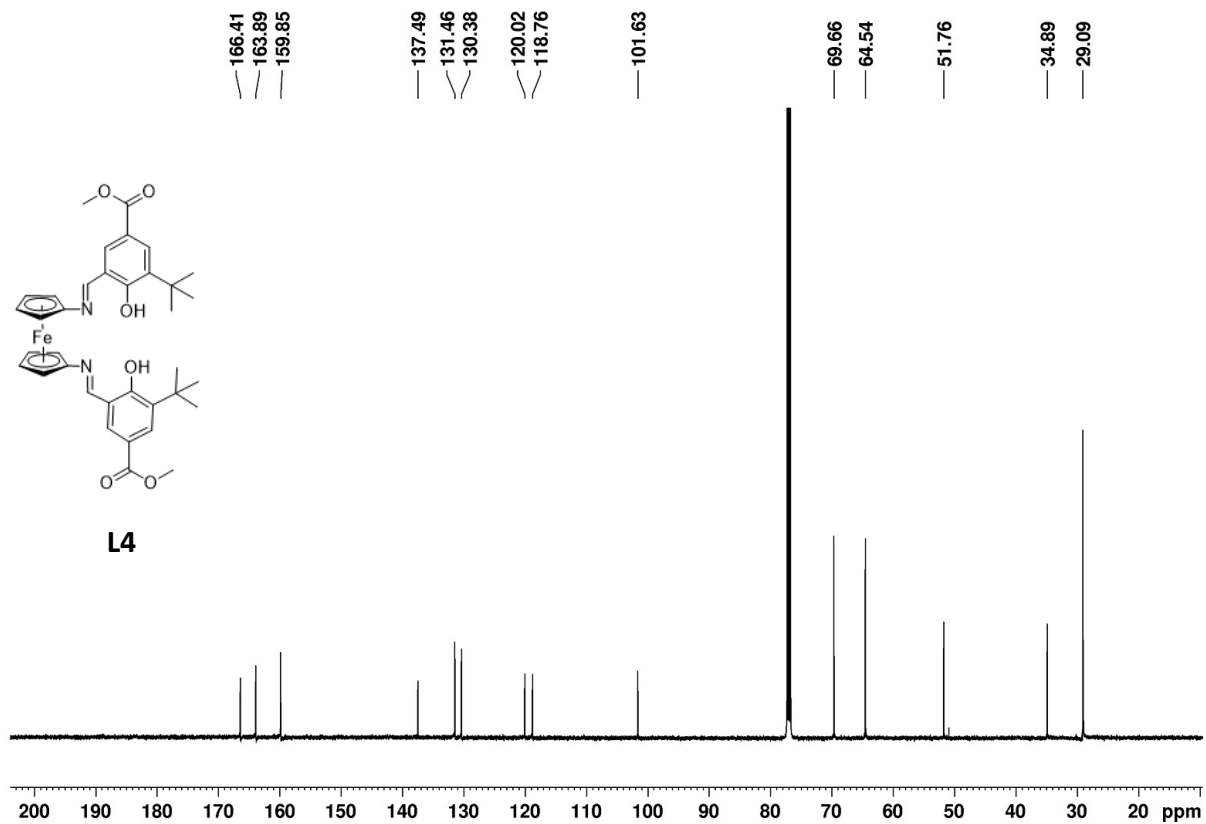


Figure C29. ^{13}C NMR (125 MHz, CDCl_3 , 25 $^\circ\text{C}$) spectrum of **L4**. δ , ppm: 166.4 ($\text{C}=\text{O}$), 163.9 (COH), 159.8 ($\text{N}=\text{C}$), 137.5, 131.5, 130.4, 120.0, 118.8, 101.6, 69.7 (C_5H_4), 64.5 (C_5H_4), 51.8 (OCH_3), 34.9 ($\text{C}(\text{CH}_3)_3$), 29.1 ($\text{C}(\text{CH}_3)_3$).

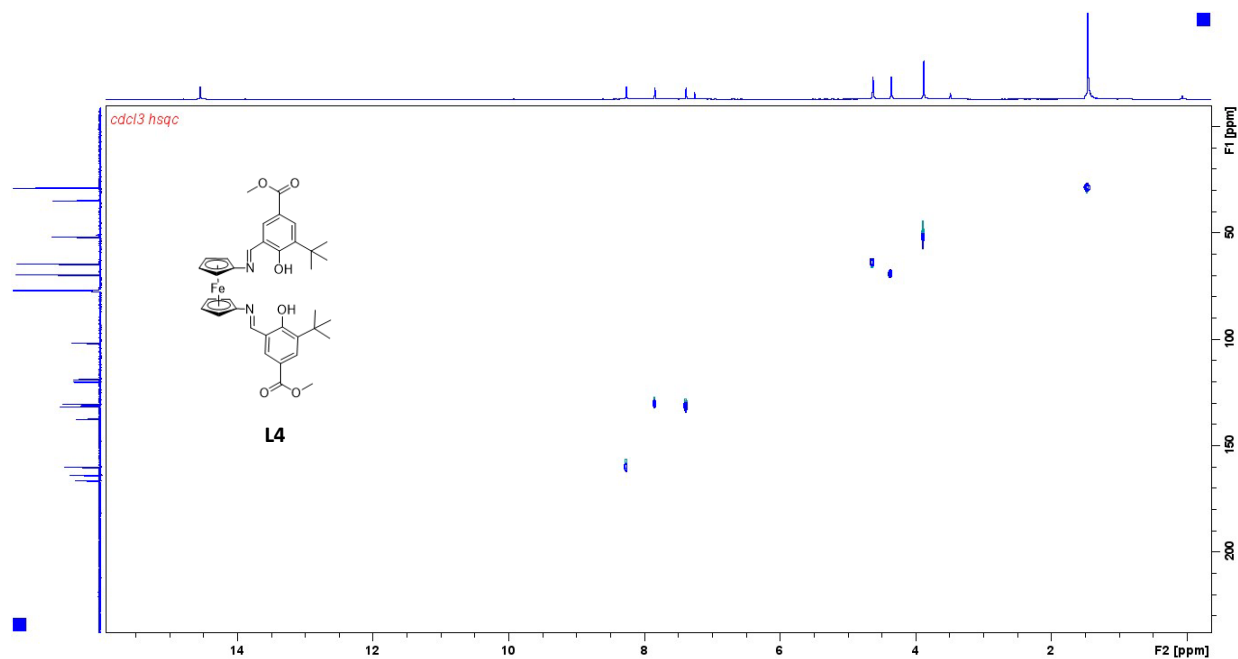


Figure C30. 2D HSQC NMR (500 MHz, CDCl_3 , 25 °C) spectrum of **L4**.

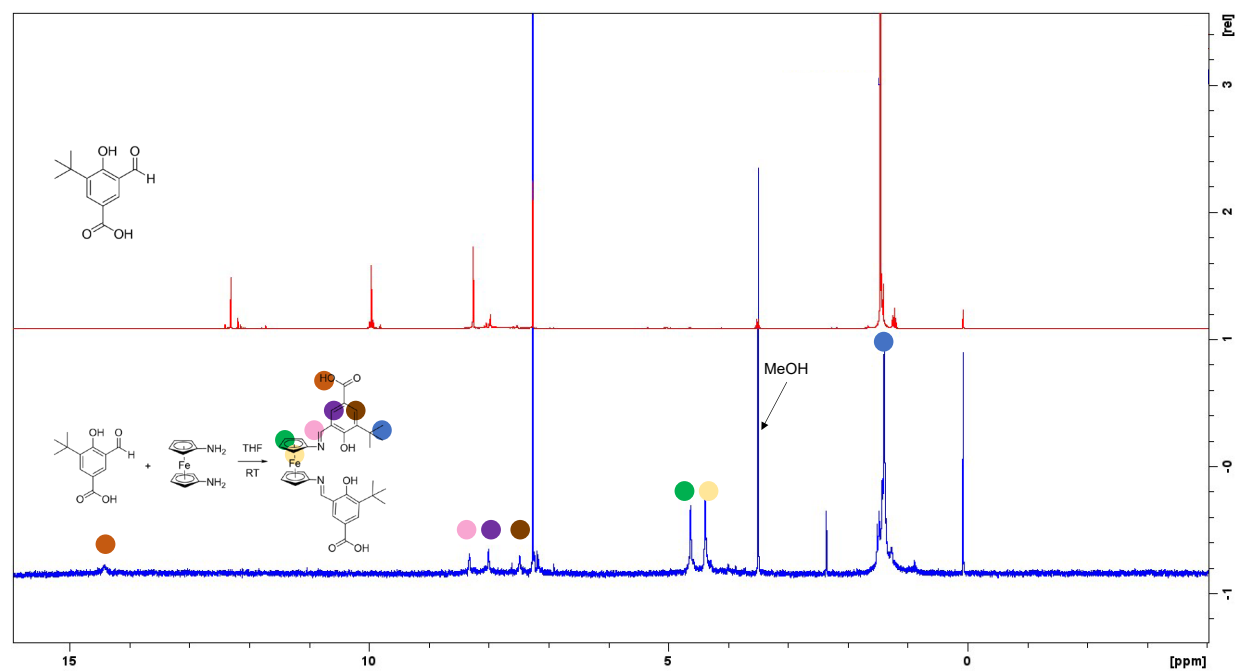


Figure C31. Overlay of ^1H NMR spectra (500 MHz, CDCl_3 , 25 °C) for the attempt to synthesize the carboxylic acid substituted salen.

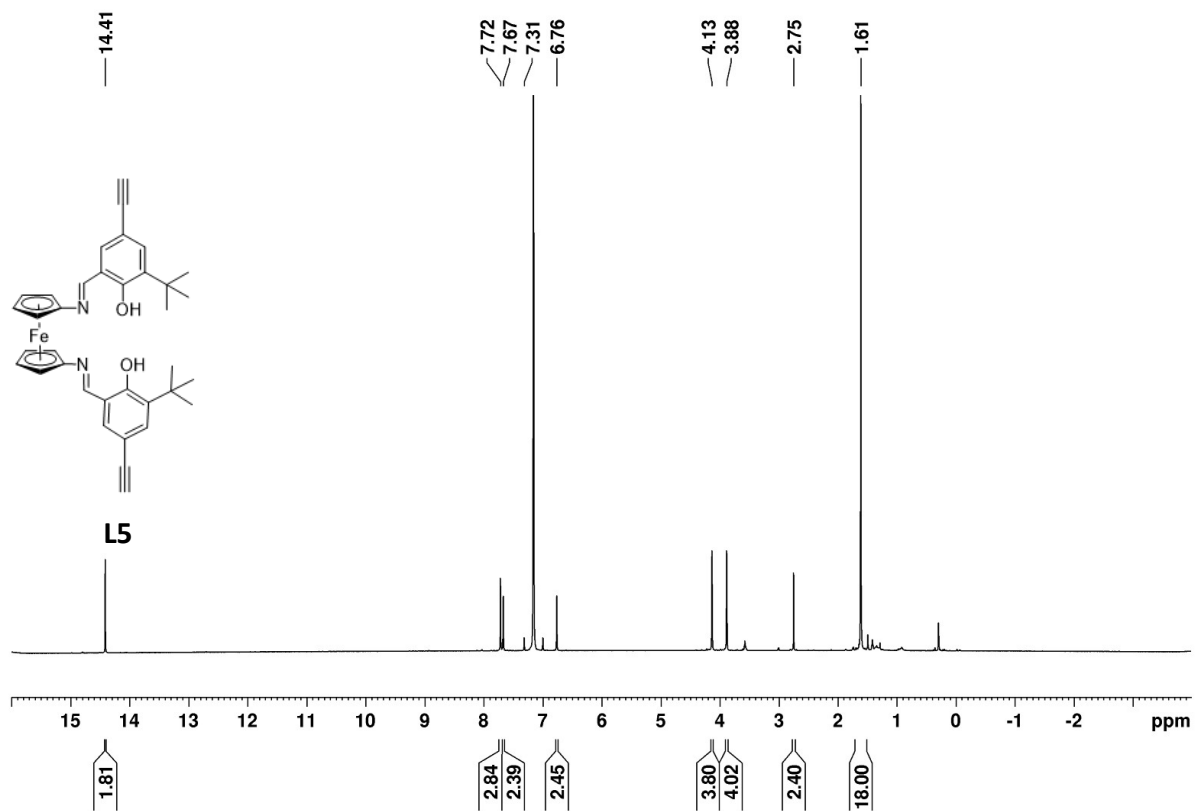


Figure C32. ^1H NMR (500 MHz, C_6D_6 , 25 $^\circ\text{C}$) spectrum of **L5**. δ , ppm: 14.41 (s, 2H, OH), 7.72 (s, 2H, N=CH), 7.67 (d, 2H, ArH), 6.76 (d, 2H, ArH), 4.13 (t, 4H, C_5H_4), 3.88 (t, 4H, C_5H_4), 2.75 (s, 2H, CCH), 1.61 (s, 18H, $\text{C}(\text{CH}_3)_3$).

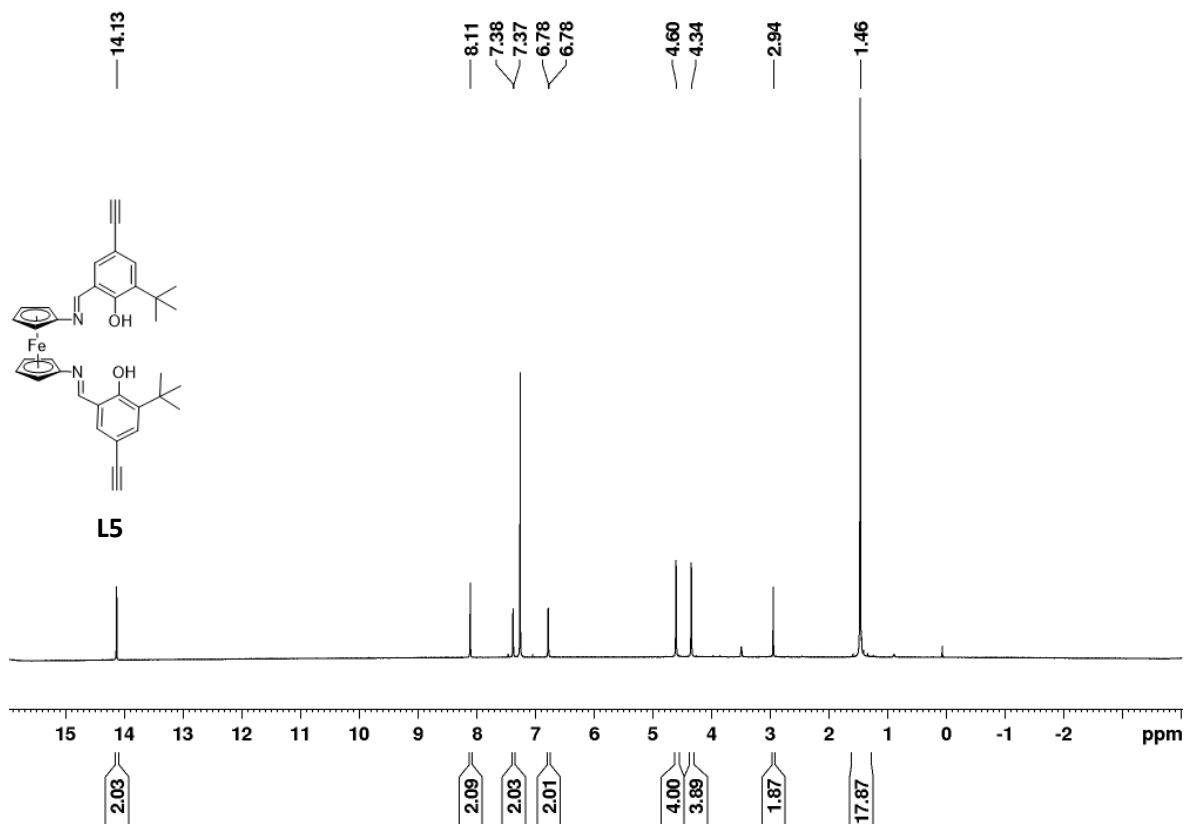


Figure C33. ^1H NMR (500 MHz, CDCl_3 , 25 $^\circ\text{C}$) spectrum of **L5**. δ , ppm: 14.13 (s, 2H, OH), 8.11 (s, 2H, N=CH), 7.38 (d, 2H, ArH), 6.78 (d, 2H, ArH), 4.60 (t, 4H, C_5H_4), 4.34 (t, 4H, C_5H_4), 2.94 (s, 2H, CCH), 1.46 (s, 18H, $\text{C}(\text{CH}_3)_3$).

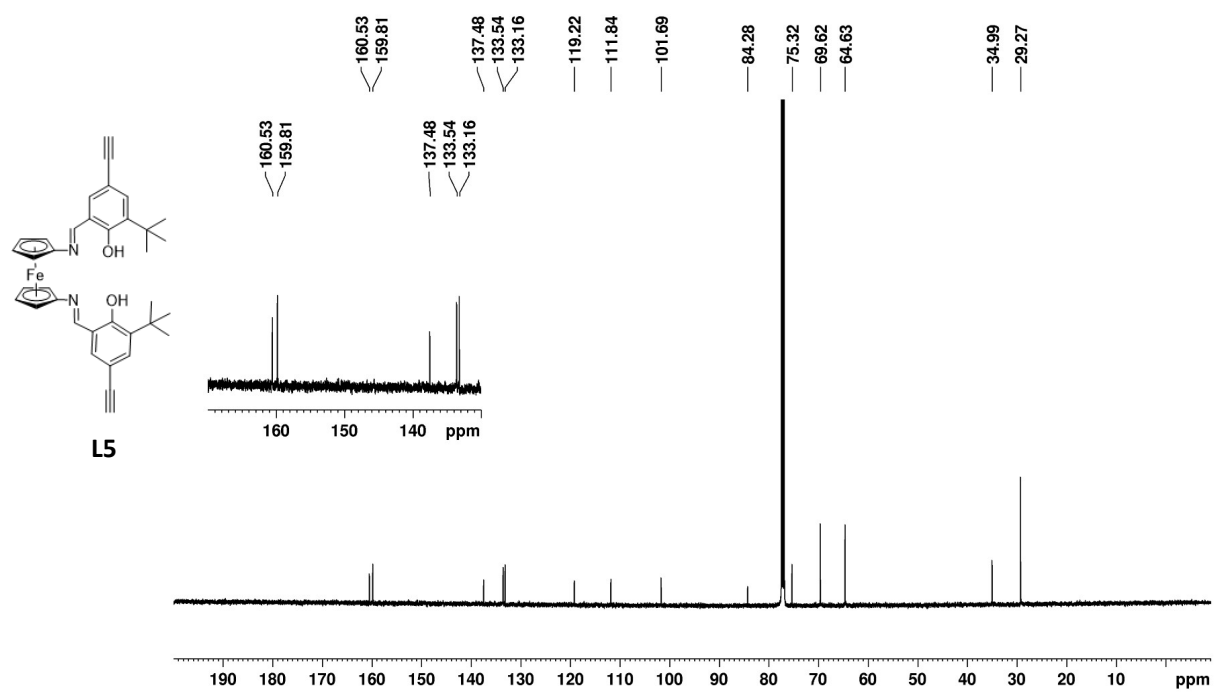


Figure C34. ^{13}C NMR (125 MHz, CDCl_3 , 25 $^\circ\text{C}$) spectrum of **L5**. δ , ppm: 160.5 (COH), 159.8 (N=C), 137.5, 133.5, 133.2, 119.2, 111.8, 101.7, 84.3 (CCH), 75.3 (CCH), 69.6 (C_5H_4), 64.6 (C_5H_4), 35.0 ($\text{C}(\text{CH}_3)_3$), 29.3 ($\text{C}(\text{CH}_3)_3$).

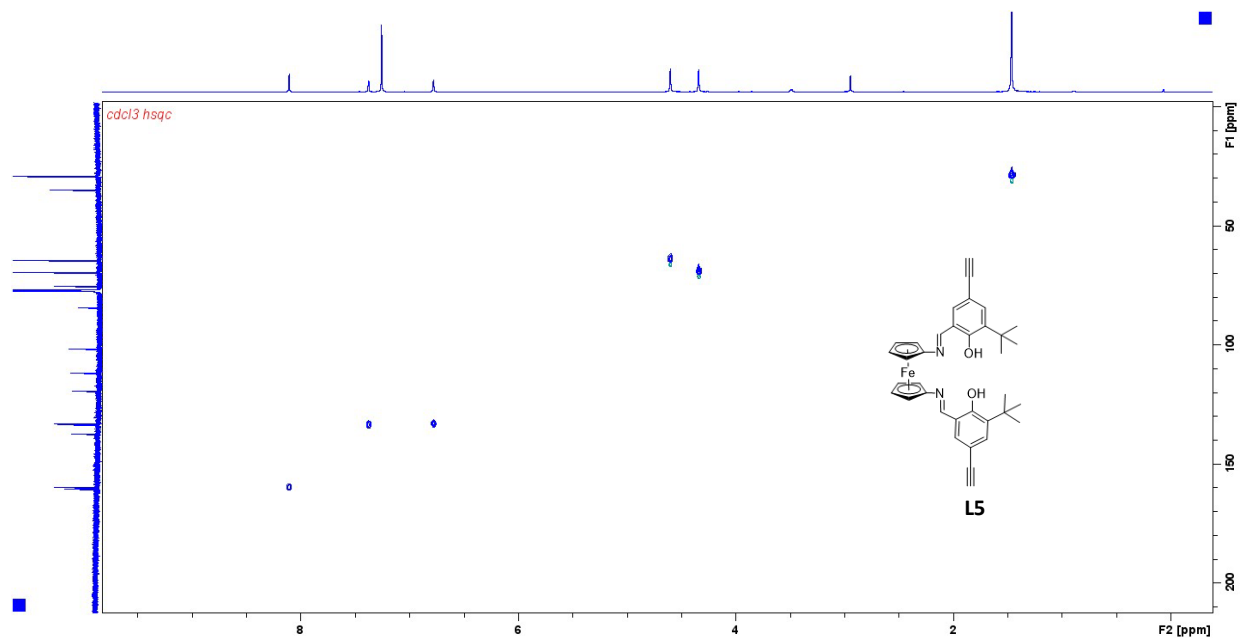


Figure C35. 2D HSQC NMR (500 MHz, CDCl_3 , 25 °C) spectrum of **L5**.

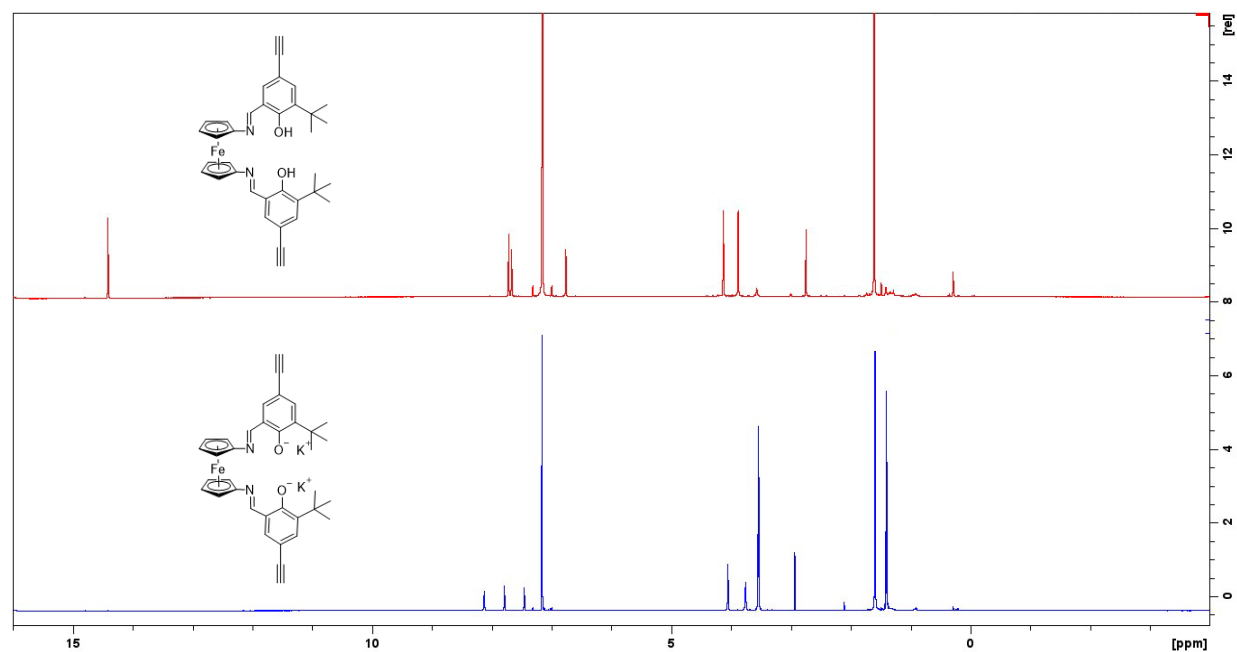


Figure C36. Overlay of ^1H HSQC NMR (500 MHz, C_6D_6 , 25 °C) spectra of **L5** (top) and deprotonated $[\text{L5}]^-\text{K}_2^+$ (bottom). Peaks at 3.57 and 1.40 ppm are attributed to residual THF.

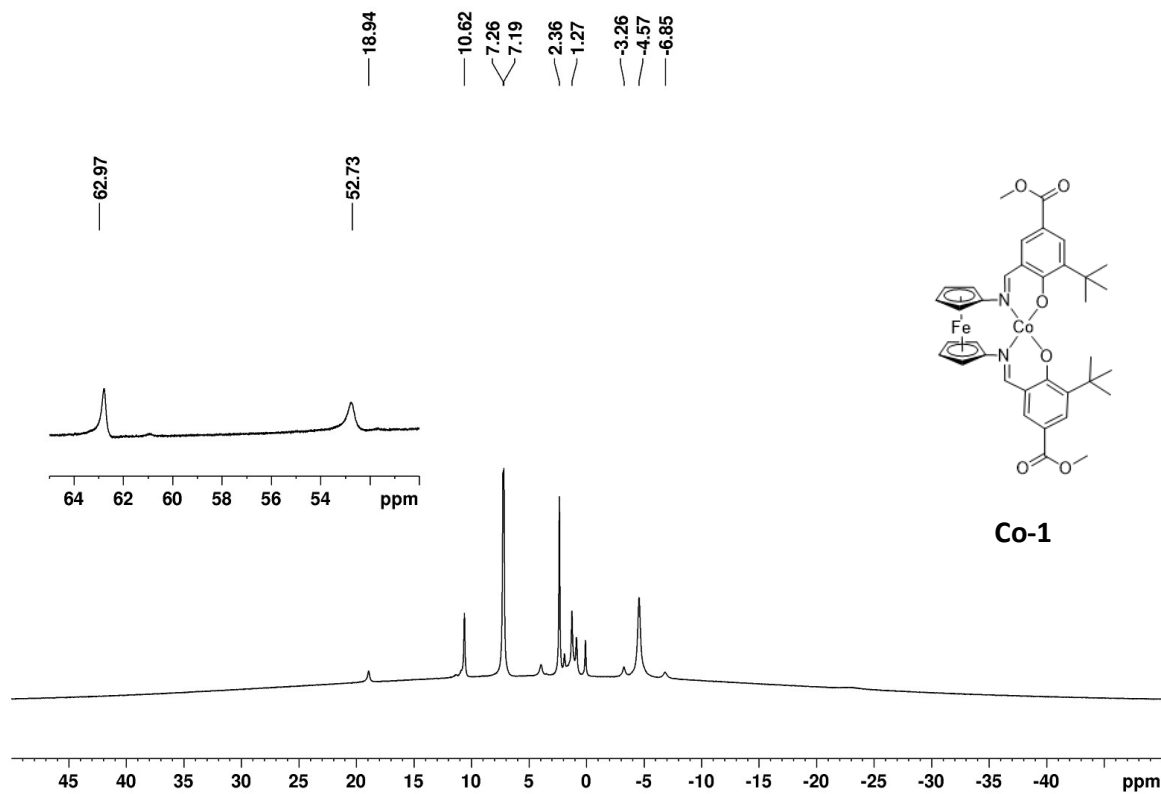


Figure C37. ¹H NMR (500 MHz, CDCl₃, 25 °C) spectrum of **Co-1**. δ, ppm: 62.97 (s, ArH), 52.73 (s, ArH), 18.94 (s, C₅H₄), 10.62 (s, C₅H₄), -3.26 (s, N=CH), -4.57 (s, C(CH₃)₃), -6.85 (s, OCH₃). Peaks at 2.36 and 7.19 ppm are attributed to residual toluene. Peaks at 1.27 and 0.83 ppm are attributed to residual hexanes.

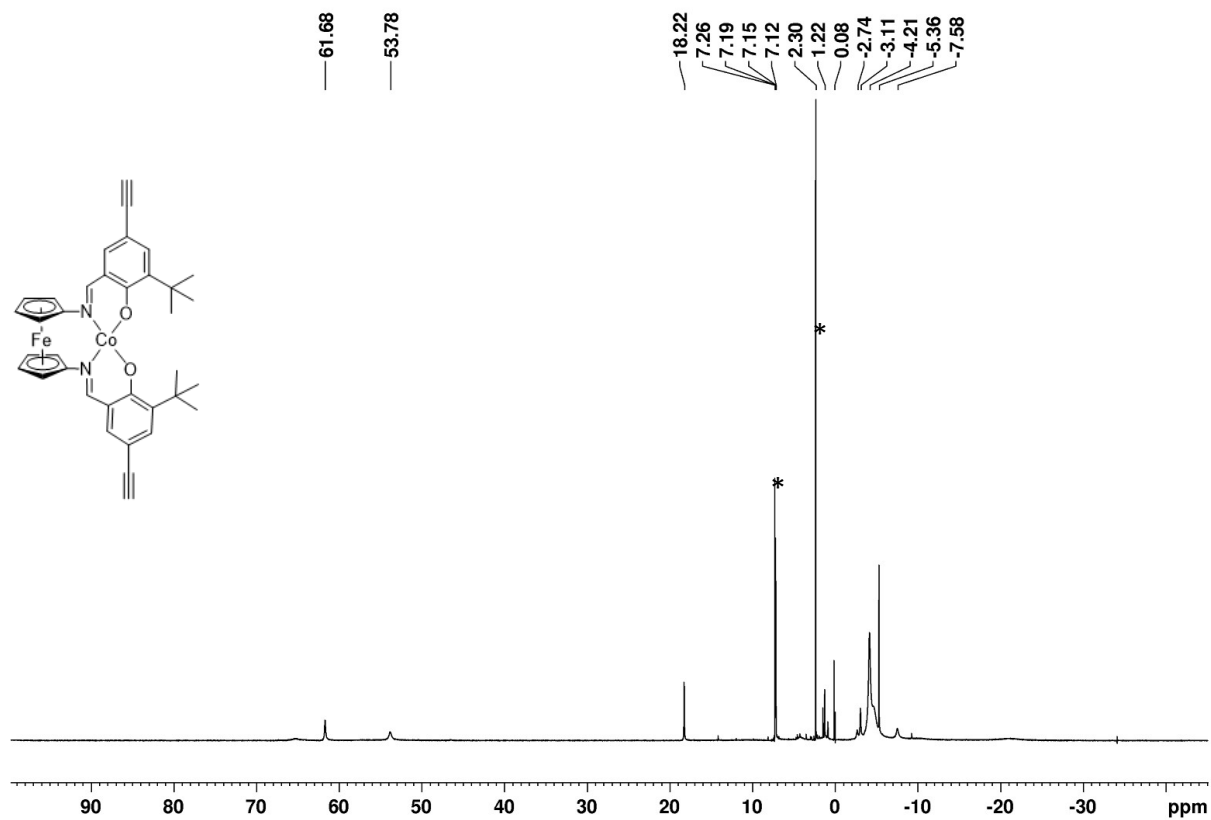


Figure C38. ^1H NMR (500 MHz, CDCl_3 , 25 $^\circ\text{C}$) spectrum of **Co-2**. δ , ppm: 61.68 (s, ArH), 53.78 (s, ArH), 18.22 (s, C_5H_4), -2.74 (s, C_5H_4), -3.11 (s, $\text{C}(\text{CH}_3)_3$), -4.21 (s, $\text{C}(\text{CH}_3)_3$), -5.36 (s, CCH), -7.58 (s, N=CH). *residual toluene.

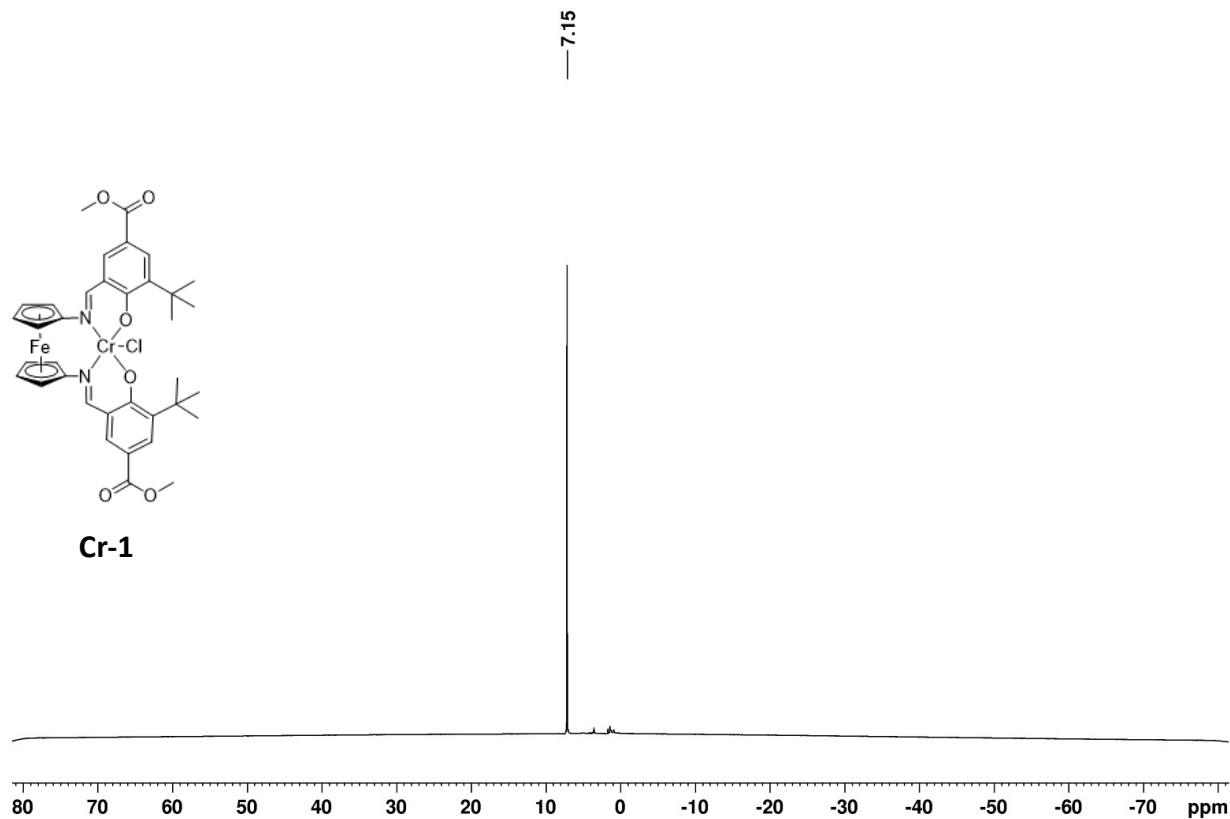


Figure C39. ¹H NMR (500 MHz, C₆D₆, 25 °C) spectrum of **Cr-1**.

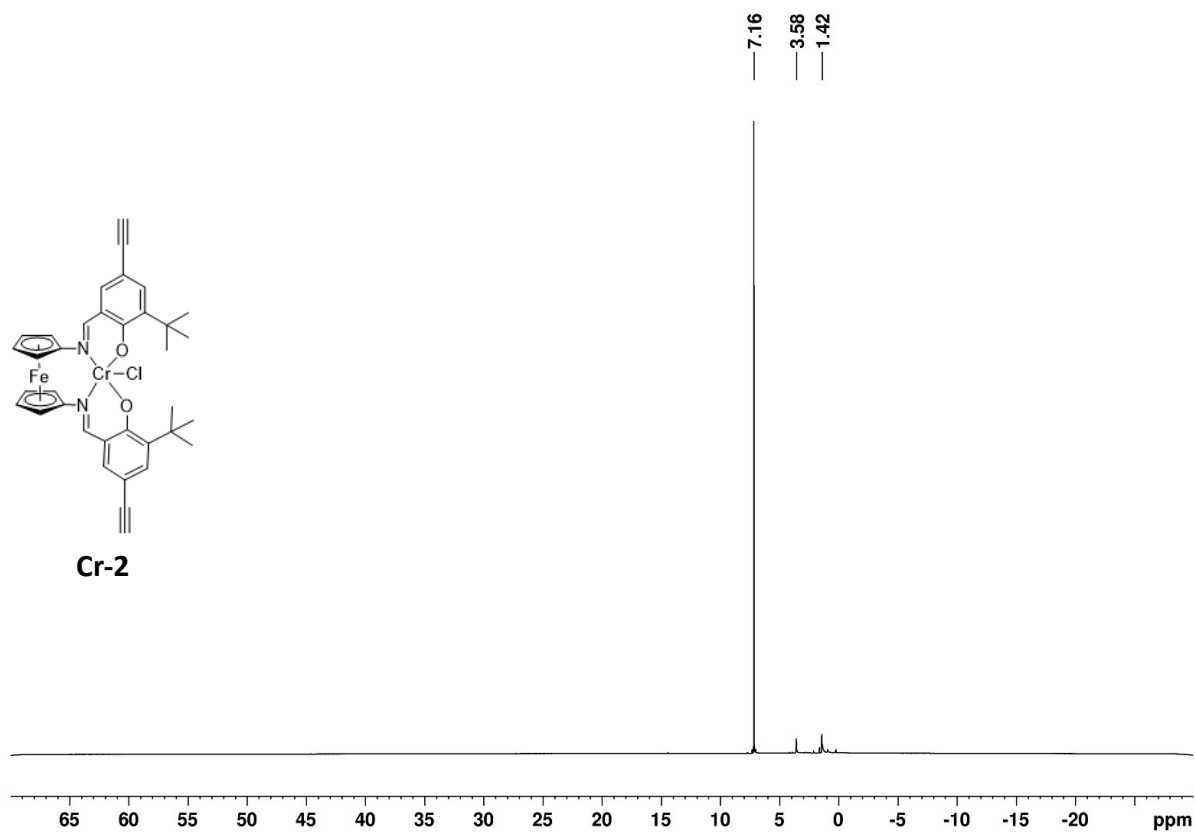


Figure C40. ¹H NMR (500 MHz, C₆D₆, 25 °C) spectrum of **Cr-2**.

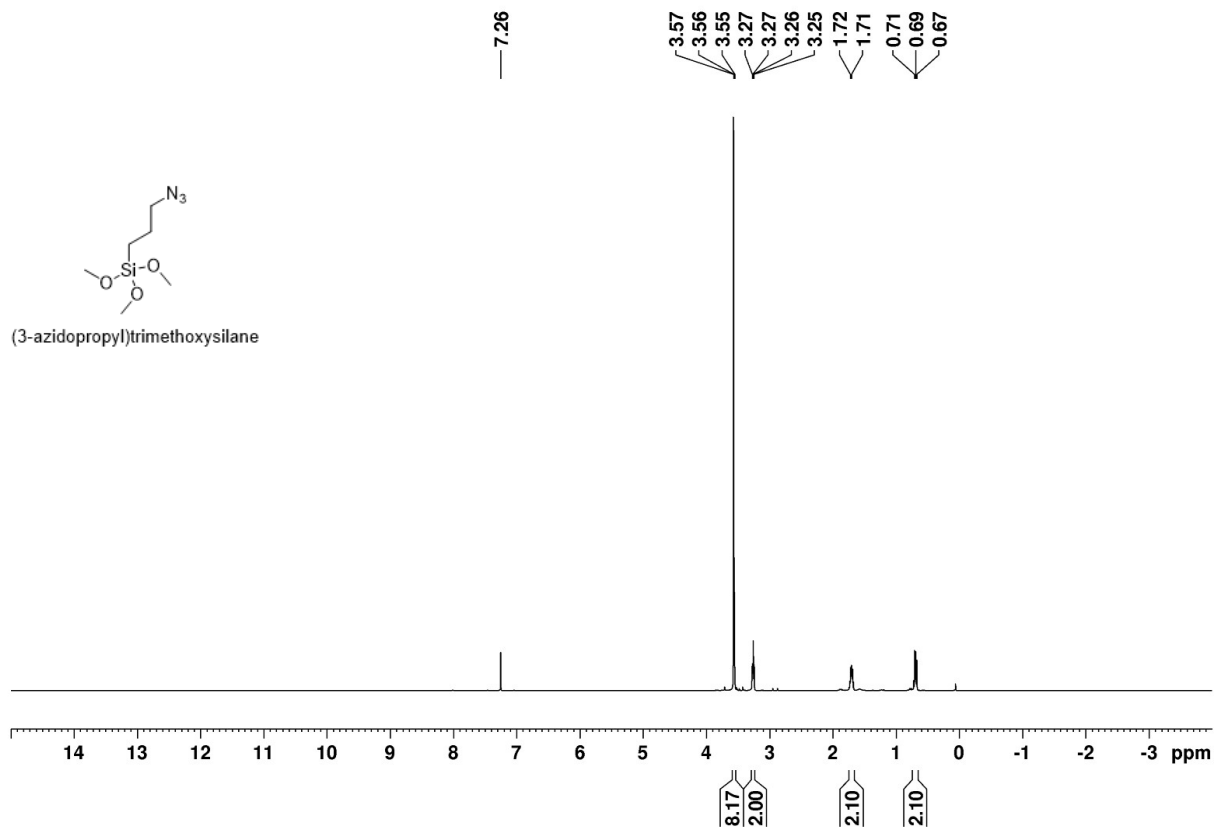


Figure C41. ^1H NMR (500 MHz, CDCl_3 , 25 $^\circ\text{C}$) spectrum of (3-azidopropyl)trimethoxysilane. δ , ppm: 3.57 (s, 9H, $\text{Si}(\text{OCH}_3)_3$), 3.27 (t, 2H, $\text{SiCH}_2\text{CH}_2\text{CH}_2\text{N}_3$), 1.72 (m, 2H, $\text{SiCH}_2\text{CH}_2\text{CH}_2\text{N}_3$), 0.71 (m, 2H, $\text{SiCH}_2\text{CH}_2\text{CH}_2\text{N}_3$).

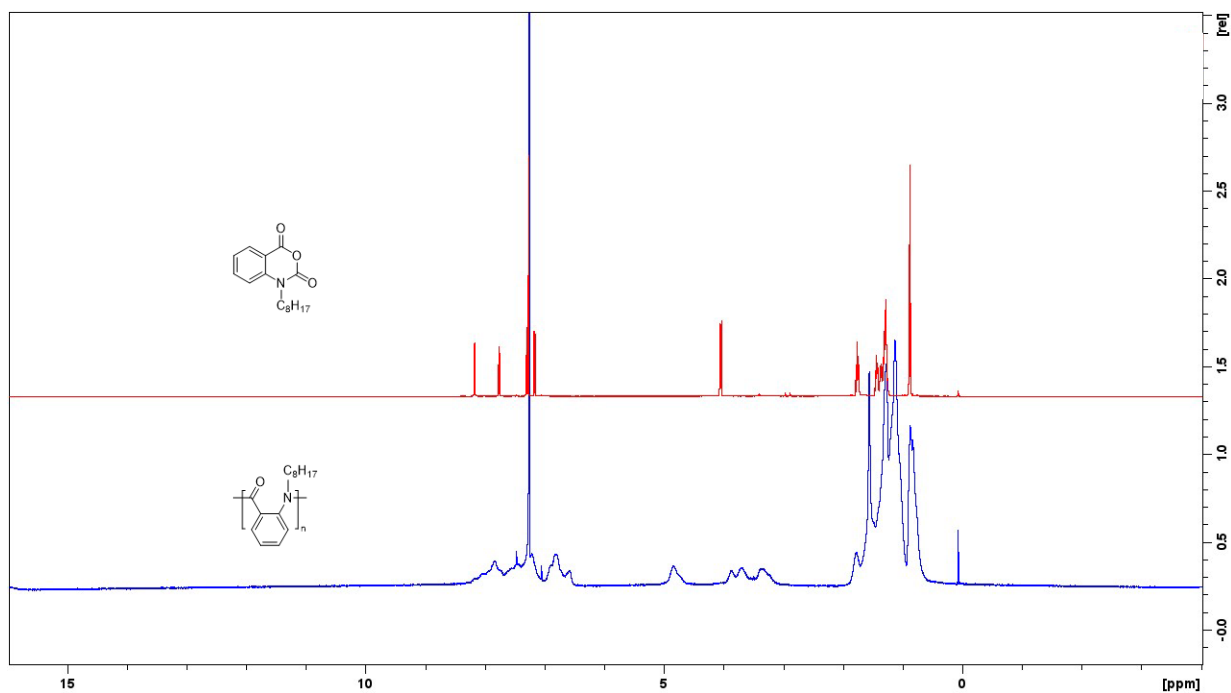


Figure C42. Overlay of ¹H NMR (300 MHz, CDCl₃, 25 °C) spectra of 6-NCA-C₈H₁₇ (top) and poly(6-NCA-C₈H₁₇) (bottom).

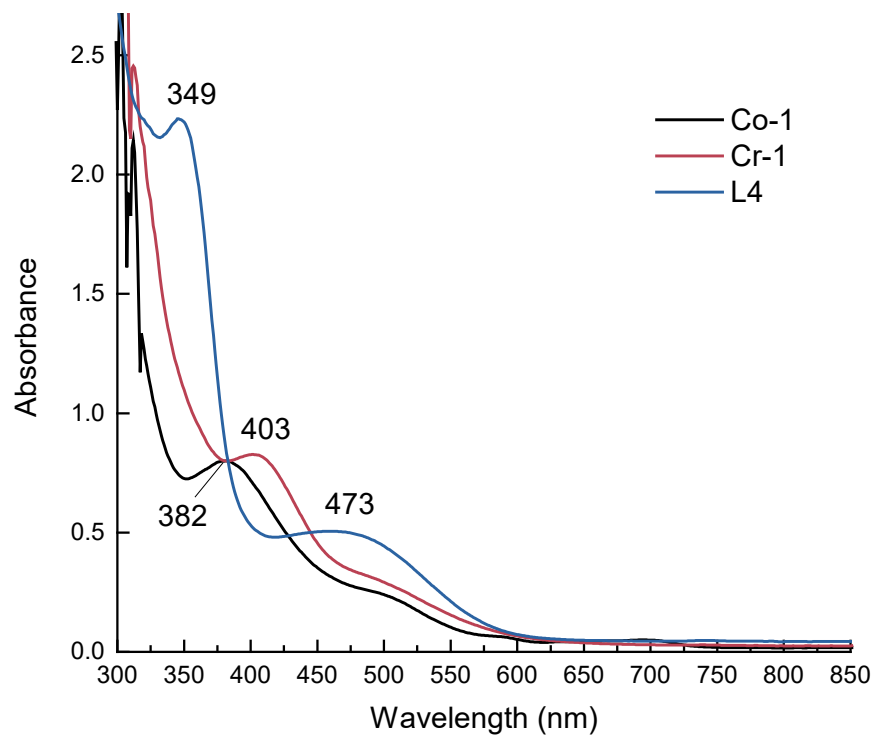


Figure C43. Normalized UV-Vis spectra of **Co-1** (black), **Cr-1** (red), **L4** (blue).

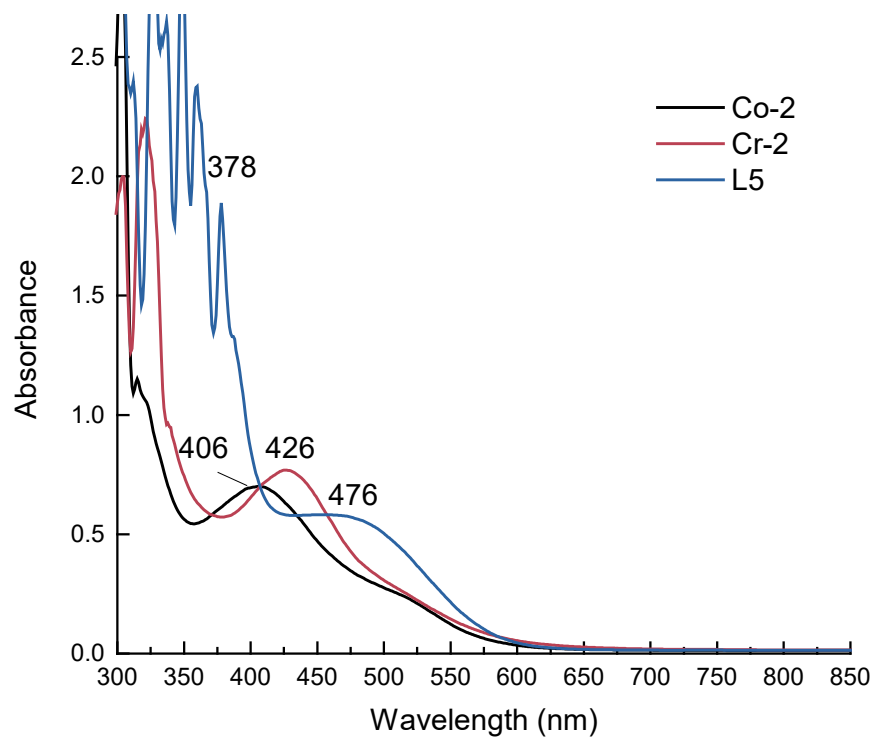


Figure C44. Normalized UV-Vis spectra of **Co-2** (black), **Cr-2** (red), **L5** (blue).

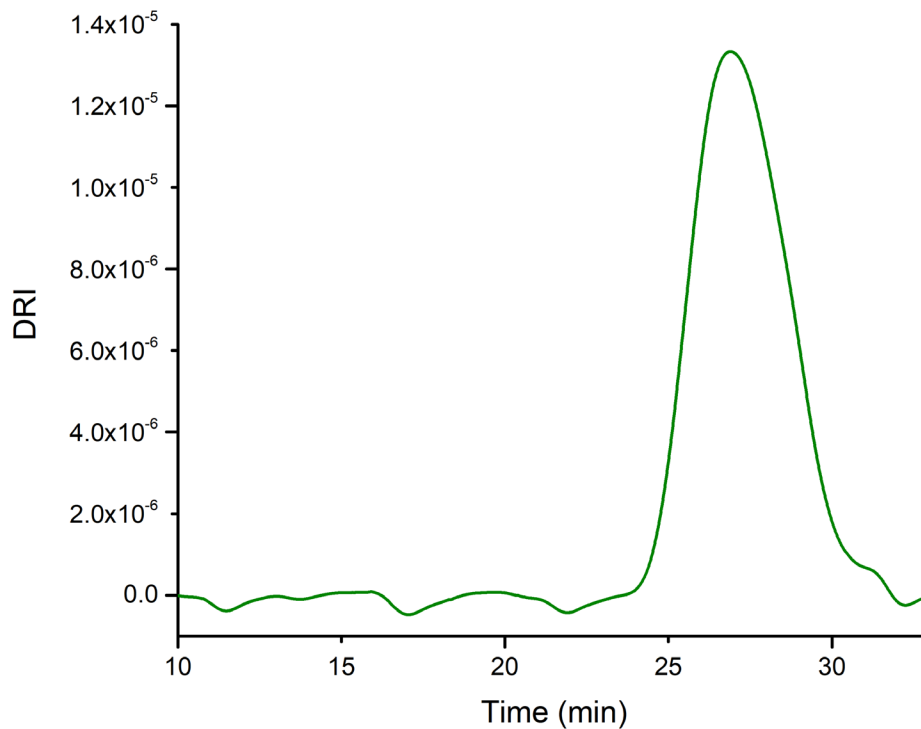


Figure C45. SEC trace of poly(6-NCA-C₈H₁₇) for **Table 5.2**, entry 1.

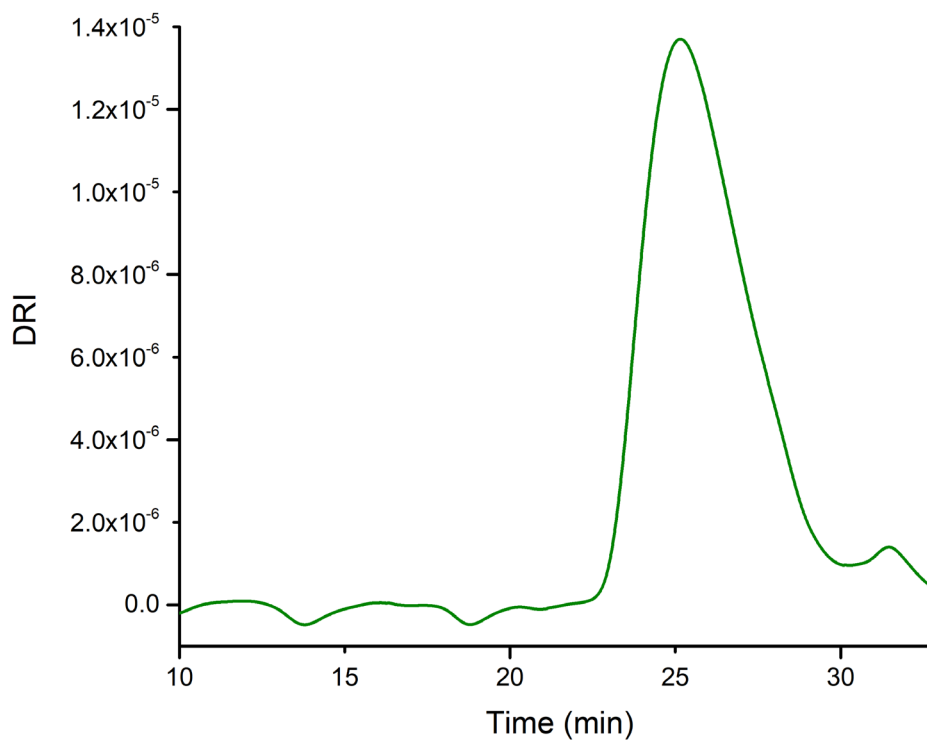


Figure C46. SEC trace of poly(6-NCA-C₈H₁₇) for **Table 5.2**, entry 3.

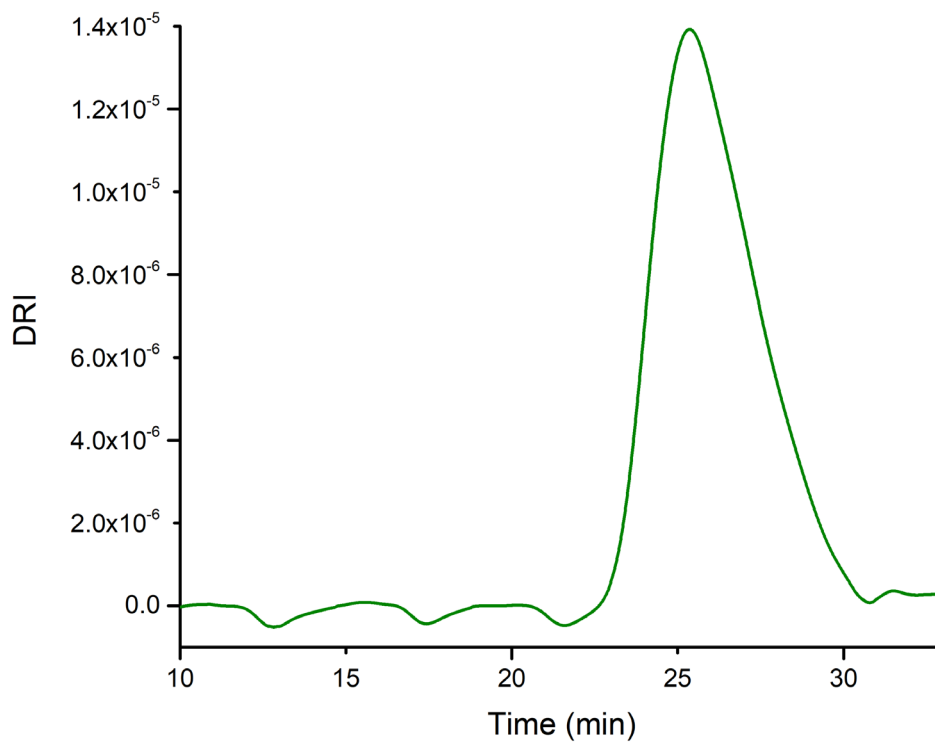


Figure C47. SEC trace of poly(6-NCA-C₈H₁₇) for **Table 5.2**, entry 2.

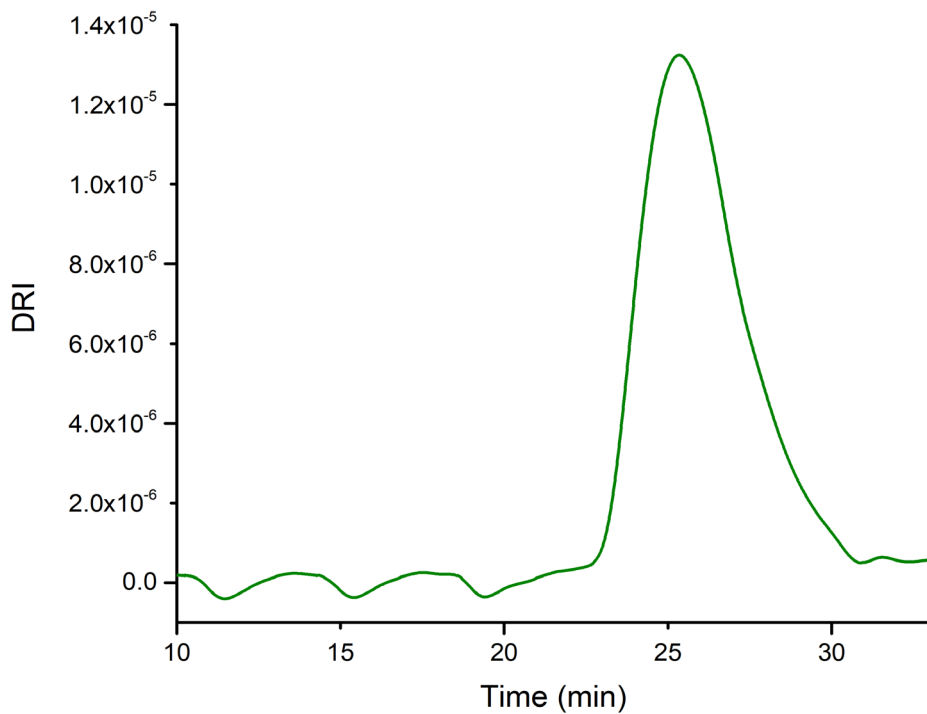


Figure C48. SEC trace of poly(6-NCA-C₈H₁₇) for **Table 5.2**, entry 4.

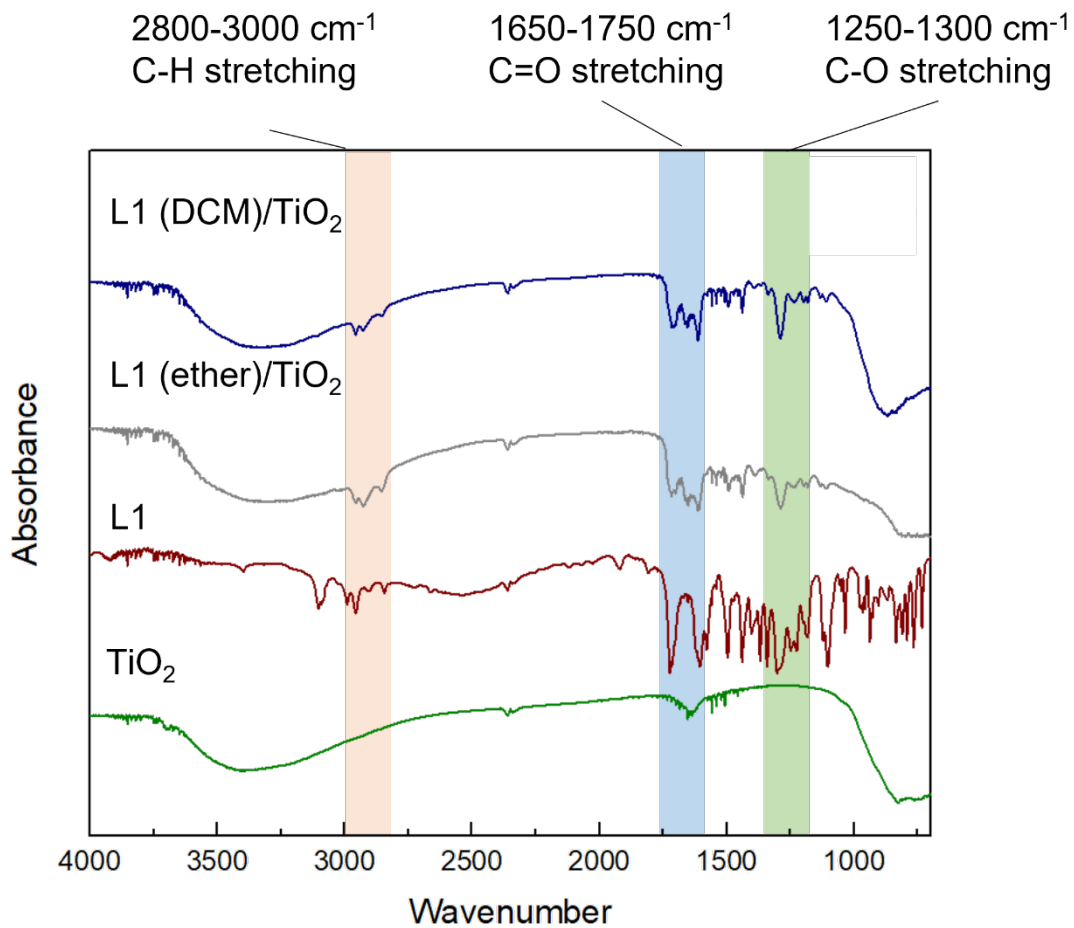


Figure C49. IR spectra of TiO₂ nanoparticles (green), L1 (brown), L1 immobilized TiO₂ nanoparticles using diethyl ether as solvent (gray), and DCM as solvent (gray).

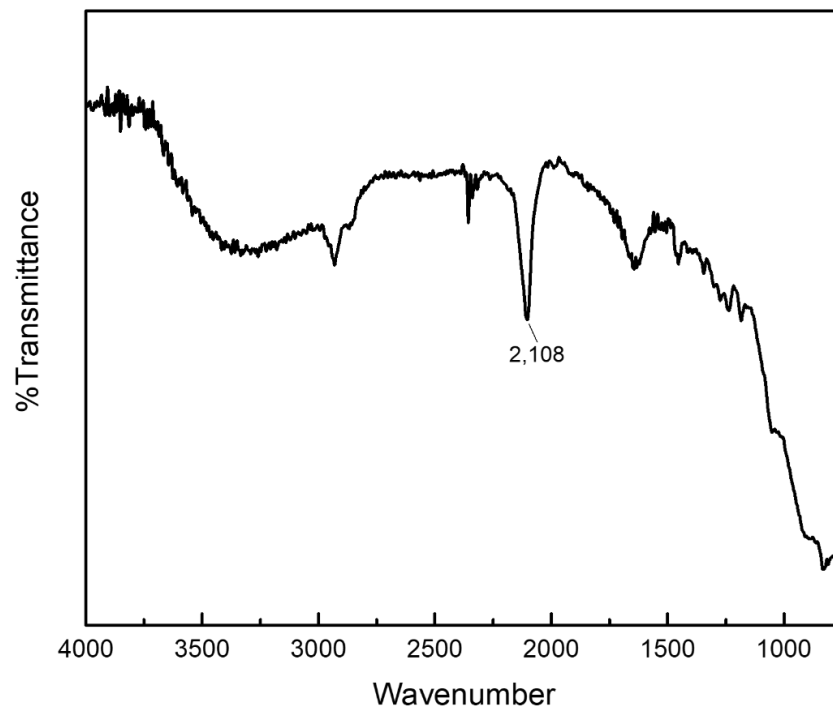


Figure C50. IR spectrum of (3-azidopropyl)trimethoxysilane functionalized TiO₂ nanoparticles.

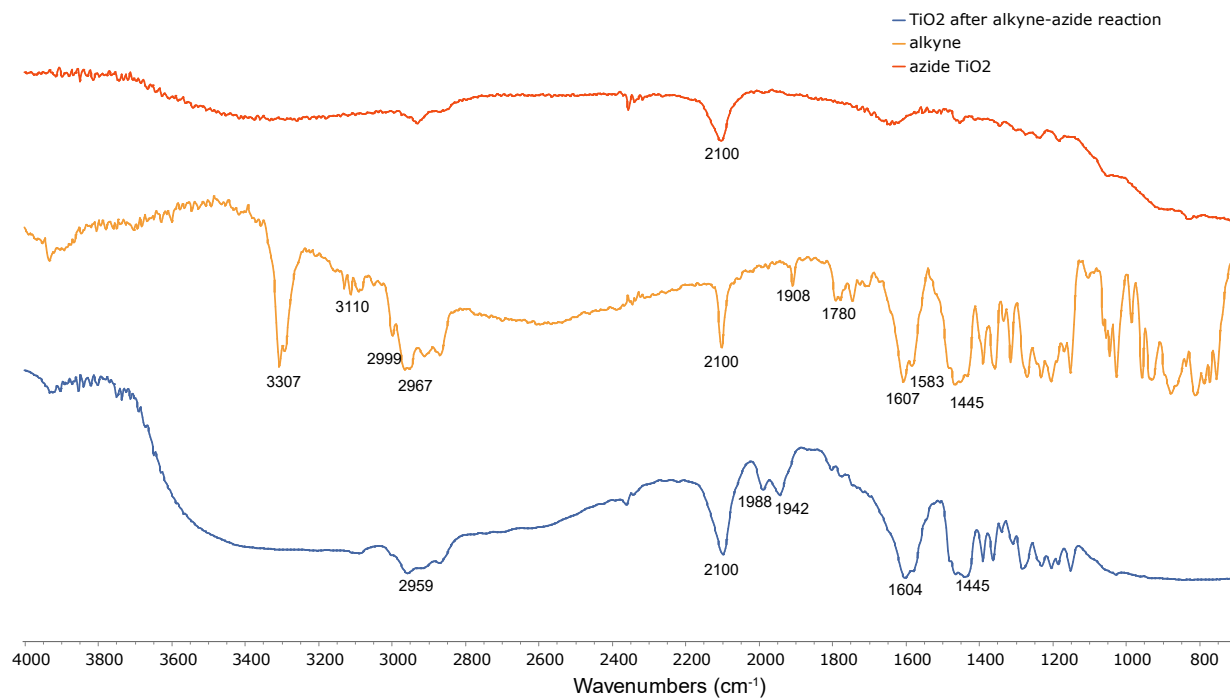


Figure C51. IR spectra of (3-azidopropyl)trimethoxysilane functionalized TiO₂ nanoparticles (azide/TiO₂, red), L5 (yellow) and L5 immobilized TiO₂ nanoparticles through

“click” reaction (**L5/TiO₂**, blue).

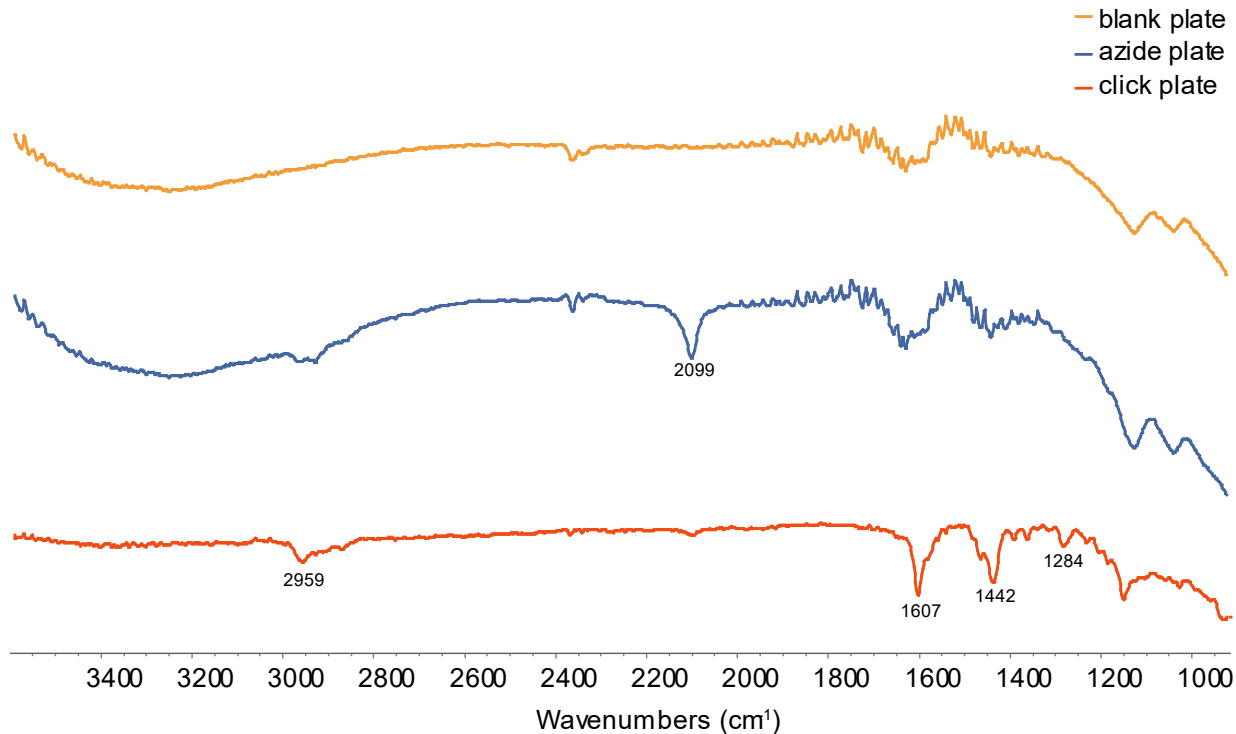


Figure C52. IR spectra of TiO₂ coated FTO plate (**TiO₂/FTO**, yellow), (3-azidopropyl)trimethoxysilane functionalized TiO₂ coated FTO plate (**azide/TiO₂/FTO**, blue), and **L5** immobilized TiO₂ coated FTO plate through “click” reaction (**L5/TiO₂/FTO**, red).

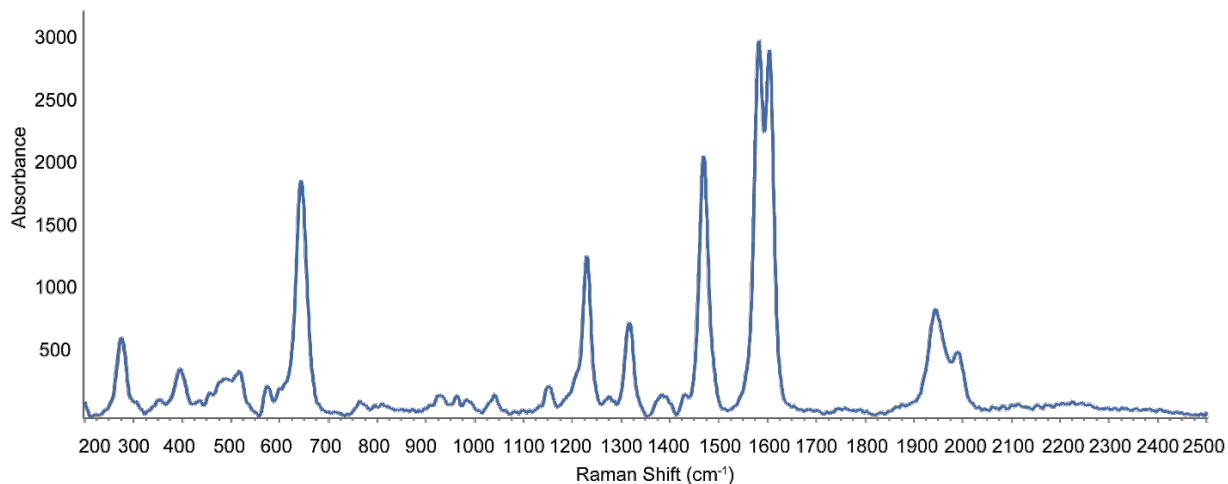


Figure C53. Raman spectrum of **L5** immobilized TiO₂ nanoparticles through “click” reaction.

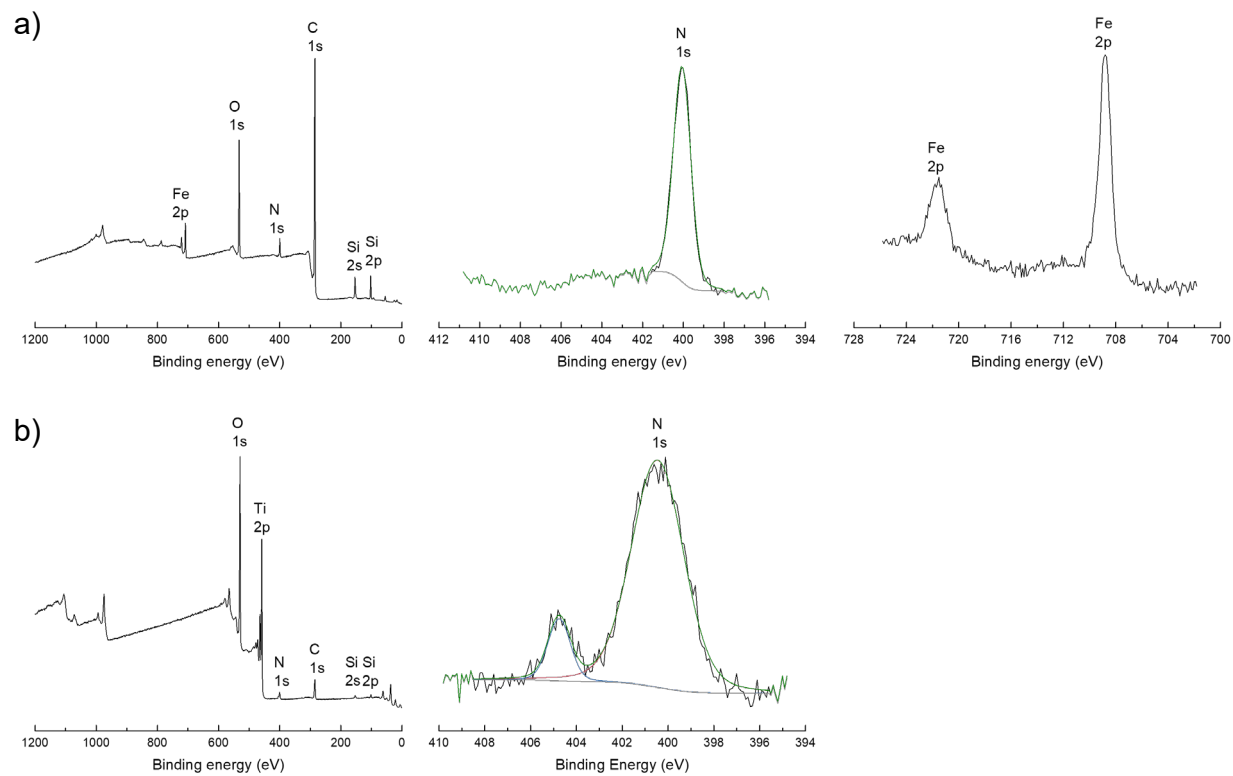


Figure C54. XPS spectra of (a) L5, and (b) (3-azidopropyl)trimethoxysilane functionalized TiO₂ nanoparticles (azide/TiO₂).

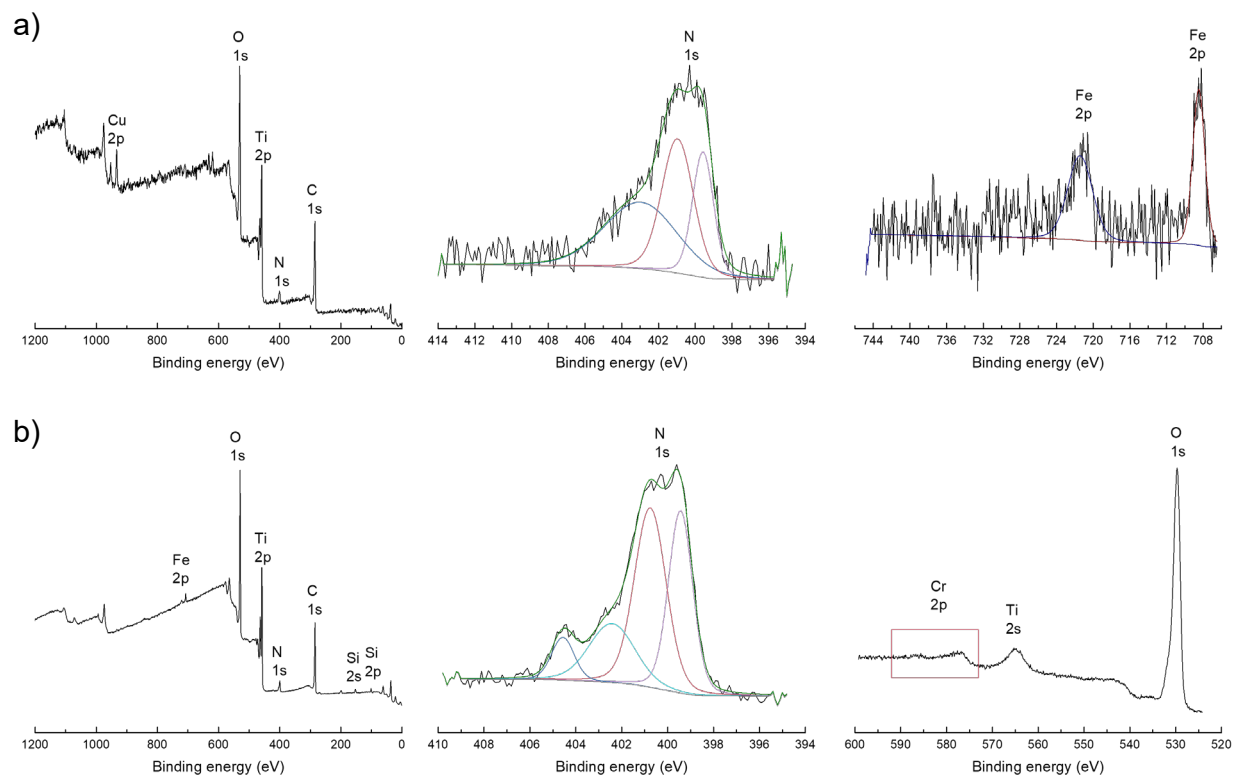


Figure C55. XPS spectra of (a) L5 immobilized TiO₂ nanoparticles through “click” reaction (L5/TiO₂) and (b) Cr-2 immobilized TiO₂ nanoparticles through “click” reaction (Cr-2/TiO₂)

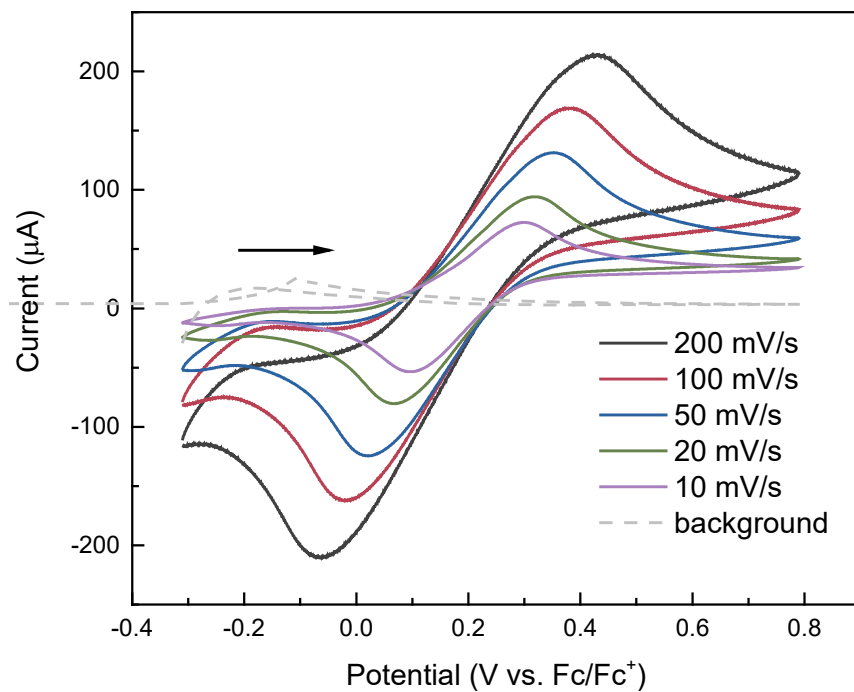


Figure C56. Cyclic voltammograms of L5 in *o*-DFB (1 mM L5, 100 mM TBAPF₆).

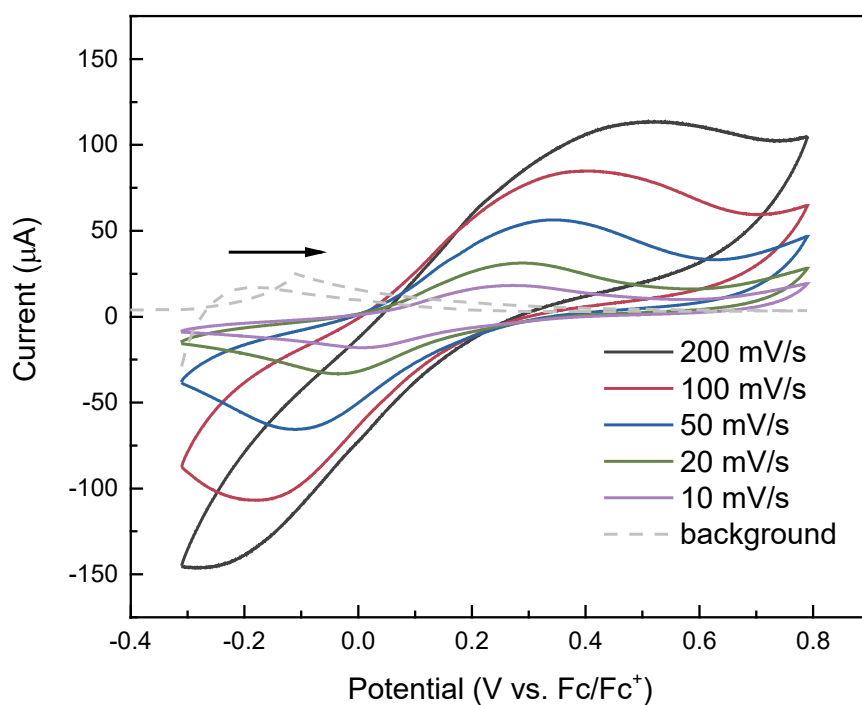


Figure C57. Cyclic voltammograms of L5 immobilized TiO₂ coated FTO plate through “click” reaction (L5/TiO₂/FTO, working electrode) in *o*-DFB (100 mM TBAPF₆).

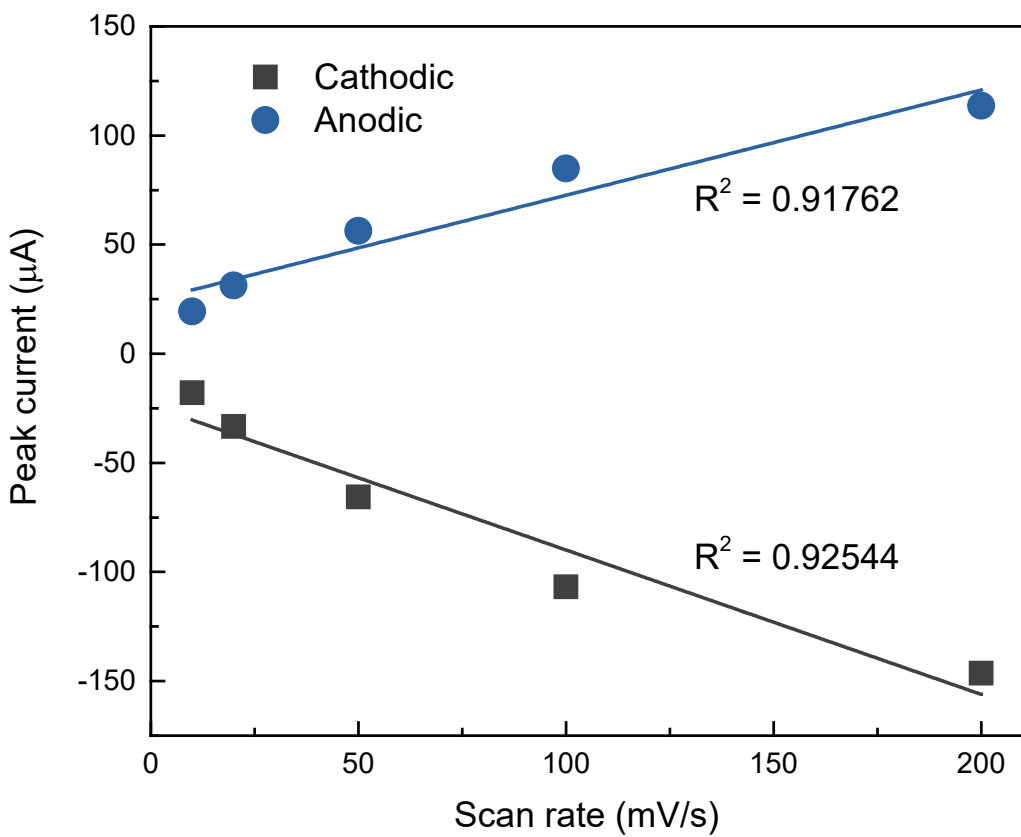
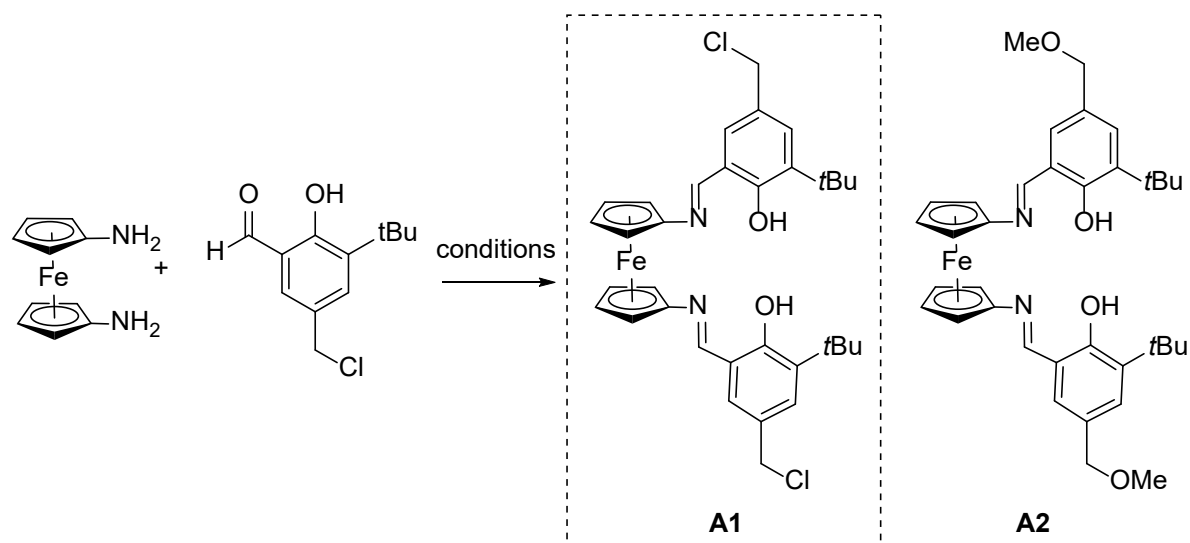


Figure C58. Peak current vs scan rate.

Table C1. Attempts to synthesize salfen derivatives with alkyl substitution.



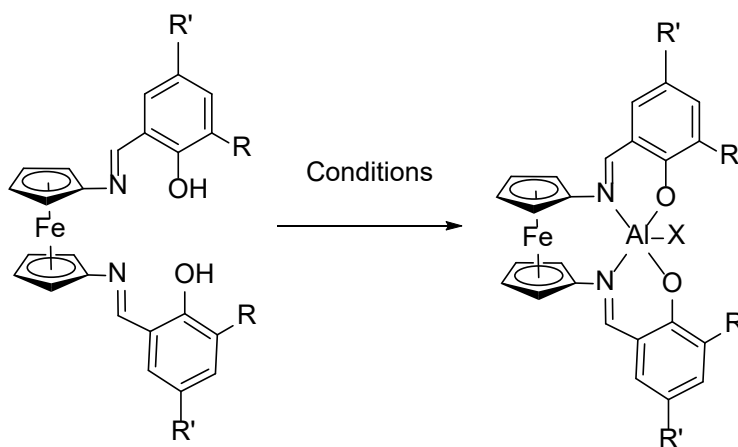
Entry ^a	Solvent	Acid	Sieves	Results ^c
1	MeOH	N/A	No	3-(<i>tert</i> -butyl)-5-(methoxymethyl)-2-hydroxybenzaldehyde
2	C ₆ D ₆	N/A	No	No reaction
3	DCM	N/A	Yes	No reaction
4 ^b	MeOH	HCl	Yes	A2
5 ^b	DCM	HCl	Yes	No reaction
6 ^b	Ether	HCl	Yes	No reaction
7	THF	N/A	Yes	No reaction
8	DCM/MeCN 1:1	N/A	Yes	No reaction
9 ^b	DCM/MeCN 1:1	HCl	Yes	No reaction

a. All reactions were carried out with 1 equivalent of 1,1'-diaminoferrrocene which was added to a stirring solution of 2 equivalents of 3-(*tert*-butyl)-5-(chloromethyl)-2-hydroxybenzaldehyde in the specified solvent/solvent combination and stirred overnight at room temperature. Precipitates were isolated on top of a medium frit if formed.

b. HCl (0.8 equiv., 2.0 M in diethyl ether) was added to the aldehyde before the addition of 1,1'-diaminoferrocene.

c. The reactions were analyzed by ^1H NMR spectroscopy.

Table C2. Attempts to synthesize alumina complex supported by **L1-3** or **L5**.



Entry ^a	R	R'	X	Solvent	T (°C)	Time	Results ^c
1	H	COOMe	OiPr	Toluene	80	2 days	Messy
2	H	COOMe	OiPr	Toluene/DCM	80	2 days	Messy
3	H	COOMe	OiPr	Toluene	RT	3 days	Messy
4	H	COOMe	OiPr	Toluene	80	3.5 h	Messy
5	MeO	COOMe	OiPr	Toluene	RT	16 h	No reaction
6	MeO	COOMe	OiPr	Toluene	60	34 h	Messy
7	MeO	COOMe	OiPr	C ₆ D ₆	RT	20 h	No reaction
8	MeO	COOMe	OiPr	C ₆ D ₆	40	overnight	Messy
9	MeO	COOMe	OiPr	CDCl ₃	RT	20 h	No reaction
10	MeO	COOMe	OiPr	CDCl ₃	40	overnight	Messy
11 ^b	MeO	COOMe	Cl	Toluene	RT	overnight	Messy
12 ^b	MeO	COOMe	Cl	Toluene/DCM	RT	4 h	Messy
13	MeO	COOMe	OiPr	DCE	RT	3 days	Messy

14 ^b	Me	COOMe	Cl	Toluene/DCM	RT	overnight	Messy
15	Me	COOMe	O <i>i</i> Pr	C ₆ D ₆	RT	one week	No reaction
16	Me	COOMe	O <i>i</i> Pr	C ₆ D ₆	80	overnight	Messy
17	<i>t</i> Bu	C≡CH	O <i>i</i> Pr	C ₆ D ₆	RT	one week	No reaction
18	<i>t</i> Bu	C≡CH	O <i>i</i> Pr	C ₆ D ₆	80	4 h	Messy

- a. Reactions were carried out by mixing 1 equivalent of proligand and 1.1 equivalents of Al(O*i*Pr)₃ at room temperature in the specified solvent and then elevated to the designated temperature.
- b. Reactions were carried out by adding 1.3 equivalents of AlEt₂Cl (0.9 M in toluene) to 1 equivalent of proligand at -78 °C and slowly warmed up to room temperature.
- c. The reactions were monitored by ¹H NMR spectroscopy.

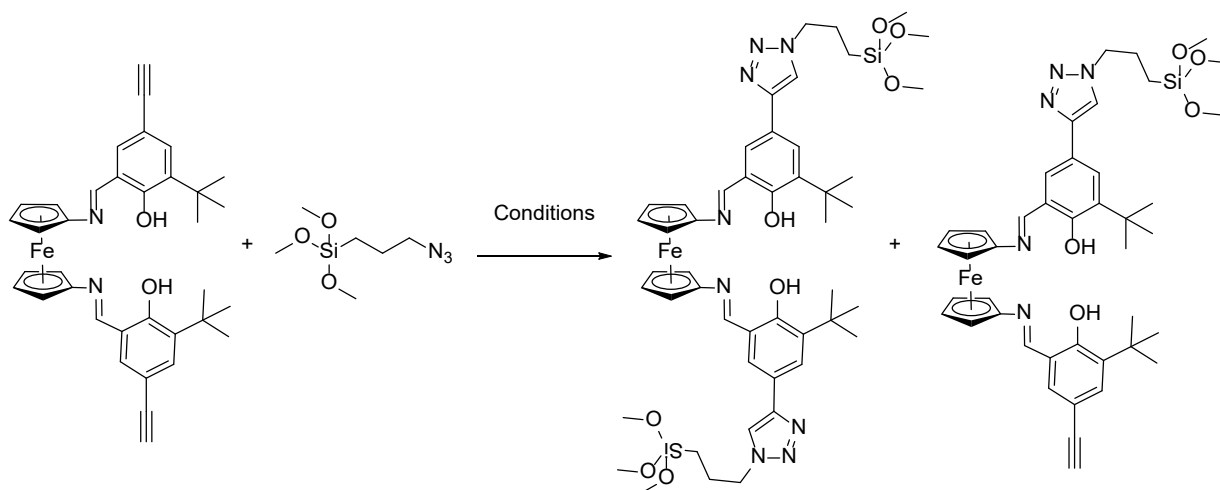


Table C3. Investigating conditions for “click” reaction between **L5** and (3-azidopropyl)trimethoxysilane.

Entry ^a	Solvent	[Cu]	Base	Reductant	Temp	Results ^f
1 ^b	THF	CuI	DIPEA	N/A	RT to 50 °C	RT overnight: no reaction 50 °C, 35 h: mixture of products

2 ^c	THF	CuI	Et ₃ N	N/A	RT to 50 °C	RT overnight: no reaction 50 °C, 35 h: mixture of products
3 ^d	MeOH/ water	CuSO ₄ ·5H ₂ O	N/A	Na ascorbate	RT	No reaction after 48 h
4 ^{d,e}	DCM/ water	CuSO ₄ ·5H ₂ O	N/A	Na ascorbate	RT	RT overnight: a mixture of products
5 ^c	DCM	CuI	Et ₃ N	N/A	RT	RT 3 days: a mixture of products

- a. All experiments were conducted with 1 equivalent of **L5** with 2 equivalent (3-azidopropyl)trimethoxysilane.
- b. 5 equivalents of DIPEA, 0.1 equivalent of CuI.
- c. 1.5 equivalents of triethylamine, 0.1 equivalent of CuI, in the specified solvent.
- d. 0.1 equivalent of CuSO₄·5H₂O, 0.2 equivalent of sodium ascorbate in 1:1 mixture of solvents.
- e. The reaction was washed with ethyl acetate and water and dried with Na₂SO₄.
- f. The reactions were monitored by ¹H NMR spectroscopy.

Table C4. ICP-MS results of surface anchoring attempts and controls.^a

Entry	Sample	Fe		Al		Cr		Co		Cu	
		Conc. [µg/mL]	TiO ₂ loading [wt%]	Conc. [µg/mL]	TiO ₂ loading [wt%]	Conc. [µg/mL]	TiO ₂ loading [wt%]	Conc. [µg/mL]	TiO ₂ loading [wt%]	Conc. [µg/mL]	TiO ₂ loading [wt%]
1	Salfen/TiO ₂	1.188	0.302	-	-	-	-	-	-	-	-
2	(Salfen)Al(O/Pr)/TiO ₂	1.087	0.137	0.910	0.115	-	-	-	-	-	-
3	SalfenCo/TiO ₂	1.593	0.168	-	-	-	-	1.779	0.187	-	-
4	L1 /TiO ₂ -DCM	2.060	0.443	-	-	-	-	-	-	-	-
5	L1 /TiO ₂ -DCM-2	3.087	0.428	-	-	-	-	-	-	-	-
6	L1 /TiO ₂ -ether	1.879	0.380	-	-	-	-	-	-	-	-
7	L1 /TiO ₂ -ether-2	1.987	0.356	-	-	-	-	-	-	-	-
8	Co-1 /TiO ₂	0.966	0.147	-	-	-	-	1.778	0.270	-	-
9	Cr-1 /TiO ₂	0.933	0.110	-	-	1.733	0.204	-	-	-	-
10	"Click" L5 /TiO ₂	8.824	0.957	-	-	-	-	-	-	32.587	3.54
11	"Click" L5 /TiO ₂ -2	1.428	0.199	-	-	-	-	-	-	0.319	0.040
12	"Click" Cr-2 /TiO ₂	2.372	0.296	-	-	1.074	0.134	-	-	0.294	0.037
13	TiO ₂	0.172	0.025	-	-	0.047	0.007	0.000	0	0.008	0.001

a. ICP samples were prepared by digesting solid powders into 2% nitric acid for 2-3 days. Each sample was done in triplicated measurements with background correction.

Chapter 5. Ytterbium(III) complexes with ultra-narrow absorption: steps toward magnetic field and liquid cell quantum sensing

5.1 Introduction

Lanthanide molecular materials have emerged as invaluable tools in a wide range of areas including catalysis,^{234, 235} single-molecular magnets (SMMs),²³⁶⁻²³⁸ electromagnetic field sensing,^{239, 240} and quantum information processing (QIP).²⁴¹ Molecular materials composing lanthanide elements exhibit exceptional properties due to their special electronic structure. Sharp absorption and emission bands are often observed for f-f transition due to the shielding of the 4f subshell by the 5s and 5p orbitals, which allows distinct electronic transitions with well-defined energy levels. In the realm of quantum information processing, lanthanide complexes represented by Ln(trensal) (H₃(trensal) = 2,2',2''-tris(salicylideneimino)triethylamine) processing unique quantum properties such as long coherence times and robust spin interactions renders them a highly promising paradigm for quantum computing.^{242, 243} Besides the immense potential for QIP, lanthanide complexes offer unparalleled sensitivity and selectivity in electromagnetic field sensing.

Atomic vapor cells (AVCs) are one of the most sensitive and widely deployed methods of detecting electromagnetic fields that are typically derived from K, Cs, or Rb with limitations on collision-based dephasing cite/our paper. A liquid analogue to an AVC, e.g. an atomic-like molecular sensor (ALMS), would utilize atomic-like transitions while minimizing drawbacks by accessing much higher number densities. In this regard, a molecular system with a designed ligand supporting a lanthanide center featuring discrete electronic transition represents an appealing class of candidates for liquid cell sensing. This design approach allows a convenient integration of a tunable chemical backbone and a lanthanide center that governs the opto-

magnetic properties of the system. It allows the unraveling of the mechanisms during the development and enables intentional modifications, optimization, and a combination of multiple functionalities to attain the desired properties for the designated application.

Among lanthanides, Yb^{3+} with the $4f^{13}$ electron configuration allows for well-protected electronic transitions between a small manifold of spin-orbit electron configurations. Therefore, we consider it a viable candidate for the applications of our interest. It is important to note that crystal field asymmetry in a Yb^{3+} coordination complex results in coupling between $5d$ and $4f$ orbitals. Solubilization allows for a high number density of these species in a set volume, reaching upwards of 10^{19} molecules per cm^3 (i.e., 10 mM), a value eight orders of magnitude greater than the average density of their AVC counterparts.²⁴⁴⁻²⁴⁶ Here we present an unprecedented ultranarrow (<1 meV) linewidth achieved in a solution at room temperature for a molecular ytterbium system with in-depth opto-magnetic investigation supported by electronic structure calculations. The developed system allows for liquid-based optical measurements of magnetic fields through direct transmission of circularly polarized light, down to the Earth's magnetic field (~ 0.25 G),²⁴⁰ paving the way toward a novel liquid-based magnetometry method (Figure 5.1). This chapter is a reproduction of a submitted manuscript Shin, A. J.;* Zhao, C.;* **Shen, Y.;*** Dickerson, C.;* Li, B.; Bim, D.; Atallah, T. L.; Oyala, P. H.; He, Y.; Roshandel, H.; Alson, L. K.; Alexandrova, A. N.; Diaconescu, P. L.; Campbell, W. C.; Caram, J. R., **Toward liquid cell quantum sensing: Ytterbium (III) complexes with ultra-narrow absorption**, *authors contributed equally. The present chapter will be focusing on the synthesis and characterization of a series of molecular ytterbium systems.

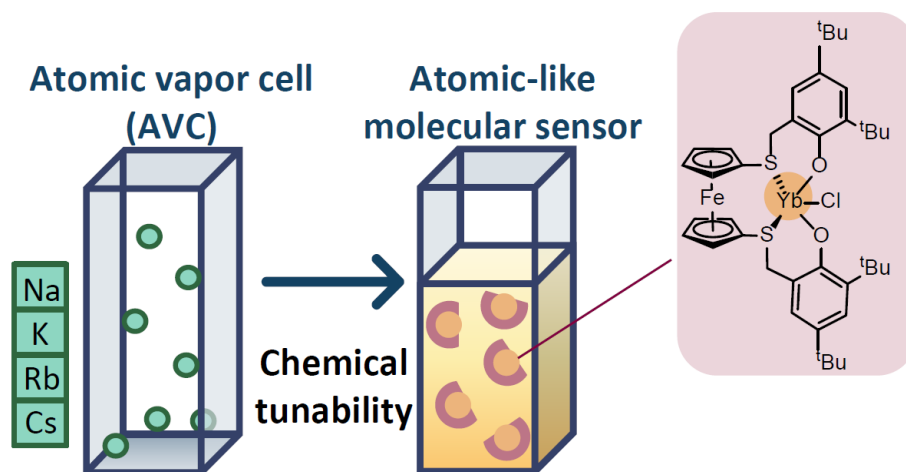
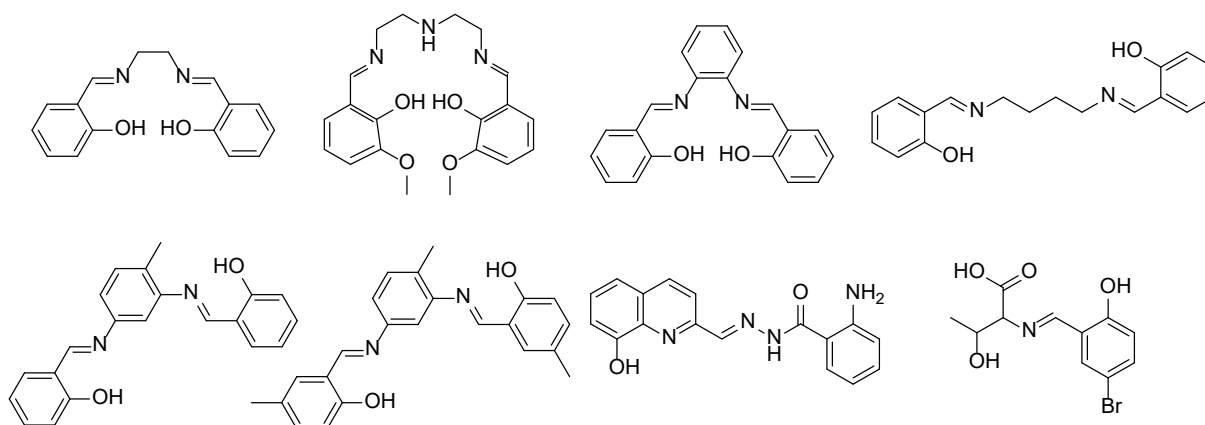


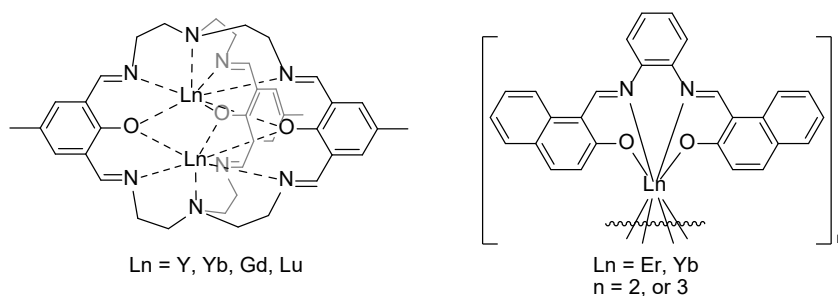
Figure 5.1. Molecular ytterbium system for atomic-like molecular sensing.

Molecular lanthanide systems applied in the realms of single-molecular magnets (SMMs), electromagnetic field sensing, and quantum information processing (QIP) have been intensively investigated based on various supporting ligands.^{238, 240, 241} Schiff base compounds are particularly attractive due to their unique coordination environment.²⁴⁷⁻²⁵² Modifications on the molecular structure are also readily accessible, which confers appealing functionality to the coordination ligand. The optical and/or magnetic properties of selected examples of lanthanide complexes supported by Schiff base compounds are presented in Figure 5.2. Moreover, amide versions of Schiff base compounds and other types of [ONNO]-based ligands, for example, salan, as well as [OSSO]-type of ligands are potential candidates for molecular lanthanide system.^{66, 253-258}

Schiff base compounds



Schiff base supported lanthanide complexes



[OSSO]-type of ligands for RE metal coordination

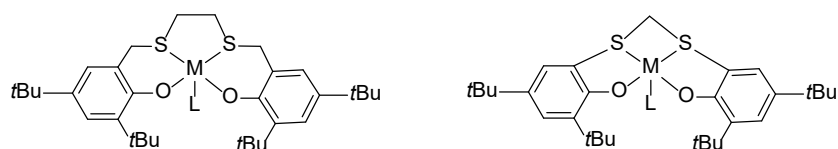
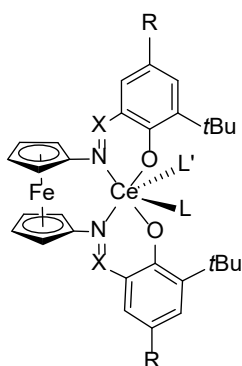


Figure 5.2. Selection of Schiff base compounds (top), their supported lanthanide complexes (middle), and representations of [OSSO]-type of ligands for rare earth metal coordination (bottom).^{247, 250, 258, 259}

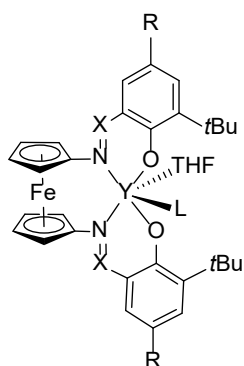
Our group has developed a series of ferrocene-based compounds and has established a list of lanthanide complexes supported by those compounds (Figure 5.3).^{73, 92, 260-263} The ferrocene-diimide and ferrocene-dithiol-supported rare earth complexes exhibited impressive activity in ring-opening polymerization in the comprehensive studies, however, they were less

investigated in their optical and magnetic properties.^{66, 73, 261, 262} On the other hand, ferrocene diamide ligand, NN^{TBS} , was investigated supporting Dy complex. The constructed Dy complex exhibited unprecedented uniaxial anisotropy, which was leveraged to enhance its SMM properties.²⁶⁴ Here, we first time demonstrate the investigation of ferrocene-based [OSSO]-ligand-supported ytterbium complexes and their unique optical and magnetic properties.

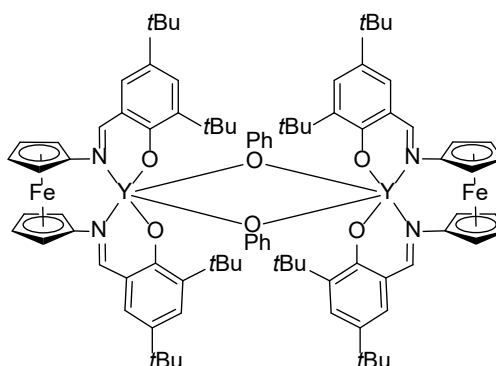
Ferrocene-based Schiff base compounds



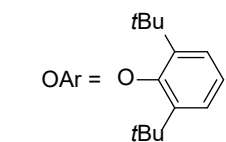
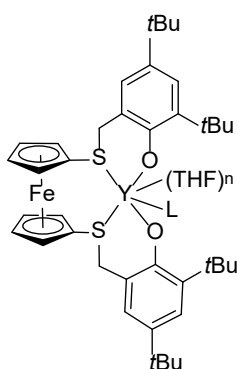
salfen: X = CH, R = tBu
 phosfen: X = PPh₂, R = H
 L = N(SiMe₃)₂, OtBu, Cl
 L' = THF, OtBu



salfen: X = CH, R = tBu
 phosfen: X = PPh₂, R = H
 L = OtBu, Cl

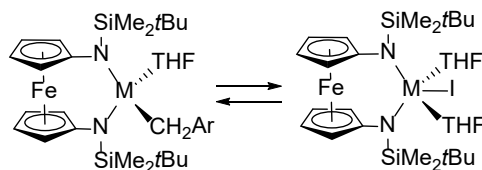


Ferrocene-based [OSSO]-type ligand, H₂(thioifan)



L = N(SiMe₃)₂, OAr, Cl, OtBu
 n = 0, or 1

Ferrocene diamide ligand, NN^{TBS}



M = Sc, Y, La, Ce, Pr, Nd, Sm,
 Gd, Tb, Dy, Ho, Er, Tm, Lu

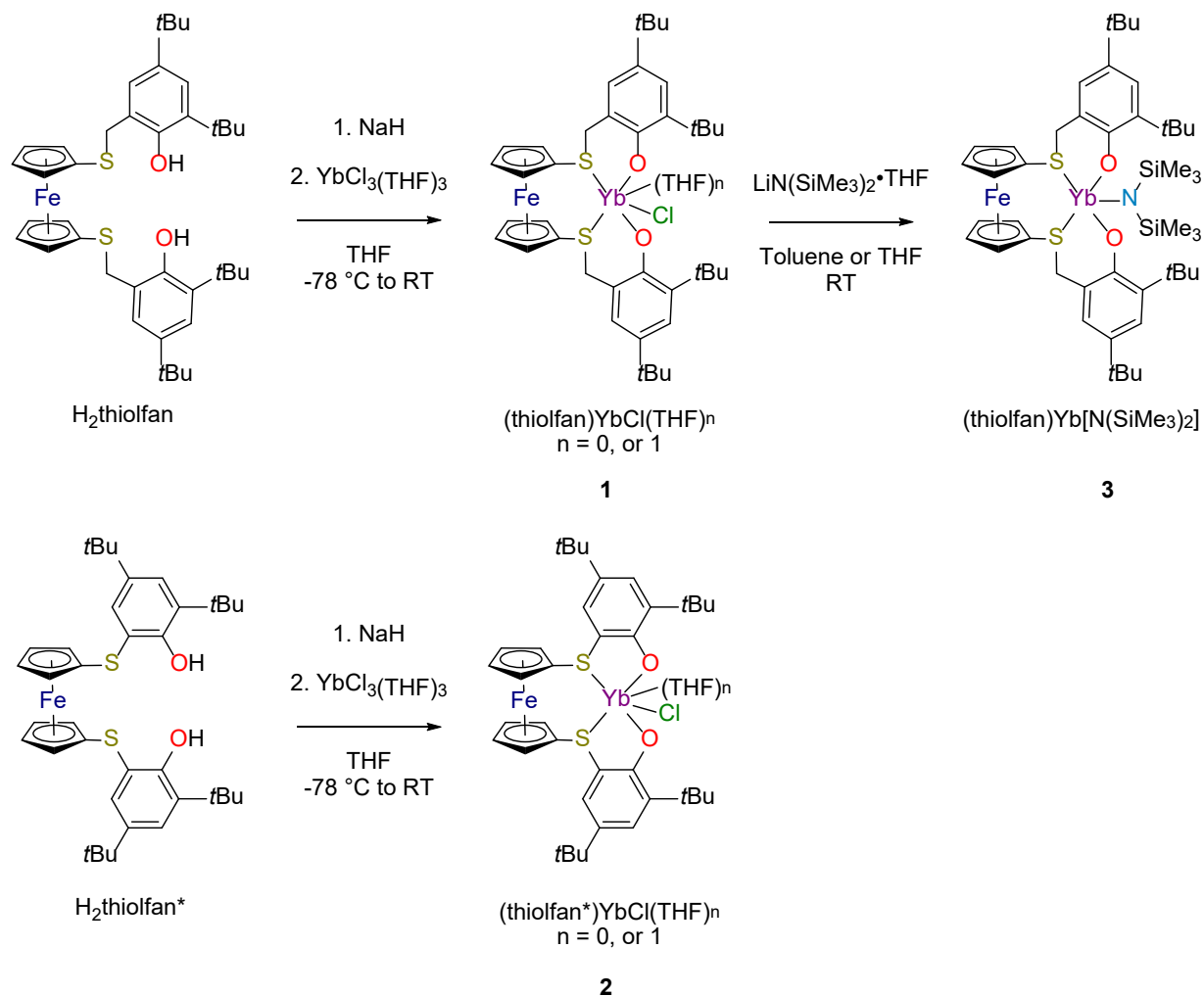
Figure 5.3. Selection of ferrocene-base ligand-supported rare earth metal complexes developed by the Diaconescu group.^{73, 260, 261, 263, 265}

5.2 Results and discussion

Synthesis and characterization of ytterbium complexes

H₂(thiolfan) and H₂(thiolfan*) have been synthesized according to previously published procedures (thiolfan = 1,1'-bis(2,4-di-*tert*-butyl-6-thiomethylenephenoxy)ferrocene, thiolfan* = 1,1'-bis(2,4-di-*tert*-butyl-6-thiophenoxy)ferrocene).^{75, 260} The Yb³⁺ complexes supported by the ferrocene-based [OSSO]-type of ligands was synthesized following a published procedure with minor modifications (Scheme 5.1).²⁶⁰ H₂(thiolfan) was deprotonated with excess sodium hydride at room temperature, followed by a reaction with YbCl₃(THF)₃ (THF = tetrahydrofuran) at -78 °C. After crystallizing in concentrated toluene solution layered with hexanes at -30°C, an orange-yellow crystalline product was obtained in moderate yields. To investigate the relationship between the structural and spectral properties of this class of Yb³⁺ compounds, two derivatives of (thiolfan)YbCl(THF) were synthesized: (thiolfan*)YbCl(THF), **2**, and (thiolfan)Yb[N(SiMe₃)₂], **3**. (thiolfan*)YbCl(THF), was synthesized following a similar procedure for the synthesis of (thiolfan)YbCl(THF) where H₂(thiolfan*) was deprotonated with excess sodium hydride at room temperature, followed by a reaction with YbCl₃(THF)₃ at -78 °C. Crystallization in concentrated toluene solution layered with hexanes afforded semi-crystalline products in moderate yield, however, not suitable for single crystal x-ray diffraction analysis. Moreover, an amide version of (thiolfan)YbCl(THF) was prepared through the reaction of [(thiolfan)YbCl]₂ with LiN(SiMe₃)₂ in the presence of THF. (thiolfan)Yb[N(SiMe₃)₂] was obtained as a yellow-whitish powder from a crystallization solution in hexanes and isolated by decanting hexanes. The solid was collected on top of a fine frit. Due to the paramagnetic nature of the complex, proton peaks in the obtained ¹H NMR spectra of the three complexes could not be accurately assigned. Instead, all three complexes were characterized by elemental analysis, UV-Vis and Fourier transform infrared (FTIR)

spectroscopy. Unfortunately, attempts to characterize by mass spectroscopy techniques only reflected free ligands after complex degradation. IR spectroscopy analysis using Nujol mulls sandwiched between NaCl optical plates revealed small amounts of compound degradation (Figure D23-25).



Scheme 5.1. Synthesis of ytterbium complexes: (thiolfan)YbCl(THF) **1**, (thiolfan*)YbCl(THF) **2**, and (thiolfan)Yb[N(SiMe₃)₂] **3**.

Attempts to obtain crystals suitable for X-ray diffraction analysis for (thiolfan*)YbCl(THF) and (thiolfan)Yb[N(SiMe₃)₂] in concentrated toluene layered with

hexanes or saturated hexanes solution were unsuccessful. However, the solid-state molecular structure of the ytterbium chloride complex supported by thiofan crystallized out of toluene revealed a dinuclear compound, $[(\text{thiofan})\text{YbCl}]_2$, where two ytterbium centers bridged by two chlorides (Figure 5.4, left). The mononuclear compound with THF coordination, $(\text{thiofan})\text{YbCl}(\text{THF})$, was crystallized out of concentrated THF solution layered with hexanes at low temperature, revealing one ytterbium center in the structure (Figure 5.4, right). A similar observation of the bridged versus THF coordinated structures of a rare earth metal complex has been reported previously for the yttrium analogue.²⁶⁰ The spectral measurements performed in THF or 2-MeTHF (2-Methyltetrahydrofuran) are expected to reveal the nature of the mononuclear ytterbium compound $(\text{thiofan})\text{YbCl}(\text{THF})$, whereas the investigation on the solid form or in the non-coordinating solvent of the ytterbium compound crushed out of toluene is based on the dimeric form of the ytterbium compound, $[(\text{thiofan})\text{YbCl}]_2$ unless otherwise noted.

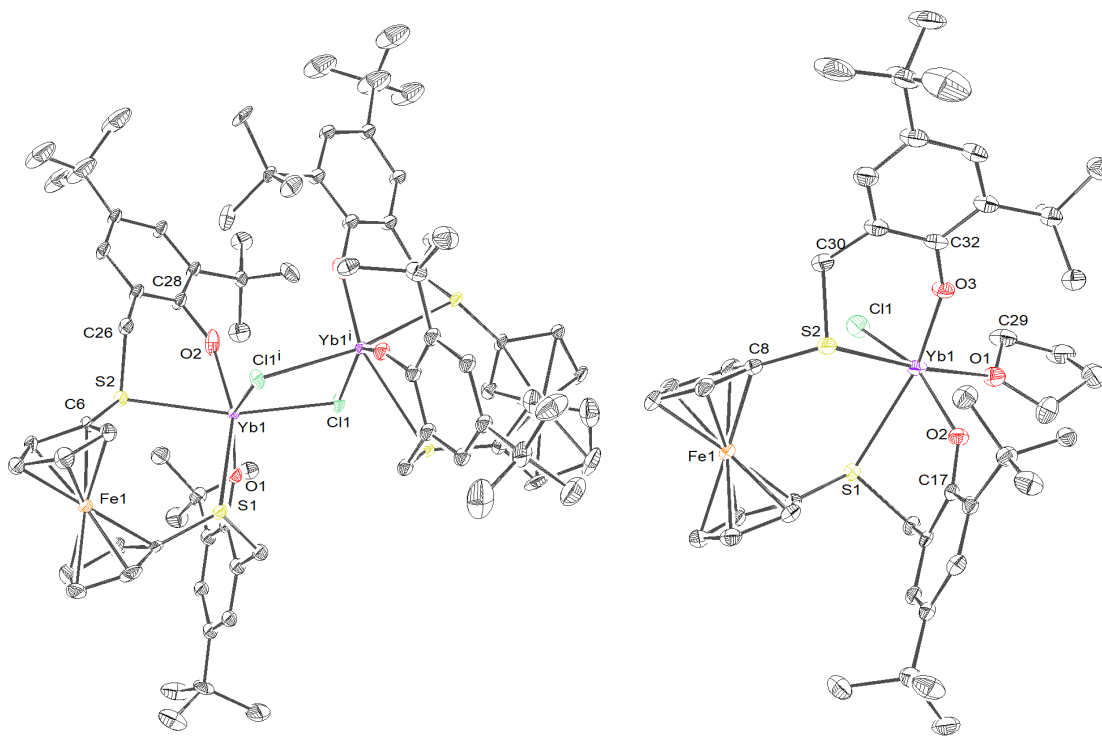


Figure 5.4. Left: thermal ellipsoid (50% probability) representation of $[(\text{thiolfan})\text{YbCl}]_2$. Right: Thermal ellipsoid (50% probability) representation of $(\text{thiolfan})\text{YbCl}(\text{THF})$. Hydrogen and disordered atoms are omitted for clarity.

Preliminary results on conducting UV-Vis spectroscopy measurements on the ytterbium complex supported by thiolfan in toluene revealed two peaks between 980-985 nm. In contrast, the spectrum taken in THF reflected only one peak at 980 nm. Dilution of the sample in toluene with serial addition of THF indicated a gradual spectral shift from the bimodal absorbance feature in toluene to the unimodal feature in THF (Figure 5.5).

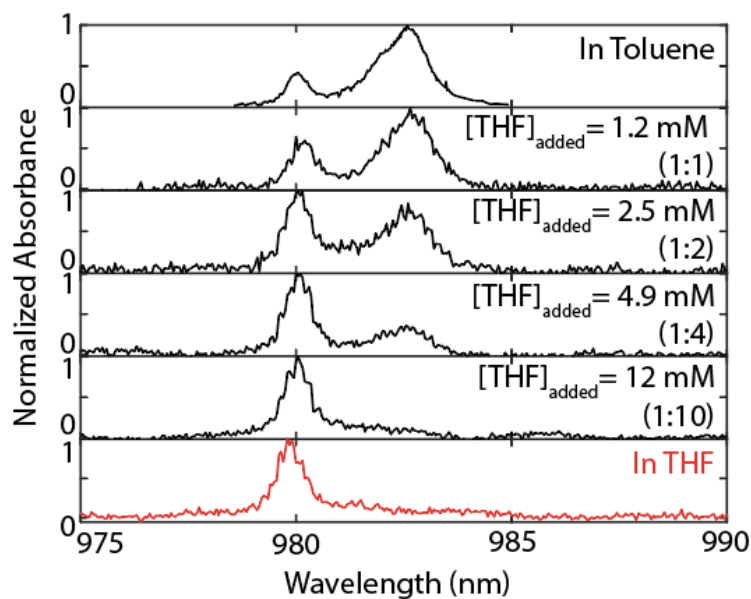


Figure 5.5. Dilution of $[(\text{thiolfan})\text{YbCl}]_2$ in toluene with small additions of THF. The ratio of the monomer to THF concentrations are shown in brackets. The sample absorption spectra in toluene and in THF are shown on the top (black) and bottom (red) for comparison to the dilution trend.

We speculated that the shift in the absorption peak observed upon the addition of THF to the sample in toluene was attributed to the THF coordination and breaking of the dinuclear structure of [(thiolfan)YbCl]₂. It was further supported by a diffusion-ordered spectroscopy (DOSY) experiment on the yttrium analogue (Figure 5.6). Due to the broadness of the peaks in the ¹H NMR spectrum of [(thiolfan)YbCl]₂, we performed DOSY experiments on the yttrium analogue [(thiolfan)YCl]₂, which also crystalizes as a dinuclear complex with chlorides bridging the two yttrium centers in a similar way as the ytterbium chloride complex.²⁶⁰ It is important to point out that the ¹H NMR spectrum of [(thiolfan)YCl]₂ indicated 1 equivalent of THF coordination to the complex when residual THF was present. The DOSY experiment was conducted on [(thiolfan)YCl]₂ in THF-d₈ with tetrakis(trimethylsilyl)silane (TMSS) used as an internal standard.²⁶⁶ The hydrodynamic radius (*r_H*) of (thiolfan)YCl(THF) was derived from the Stokes-Einstein equation:²⁶⁷

$$D_t = \frac{kT}{6\pi\eta r_H}$$

where *k* is the Boltzmann constant, *T* is the temperature, and *η* is the solution viscosity (298 K, 0.46 mPa·s, respectively). *r_H* = 6.70 Å was calculated using this equation and compared to the radius of the dimeric structure in the solid state (*r_{X-ray}* = 11.20 Å estimated by measuring the distance from the center of the dimeric molecule to the farthest atom using X-ray crystallographic data), which is 1.67 times the radius calculated in solution.

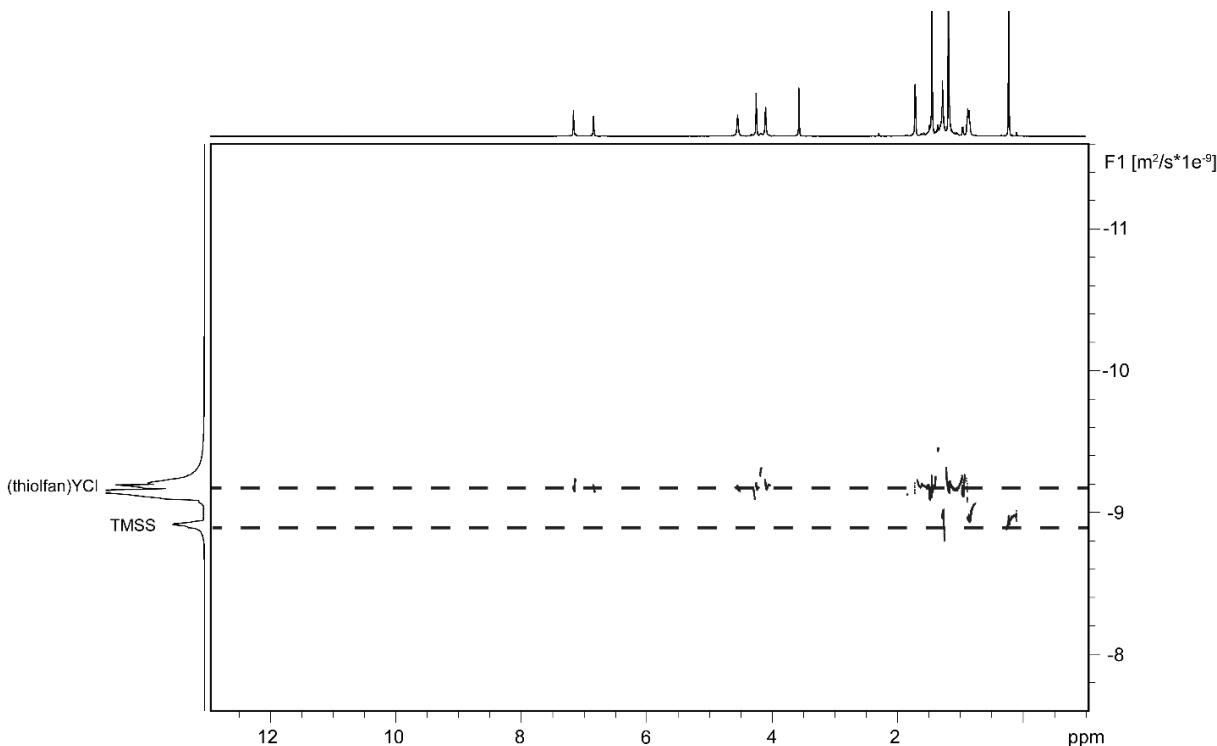


Figure 5.6. DOSY (298 K, 500 MHz, THF- d_8) of (thiolfan)YbCl(THF) with TMSS as an internal standard.

Electronic spectroscopy

In-depth investigations on the optical property of (thiolfan)YbCl(THF) using electronic spectroscopy were conducted using a conventional UV-Vis spectrometer. We observe several features: a broad ligand absorption band (**I**) in the visible range around 400-600 nm (Figure D26), several weakly absorbing transitions (**II** and **III**) from 880-950 nm, and the transition of primary interest: the strongly absorbing, ultranarrow transition (**IV**) at 980 nm (Figure 5.7). A high-resolution spectrum of our primary focus, the extraordinary narrow transition **IV**, was collected using a narrowband, continuous-wave Ti:sapphire laser to scan the transmission (see experimental section for details). A center energy of 1.2637 eV with a full width at half maximum (FWHM) of 0.625 ± 0.006 meV was found (Figure 5.7, bottom left).

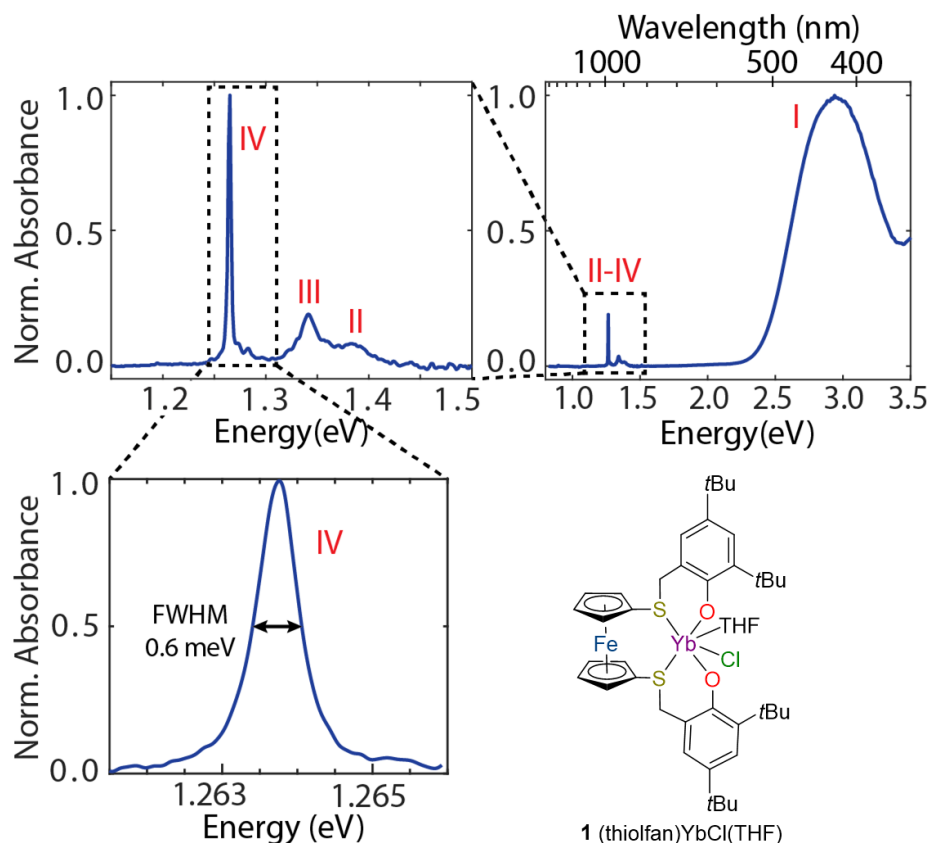


Figure 5.7. Optical characterization of (thiolfan)YbCl(THF). Wide-field absorption spectrum with zoomed-in absorption spectrum around the Yb features, showing a high-resolution absorption scan of the Yb transition with the highest oscillator strength around 980 nm or 1.262 eV in the bottom left. The absorption spectra were taken with a 3 mM solution in THF at room temperature.

The feature of interest for (thiolfan)YbCl(THF) at 980 nm remained unimodal in the collected absorption spectra at cryogenic temperatures (Figure 5.8a) in glass-forming solvent 2-MeTHF. A slight broadening and blue shift in peak energy was observed at increased temperatures (300 K and above). Overall, we postulated that transition IV is dominated by an inhomogeneously broadened transitions since no underlying feature was resolved at cryogenic temperatures.

Nonetheless, (thiolfan)YbCl(THF) presented a narrower room temperature solution linewidth compared to those of other molecular Yb³⁺ systems (Figure 5.8b).^{242, 268-270} We hypothesize that the observed ultra-narrow linewidth of (thiolfan)YbCl(THF) is due to the unprecedented ferrocene-based ligand incorporated in the molecular ytterbium system. For comparison, Yb(trensal) presents a linewidth of 4.6 meV with more absorption features due to other spin-orbital transitions and vibrations.²⁴²

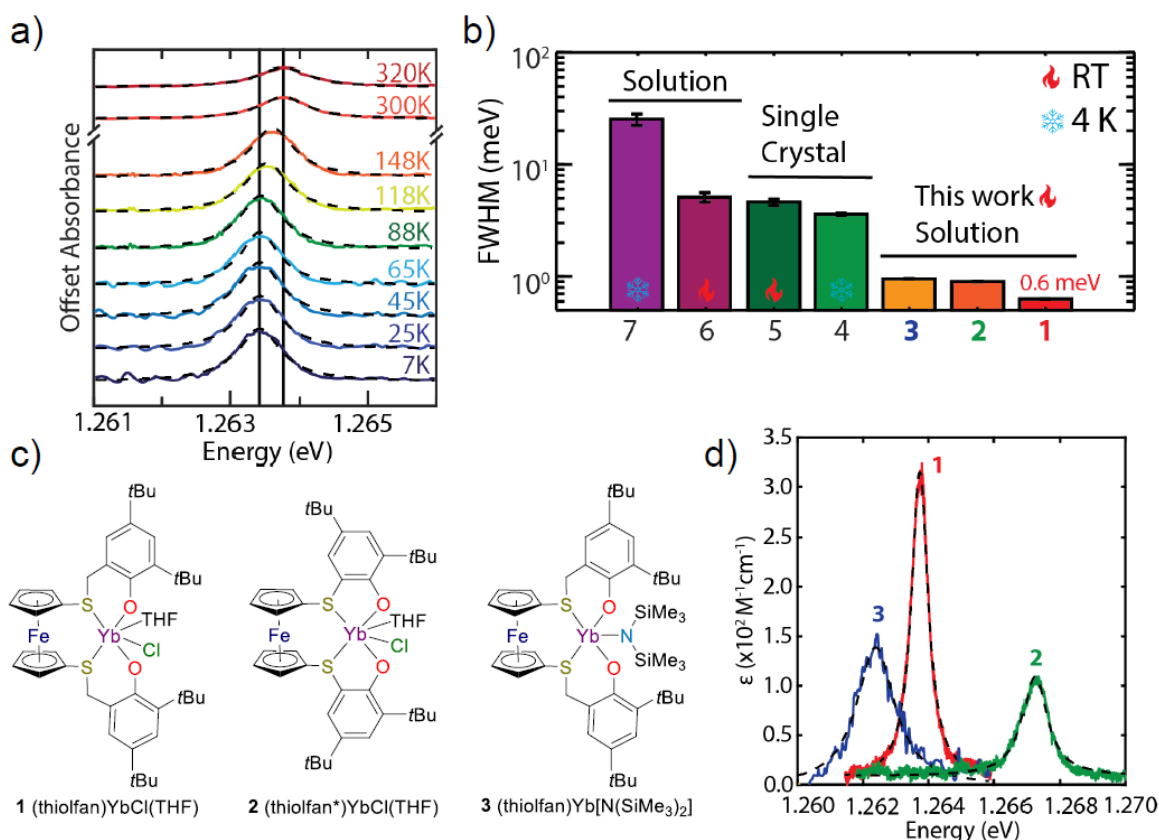


Figure 5.8. a) Temperature-dependent absorption scans of (thiolfan)YbCl(THF), using liquid N₂ and He for cooling. The dashed lines indicate the corresponding Lorentzian fits. Solid vertical lines are a visual guide to emphasize the shift in peak center; b) Absorption FWHM comparison to other Yb³⁺ complexes;^{242, 268-270} c) Molecular representations of ytterbium compounds 1, 2, 3; d) Absorption peaks of compounds 1, 2, 3 at 3 mM concentration in THF.

To perform a systematic study of the molecular ytterbium system incorporating ferrocene backbones, we conducted UV-Vis spectroscopy measurements on **2**, **3** at 3 mM concentration in THF. For all three variants, the narrow linewidth of transition **IV** is preserved with the full width at half maximum (FWHM) of **2** at 0.902 ± 0.007 meV and **3** at 0.947 ± 0.005 meV, comparable to that of **1** (Figure 5.8d). Compared to the thiofan backbone, the thiofan* backbone incorporated in **2** has one less carbon from the sulfur atom attaching the ferrocene moiety to the phenoxy, which is postulated to account for the broadening of the linewidth and the shift of the peak. Replacing -Cl with -N(SiMe₃)₂ in **3** resulted in a similar observation likely due to the different ligand field strength of -Cl versus -N(SiMe₃)₂. Ambiguity in solvent coordination for **3** hindered our ability to proceed with further investigation. Although the underlying mechanism of those changes in linewidth and shift in energy is uncovered, it is important to highlight that all three ytterbium complexes display near record linewidths in solution, despite shifts in the primary transition energy that can be attributed to slight deviations in the coordination geometry. The narrow linewidth originated from the ferrocene-based ligand in the present ytterbium complexes provides a novel platform for designing molecular lanthanide systems for narrow optical transitions.

Magnetic properties

The magnetic properties of all three ytterbium compounds in solid form were investigated using a superconducting quantum interference device (SQUID). Analyses were performed on crushed polycrystalline samples obtained from a solution of toluene/hexanes and sealed in a polyethylene membrane under an inert atmosphere. Direct current (dc) susceptibility measurements were performed in a magnetic field, B, of 1000 Oe and at a temperature range of 2

K to 290 K. Solid-state molecular structure of [(thiolfan)YbCl]₂ revealed a dinuclear complex, therefore, at 290 K, $\chi_m T = 4.77 \text{ emu} \cdot \text{K/mol}$ after diamagnetic correction is comparable with the reported two ytterbium centers ($5.14 \text{ emu} \cdot \text{K/mol}$, $^2F_{7/2}$, $g_J = 8/7$) at room temperature.^{252, 271-278} Upon cooling, $\chi_m T$ decreased gradually to $3.67 \text{ emu} \cdot \text{K/mol}$ at 2 K as a result of depopulation of the excited crystal field sublevels of Yb³⁺ and/or antiferromagnetic interactions between the two Yb³⁺ centers (Figure 5.9). At low temperatures, the magnetization value rose rapidly at low fields, and increases slowly at high fields, then reaches a maximum of $3.76 \mu_B$ at 7 T (Figure D9a). Such field dependence of the magnetization of [(thiolfanYbCl)₂] is typically observed for weakly interacting Yb³⁺ ions.^{271-273, 275, 277} Attempts to fit the field-dependent magnetization data using Brillouin function of two non-interacting Yb³⁺ ions gave incongruent results, as the magnetization value at 7 T and 2 K for [(thiolfanYbCl)₂] than expected two uncoupled Yb³⁺ centers, suggesting that crystal field effects, exchange interactions and/or the presence of low-lying states shall be considered to obtain a reliable fitting.^{278, 279} The discrepancy between the Brillouin function of two uncoupled $J = \pm 2/7$ states verse the experimental data of [(thiolfanYbCl)₂] may also be attributed to the magnetic anisotropy. The lack of perfect superimposition of the M versus H/T curves at 2, 4, 6, 8, and 10 K suggested the presence of magnetic anisotropy and/or low-lying excited states for the ytterbium complex (Figure D9b). However, the measurement was performed on a polycrystalline sample which is insufficient to probe the orientation sensitivity of the anisotropic exchange contribution.²⁷² A linear curve was observed in $1/\chi$ vs T and Curie constant was calculated based on the linear fit ($c = 4.39 \text{ emu K/mol}$). According to Curie-Weiss law, a negative Weiss constant ($\theta = -4.46\text{K}$) was obtained from the graph, indicating antiferromagnetic coupling (Figure D10). A linear curve was also observed in the M vs H measurement

passing through the origin, confirming the paramagnetic properties of the compound. No hysteresis in isothermal magnetization measurements was observed (Figure D11).

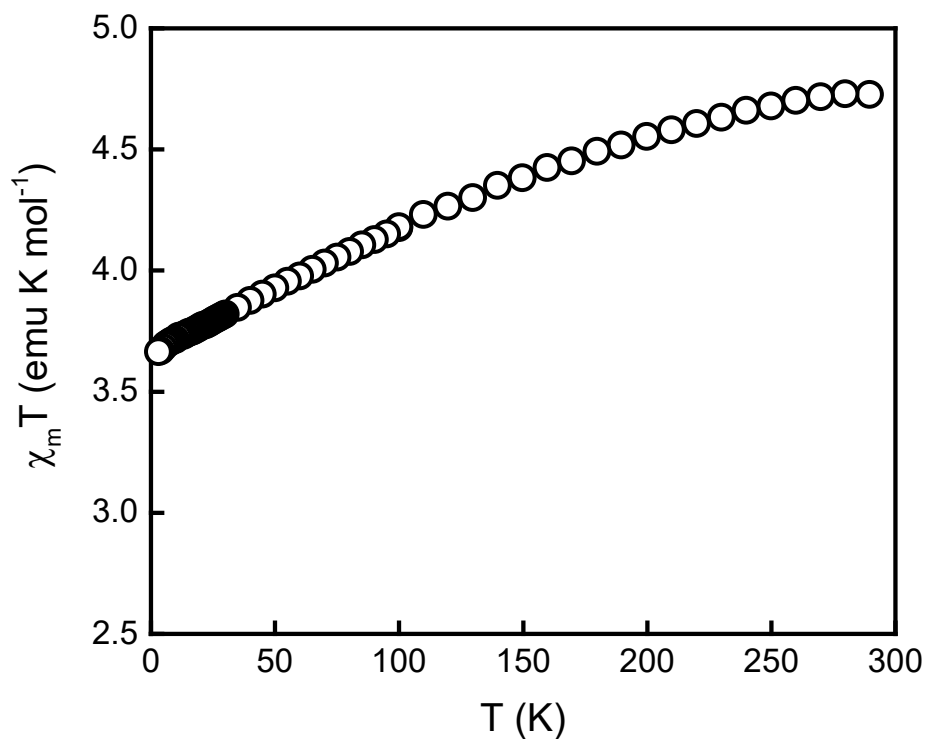


Figure 5.9. Plot of $\chi_m T$ versus T for $[(\text{thiolfan})\text{YbCl}]_2$ under a 1000 Oe dc field in the temperature range 2-290 K.

Similarly, direct current (dc) susceptibility measurements in a magnetic field, B , of 1000 Oe and at a temperature range of 2 K to 300 K were also conducted for $(\text{thiolfan}^*)\text{YbCl}(\text{THF})_n$ and $(\text{thiolfan})\text{Yb}[\text{N}(\text{SiMe}_3)_2]$. For $(\text{thiolfan}^*)\text{YbCl}(\text{THF})_n$, the room temperature molecular susceptibility and effective magnetic moment $\chi_m T = 2.11 \text{ emu} \cdot \text{K/mol}$ and $\mu_{eff} = 4.11$ per ytterbium center were calculated based on experimental results (Figure D12). In the context of $(\text{thiolfan})\text{Yb}[\text{N}(\text{SiMe}_3)_2]$, the room temperature molecular susceptibility and effective magnetic moment $\chi_m T = 2.12 \text{ emu} \cdot \text{K/mol}$ and $\mu_{eff} = 4.12$ per ytterbium center were found (Figure

D15). Both are comparable with the expected values for one ytterbium center ($2.57 \text{ emu} \cdot \text{K/mol}$ and $\mu_{eff} = 4.54$) assuming a $J = 7/2$ ($S = 1/2$, $L = 3$, $g_J = 8/7$) ground state.²³⁶

Interestingly, upon cooling, $\chi_m T$ of (thiolfan*)YbCl(THF) first decreased gradually as temperature decreases to $1.73 \text{ emu} \cdot \text{K/mol}$ at 17 K, then slowly increased to $1.75 \text{ emu} \cdot \text{K/mol}$ at 6 K, followed by a sharp decrease to $1.69 \text{ emu} \cdot \text{K/mol}$ at 2 K (Figure D12). A linear curve was observed in $1/\chi$ vs T . Curie constant was calculated based on the linear fit ($c = 2.13 \text{ emu K/mol}$), which is comparable to the value of $\chi_m T = 2.11 \text{ emu} \cdot \text{K/mol}$ previously calculated for one ytterbium center in the formula of (thiolfan*)YbCl(THF). According to Curie-Weiss law, a negative Weiss constant ($\theta = -5.89 \text{ K}$) was obtained from the graph, indicating a net anti-ferromagnetic coupling in the bulk sample (Figure D13). A linear curve was also observed in the M vs H measurement passing through the origin, confirming the paramagnetic properties of this compound (Figure D14). On the contrary, $\chi_m T$ of (thiolfan)Yb[N(SiMe₃)₂] only decreased as temperature decreased until reached the minimum $1.55 \text{ emu} \cdot \text{K/mol}$ at 2 K (Figure D15). Similarly, A linear curve was also observed in the M vs H measurement passing through the origin, confirming the paramagnetic properties of the amide derivative (Figure D17), with a negative Weiss constant ($\theta = -4.08 \text{ K}$) obtained based on the linear fitting in $1/\chi$ vs T (Figure D16). Curie constant was calculated based on the linear fit ($c = 2.14 \text{ emu K/mol}$), which is comparable to the value of $\chi_m T = 2.12 \text{ emu} \cdot \text{K/mol}$ previously calculated for one ytterbium center associated with the amide complex.

The magnetic susceptibility of each ytterbium compound in solution was measured by NMR spectroscopy using Evans' method in deuterated solvents.²⁸⁰ The molar susceptibility and Bohr magnetons (μ_{eff}) of each compound was calculated based on the following formulas:

$$\chi_m T = \frac{3 \times 10^3 \Delta f}{4\pi f_m c} - \chi_D$$

$$\mu_{eff} = 2.827 \sqrt{\chi_m T}$$

where χ_m is the corrected paramagnetic molar susceptibility, and T (in K) is the absolute temperature at which the NMR was taken. Δf (in Hz) is the chemical shift difference of the NMR reference in the presence and absence of the paramagnetic compound (shift of the deuterated solvent referencing peak); f_m (in Hz) is the external magnetic field, C (in mol/L) is the concentration of the sample and χ_D is the diamagnetic susceptibility. For simplicity, χ_D of (thiolfan*)YbCl(THF)_n (n = 0 or 1) and (thiolfan)Yb[N(SiMe₃)₂] are estimated based on:

$$\chi_D \approx -\frac{M}{2} \times 10^{-6}$$

where M (in g/mol) is the molecular mass.

The paramagnetic properties of (thiolfan)YbCl(THF)_n were investigated in THF-d₈, C₆D₆, and Tol-d₈ (Figure D18-20). A $\chi_m T = 2.68 \text{ emu} \cdot \text{K/mol}$ was calculated along with a $\mu_{eff} = 4.63$ based on the difference in δ (ppm) observed in the ¹H NMR spectrum after diamagnetic correction in THF-d₈, as expected for one ytterbium center ($2.57 \text{ emu} \cdot \text{K/mol}$ and $\mu_{eff} = 4.54$) assuming a J = 7/2 (S = 1/2, L = 3, g_J = 8/7) ground state.²³⁶ Similar results were obtained using other two solvents, $\chi_m T = 2.08 \text{ emu} \cdot \text{K/mol}$ was calculated for C₆D₆, and $2.68 \text{ emu} \cdot \text{K/mol}$ was calculated for Tol-d₈ per ytterbium center. Effective magnetic moments of (thiolfan)YbCl(THF) were calculated based on the formulas above suggesting $\mu_{eff} = 4.63$ in THF-d₈, 4.08 in C₆D₆, and 4.63 in Tol-d₈.

Similarly, the molar susceptibility and effective magnetic moment were calculated for (thiolfan*)YbCl(THF)_n (n = 0 or 1) and (thiolfan)Yb[N(SiMe₃)₂] in C₆D₆. A $\chi_m T = 2.05 \text{ emu} \cdot$

K/mol and $\mu_{eff} = 4.05$ per ytterbium center was found for (thiolfan*)YbCl(THF)_n (calculated based on $n = 0$) (Figure D21). A $\chi_m T = 2.33 \text{ emu} \cdot K/mol$ and $\mu_{eff} = 4.32$ per ytterbium center was found for (thiolfan)Yb[N(SiMe₃)₂] (Figure D22). These results are consistent with the findings for (thiolfan)YbCl(THF)_n, and the reported values per ytterbium center.²³⁶ Although no single-molecule magnet (SMM) property was observed in the current study, our investigations in the magnetic property of the three ytterbium complexes provided us valuable insights into the future design of functional SMMs.

5.3 Conclusion and outlook

In summary, we have discovered a molecular ytterbium system, namely (thiolfan)YbCl(THF), which exhibits an extraordinarily narrow $^2F_{7/2}$ to $^2F_{5/2}$ transition in solution at room temperature. Although the underlying mechanism of the ferrocene-based ligand in the ytterbium system needs to be further explored, we proposed that the orbital mixing of ytterbium with the ligand orbital lead to a non-zero oscillator strength of the observed transition. The postulation is supported by theoretical and spectroscopic work which are demonstrated comprehensively in the submitted manuscript. In addition, our investigation on the magnetic property of the (thiolfan)YbCl(THF) paves the way toward its immediate application in the imaging of weak magnetic fields. In light of our discoveries on (thiolfan)YbCl(THF), we hypothesize that a thorough exploration of quantum state preparations of the molecular ytterbium system incorporating ferrocene backbone will result in enhanced sensitivities similar to the AVCs and potentially lead to precise quantum sensing applications.

5.4 Experimental section

General considerations

All compounds were manipulated and handled under a dry nitrogen atmosphere using standard Schlenk techniques or an MBraun inert-gas glovebox. Solvents were purified using a two-column solid-state purification system by the method of Grubbs and transferred to the glovebox without exposure to air.¹³⁶ 2-methyl tetrahydrofuran (2-MeTHF) was distilled over calcium hydride under nitrogen. All solvents were stored on activated molecular sieves and/or sodium for at least a day prior to use. NMR solvents were obtained from Cambridge Isotope Laboratories, degassed, and stored over activated molecular sieves prior to use. Nuclear magnetic resonance spectra were recorded on Bruker AV300, Bruker DRX500, and Bruker AV500 spectrometers at 25 °C in C₆D₆, THF-d₈, and toluene-d₈ unless otherwise specified. Chemical shifts are reported with respect to solvent residual peaks (C₆D₆ at 7.16 ppm, C₄D₈O at 1.73 ppm, C₇D₈ at 2.08, 6.97, 7.01, and 7.09 ppm). YbCl₃(THF)₃ was prepared by stirring YbCl₃ in THF. Lithium bis(trimethylsilyl) amide tetrahydrofuran (LiN(SiMe₃)₂·THF) was synthesized according to a published procedure.²⁸¹ H₂(thiolfan) (1,1'-bis(2,4-di-*tert*-butyl-6-thiomethylenephenol)ferrocene) and H₂(thiolfan*) (thiolfan* = 1,1'-bis(2,4-di-*tert*-butyl-6-thiophenoxy)ferrocene) were synthesized according to the literature.^{75, 260} IR spectra were measured on an Agilent Technologies Cary 620 Fourier transform infrared spectrometer (FTIR) fitted with a Cary 600 Series FTIR Microscope using Nujol mulls sandwiched between NaCl optical plates. CHN analyses were performed in-house on a CE-440 elemental analyzer manufactured by Exeter Analytical, Inc.

Magnetic susceptibility measurements were obtained using a Quantum Design SQUID magnetometer MPMS-XL7 operating between 2 and 300 K for direct-current (DC) applied fields

ranging from -7 to $+7$ T. DC analyses were performed on polycrystalline samples sealed in a polyethylene membrane (prepared in an inert atmosphere) under a field ranging from 0 to 7 T and temperatures between 1.8 and 300 K. In addition, data were collected on different batches to check for consistency. Diamagnetic corrections were applied for the sample holder and the core diamagnetism from the sample (estimated with Pascal constants).⁴⁴

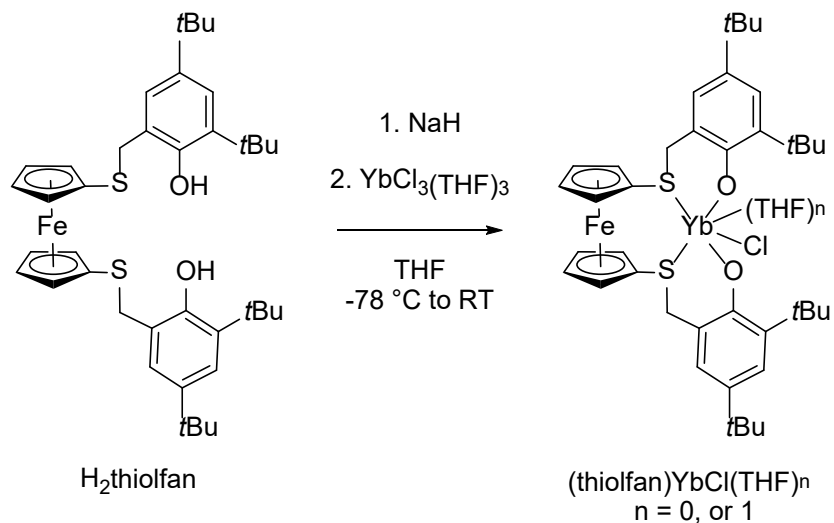
Continuous-Wave (CW) X-band (9.6 GHz) EPR spectra were acquired using a Bruker EMX CW-EPR spectrometer equipped with an ER-4116DM Dual Mode resonator operating in perpendicular mode. Temperature control was achieved through the use of an Oxford Instruments ESR-900 liquid helium flow cryostat and an ITC-503 temperature controller. Pulse EPR data were acquired using a Bruker ELEXSYS E-580 pulse EPR spectrometer operating at X-band with a microwave frequency of 9.36 GHz using a MS-5 split ring resonator, with temperature control achieved through the use of an Oxford Instruments CF-935 liquid helium flow cryostat and a Mercury temperature controller. Electron spin-echo (ESE) detected field-swept EPR spectra were collected using a Hahn-echo pulse sequence ($\frac{\pi}{2} - \tau - \pi - \tau - echo$) where τ is a fixed time delay of 300 ns, and $\frac{\pi}{2}$ and π pulse lengths were 40 and 80 ns, respectively. The broad band absorption spectra reported in the manuscript were collected using the Shimadzu UV-3101PC UV-VIS-NIR scanning spectrophotometer.

A high-resolution transmission/absorption spectrum of the sample was measured with a tunable narrow band CW laser (M Squared SolsTiS Ti:Sapph laser). The laser beam is split into two paths by a polarizing beam splitter (PBS). One beam measures the absorption of the solvent and the other measures the absorption of the sample. The quarter waveplate is used to change the polarization of the laser beam so that we can measure the absorption of σ^+ and σ^- light. The two permanent magnets create a strong static magnetic field to induce Zeeman splitting. The

translational stage allows us to control the distance between the magnet and the sample and to vary the strength of the magnetic field at the sample's location.

X-ray quality crystals were obtained from various concentrated solutions placed in a $-36\text{ }^{\circ}\text{C}$ freezer in the glovebox. Inside the glovebox, the crystals were coated with oil (STP Oil Treatment) on a microscope slide, and then brought outside the glovebox. The X-ray data collections were carried out on a Bruker SMART APEX II single crystal X-ray diffractometer using $\text{Mo K}\alpha$ ($\lambda = 0.71073\text{ \AA}$) or $\text{Cu K}\alpha$ ($\lambda = 1.54178\text{ \AA}$) radiation and a SMART APEX CCD detector at 100 K. The data were reduced by SAINTPLUS, and an empirical absorption correction was applied using the package SADABS.²⁸² The structure was solved using SHELXT and refined using SHELXL *via* OLEX 2 as a graphical user interface.²⁸³⁻²⁸⁵ The structures were then visualized using ORTEP 3.

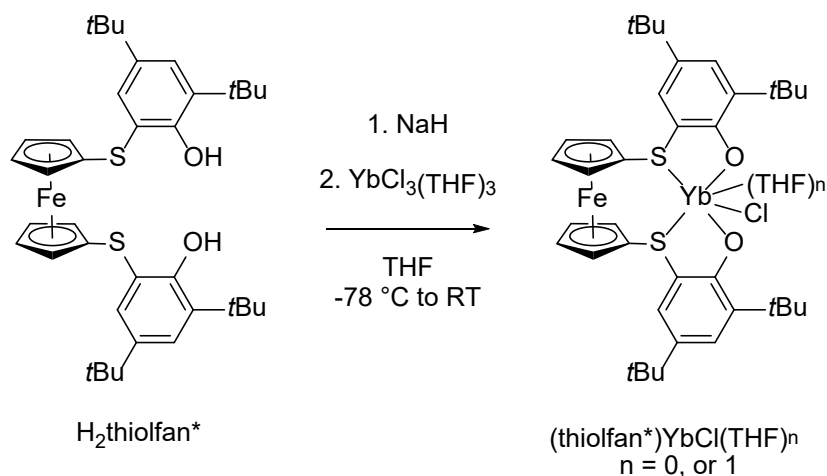
Synthesis of (thiolfan)YbCl(THF)_n



In a nitrogen-filled glovebox, 179.5 mg (0.26 mmol, 1 equiv.) of $\text{H}_2(\text{thiolfan})$ was dissolved in 3 mL of THF and added dropwise to a stirring slurry of NaH (63.0 mg, 10 equiv., 2.6 mmol) in 2 mL of THF. The mixture was stirred at room temperature for 2 h and then filtered through glass

fiber filter paper twice. The filtrate was cooled to $-78\text{ }^{\circ}\text{C}$ and added to the stirring slurry of $\text{YbCl}_3(\text{THF})_3$ (128.9 mg, 1 equiv., 0.26 mmol). The reaction was stirred at $-78\text{ }^{\circ}\text{C}$ for 15 min then slowly brought to room temperature and stirred for another 2 h. The volatiles were removed under a reduced pressure and the residue was extracted with toluene and filtered through glass fiber filter paper twice. The filtrate was concentrated and layered with hexanes, then stored at $-36\text{ }^{\circ}\text{C}$. Yellow crystals were obtained in moderate yield (114.0 mg, 49%). X-ray quality single crystals of $[(\text{thiolfan})\text{YbCl}]_2$ were grown from a solution of toluene layered with *n*-pentane at $-36\text{ }^{\circ}\text{C}$. X-ray quality single crystals of $(\text{thiolfan})\text{YbCl}(\text{THF})$ were grown from a solution of THF layered with hexanes in a 2 mL glass autosampler vial at $-36\text{ }^{\circ}\text{C}$. Due to the paramagnetic nature of the ytterbium complex, peaks are not assigned in the ^1H NMR spectrum. However, a peak at -8.66 ppm and a shoulder at -10.6 ppm were observed in C_6D_6 (fig. S3). Elemental analysis for $[\text{C}_{40}\text{H}_{52}\text{FeClO}_2\text{S}_2\text{Yb}]_2$, calculated: C, 53.78%, H, 5.87%, N, 0.00%; found: C, 54.59%, H, 5.87%, N, 0.00%.

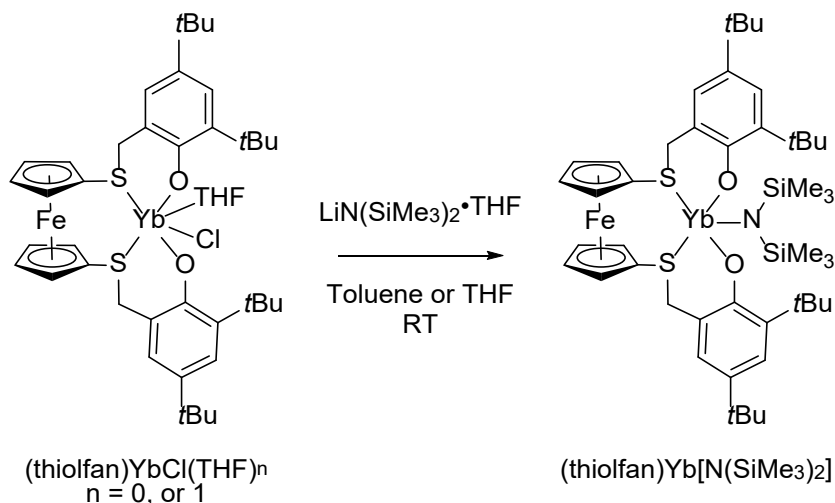
Synthesis of $(\text{thiolfan}^*)\text{YbCl}(\text{THF})_n$



In a nitrogen-filled glovebox, 108.7 mg (0.16 mmol, 1 equiv.) of $\text{H}_2(\text{thiolfan}^*)$ was dissolved in 3 mL of THF and added dropwise to a stirring slurry of NaH (40.0 mg, 10 equiv., 1.6

mmol) in 2 mL of THF. The mixture was stirred at room temperature for 2 h and then filtered through glass fiber filter paper twice. The filtrate was cooled to -78 °C and added to a stirring slurry of YbCl₃(THF)₃ (81.3 mg, 1 equiv., 0.16 mmol). The reaction was stirred at -78 °C for 15 min then slowly brought to room temperature and stirred for another 2 h. The volatiles were removed under a reduced pressure and the residue was extracted with toluene and filtered through glass fiber filter paper twice. The filtrate was concentrated and layered with hexanes, then stored at -36 °C. Yellow crystals were obtained in moderate yield (58.0 mg, 41%). Due to the paramagnetic nature of the ytterbium complex, peaks are not assigned in the ¹H NMR spectrum (fig. S4). Unfortunately, no crystals suitable for X-ray diffraction analysis were obtained. Elemental analysis for C₃₈H₄₈FeClO₂S₂Yb, calculated: C, 52.75%, H, 5.57%, N, 0.00%; found: C, 52.74%, H, 6.04%, N, 0.00%.

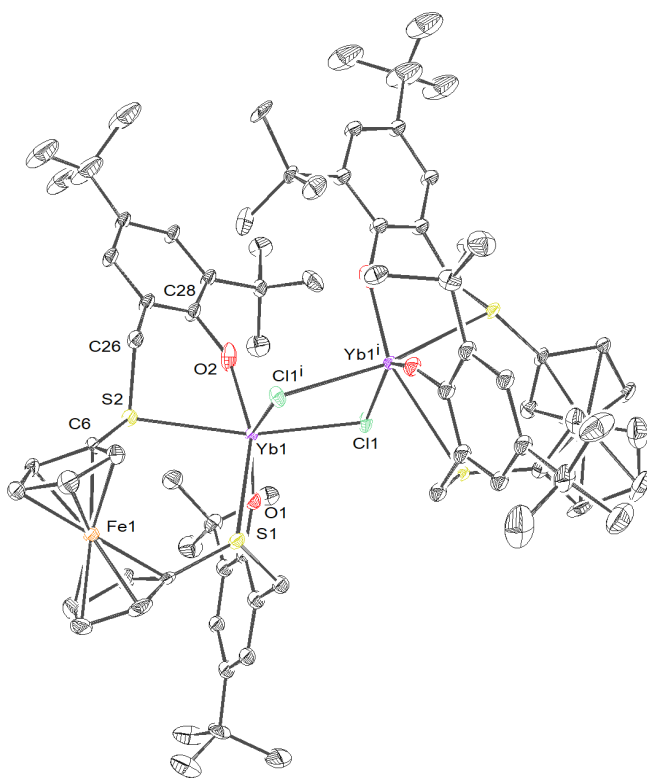
Synthesis of (thiofan) Yb[N(SiMe₃)₂]



In a nitrogen-filled glovebox, 202.8 mg (0.23 mmol, 1 equiv.) of (thiofan)YbCl was dissolved in 5 mL of toluene and added dropwise to a stirring solution of lithium bis(trimethylsilyl)amide·THF (54.4 mg, 1 equiv., 0.23 mmol) in 2 mL of toluene. The mixture was stirred at room temperature for 2 h and then filtered through glass fiber filter paper. The volatiles

were removed under reduced pressure. The solid was re-dissolved in hexanes and then stored at -36 °C. The solution was decanted to collect the semicrystalline product on the wall and the solid precipitated at the bottom of the vial was collected on top of a frit (77.9 mg, 34%). Due to the paramagnetic nature of the ytterbium complex, peaks are not assigned in the ^1H NMR spectrum (fig. S5). Unfortunately, no crystals suitable for X-ray crystallography analysis were obtained. Elemental analysis for $\text{C}_{46}\text{H}_{70}\text{FeNO}_2\text{S}_2\text{Si}_2\text{Yb}$, calculated: C, 54.26%, H, 6.93%, N, 1.38%; found: C, 54.43%, H, 7.10%, N, 0.86%.

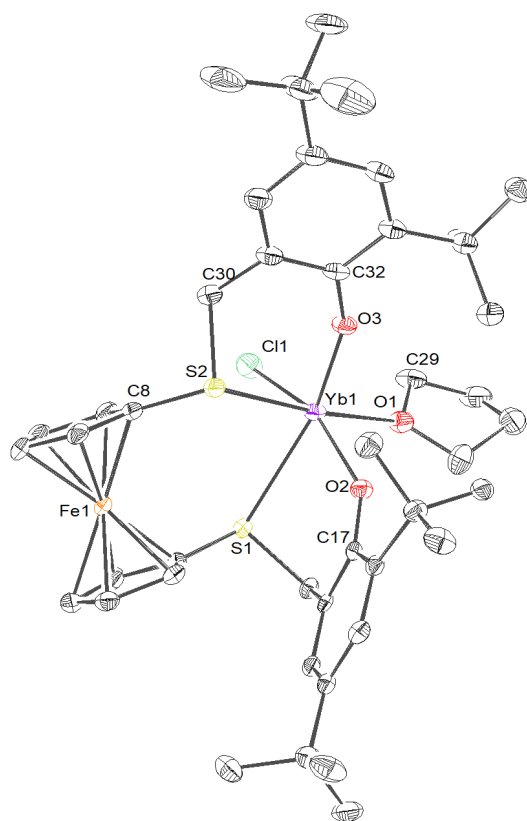
5.5 Appendix D



Selected distances (Å) and angles (°) of [(thiolfan)YbCl]₂

Distances	Yb-Cl ₁	2.654(2)	Yb-S ₂	2.828(2)
	Yb-O ₁	2.041(6)	Yb-Cl ⁱ	2.659(2)
	Yb-O ₂	2.082(8)	Yb-Fe	4.756(2)
	Yb-S ₁	2.931(2)	Yb-Yb ⁱ	4.000(2)
Angles	Cl ₁ -Yb-O ₁	89.9(2)	O ₂ -Yb-S ₁	157.2(2)
	Cl ₁ -Yb-O ₂	96.6(2)	O ₂ -Yb-S ₂	71.5(2)
	Cl ₁ -Yb-S ₁	104.79(7)	S ₁ -Yb-S ₂	86.17(6)
	Cl ₁ -Yb-S ₂	166.08(7)	S ₁ -Yb-Cl ₁	75.35(6)
	Cl ₁ -Yb-Cl ₁ ⁱ	81.22(7)	S ₂ -Yb-Cl ₁	93.57(7)
	O ₁ -Yb-O ₂	111.8(2)	C ₆ -S ₂ -C ₂₆	99.6(4)
	O ₁ -Yb-S ₁	76.4(2)	Yb-O ₁ -C ₁₃	151.9(6)
	O ₁ -Yb-S ₂	101.1(2)	Yb-O ₂ -C ₂₈	154.4(6)

Figure D1. Thermal ellipsoid (50% probability) representation of [(thiolfan)YbCl]₂, without (top) and with (bottom) *t*-butyl groups. Two crystallographically independent molecules are in the unit cell. Hydrogen atoms and solvent molecules (toluene and diethyl ether) are omitted for clarity. Atoms labeled with ⁱ represent the inverted asymmetric unit of the neighboring unit cell.



Selected distances (Å) and angles (°) of (thiofan)YbCl(THF)				
Distances	Yb-O ₁	2.316(2)	Yb-S ₁	2.9073(7)
	Yb-O ₂	2.087(2)	Yb-S ₂	2.8830(9)
	Yb-O ₃	2.053(2)	Yb-Fe	4.719(7)
	Yb-Cl ₁	2.5534(7)		
Angles	O ₁ -Yb-O ₂	85.83(8)	S ₁ -Yb-S ₂	88.57(2)
	O ₁ -Yb-O ₃	98.47(8)	S ₂ -Yb-O ₁	172.61(6)
	O ₂ -Yb-O ₃	105.00(8)	S ₂ -Yb-O ₂	93.70(6)
	Cl ₁ -Yb-S ₁	80.30(2)	S ₂ -Yb-O ₃	74.51(6)
	Cl ₁ -Yb-S ₂	95.67(2)	C ₈ -S ₂ -C ₃₀	99.7(1)
	Cl ₁ -Yb-O ₁	87.79(6)	Yb-O ₁ -C ₂₉	124.3(1)
	Cl ₁ -Yb-O ₂	154.50(6)	Yb-O ₂ -C ₁₇	146.4(2)
	Cl ₁ -Yb-O ₃	100.35(6)	Yb-O ₃ -C ₃₂	153.7(2)

Figure D2. Thermal ellipsoid (50% probability) representation of (thiofan)YbCl(THF) Hydrogen and disordered atoms are omitted for clarity

Table D1. Selected crystal data for [(thiofan)YbCl]₂ and (thiofan)YbCl(THF)

Crystal system	monoclinic	triclinic
Space group	<i>P2/c</i>	<i>P</i> $\bar{1}$
a [Å]	18.2162(18)	10.0390(2)
b [Å]	15.0982(15)	15.3323(3)
c [Å]	32.972(3)	15.4616(4)
α [°]	90	85.0770(10)
β [°]	102.091(2)	75.2870(10)
γ [°]	90	87.8680(10)
Volume [Å ³]	8867.2(15)	2293.04(9)
Z	4	2
ρ_{calc} [g/cm ³]	1.463	1.398
μ [mm ⁻¹]	2.614	7.857
F(000)	3992	986
Crystal size [mm ³]	0.090×0.080×0.070	0.1 × 0.1 × 0.05
Crystal color	Clear yellow and green (dichroic)	clear light yellow
Crystal shape	block	plate

Radiation	MoK α ($\lambda=0.71073$ Å)	CuK α ($\lambda=1.54178$ Å)
2 Θ range for data collection [°]	2.29 to 56.76 (0.75 Å)	5.93 to 136.85 (0.83 Å)
Index ranges	-24 \leq h \leq 24 -20 \leq k \leq 20 -43 \leq l \leq 44	-11 \leq h \leq 12 -18 \leq k \leq 18 -18 \leq l \leq 18
Reflections collected	130664	37470
Independent reflections	22122 $R_{\text{int}} = 0.0830$ $R_{\text{sigma}} = 0.0675$	8103 $R_{\text{int}} = 0.0421$ $R_{\text{sigma}} = 0.0340$
Data/restraints /parameters	22122/0/724	8103/134/488
Goodness-of-fit on F ²	1.134	1.068
Final R indexes [$I \geq 2\sigma(I)$]	$R_1 = 0.0724$ $wR_2 = 0.1454$	$R_1 = 0.0285$ $wR_2 = 0.0703$
Final R indexes [all data]	$R_1 = 0.1176$ $wR_2 = 0.1611$	$R_1 = 0.0330$ $wR_2 = 0.0720$
Largest diff. peak/hole e Å ³	4.14/-4.24	1.15/-1.05

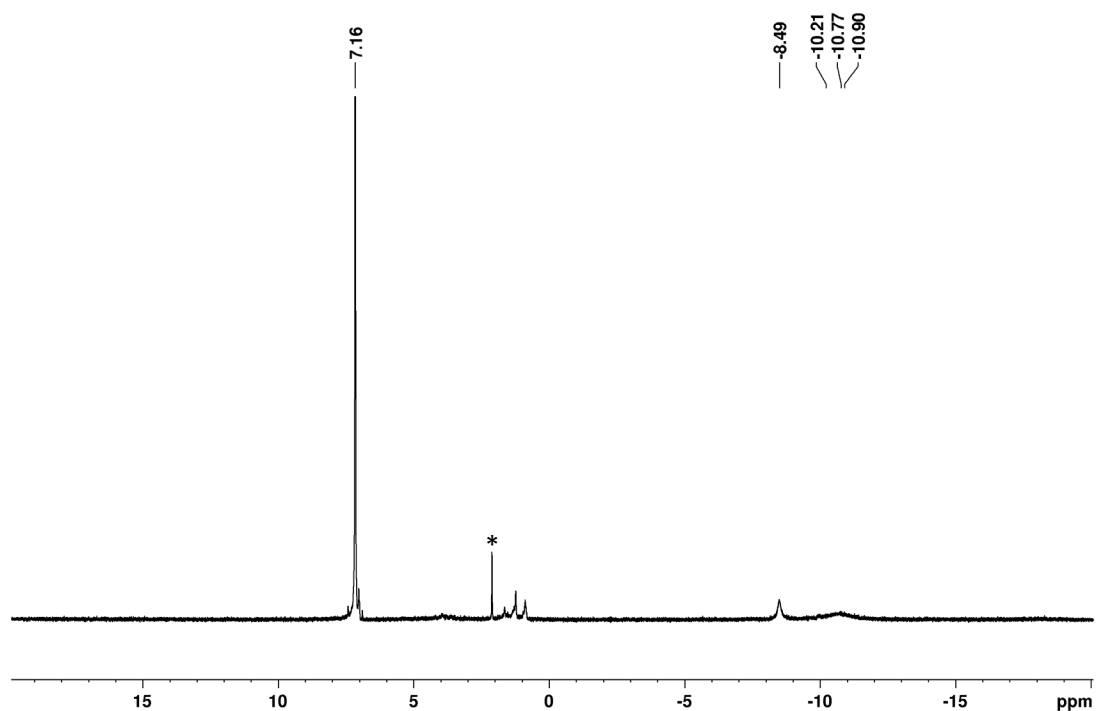


Figure D3. ¹H NMR spectrum (298 K, 500 MHz, C₆D₆) of [(thiofan)YbCl]₂ (*residual toluene).

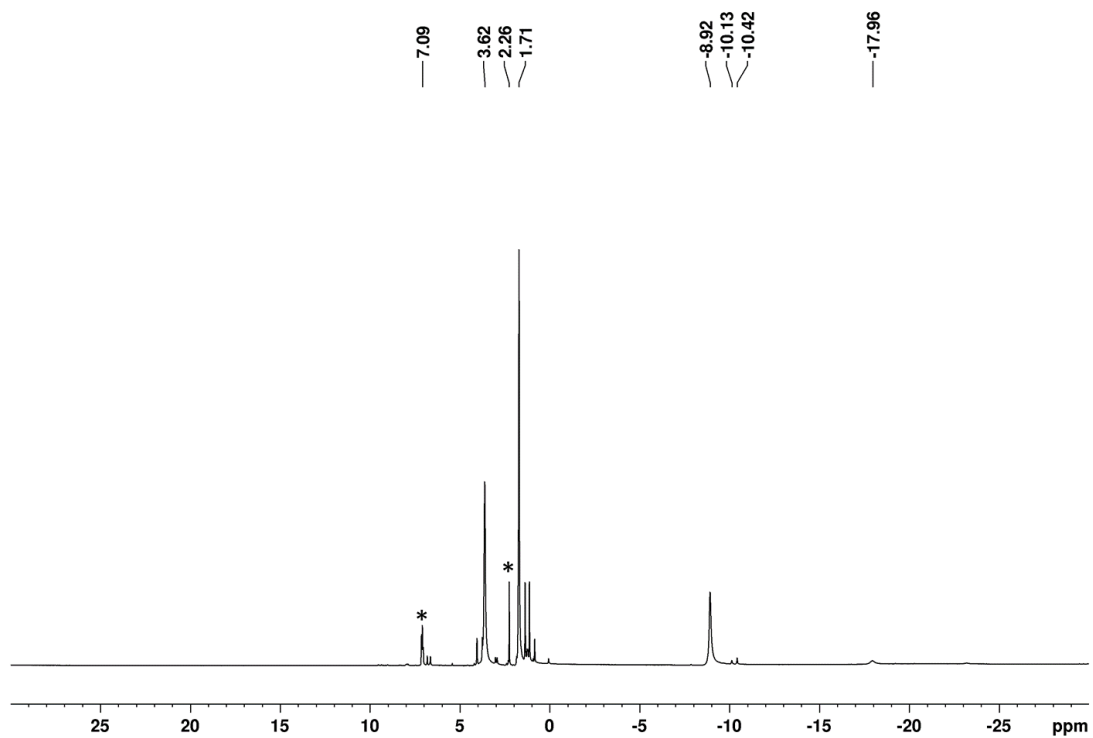


Figure D4. ^1H NMR spectra (298 K, 500 MHz, THF-d_8) of (thiolfan) $\text{YbCl}(\text{THF})$ (*residual toluene).

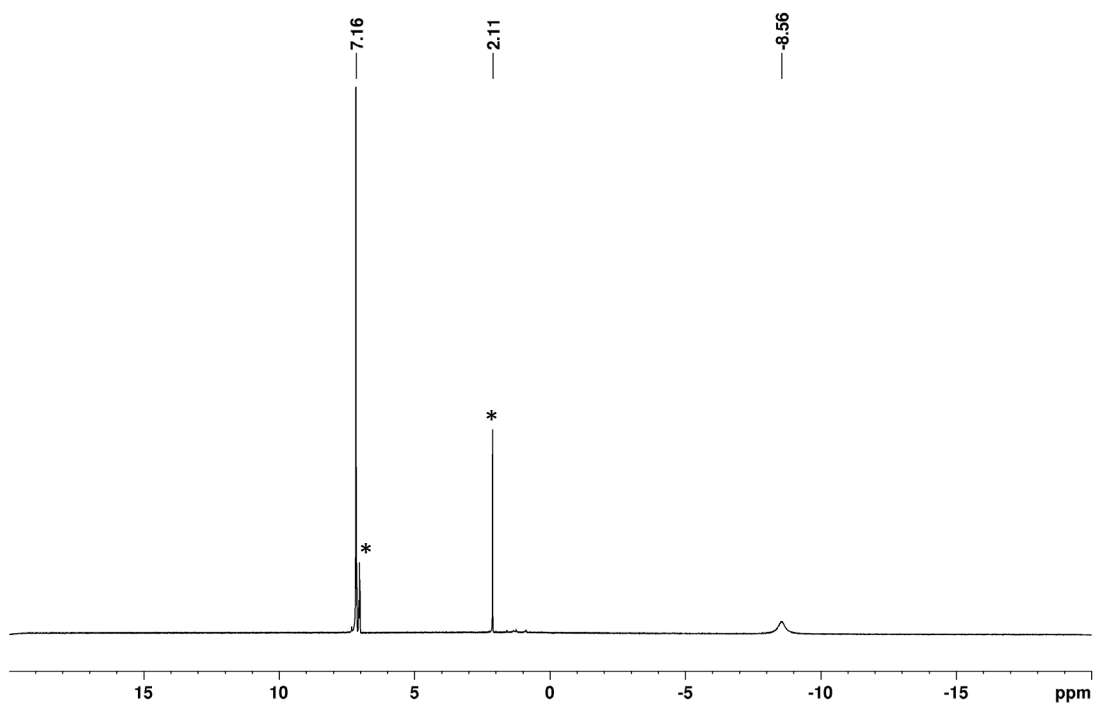


Figure D5. ^1H NMR spectrum (298 K, 500 MHz, C_6D_6) of (thiolfan*) $\text{YbCl}(\text{THF})_n$ ($n=0$, or 1) (*residual toluene).

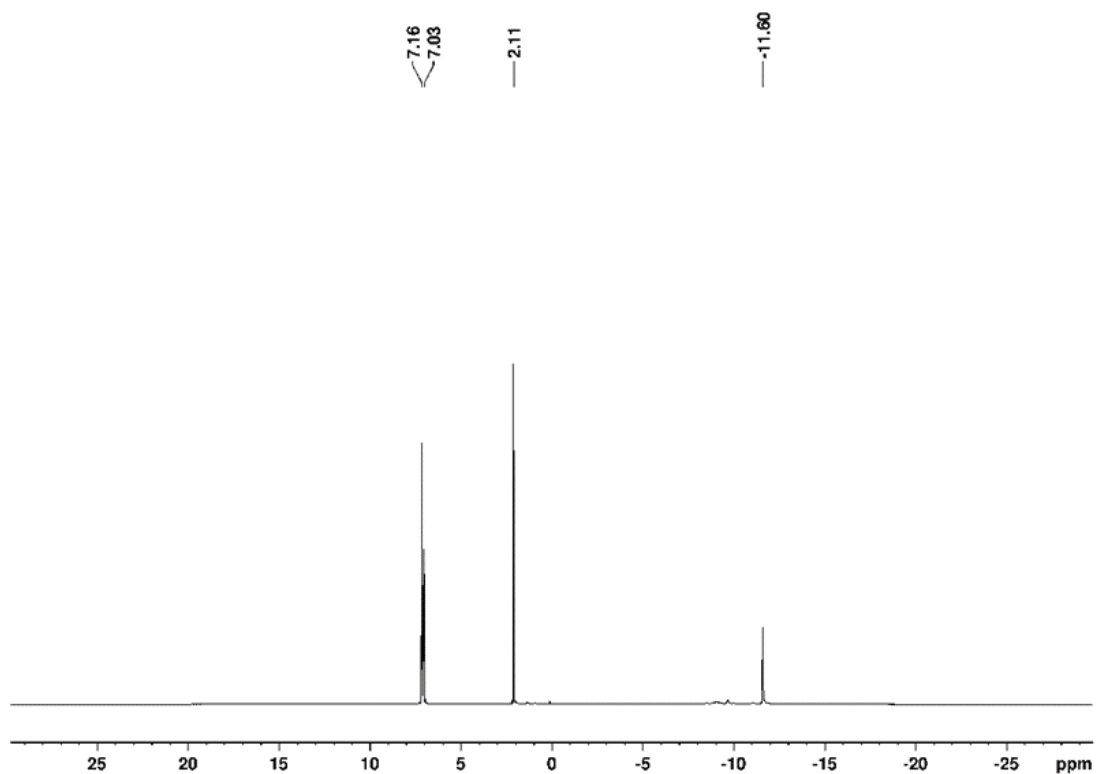


Figure D6. ^1H NMR spectrum (298 K, 500 MHz, C_6D_6) of (thiolfan) $\text{Yb}[\text{N}(\text{SiMe}_3)_2]$. The peak at 2.11 is residual toluene.

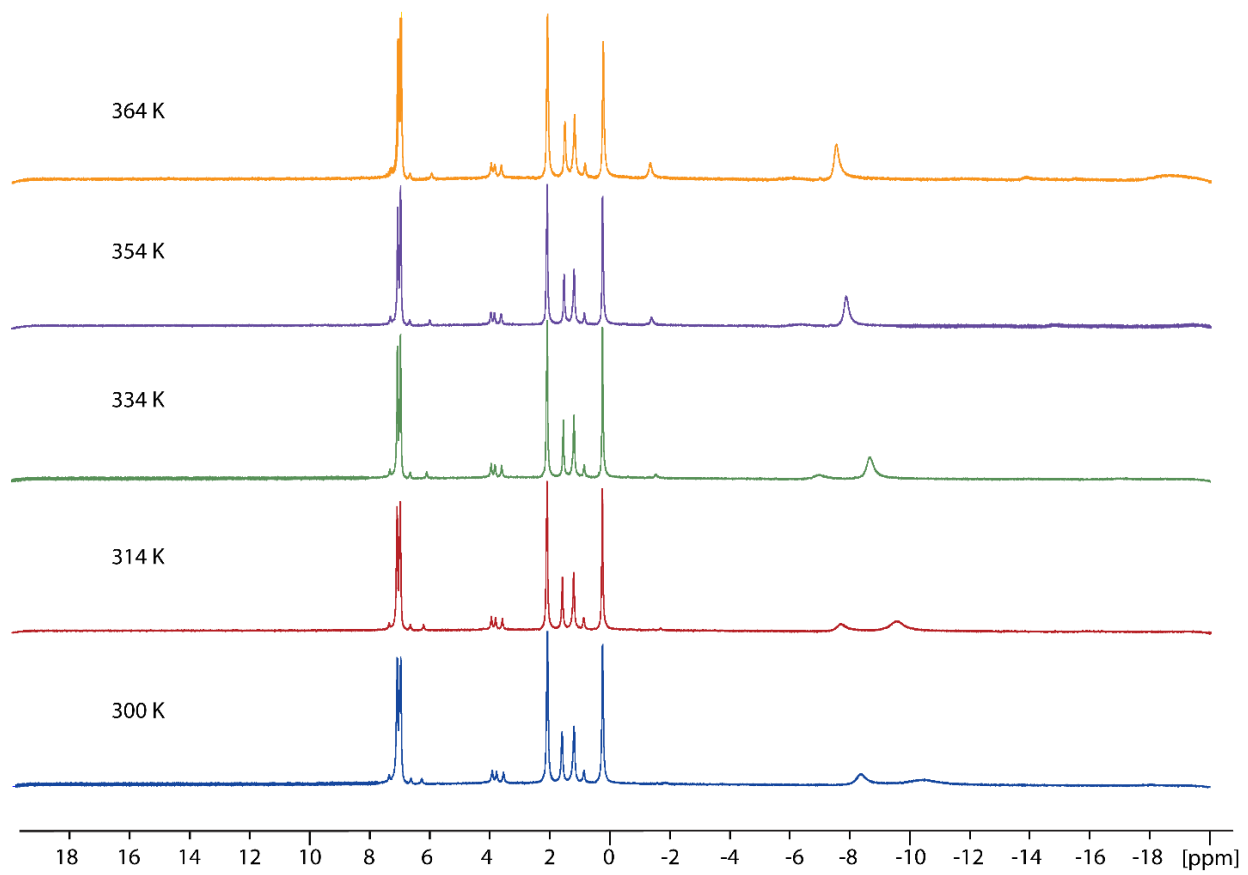


Figure D7. Variable temperature ¹H NMR study (500 MHz, toluene-d₈) of [(thiofan)YbCl]₂.

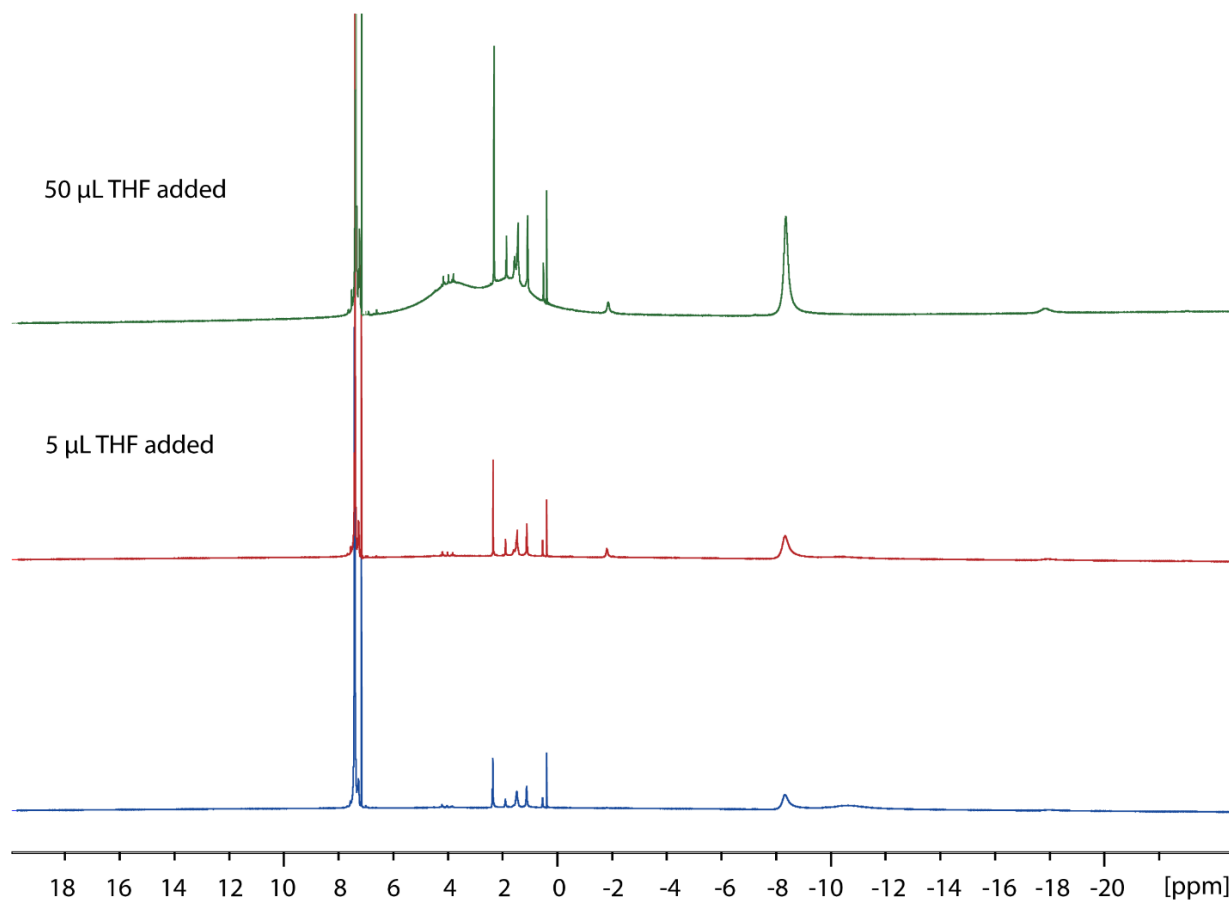


Figure D8. ^1H NMR spectra (298 K, 500 MHz, C_6D_6) of $[(\text{thiolfan})\text{YbCl}]_2$ before and after the addition of THF.

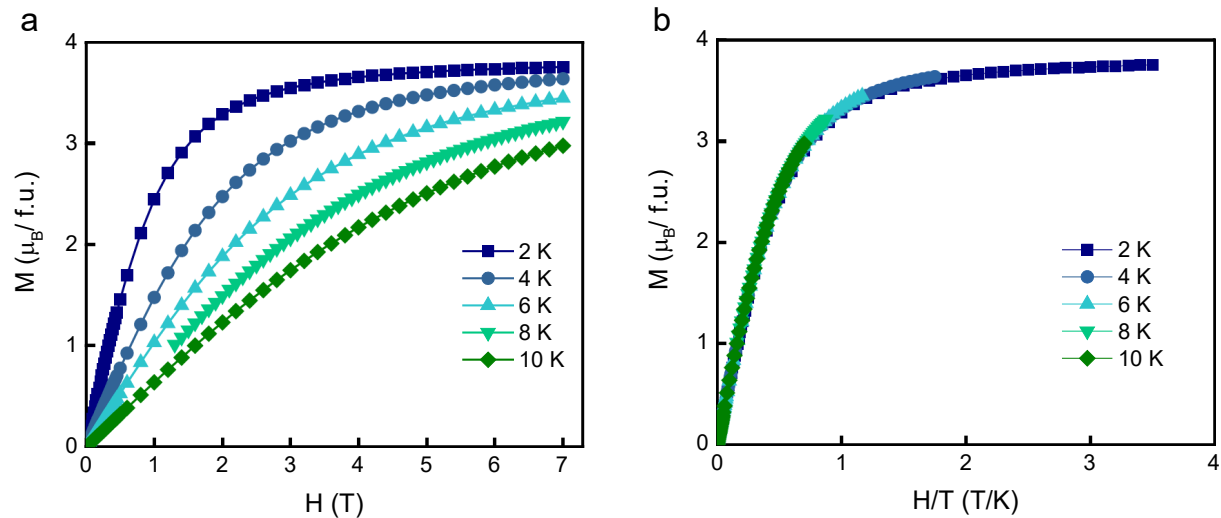


Figure D9. Isothermal M vs. H plots at 2, 4, 6, 8, and 10 K (a). M vs. H/T plots at 2, 4, 6, 8, and 10 K (b) of $[(\text{thiolfan})\text{YbCl}]_2$.

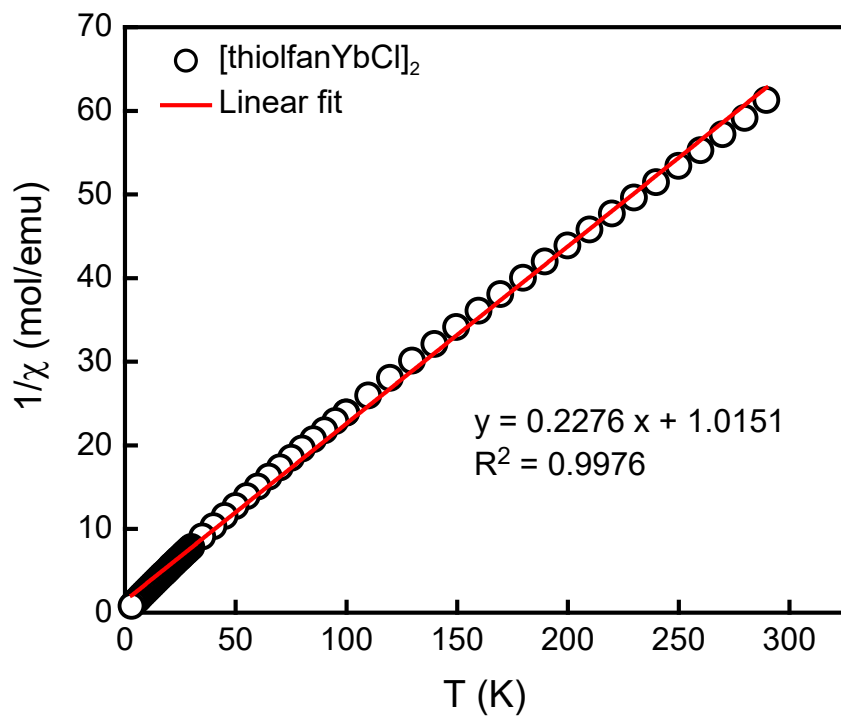


Figure D10. Plot of $1/\chi$ versus T for $[(\text{thiolfan})\text{YbCl}]_2$.

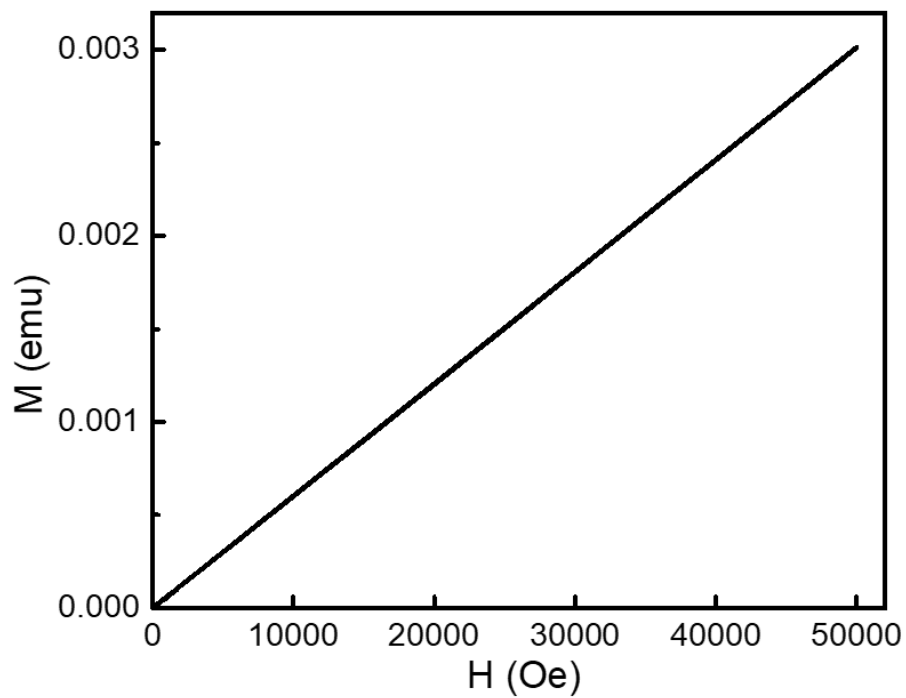


Figure D11. Plot of M versus H at 300 K for [(thiolfan)YbCl]₂.

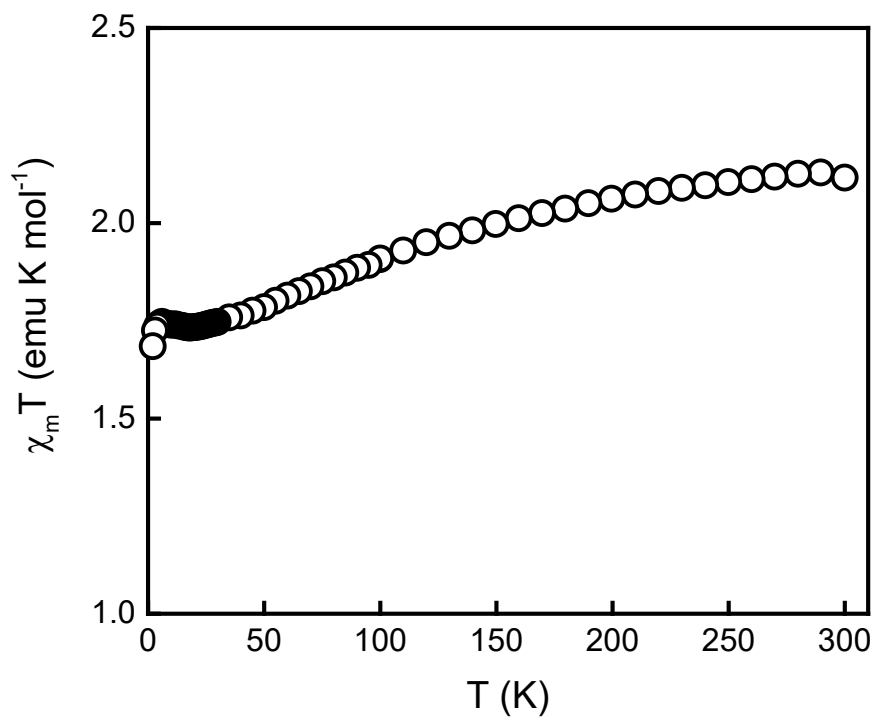


Figure D12. Plot of $\chi_m T$ versus T for (thiolfan*)YbCl(THF)_n under a 1000 Oe dc field in the temperature range 2-300 K.

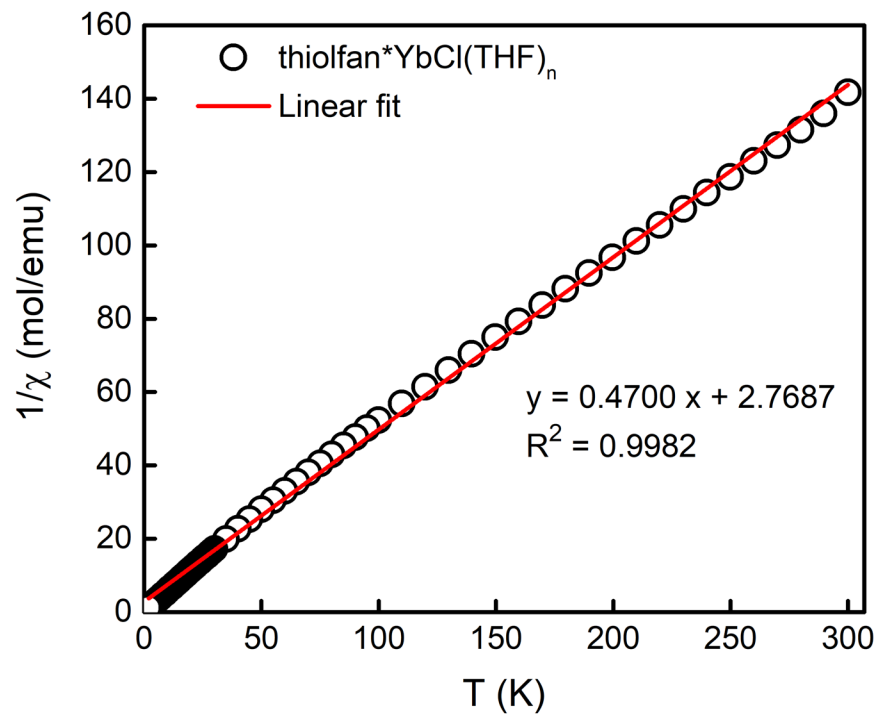


Figure D13. Plot of $1/\chi$ versus T for (thiofan*)YbCl(THF)_n.

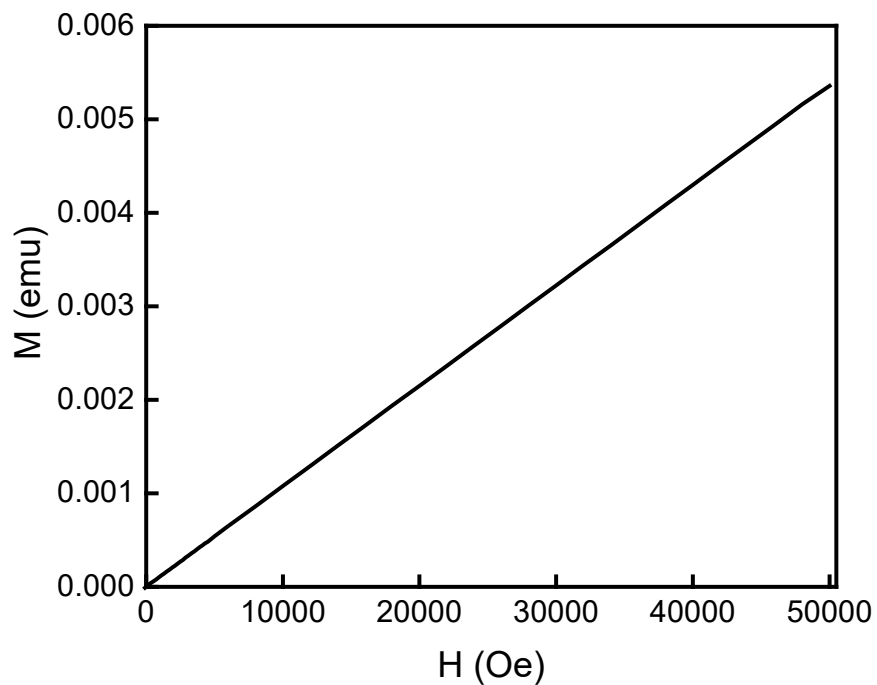


Figure D14. Plot of M versus H at 300 K for (thiofan*)YbCl(THF)_n.

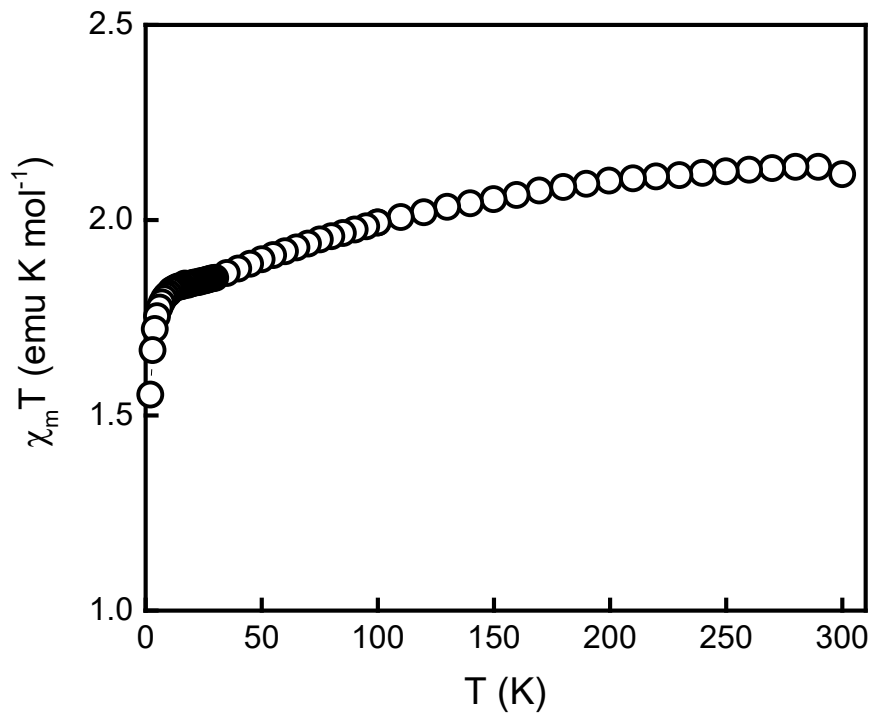


Figure D15. Plot of $\chi_m T$ versus T for (thiolfan)Yb[N(SiMe₃)₂] under a 1000 Oe dc field in the temperature range 2-300 K.

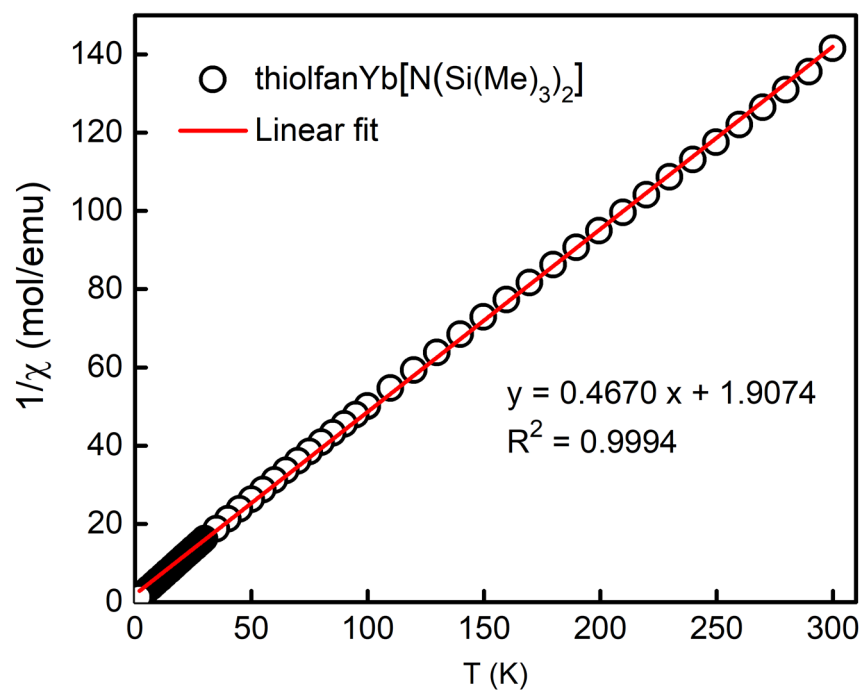


Figure D16. Plot of $1/\chi$ versus T for (thiolfan)Yb[N(SiMe₃)₂].

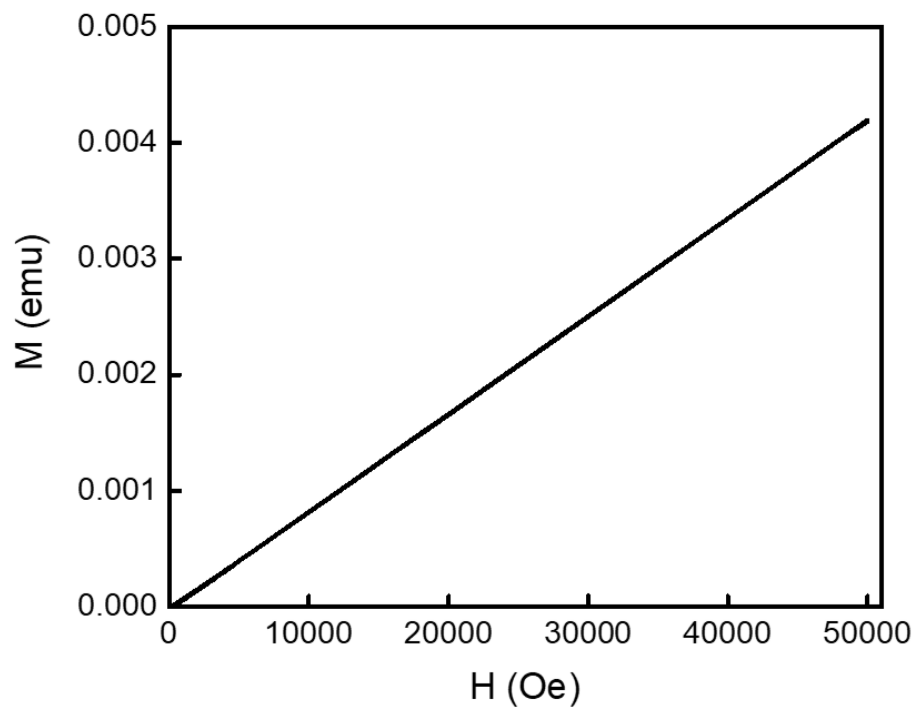


Figure D17. Plot of M versus H at 300 K for (thiolfan)Yb[N(SiMe₃)₂].

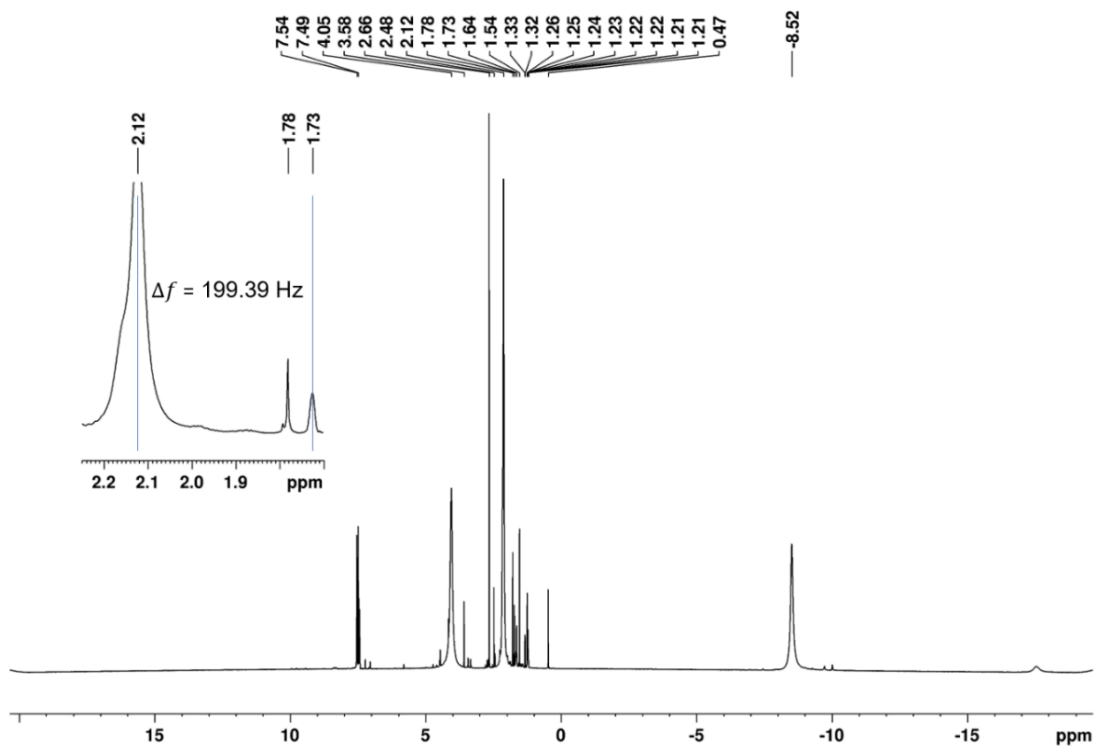


Figure D18. ^1H NMR spectrum (298 K, 500 MHz, THF-d_8) of $(\text{thiolfan})\text{YbCl}(\text{THF})_n$ (chemical shift of intact $\text{THF-d}_8 = 1.72, 3.58$ ppm).

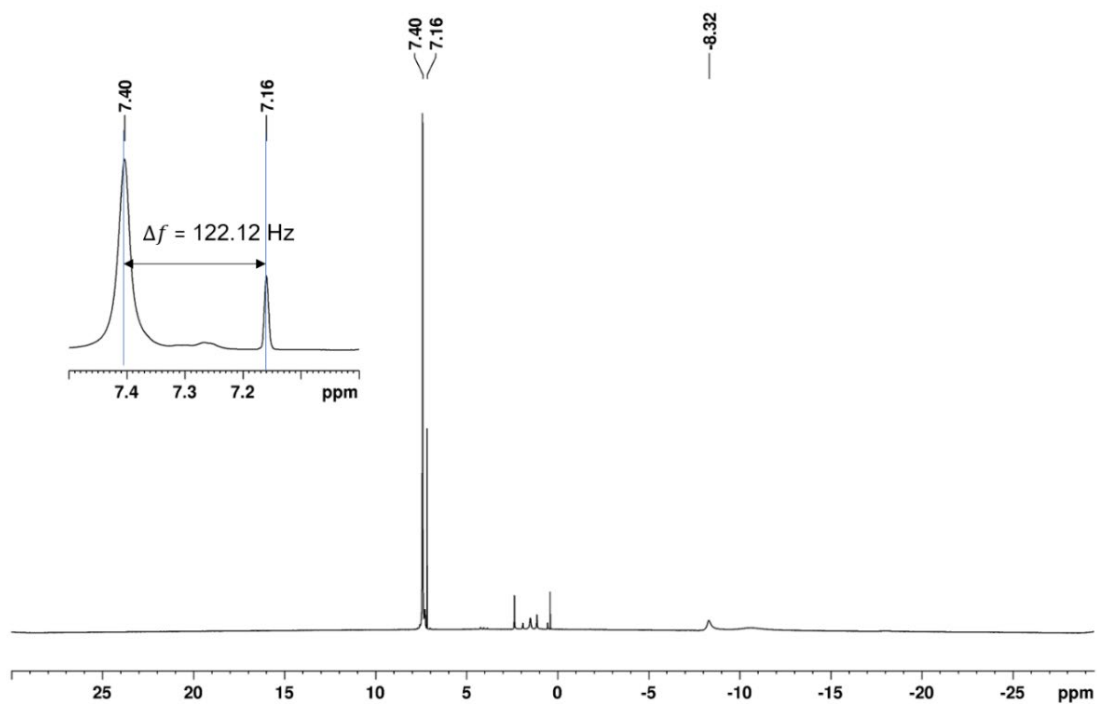


Figure D19. ^1H NMR spectrum (298 K, 500 MHz, C_6D_6) of $(\text{thiolfan})\text{YbCl}(\text{THF})_n$ (chemical shift of intact $\text{C}_6\text{D}_6 = 7.16$ ppm).

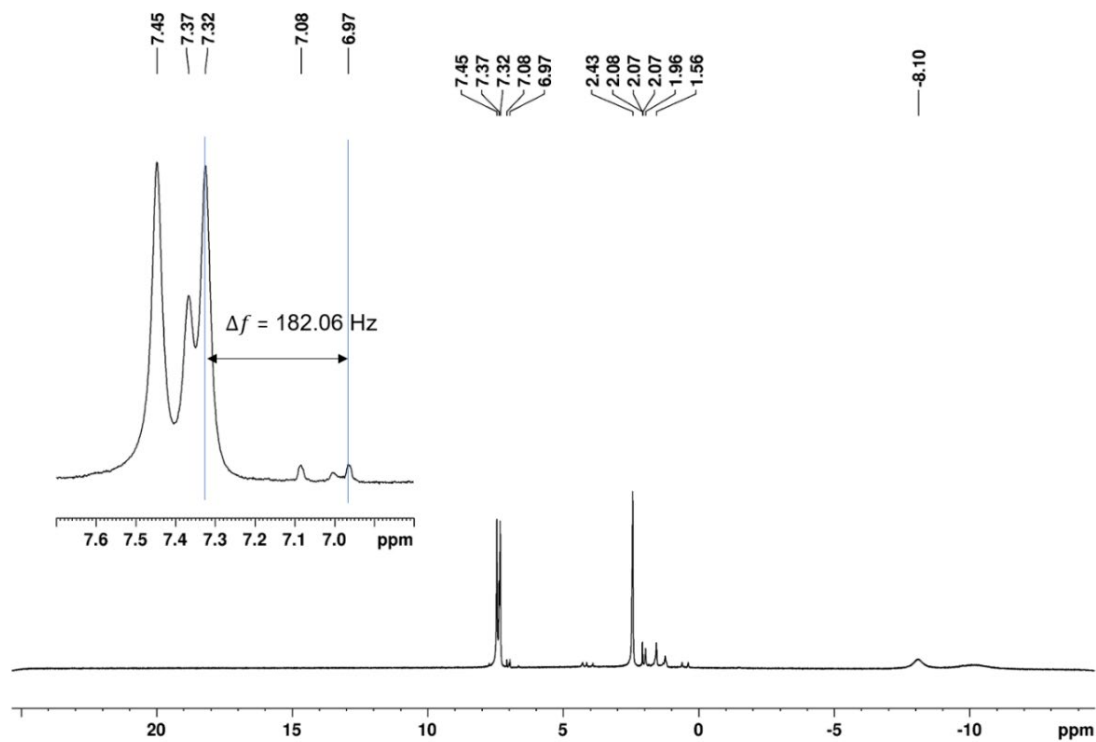


Figure D20. ^1H NMR spectrum (296 K, 500 MHz, Tol- d_8) of (thiolfan)YbCl(THF) $_n$ (chemical shift of intact Tol- d_8 = 2.08, 6.97, 7.01, 7.09 ppm).

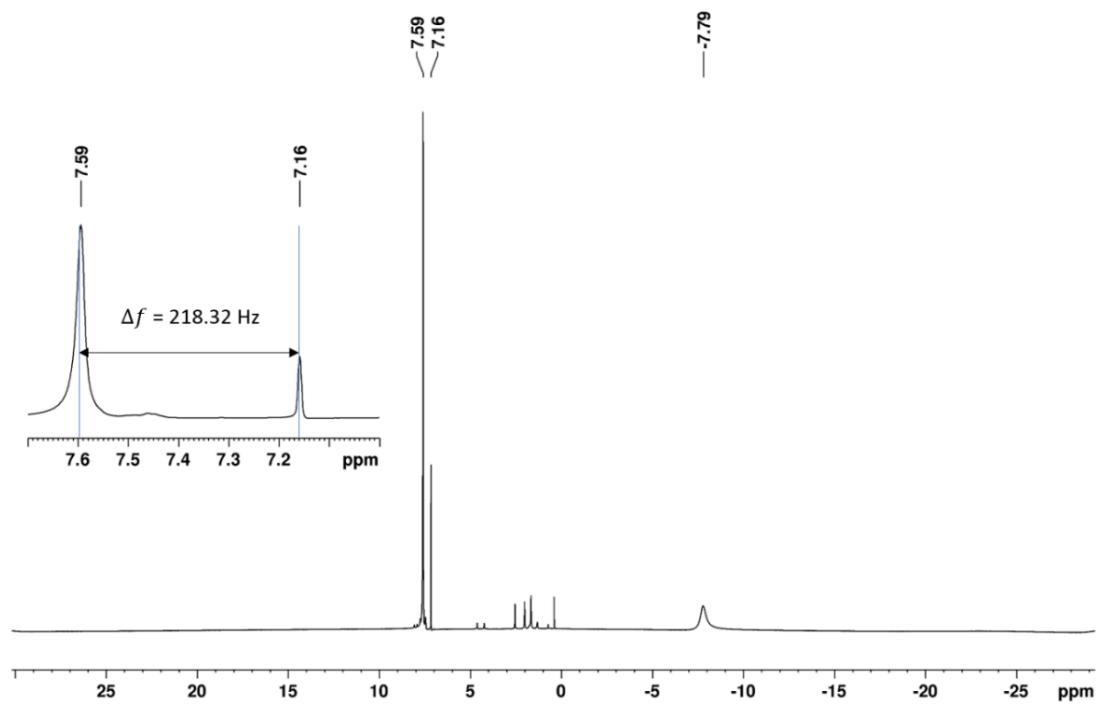


Figure D21. ^1H NMR spectrum (298 K, 500 MHz, C_6D_6) of (thiofan*) $\text{YbCl}(\text{THF})_n$ (chemical shift of intact $\text{C}_6\text{D}_6 = 7.16$ ppm).

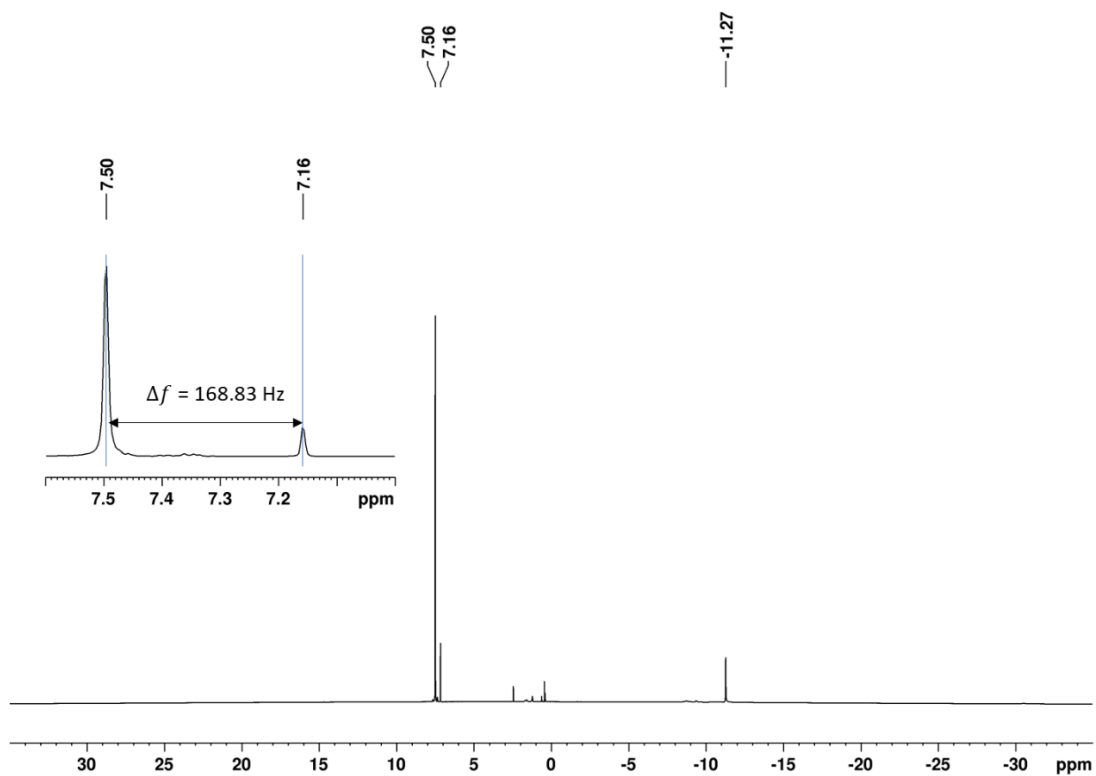


Figure D22. ^1H NMR spectrum (298 K, 500 MHz, C_6D_6) of (thiofan) $\text{Yb}[\text{N}(\text{SiMe}_3)_2]$ (chemical shift of intact $\text{C}_6\text{D}_6 = 7.16$ ppm).

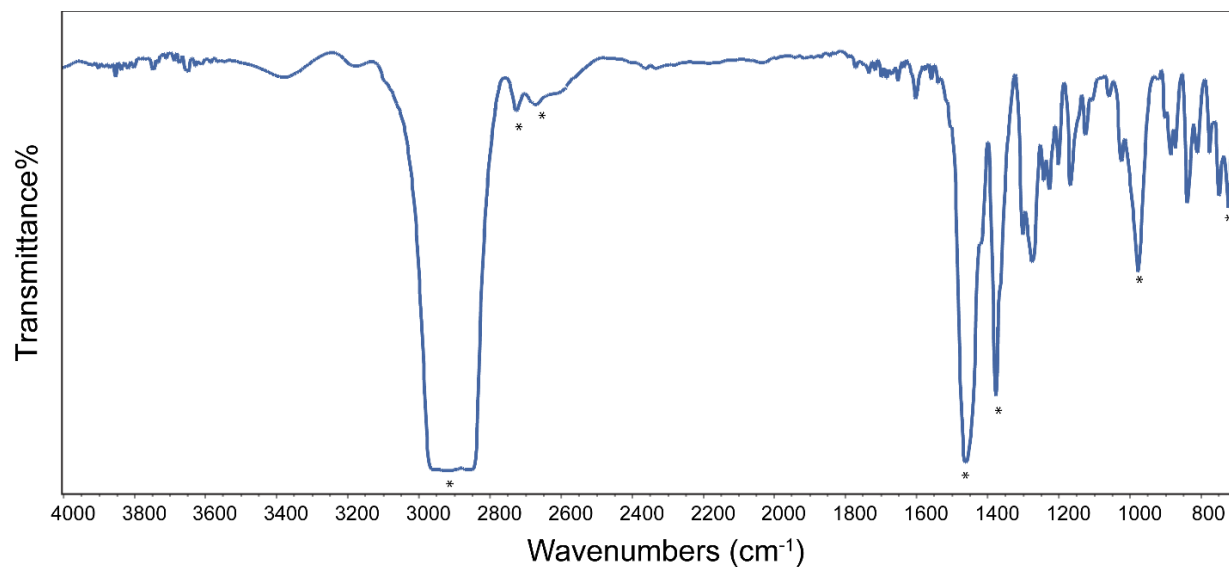


Figure D23. IR (Nujol) spectrum of [(thiolfan)YbCl]₂ (*: Nujol).

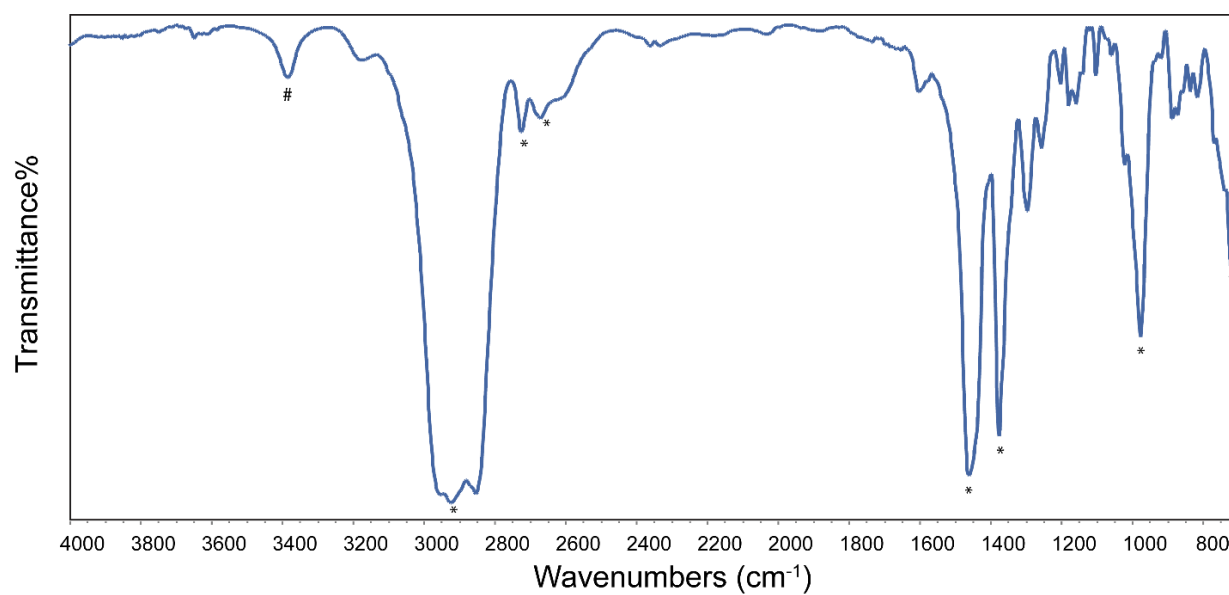


Figure D24. IR (Nujol) spectrum of (thiolfan*)YbCl(THF)_n (*: Nujol; #: trace OH due to minor decomposition of the compound during the measurement).

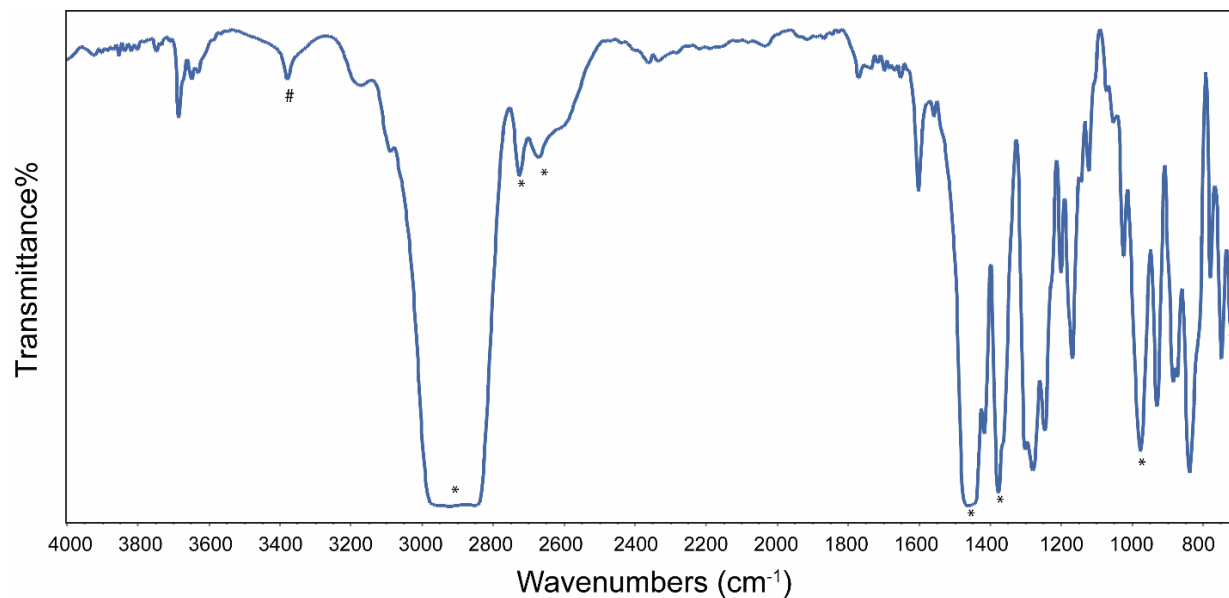


Figure D25. IR (Nujol) spectrum of (thiolfan)Yb[N(SiMe₃)₂] (*: Nujol; #: trace OH/NH due to minor decomposition of the compound during the measurement).

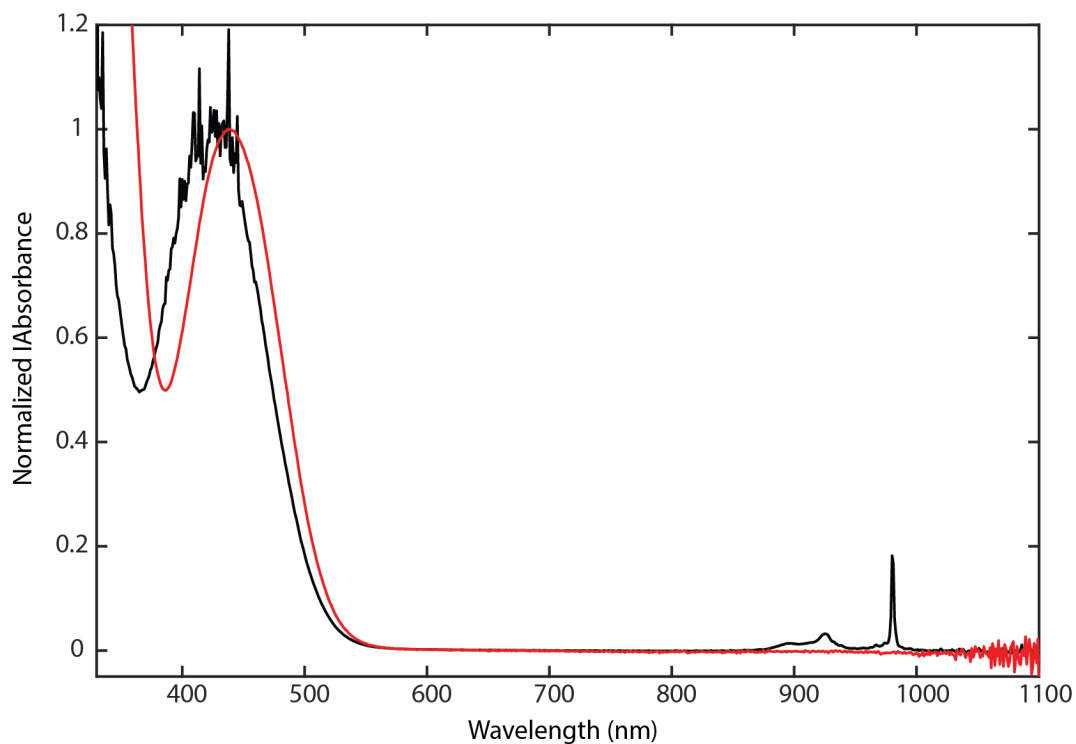


Figure D26. Absorbance of (thiolfan)YbCl(THF) in black and H₂(thiolfan) in red.

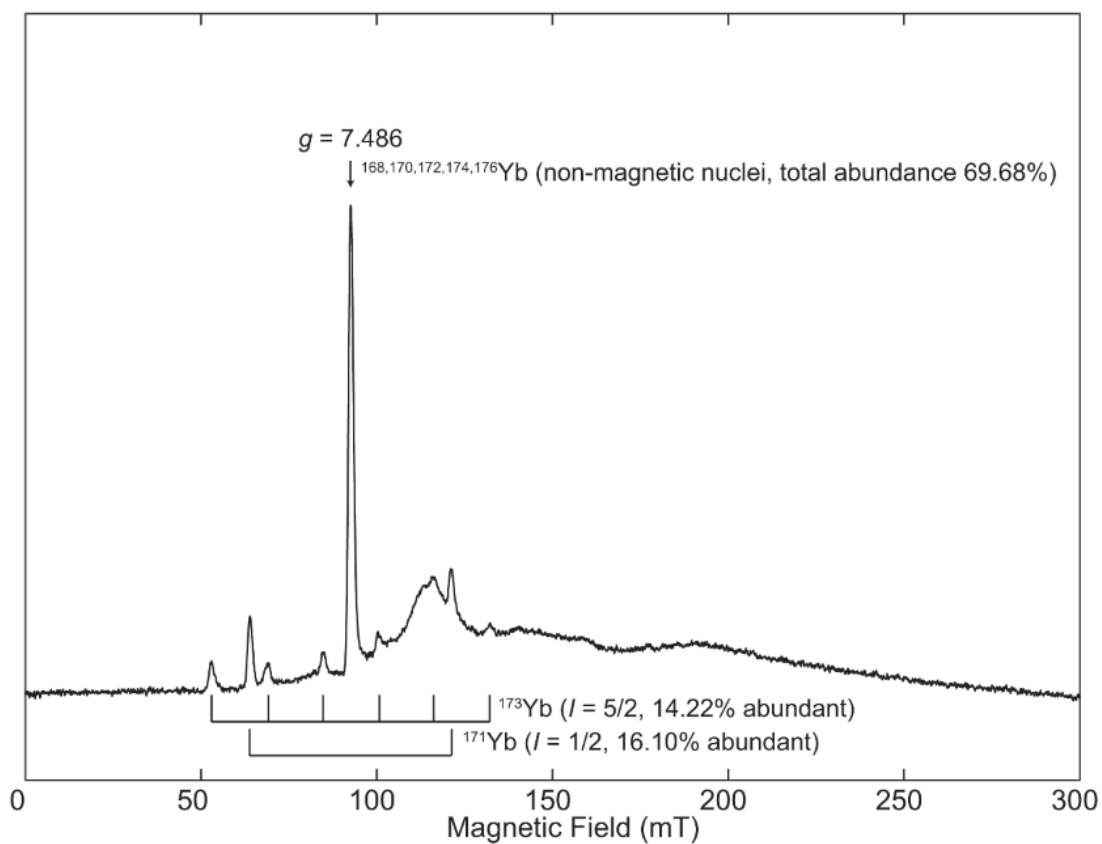


Figure D27. X-band CW-EPR spectrum of (thiolfan)YbCl(THF) in frozen 2-MeTHF glass in the region from 0-300 mT, with resolved features arising from hyperfine couplings to magnetic ^{171}Yb and ^{173}Yb nuclei indicated below. Acquisition parameters: temperature = 5 K; microwave frequency = 9.638 GHz; MW power = 8.8 mW; modulation amplitude = 0.8 mT; conversion time = 10 ms.

References

1. Buglioni, L.; Raymenants, F.; Slattery, A.; Zondag, S. D. A.; Noel, T., Technological Innovations in Photochemistry for Organic Synthesis: Flow Chemistry, High-Throughput Experimentation, Scale-up, and Photoelectrochemistry. *Chem. Rev.* **2021**, *122* (2), 2752–2906.
2. De Luna, P.; Hahn, C.; Higgins, D.; Jaffer, S. A.; Jaramillo, T. F.; Sargent, E. H., What would it take for renewably powered electrosynthesis to displace petrochemical processes? *Science* **2019**, *364* (6438).
3. Hussain, A.; Arif, S. M.; Aslam, M., Emerging renewable and sustainable energy technologies: State of the art. *Renew. Sust. Energ. Rev.* **2017**, *71*, 12-28.
4. Seh, Z. W.; Kibsgaard, J.; Dickens, C. F.; Chorkendorff, I. B.; Norskov, J. K.; Jaramillo, T. F., Combining theory and experiment in electrocatalysis: Insights into materials design. *Science* **2017**, *355* (6321), ead4998.
5. Lohr, T. L.; Marks, T. J., Orthogonal tandem catalysis. *Nat. Chem.* **2015**, *7* (6), 477-482.
6. Grignard, B.; Gennen, S.; Jerome, C.; Kleij, A. W.; Detrembleur, C., Advances in the use of CO₂ as a renewable feedstock for the synthesis of polymers. *Chem. Soc. Rev.* **2019**, *48* (16), 4466-4514.
7. Mohanty, A. K.; Wu, F.; Mincheva, R.; Hakkarainen, M.; Raquez, J.-M.; Mielewski, D. F.; Narayan, R.; Netravali, A. N.; Misra, M., Sustainable polymers. *Nat Rev Methods Primers* **2022**, *2*, 1-27.
8. Sahoo, P. K.; Zhang, Y.; Das, S., CO₂-Promoted Reactions: An Emerging Concept for the Synthesis of Fine Chemicals and Pharmaceuticals. *ACS Catal.* **2021**, *11* (6), 3414-3442.

9. Ye, R.; Zhao, J.; Wickemeyer, B. B.; Toste, F. D.; Somorjai, G. A., Foundations and strategies of the construction of hybrid catalysts for optimized performances. *Nat. Catal.* **2018**, *1* (5), 318-325.
10. Martínez, S.; Veth, L.; Lainer, B.; Dydio, P., Challenges and Opportunities in Multicatalysis. *ACS Catal.* **2021**, *11* (7), 3891-3915.
11. Bruggink, A.; Schoevaart, R.; Kieboom, T., Concepts of nature in organic synthesis: Cascade catalysis and multistep conversions in concert. *Org. Process Res. Dev.* **2003**, *7* (5), 622-640.
12. Fogg, D. E.; dos Santos, E. N., Tandem catalysis: a taxonomy and illustrative review. *Coord. Chem. Rev.* **2004**, *248*, 2365-2379.
13. Wasilke, J. C.; Obrey, S. J.; Baker, R. T.; Bazan, G. C., Concurrent tandem catalysis. *Chem. Rev.* **2005**, *105*, 1001-1020.
14. Robert, C.; Thomas, C. M., Tandem catalysis: a new approach to polymers. *Chem. Soc. Rev.* **2013**, *42* (24), 9392-9402.
15. Upitak, K.; Thomas, C. M., One-Pot Catalysis: A Privileged Approach for Sustainable Polymers? *Acc. Chem. Res.* **2022**, *55* (16), 2168-2179.
16. Heuson, E.; Dumeignil, F., The various levels of integration of chemo- and bio-catalysis towards hybrid catalysis. *Catal. Sci. Technol.* **2020**, *10* (21), 7082-7100.
17. Jia, F.; Chen, X.; Zheng, Y.; Qin, Y.; Tao, Y.; Wang, X., One-pot atom-efficient synthesis of bio-renewable polyesters and cyclic carbonates through tandem catalysis. *Chem. Commun.* **2015**, *51* (40), 8504-8507.
18. Robert, C.; de Montigny, F.; Thomas, C. M., Tandem synthesis of alternating polyesters from renewable resources. *Nat. Commun.* **2011**, *2*, 586.

19. Si, G.; Qi, M.; Tan, C.; Chen, C., Tandem Catalysts Combining Polymer Synthesis, Postpolymerization Modification, and Vitriimer Formation. *Macromolecules* **2021**, *54* (13), 6153-6160.
20. Fouilloux, H.; Qiang, W.; Robert, C.; Placet, V.; Thomas, C. M., Multicatalytic Transformation of (Meth)acrylic Acids: a One-Pot Approach to Biobased Poly(meth)acrylates. *Angew. Chem. Int. Ed.* **2021**, *60* (35), 19374-19382.
21. Guillaume, L.; Marshall, A.; Niessen, N.; Ni, P.; Gauvin, R. M.; Thomas, C. M., Multicatalysis from renewable resources: a direct route to furan-based polyesters. *Green Chem.* **2021**, *23* (18), 6931-6935.
22. Raman, S. K.; Brule, E.; Tschan, M. J.; Thomas, C. M., Tandem catalysis: a new approach to polypeptides and cyclic carbonates. *Chem. Commun.* **2014**, *50* (89), 13773-13776.
23. Schmid, T. E.; Robert, C.; Richard, V.; Raman, S. K.; Guérineau, V.; Thomas, C. M., Aluminum-Catalyzed One-Pot Synthesis of Polyester-b-Polypeptide Block Copolymers by Ring-Opening Polymerization. *Macromol. Chem. Phys* **2019**, *220* (14).
24. Caron, A.; Morin, É.; Collins, S. K., Bifunctional Copper-Based Photocatalyst for Reductive Pinacol-Type Couplings. *ACS Catal.* **2019**, *9* (10), 9458-9464.
25. Fu, R.; Yang, Y.; Feng, W.; Ge, Q.; Feng, Y.; Zeng, X.; Chai, W.; Yi, J.; Yuan, R., An efficient, eco-friendly and sustainable tandem oxidative amidation of alcohols with amines catalyzed by heteropolyanion-based ionic liquids via a bifunctional catalysis process. *Tetrahedron* **2016**, *72* (50), 8319-8326.
26. Jagadeesan, D., Multifunctional nanocatalysts for tandem reactions: A leap toward sustainability. *Appl. Catal. A: Gen.* **2016**, *511*, 59-77.

27. Kenny, R.; Liu, F., Cooperative Trifunctional Organocatalysts for Proficient Proton Transfer Reactions. *Chem. Rec.* **2017**, *17* (5), 535-553.
28. Lidston, C. A. L.; Severson, S. M.; Abel, B. A.; Coates, G. W., Multifunctional Catalysts for Ring-Opening Copolymerizations. *ACS Catal.* **2022**, *12* (18), 11037-11070.
29. Burgener, S.; Luo, S.; McLean, R.; Miller, T. E.; Erb, T. J., A roadmap towards integrated catalytic systems of the future. *Nat. Catal.* **2020**, *3* (3), 186-192.
30. Dodge, H. M.; Natinsky, B. S.; Jolly, B. J.; Zhang, H.; Mu, Y.; Chapp, S. M.; Tran, T. V.; Diaconescu, P. L.; Do, L. H.; Wang, D.; Liu, C.; Miller, A. J. M., Polyketones from Carbon Dioxide and Ethylene by Integrating Electrochemical and Organometallic Catalysis. *ACS Catal.* **2023**, *13*, 4053-4059.
31. Deng, S.; Jolly, B. J.; Wilkes, J. R.; Mu, Y.; Byers, J. A.; Do, L. H.; Miller, A. J. M.; Wang, D.; Liu, C.; Diaconescu, P. L., Spatiotemporal control for integrated catalysis. *Nat Rev Methods Primers* **2023**, *3*.
32. Lee, S. H.; Kumari, N.; Dutta, S.; Jin, X.; Kumar, A.; Koo, J. H.; Lee, I. S., Nanosilica-Confined Synthesis of Orthogonally Active Catalytic Metal Nanocrystals in the Compartmentalized Carbon Framework. *Small* **2019**, *15* (25).
33. Leenders, S. H. A. M.; Gramage-Doria, R.; Bruin, B. d.; Reek, J. N. H., Transition metal catalysis in confined spaces. *Chem. Soc. Rev.* **2015**, *44* (2), 433-448.
34. Lu, J.; Dimroth, J.; Weck, M., Compartmentalization of Incompatible Catalytic Transformations for Tandem Catalysis. *J. Am. Chem. Soc.* **2015**, *137* (40), 12984-12989.
35. Qu, P.; Kuepfert, M.; Hashmi, M.; Weck, M., Compartmentalization and Photoregulating Pathways for Incompatible Tandem Catalysis. *J. Am. Chem. Soc.* **2021**, *143*, 4705-4713.

36. Qu, P. Y.; Kuepfert, M.; Jockusch, S.; Weck, M., Compartmentalized Nanoreactors for One-Pot Redox-Driven Transformations. *ACS Catal.* **2019**, *9* (4), 2701-2706.
37. Rayder, T. M.; Bensalah, A. T.; Li, B.; Byers, J. A.; Tsung, C. K., Engineering Second Sphere Interactions in a Host-Guest Multicomponent Catalyst System for the Hydrogenation of Carbon Dioxide to Methanol. *J. Am. Chem. Soc.* **2021**, *143* (3), 1630-1640.
38. Sato, H.; Hummel, W.; Gröger, H., Cooperative Catalysis of Noncompatible Catalysts through Compartmentalization: Wacker Oxidation and Enzymatic Reduction in a One-Pot Process in Aqueous Media. *Angew. Chem. Int. Ed.* **2015**, *54* (15), 4488-4492.
39. Womble, C. T.; Kuepfert, M.; Weck, M., Multicompartment Polymeric Nanoreactors for Non-Orthogonal Cascade Catalysis. *Macromol. Rapid Commun.* **2019**, *40* (1), e1800580.
40. Xie, G. X.; Zhang, J. N.; Ma, X. B., Compartmentalization of Multiple Catalysts into Outer and Inner Shells of Hollow Mesoporous Nanospheres for Heterogeneous Multi-Catalyzed/Multi-Component Asymmetric Organocascade. *ACS Catal.* **2019**, *9* (10), 9081-9086.
41. Blanco, V.; Leigh, D. A.; Marcos, V., Artificial switchable catalysts. *Chem. Soc. Rev.* **2015**, *44* (15), 5341-5370.
42. Choudhury, J., Recent developments on artificial switchable catalysis. *Tetrahedron Lett.* **2018**, *59* (6), 487-495.
43. De, S.; Pramanik, S.; Schmittel, M., A Toggle Nanoswitch Alternately Controlling Two Catalytic Reactions. *Angew. Chem. Int. Ed.* **2014**, *53* (51), 14255-14259.
44. Miller, A. J. M., Controlling ligand binding for tunable and switchable catalysis: cation-modulated hemilability in pincer-crown ether ligands. *Dalton Trans.* **2017**, *46* (36), 11987-12000.

45. Doerr, A. M.; Burroughs, J. M.; Gitter, S. R.; Yang, X.; Boydston, A. J.; Long, B. K., Advances in Polymerizations Modulated by External Stimuli. *ACS Catal.* **2020**, *10* (24), 14457-14515.
46. Guillaume, S. M.; Kirillov, E.; Sarazin, Y.; Carpentier, J. F., Beyond stereoselectivity, switchable catalysis: some of the last frontier challenges in ring-opening polymerization of cyclic esters. *Chem. Eur. J.* **2015**, *21* (22), 7988-8003.
47. Kaler, S.; Jones, M. D., Recent advances in externally controlled ring-opening polymerisations. *Dalton Trans.* **2022**, *51* (4), 1241-1256.
48. Romain, C.; Zhu, Y.; Dingwall, P.; Paul, S.; Rzepa, H. S.; Buchard, A.; Williams, C. K., Chemoselective Polymerizations from Mixtures of Epoxide, Lactone, Anhydride, and Carbon Dioxide. *J. Am. Chem. Soc.* **2016**, *138* (12), 4120-4131.
49. Teator, A. J.; Lastovickova, D. N.; Bielawski, C. W., Switchable Polymerization Catalysts. *Chem. Rev.* **2016**, *116* (4), 1969-1992.
50. Lai, A.; Hern, Z. C.; Shen, Y.; Dai, R.; Diaconescu, P. L., Metal Complexes for Redox Switching and Control of Reactivity. In *Comprehensive Coordination Chemistry III*, Constable, E. C.; Parkin, G.; Que Jr, L., Eds. Elsevier: Oxford, **2021**; pp 155-180.
51. Natinsky, B. S.; Lu, S.; Copeland, E. D.; Quintana, J. C.; Liu, C., Solution Catalytic Cycle of Incompatible Steps for Ambient Air Oxidation of Methane to Methanol. *ACS Cent. Sci.* **2019**, *5* (9), 1584-1590.
52. Qi, M.; Zhang, H.; Dong, Q.; Li, J.; Musgrave, R. A.; Zhao, Y.; Dulock, N.; Wang, D.; Byers, J. A., Electrochemically switchable polymerization from surface-anchored molecular catalysts. *Chem. Sci.* **2021**, *12* (26), 9042-9052.

53. Bajada, M. A.; Sanjose-Orduna, J.; Di Liberto, G.; Tosoni, S.; Pacchioni, G.; Noel, T.; Vile, G., Interfacing single-atom catalysis with continuous-flow organic electrosynthesis. *Chem. Soc. Rev.* **2022**, *51* (10), 3898-3925.
54. Coperet, C.; Chabanas, M.; Saint-Arroman, R. P.; Basset, J. M., Homogeneous and heterogeneous catalysis: Bridging the gap through surface organometallic chemistry. *Angew. Chem. Int. Ed.* **2003**, *42* (2), 156-181.
55. Yoon, K. Y.; Noh, J.; Gan, Q.; Edwards, J. P.; Tuba, R.; Choi, T. L.; Grubbs, R. H., Scalable and continuous access to pure cyclic polymers enabled by 'quarantined' heterogeneous catalysts. *Nat. Chem.* **2022**, *14* (11), 1242-1248.
56. Choudhury, J.; Semwal, S., Emergence of Stimuli-Controlled Switchable Bifunctional Catalysts. *Synlett* **2018**, *29* (2), 141-147.
57. Neilson, B. M.; Bielawski, C. W., Illuminating Photoswitchable Catalysis. *ACS Catal.* **2013**, *3* (8), 1874-1885.
58. Leibfarth, F. A.; Mattson, K. M.; Fors, B. P.; Collins, H. A.; Hawker, C. J., External regulation of controlled polymerizations. *Angew. Chem. Int. Ed.* **2013**, *52* (1), 199-210.
59. Zhu, S.; Zhao, M.; Zhou, H.; Wen, Y.; Wang, Y.; Liao, Y.; Zhou, X.; Xie, X., One-pot synthesis of hyperbranched polymers via visible light regulated switchable catalysis. *Nat. Commun.* **2023**, *14* (1), 1622.
60. Eisenreich, F.; Kathan, M.; Dallmann, A.; Ihrig, S. P.; Schwaar, T.; Schmidt, B. M.; Hecht, S., A photoswitchable catalyst system for remote-controlled (co)polymerization in situ. *Nat. Catal.* **2018**, *1* (7), 516-522.

61. Raman, S. K.; Raja, R.; Arnold, P. L.; Davidson, M. G.; Williams, C. K., Waste not, want not: CO₂ (re)cycling into block polymers. *Chem. Commun.* **2019**, 55 (51), 7315-7318.
62. Biernesser, A. B.; Delle Chiaie, K. R.; Curley, J. B.; Byers, J. A., Block Copolymerization of Lactide and an Epoxide Facilitated by a Redox Switchable Iron-Based Catalyst. *Angew. Chem. Int. Ed.* **2016**, 55 (17), 5251-5254.
63. Biernesser, A. B.; Li, B.; Byers, J. A., Redox-controlled polymerization of lactide catalyzed by bis(imino)pyridine iron bis(alkoxide) complexes. *J. Am. Chem. Soc.* **2013**, 135 (44), 16553-16560.
64. Chen, C., Redox-Controlled Polymerization and Copolymerization. *ACS Catal.* **2018**, 8 (6), 5506-5514.
65. Chen, M.; Yang, B.; Chen, C., Redox-Controlled Olefin (Co)Polymerization Catalyzed by Ferrocene-Bridged Phosphine-Sulfonate Palladium Complexes. *Angew. Chem. Int. Ed.* **2015**, 54 (51), 15520-15524.
66. Hermans, C.; Rong, W.; Spaniol, T. P.; Okuda, J., Lanthanum complexes containing a bis(phenolate) ligand with a ferrocene-1,1'-diylidithio backbone: synthesis, characterization, and ring-opening polymerization of rac-lactide. *Dalton Trans.* **2016**, 45 (19), 8127-8133.
67. Kaiser, J. M.; Long, B. K., Recent developments in redox-active olefin polymerization catalysts. *Coord. Chem. Rev.* **2018**, 372, 141-152.
68. Qi, M.; Dong, Q.; Wang, D.; Byers, J. A., Electrochemically Switchable Ring-Opening Polymerization of Lactide and Cyclohexene Oxide. *J. Am. Chem. Soc.* **2018**, 140 (17), 5686-5690.
69. Sauer, A.; Buffet, J.-C.; Spaniol, T. P.; Nagaie, H.; Mashima, K.; Okuda, J., Switching the Lactide Polymerization Activity of a Cerium Complex by Redox Reactions. *ChemCatChem* **2013**, 5 (5), 1088-1091.

70. Zhao, M.; Chen, C., Accessing Multiple Catalytically Active States in Redox-Controlled Olefin Polymerization. *ACS Catal.* **2017**, *7* (11), 7490-7494.
71. Zou, W.; Pang, W.; Chen, C., Redox control in palladium catalyzed norbornene and alkyne polymerization. *Inorg. Chem. Front.* **2017**, *4* (5), 795-800.
72. Broderick, E. M.; Guo, N.; Vogel, C. S.; Xu, C.; Sutter, J.; Miller, J. T.; Meyer, K.; Mehrkhodavandi, P.; Diaconescu, P. L., Redox control of a ring-opening polymerization catalyst. *J. Am. Chem. Soc.* **2011**, *133* (24), 9278-9281.
73. Broderick, E. M.; Guo, N.; Wu, T.; Vogel, C. S.; Xu, C.; Sutter, J.; Miller, J. T.; Meyer, K.; Cantat, T.; Diaconescu, P. L., Redox control of a polymerization catalyst by changing the oxidation state of the metal center. *Chem. Commun.* **2011**, *47* (35), 9897-9899.
74. Quan, S. M.; Wang, X.; Zhang, R.; Diaconescu, P. L., Redox Switchable Copolymerization of Cyclic Esters and Epoxides by a Zirconium Complex. *Macromolecules* **2016**, *49* (18), 6768-6778.
75. Wei, J.; Riffel, M. N.; Diaconescu, P. L., Redox Control of Aluminum Ring-Opening Polymerization: A Combined Experimental and DFT Investigation. *Macromolecules* **2017**, *50* (5), 1847-1861.
76. Dai, R.; Diaconescu, P. L., Investigation of a zirconium compound for redox switchable ring opening polymerization. *Dalton Trans.* **2019**, *48* (9), 2996-3002.
77. Wei, J. N.; Diaconescu, P. L., Redox-Switchable Ring-Opening Polymerization with Ferrocene Derivatives. *Acc. Chem. Res.* **2019**, *52* (2), 415-424.
78. Abubekеров, M.; Khan, S. I.; Diaconescu, P. L., Ferrocene-bis(phosphinimine) Nickel(II) and Palladium(II) Alkyl Complexes: Influence of the Fe–M (M = Ni and Pd) Interaction on Redox Activity and Olefin Coordination. *Organometallics* **2017**, *36* (22), 4394-4402.

79. Abubekеров, M.; Shepard, S. M.; Diaconescu, P. L., Switchable Polymerization of Norbornene Derivatives by a Ferrocene-Palladium(II) Heteroscorpionate Complex. *Eur. J. Inorg. Chem.* **2016**, *2016* (15-16), 2634-2640.
80. Wang, X.; Thevenon, A.; Brosmer, J. L.; Yu, I.; Khan, S. I.; Mehrkhodavandi, P.; Diaconescu, P. L., Redox control of group 4 metal ring-opening polymerization activity toward L-lactide and epsilon-caprolactone. *J. Am. Chem. Soc.* **2014**, *136* (32), 11264-11267.
81. Lowe, M. Y.; Shu, S.; Quan, S. M.; Diaconescu, P. L., Investigation of redox switchable titanium and zirconium catalysts for the ring opening polymerization of cyclic esters and epoxides. *Inorg. Chem. Front.* **2017**, *4* (11), 1798-1805.
82. Quan, S. M.; Wei, J.; Diaconescu, P. L., Mechanistic Studies of Redox-Switchable Copolymerization of Lactide and Cyclohexene Oxide by a Zirconium Complex. *Organometallics* **2017**, *36* (22), 4451-4457.
83. Abubekеров, M.; Vlcek, V.; Wei, J.; Miehlich, M. E.; Quan, S. M.; Meyer, K.; Neuhauser, D.; Diaconescu, P. L., Exploring Oxidation State-Dependent Selectivity in Polymerization of Cyclic Esters and Carbonates with Zinc(II) Complexes. *iScience* **2018**, *7*, 120-131.
84. Dai, R.; Lai, A.; Alexandrova, A. N.; Diaconescu, P. L., Geometry Change in a Series of Zirconium Compounds during Lactide Ring-Opening Polymerization. *Organometallics* **2018**, *37* (21), 4040-4047.
85. Gregson, C. K.; Blackmore, I. J.; Gibson, V. C.; Long, N. J.; Marshall, E. L.; White, A. J., Titanium-salen complexes as initiators for the ring opening polymerisation of rac-lactide. *Dalton Trans.* **2006**, (25), 3134-3140.

86. Lai, A.; Hern, Z. C.; Diaconescu, P. L., Switchable Ring-Opening Polymerization by a Ferrocene Supported Aluminum Complex. *ChemCatChem* **2019**, *11* (16), 4210-4218.
87. Fang, Y. Y.; Gong, W. J.; Shang, X. J.; Li, H. X.; Gao, J.; Lang, J. P., Synthesis and structure of a ferric complex of 2,6-di(1H-pyrazol-3-yl)pyridine and its excellent performance in the redox-controlled living ring-opening polymerization of epsilon-caprolactone. *Dalton Trans.* **2014**, *43* (22), 8282-8289.
88. Shen, Y.; Shepard, S. M.; Reed, C. J.; Diaconescu, P. L., Zirconium complexes supported by a ferrocene-based ligand as redox switches for hydroamination reactions. *Chem. Commun.* **2019**, *55* (39), 5587-5590.
89. Shepard, S. M.; Diaconescu, P. L., Redox-Switchable Hydroelementation of a Cobalt Complex Supported by a Ferrocene-Based Ligand. *Organometallics* **2016**, *35* (15), 2446-2453.
90. Tran, T. V.; Shen, Y.; Nguyen, H. D.; Deng, S.; Roshandel, H.; Cooper, M. M.; Watson, J. R.; Byers, J. A.; Diaconescu, P. L.; Do, L. H., N-Carboxyanhydrides directly from amino acids and carbon dioxide and their tandem reactions to therapeutic alkaloids. *Green Chem.* **2022**, *24* (23), 9245-9252.
91. Lorkovic, I. M.; Duff, R. R.; Wrighton, M. S., Use of the Redox-Active Ligand 1,1'-Bis(Diphenylphosphino)Cobaltocene to Reversibly Alter the Rate of the Rhodium(I)-Catalyzed Reduction and Isomerization of Ketones and Alkenes. *J. Am. Chem. Soc.* **1995**, *117* (12), 3617-3618.
92. Huang, W.; Diaconescu, P. L., Reactivity and Properties of Metal Complexes Enabled by Flexible and Redox-Active Ligands with a Ferrocene Backbone. *Inorg. Chem.* **2016**, *55* (20), 10013-10023.

93. Hern, Z. C.; Quan, S. M.; Dai, R.; Lai, A.; Wang, Y.; Liu, C.; Diaconescu, P. L., ABC and ABAB Block Copolymers by Electrochemically Controlled Ring-Opening Polymerization. *J. Am. Chem. Soc.* **2021**, *143* (47), 19802-19808.
94. Liu, G.; He, H.; Wang, J., Ferrocene Redox Controlled Reversible Immobilization of Ruthenium Carbene in Ionic Liquid: A Versatile Catalyst for Ring-Closing Metathesis. *Adv. Synth. Catal.* **2009**, *351* (10), 1610-1620.
95. Süßner, M.; Plenio, H., Redox-switchable phase tags for recycling of homogeneous catalysts. *Angew. Chem. Int. Ed.* **2005**, *44* (42), 6885-6888.
96. Lastovickova, D. N.; Teator, A. J.; Shao, H.; Liu, P.; Bielawski, C. W., A redox-switchable ring-closing metathesis catalyst. *Inorg. Chem. Front.* **2017**, *4* (9), 1525-1532.
97. Hettmanczyk, L.; Manck, S.; Hoyer, C.; Hohloch, S.; Sarkar, B., Heterobimetallic complexes with redox-active mesoionic carbenes as metalloligands: electrochemical properties, electronic structures and catalysis. *Chem. Commun.* **2015**, *51* (54), 10949-10952.
98. Klenk, S.; Rupf, S.; Suntrup, L.; van der Meer, M.; Sarkar, B., The Power of Ferrocene, Mesoionic Carbenes, and Gold: Redox-Switchable Catalysis. *Organometallics* **2017**, *36* (10), 2026-2035.
99. Hettmanczyk, L.; Suntrup, L.; Klenk, S.; Hoyer, C.; Sarkar, B., Heteromultimetallic Complexes with Redox-Active Mesoionic Carbenes: Control of Donor Properties and Redox-Induced Catalysis. *Chem. Eur. J.* **2017**, *23* (3), 576-585.
100. Ibáñez, S.; Poyatos, M.; Dawe, L. N.; Gusev, D.; Peris, E., Ferrocenyl-Imidazolylidene Ligand for Redox-Switchable Gold-Based Catalysis. A Detailed Study on the Redox-Switching Abilities of the Ligand. *Organometallics* **2016**, *35* (16), 2747-2758.

101. Feyrer, A.; Armbruster, M. K.; Fink, K.; Breher, F., Metal Complexes of a Redox-Active [1]Phosphaferrocenophane: Structures, Electrochemistry and Redox-Induced Catalysis. *Chem. Eur. J.* **2017**, *23* (31), 7402-7408.
102. Tennyson, A. G.; Lynch, V. M.; Bielawski, C. W., Arrested Catalysis: Controlling Kumada Coupling Activity via a Redox-Active N-Heterocyclic Carbene. *J. Am. Chem. Soc.* **2010**, *132*, 9420–9429.
103. Feyrer, A.; Breher, F., Palladium complexes of ferrocene-based phosphine ligands as redox-switchable catalysts in Buchwald–Hartwig cross-coupling reactions. *Inorg. Chem. Front.* **2017**, *4* (7), 1125-1134.
104. Yang, H.; Gabbai, F. P., Activation of a Hydroamination Gold Catalyst by Oxidation of a Redox-Noninnocent Chlorostibine Z-Ligand. *J. Am. Chem. Soc.* **2015**, *137* (41), 13425-13432.
105. Slone, C. S.; Mirkin, C. A.; Yap, G. P. A.; Guzei, I. A.; Rheingold, A. L., Oxidation-State-Dependent Reactivity and Catalytic Properties of a Rh(I) Complex Formed from a Redox-Switchable Hemilabile Ligand. *J. Am. Chem. Soc.* **1997**, *119*, 10743-10753.
106. Kourkine, I. V.; Slone, C. S.; Mirkin, C. A., Small Molecule-Induced Intramolecular Electron “Pitch and Catch” in a Rhodium(I) Complex with Substitutionally Inert Redox-Active Ligands. *Inorg. Chem.* **1999**, *38*, 2758-2759.
107. Fleckenstein, C. A.; Plenio, H., Redox-Switchable Phase Tags – Facile Mitsunobu Reactions using Ferrocenyl-Tagged Triphenylphosphine. *Adv. Synth. Catal.* **2006**, *348* (9), 1058-1062.
108. Ringenberg, M. R.; Kokatam, S. L.; Heiden, Z. M.; Rauchfuss, T. B., Redox-Switched Oxidation of Dihydrogen Using a Non-Innocent Ligand. *J. Am. Chem. Soc.* **2008**, *130*, 788-789.

109. Kato, H.; Ishigame, T.; Oshima, N.; Hoshiya, N.; Shimawaki, K.; Arisawa, M.; Shuto, S., One-Pot Ring-Closing Metathesis (RCM)/Oxidation by an Assisted Tandem Ruthenium Catalysis for the Synthesis of 2-Quinolones. *Adv. Synth. Catal.* **2011**, *353* (14-15), 2676-2680.
110. Varnado, C. D., Jr.; Rosen, E. L.; Collins, M. S.; Lynch, V. M.; Bielawski, C. W., Synthesis and study of olefin metathesis catalysts supported by redox-switchable diaminecarbene[3]ferrocenophanes. *Dalton Trans.* **2013**, *42* (36), 13251-13264.
111. Neumann, P.; Dib, H.; Caminade, A. M.; Hey-Hawkins, E., Redox control of a dendritic ferrocenyl-based homogeneous catalyst. *Angew. Chem. Int. Ed.* **2015**, *54* (1), 311-314.
112. Zhang, Y.; Sun, Q.; Wang, Y.; Yuan, D.; Yao, Y.; Shen, Q., Intramolecular hydroamination reactions catalyzed by zirconium complexes bearing bridged bis(phenolato) ligands. *RSC Adv.* **2016**, *6* (13), 10541-10548.
113. Wang, X.; Chen, Z.; Sun, X.-L.; Tang, Y.; Xie, Z., Intramolecular Hydroamination of Aminoalkenes Catalyzed by a Cationic Zirconium Complex. *Org. Lett.* **2011**, *13*, 4758-4761.
114. Müller, C.; Saak, W.; Doye, S., Neutral Group-IV Metal Catalysts for the Intramolecular Hydroamination of Alkenes. *Eur. J. Org. Chem.* **2008**, *2008* (16), 2731-2739.
115. Majumder, S.; Odom, A. L., Group-4 Dipyrrrolylmethane Complexes in Intramolecular Olefin Hydroamination. *Organometallics* **2008**, *27*, 1174-1177.
116. Knight, P. D.; Munslow, I.; O'Shaughnessy, P. N.; Scott, P., Zirconium catalysed enantioselective hydroamination/cyclisation. *Chem. Commun.* **2004**, (7), 894-895.
117. Hu, Y.-C.; Liang, C.-F.; Tsai, J.-H.; Yap, G. P. A.; Chang, Y.-T.; Ong, T.-G., Zirconium Complexes Supported by Imidazolones: Synthesis, Characterization, and Application of Precatalysts for the Hydroamination of Aminoalkenes. *Organometallics* **2010**, *29* (15), 3357-3361.

118. Lee, A. V.; Schafer, L. L., Modular N, O-Chelating Ligands: Group-4 Amidate Complexes for Catalytic Hydroamination. *Eur. J. Inorg. Chem.* **2007**, 2007 (16), 2245-2255.
119. Luconi, L.; Klosin, J.; Smith, A. J.; Germain, S.; Schulz, E.; Hannedouche, J.; Giambastiani, G., Cationic Group-IV pincer-type complexes for polymerization and hydroamination catalysis. *Dalton Trans.* **2013**, 42 (45), 16056-16065.
120. Manssen, M.; Schafer, L. L., Titanium catalysis for the synthesis of fine chemicals - development and trends. *Chem. Soc. Rev.* **2020**, 49 (19), 6947-6994.
121. Müller, C.; Loos, C.; Schulenberg, N.; Doye, S., Neutral Ti Catalysts for the Intramolecular Hydroamination of Alkenes. *Eur. J. Org. Chem.* **2006**, 2006 (11), 2499-2503.
122. Stubbert, B. D.; Marks, T. J., Mechanistic Investigation of Intramolecular Aminoalkene and Aminoalkyne Hydroamination/Cyclization Catalyzed by Highly Electrophilic, Tetravalent Constrained Geometry 4d and 5f Complexes. Evidence for an M-N σ -Bonded Insertive Pathway. *J. Am. Chem. Soc.* **2007**, 129, 6149-6167
123. Zhou, X.; Wei, B.; Sun, X. L.; Tang, Y.; Xie, Z., Asymmetric hydroamination catalyzed by a new chiral zirconium system: reaction scope and mechanism. *Chem. Commun.* **2015**, 51 (26), 5751-5753.
124. Jiang, Z.; Wang, Y.; Liu, W.; Li, Y., Group 4 Complexes Bearing Pyrrolide Ligand for Intramolecular Alkene Hydroamination and Activation of C \equiv N Bond. *Z. Anorg. Allg. Chem.* **2018**, 644 (15), 844-848.
125. Antunes, M. A.; Munhá, R. F.; Alves, L. G.; Schafer, L. L.; Martins, A. M., Intramolecular hydroamination catalysis using trans-N,N'-dibenzylcyclam zirconium complexes. *J. Organomet. Chem.* **2011**, 696 (1), 2-6.

126. Leitch, D. C.; Platel, R. H.; Schafer, L. L., Mechanistic elucidation of intramolecular aminoalkene hydroamination catalyzed by a tethered bis(ureate) complex: evidence for proton-assisted C-N bond formation at zirconium. *J. Am. Chem. Soc.* **2011**, *133* (39), 15453-15463.
127. Leitch, D. C.; Payne, P. R.; Dunbar, C. R.; Schafer, L. L., Broadening the Scope of Group 4 Hydroamination Catalysis Using a Tethered Ureate Ligand. *J. Am. Chem. Soc.* **2009**, *131*, 18246–18247.
128. Luconi, L.; Rossin, A.; Tuci, G.; Germain, S.; Schulz, E.; Hannedouche, J.; Giambastiani, G., Intramolecular Hydroamination Reactions Catalyzed by Neutral and Cationic Group IV Pyridylamido Complexes. *ChemCatChem* **2013**, *5* (5), 1142-1151.
129. Lauzon, J. M. P.; Schafer, L. L., Tethered Bis(amidate) and Bis(ureate) Supported Zirconium Precatalysts for the Intramolecular Hydroamination of Aminoalkenes. *Z. Anorg. Allg. Chem.* **2015**, *641* (1), 128-135.
130. Gribkov, D. V.; Hultsch, K. C., Hydroamination/cyclization of aminoalkenes using cationic zirconocene and titanocene catalyts. *Angew. Chem. Int. Ed.* **2004**, *43* (41), 5542-5546.
131. Bytschkov, I.; Doye, S., Group-IV metal complexes as hydroamination catalyts. *Eur. J. Org. Chem.* **2003**, *2003* (6), 935-946.
132. Ackermann, L.; Kaspar, L. T.; Althammer, A., Hydroaminations of unactivated alkenes with basic alkylamines: group 4 metal halide catalyts and Bronsted-acid organocatalyts. *Org. Biomol. Chem.* **2007**, *5* (12), 1975-1978.
133. Chen, J.; Goforth, S. K.; McKeown, B. A.; Gunnoe, T. B., Bronsted acid-catalysed intramolecular hydroamination of unactivated alkenes: metal triflates as an in situ source of triflic acid. *Dalton Trans.* **2017**, *46* (9), 2884-2891.

134. Hultsch, K. C.; Hampel, F.; Wagner, T., New Yttrium Complexes Bearing Diamidoamine Ligands as Efficient and Diastereoselective Catalysts for the Intramolecular Hydroamination of Alkenes and Alkynes. *Organometallics* **2004**, *23*, 2601-2612.
135. Stubbert, B. D.; Marks, R. S., Constrained Geometry Organoactinides as Versatile Catalysts for the Intramolecular Hydroamination/Cyclization of Primary and Secondary Amines Having Diverse Tethered C-C Unsaturation. *J. Am. Chem. Soc.* **2007**, *129*, 4253-4271
136. Pangborn, A. B.; Giardello, M. A.; Grubbs, R. H.; Rosen, R. K.; Timmers, F. J., Safe and Convenient Procedure for Solvent Purification. *Organometallics* **1996**, *15*, 1518-1520.
137. Bradley, D. C.; Thomas, I. M., Metallo-organic compounds containing metal-nitrogen bonds. Part I. Some dialkylamino-derivatives of titanium and zirconium. *J. Chem. Soc.* **1960**, 3857-3861.
138. Yakelis, N. A.; Bergman, R. G., Sodium Tetrakis[(3,5-trifluoromethyl)phenyl]borate (NaBArF(24)): Safe Preparation, Standardized Purification, and Analysis of Hydration. *Organometallics* **2005**, *24* (14), 3579-3581.
139. Broderick, E. M.; Gutzwiller, N. P.; Diaconescu, P. L., Inter- and Intramolecular Hydroamination with a Uranium Dialkyl Precursor. *Organometallics* **2010**, *29* (15), 3242-3251.
140. Chai, Z.; Hua, D.; Li, K.; Chu, J.; Yang, G., A novel chiral yttrium complex with a tridentate linked amido-indenyl ligand for intramolecular hydroamination. *Chem. Commun.* **2014**, *50* (2), 177-179.
141. Bender, C. F.; Widenhoefer, R. A., Platinum-Catalyzed Intramolecular Hydroamination of Unactivated Olefins with Secondary Alkylamines. *J. Am. Chem. Soc.* **2005**, *127*, 1070-1071.
142. Eedugurala, N.; Wang, Z.; Yan, K.; Boteju, K. C.; Chaudhary, U.; Kobayashi, T.; Ellern, A.; Slowing, I. I.; Pruski, M.; Sadow, A. D., β -SiH-Containing Tris(silazido) Rare-Earth Complexes as

Homogeneous and Grafted Single-Site Catalyst Precursors for Hydroamination. *Organometallics* **2017**, *36* (6), 1142-1153.

143. Jiang, H. J.; Liu, K.; Yu, J.; Zhang, L.; Gong, L. Z., Switchable Stereoselectivity in Bromoaminocyclization of Olefins: Using Bronsted Acids of Anionic Chiral Cobalt(III) Complexes. *Angew. Chem. Int. Ed.* **2017**, *56* (39), 11931-11935.

144. Li, J.; Grubbs, R. H.; Stoltz, B. M., Palladium-Catalyzed Aerobic Intramolecular Aminoacetoxylation of Alkenes Enabled by Catalytic Nitrate. *Org. Lett.* **2016**, *18* (21), 5449-5451.

145. Liu, G.-Q.; Li, W.; Wang, Y.-M.; Ding, Z.-Y.; Li, Y.-M., Ligand acceleration in ZnI₂-catalyzed intramolecular hydroamination of unfunctionalized olefins. *Tetrahedron Lett.* **2012**, *53* (33), 4393-4396.

146. Liu, Z.; Hartwig, J. F., Mild, Rhodium-Catalyzed Intramolecular Hydroamination of Unactivated Terminal and Internal Olefins with Primary and Secondary Amines. *J. Am. Chem. Soc.* **2008**, *130*, 1570-1571.

147. Manna, K.; Eedugurala, N.; Sadow, A. D., Zirconium-catalyzed desymmetrization of aminodialkenes and aminodialkynes through enantioselective hydroamination. *J. Am. Chem. Soc.* **2015**, *137* (1), 425-435.

148. Chai, Z.; Chu, J.; Qi, Y.; Tang, M.; Hou, J.; Yang, G., Half-sandwich chiral rare-earth metal complexes with linked tridentate amido-indenyl ligand: synthesis, characterization, and catalytic properties for intramolecular hydroamination. *RSC Adv.* **2017**, *7* (3), 1759-1765.

149. Hussein, L.; Purkait, N.; Biyikal, M.; Tausch, E.; Roesky, P. W.; Blechert, S., Highly enantioselective hydroamination to six-membered rings by heterobimetallic catalysts. *Chem. Commun.* **2014**, *50* (29), 3862-3864.

150. Crimmin, M. R.; Arrowsmith, M.; Barrett, A. G. M.; Casely, I. J.; Hill, M. S.; Procopiou, P. A., Intramolecular Hydroamination of Aminoalkenes by Calcium and Magnesium Complexes: A Synthetic and Mechanistic Study. *J. Am. Chem. Soc.* **2009**, *131*, 9670–9685.
151. Dhar, D.; Yee, G. M.; Spaeth, A. D.; Boyce, D. W.; Zhang, H.; Dereli, B.; Cramer, C. J.; Tolman, W. B., Perturbing the Copper(III)-Hydroxide Unit through Ligand Structural Variation. *J. Am. Chem. Soc.* **2016**, *138* (1), 356-368.
152. Chávez, I.; Alvarez-Carena, A.; Molins, E.; Maniukiewicz, W.; Roig, A.; Arancibia, A.; Arancibia, V.; Brand, H.; Manríquez, J. M., Selective oxidants for organometallic compounds containing a stabilising anion of highly reactive cations (3,5(CF₃)₂C₆H₃)₄B⁻)Cp₂Fe⁺ and (3,5(CF₃)₂C₆H₃)₄B⁻)Cp*₂Fe⁺. *J. Organomet. Chem.* **2000**, *601*, 126–132.
153. *Carbon Dioxide as Chemical Feedstock*. Wiley: 2010.
154. Alves, M.; Grignard, B.; Mereau, R.; Jerome, C.; Tassaing, T.; Detrembleur, C., Organocatalyzed coupling of carbon dioxide with epoxides for the synthesis of cyclic carbonates: catalyst design and mechanistic studies. *Catal. Sci. Technol.* **2017**, *7* (13), 2651-2684.
155. Zhang, D.; Lahasky, S. H.; Guo, L.; Lee, C.-U.; Lavan, M., Polypeptoid Materials: Current Status and Future Perspectives. *Macromolecules* **2012**, *45* (15), 5833-5841.
156. Kricheldorf, H. R., Polypeptides and 100 years of chemistry of alpha-amino acid N-carboxyanhydrides. *Angew. Chem. Int. Ed.* **2006**, *45* (35), 5752-5784.
157. Li, H. Y.; Chen, C. Y.; Cheng, H. T.; Chu, Y. H., Exploiting 1,2,3-Triazolium Ionic Liquids for Synthesis of Tryptanthrin and Chemoselective Extraction of Copper(II) Ions and Histidine-Containing Peptides. *Molecules* **2016**, *21* (10).

158. Brandão, P.; Marques, C.; Pinto, E.; Pineiro, M.; Burke, A. J., Petasis adducts of tryptanthrin – synthesis, biological activity evaluation and druglikeness assessment. *New J. Chem.* **2021**, *45* (32), 14633-14649.
159. Liang, J. L.; Park, S. E.; Kwon, Y.; Jahng, Y., Synthesis of benzo-annulated tryptanthrins and their biological properties. *Bioorg. Med. Chem.* **2012**, *20* (16), 4962-4967.
160. Gangloff, N.; Ulbricht, J.; Lorson, T.; Schlaad, H.; Luxenhofer, R., Peptoids and Polypeptoids at the Frontier of Supra- and Macromolecular Engineering. *Chem. Rev.* **2016**, *116* (4), 1753-1802.
161. Lau, K. H. A., Peptoids for biomaterials science. *Biomater. Sci.* **2014**, *2* (5), 627-633.
162. Farthing, A. C., 627. Synthetic Polypeptides. Part I. Synthesis of Oxaxolid2 : 5-diones and a New Reaction of Glycine. *J. Chem. Soc.* **1950**, 3213-3217.
163. Leuchs, H., About the glycine-carboxylic acid. *Ber. Dtsch. Chem. Ges.* **1906**, *39*, 851-861.
164. Secker, C.; Brosnan, S. M.; Luxenhofer, R.; Schlaad, H., Poly(alpha-Peptoid)s Revisited: Synthesis, Properties, and Use as Biomaterial. *Macromol. Biosci.* **2015**, *15* (7), 881-891.
165. Verma, C.; Sharma, S.; Pathak, A., A phosgene and peroxide-free one-pot tandem synthesis of isatoic anhydrides involving anthranilic acid, Boc anhydride, and 2-chloro-N-methyl pyridinium iodide. *Tetrahedron Lett.* **2013**, *54* (50), 6897-6899.
166. Laconde, G.; Amblard, M.; Martinez, J., Synthesis of alpha-Amino Acid N-Carboxyanhydrides. *Org. Lett.* **2021**, *23* (16), 6412-6416.
167. Zhang, W.-Z.; Zhang, N.; Sun, Y.-Q.; Ding, Y.-W.; Lu, X.-B., Palladium-Catalyzed Cyclization Reaction of o-Iodoanilines, CO₂, and CO: Access to Isatoic Anhydrides. *ACS Catal.* **2017**, *7* (12), 8072-8076.

168. Wang, S.; Li, X.; Zang, J.; Liu, M.; Zhang, S.; Jiang, G.; Ji, F., Palladium-Catalyzed Multistep Tandem Carbonylation/N-Dealkylation/Carbonylation Reaction: Access to Isatoic Anhydrides. *J. Org. Chem.* **2020**, *85* (4), 2672-2679.
169. Endo, T.; Sudo, A., Well-defined, environment-friendly synthesis of polypeptides based on phosgene-free transformation of amino acids into urethane derivatives and their applications. *Polym. Int.* **2019**, *69* (3), 219-227.
170. Kramer, J. R.; Deming, T. J., General Method for Purification of α -Amino acid-N-carboxyanhydrides Using Flash Chromatography. *Biomacromolecules* **2010**, *11*, 3668–3672.
171. Crosignani, S.; Gonzalez, J.; Swinnen, D., Polymer-Supported Mukaiyama Reagent: A Useful Coupling Reagent for the Synthesis of Esters and Amides. *Org. Lett.* **2004**, *6*, 4579-4582.
172. Doriti, A.; Brosnan, S. M.; Weidner, S. M.; Schlaad, H., Synthesis of polysarcosine from air and moisture stable N-phenoxy carbonyl-N-methylglycine assisted by tertiary amine base. *Polym. Chem.* **2016**, *7* (18), 3067-3070.
173. Fu, X.; Li, Z.; Wei, J.; Sun, J.; Li, Z., Schiff base and reductive amination reactions of α -amino acids: a facile route toward N-alkylated amino acids and peptoid synthesis. *Polym. Chem.* **2018**, *9* (37), 4617-4624.
174. Li, Z.; Fu, X. H.; Huang, S. X.; Sun, J.; Li, Z. B., Oligo(beta-peptoid)s with Backbone Chirality from Aspartic Acid Derivatives: Synthesis and Property Investigation. *Acs Omega* **2020**, *5* (51), 33125-33132.
175. Liu, S.; Pestano, J. P.; Wolf, C., Regioselective Copper-catalyzed C-N and C-S Bond Formation using Amines, Thiols and Halobenzoic Acids. *Synthesis* **2007**, (22), 3519-3527.

176. Wang, Y.; Zhang, M.; Cao, S.; Lin, H.; Gao, M.; Li, Z., Synthesis of 1-Substituted 4(1H)-Quinazolinones Under Solvent-Free Conditions. *Synth. Commun.* **2012**, *42* (18), 2715-2727.
177. Weaver, D. F.; Wang, Z.; Doyle, L.; Villar, L.; Vilekar, P. S. Furosemide analogues and compositions and uses thereof for treatment of alzheimer's disease. 2022.
178. Zhou, X.; Ding, Y.; Huang, H., Palladium-Catalyzed Carbonylative Difunctionalization of C=N Bond of Azaarenes or Imines to Quinazolinones. *Chem. Asian J.* **2020**, *15* (11), 1678-1682.
179. Hoorfar, A.; Ollis, W. D.; Price, J. A.; Stephanatou, J. S.; Stoddart, J. F., Conformational Behaviour of Medium-sized Rings. Part 11 .I Dianthranilides and Trianthranilides. *J. Chem. Soc. Perkin Trans. 1* **1982**, 1649-1699.
180. Matsumura, H.; Hashizume, H.; Matsushita, A.; Eigyo, M. Pyrrolo(1,4)benzodiazepine derivatives. 1989.
181. Yu, L.; Ye, J.; Zhang, X.; Ding, Y.; Xu, Q., Recyclable (PhSe)₂-catalyzed selective oxidation of isatin by H₂O₂: a practical and waste-free access to isatoic anhydride under mild and neutral conditions. *Catal. Sci. Technol.* **2015**, *5* (10), 4830-4838.
182. Li, Y.; Zhang, S.; Wang, R.; Cui, M.; Liu, W.; Yang, Q.; Kuang, C., Synthesis of novel tryptanthrin derivatives as dual inhibitors of indoleamine 2,3-dioxygenase 1 and tryptophan 2,3-dioxygenase. *Bioorg. Med. Chem. Lett.* **2020**, *30* (11), 127159.
183. Liu, K.; Wu, Y.; Xi, Y.; Li, Z., Cotton fiber modified via N-phenyl anhydride in situ ring-opening polymerization with controllable surface morphology and its wettability. *Prog. Org. Coat.* **2022**, *162*.

184. Yang, G.; Cheng, C.; Xu, G. B.; Tang, L.; Chua, K. L.; Yang, Y. Y., Synthesis and antibiofilm evaluation of 3-hydroxy-2,3-dihydroquinazolin-4(1H)-one derivatives against opportunistic pathogen *Acinetobacter baumannii*. *Bioorg. Med. Chem.* **2020**, *28* (16), 115606.
185. Abd El Sater, M.; Jaber, N.; Schulz, E., Chiral Salen Complexes for Asymmetric Heterogeneous Catalysis: Recent Examples for Recycling and Cooperativity. *ChemCatChem* **2019**, *11* (16), 3662-3687.
186. Baleizão, C., Chiral vanadyl Schiff base complex anchored on silicas as solid enantioselective catalysts for formation of cyanohydrins: optimization of the asymmetric induction by support modification. *J. Catal.* **2003**, *215* (2), 199-207.
187. Nodzevska, A.; Wadolowska, A.; Watkinson, M., Recent advances in the catalytic oxidation of alkene and alkane substrates using immobilized manganese complexes with nitrogen containing ligands. *Coord. Chem. Rev.* **2019**, *382*, 181-216.
188. Kureshy, R.; Ahmad, I.; Khan, N.; Abdi, S.; Pathak, K.; Jasra, R., Chiral Mn(III) salen complexes covalently bonded on modified MCM-41 and SBA-15 as efficient catalysts for enantioselective epoxidation of nonfunctionalized alkenes. *J. Catal.* **2006**, *238* (1), 134-141.
189. Zhang, H.; Zou, Y.; Wang, Y. M.; Shen, Y.; Zheng, X., Asymmetric epoxidation of cis/trans-beta-methylstyrene catalysed by immobilised Mn(salen) with different linkages: heterogenisation of homogeneous asymmetric catalysis. *Chem. Eur. J.* **2014**, *20* (25), 7830-7841.
190. Abd El Sater, M.; Mellah, M.; Dragoe, D.; Kolodziej, E.; Jaber, N.; Schulz, E., Chiral Chromium Salen@rGO as Multipurpose and Recyclable Heterogeneous Catalyst. *Chem. Eur. J.* **2021**, *27* (36), 9454-9460.

191. Baleizão, C.; Garcia, H., Chiral Salen Complexes: An Overview to Recoverable and Reusable Homogeneous and Heterogeneous Catalysts. *Chem. Rev.* **2006**.
192. Wannaprom, N.; Vanalabhpatana, P., Electro-Oxidation of Aldehydes in Alkaline Solution by Electropolymerized Nickel Salen-Based Film Modified Electrodes. *J. Electrochem. Soc.* **2014**, *161* (12), G86-G97.
193. Sun, L.; Reddu, V.; Fisher, A. C.; Wang, X., Electrocatalytic reduction of carbon dioxide: opportunities with heterogeneous molecular catalysts. *Energy Environ. Sci.* **2020**, *13* (2), 374-403.
194. Kuźniarska-Biernacka, I.; Silva, A. R.; Carvalho, A. P.; Pires, J.; Freire, C., Anchoring of Chiral Manganese(III) Salen Complex onto Organo Clay and Porous Clay Heterostructure and Catalytic Activity in Alkene Epoxidation. *Catal. Lett.* **2009**, *134*, 63-71.
195. Xing, C.; Deng, J.; Tan, R.; Gao, M.; Hao, P.; Yin, D.; Yin, D., Cooperative chiral salen TiIV catalyst supported on ionic liquid-functionalized graphene oxide accelerates asymmetric sulfoxidation in water. *Catal. Sci. Technol.* **2017**, *7* (24), 5944-5952.
196. Heo, J.; Ahn, H.; Won, J.; Son, J. G.; Shon, H. K.; Lee, T. G.; Han, S. W.; Baik, M. H., Electro-inductive effect: Electrodes as functional groups with tunable electronic properties. *Science* **2020**, *370*, 214-219.
197. Shen, Y.; Mu, Y.; Wang, D.; Liu, C.; Diaconescu, P. L., Tuning Electrode Reactivity through Organometallic Complexes. *ACS Appl. Mater. Interfaces* **2023**, *15* (24), 28851-28878.
198. Balas, M.; Beaudoin, S.; Proust, A.; Launay, F.; Villanneau, R., Advantages of Covalent Immobilization of Metal-Salophen on Amino-Functionalized Mesoporous Silica in Terms of Recycling and Catalytic Activity for CO₂ Cycloaddition onto Epoxides. *Eur. J. Inorg. Chem.* **2021**, *2021* (16), 1581-1591.

199. Pujari, S. P.; Scheres, L.; Marcelis, A. T.; Zuilhof, H., Covalent surface modification of oxide surfaces. *Angew. Chem. Int. Ed.* **2014**, *53* (25), 6322-6356.
200. Materna, K. L.; Crabtree, R. H.; Brudvig, G. W., Anchoring groups for photocatalytic water oxidation on metal oxide surfaces. *Chem. Soc. Rev.* **2017**, *46* (20), 6099-6110.
201. Roy, S.; Bhanja, P.; Safikul Islam, S.; Bhaumik, A.; Islam, S. M., A new chiral Fe(III)-salen grafted mesoporous catalyst for enantioselective asymmetric ring opening of racemic epoxides at room temperature under solvent-free conditions. *Chem. Commun.* **2016**, *52* (9), 1871-1874.
202. Liu, M.; Zhao, Z.-P.; Chen, K.-C.; Liu, W.-F., New chiral catalytic membrane reactor created by immobilizing salen-Mn(III) onto APTES modified ceramic membrane and its performances in epoxidation of styrene. *Catal. Commun.* **2015**, *64*, 70-74.
203. Kureshy, R. I.; Ahmad, I.; Khan, N.-u. H.; Abdi, S. H. R.; Pathak, K.; Jasra, R. V., Encapsulation of a chiral Mn(III)(salen) complex in ordered mesoporous silicas: an approach towards heterogenizing asymmetric epoxidation catalysts for non-functionalized alkenes. *Tetrahedron: Asymmetry* **2005**, *16* (21), 3562-3569.
204. Zhu, C.; Xuan, W.; Cui, Y., Luminescent microporous metal-metallosalen frameworks with the primitive cubic net. *Dalton Trans.* **2012**, *41* (14), 3928-3932.
205. Zhang, T.; Song, F.; Lin, W., Blocking bimolecular activation pathways leads to different regioselectivity in metal-organic framework catalysis. *Chem. Commun.* **2012**, *48* (70), 8766-8768.
206. Yuan, G.; Jiang, H.; Zhang, L.; Liu, Y.; Cui, Y., Metallosalen-based crystalline porous materials: Synthesis and property. *Coord. Chem. Rev.* **2019**, *378*, 483-499.
207. Song, F.; Wang, C.; Falkowski, J. M.; Ma, L.; Lin, W., Isorecticular Chiral Metal-Organic Frameworks for Asymmetric Alkene Epoxidation: Tuning Catalytic Activity by Controlling

Framework Catenation and Varying Open Channel Sizes. *J. Am. Chem. Soc.* **2010**, *132*, 15390–15398.

208. Li, J.; Yang, J.; Liu, Y. Y.; Ma, J. F., Two heterometallic-organic frameworks composed of iron(III)-salen-based ligands and d(10) metals: gas sorption and visible-light photocatalytic degradation of 2-chlorophenol. *Chem. Eur. J.* **2015**, *21* (11), 4413-4421.

209. Liang, L.; Astruc, D., The copper(I)-catalyzed alkyne-azide cycloaddition (CuAAC) “click” reaction and its applications. An overview. *Coord. Chem. Rev.* **2011**, *255* (23-24), 2933-2945.

210. Tăbăcaru, A.; Furdui, B.; Ghinea, I. O.; Cârâc, G.; Dinică, R. M., Recent advances in click chemistry reactions mediated by transition metal based systems. *Inorganica Chim. Acta* **2017**, *455*, 329-349.

211. Castro, V.; Rodriguez, H.; Albericio, F., CuAAC: An Efficient Click Chemistry Reaction on Solid Phase. *ACS Comb. Sci.* **2016**, *18* (1), 1-14.

212. Meldal, M., Polymer “Clicking” by CuAAC Reactions. *Macromol. Rapid Commun.* **2008**, *29*, 1016-1051.

213. Arslan, M.; Tasdelen, M. A., Polymer Nanocomposites via Click Chemistry Reactions. *Polymers* **2017**, *9* (10).

214. Wu, L.; Eberhart, M.; Shan, B.; Nayak, A.; Brennaman, M. K.; Miller, A. J. M.; Shao, J.; Meyer, T. J., Stable Molecular Surface Modification of Nanostructured, Mesoporous Metal Oxide Photoanodes by Silane and Click Chemistry. *ACS Appl. Mater. Interfaces* **2019**, *11* (4), 4560-4567.

215. Yao, S. A.; Ruther, R. E.; Zhang, L.; Franking, R. A.; Hamers, R. J.; Berry, J. F., Covalent attachment of catalyst molecules to conductive diamond: CO₂ reduction using “smart” electrodes. *J. Am. Chem. Soc.* **2012**, *134* (38), 15632-15635.

216. Bartocci, S.; Sabaté, F.; Yafteh Mihan, F.; Bosque, R.; Rodríguez, L.; Dalla Cort, A., Novel uranyl(VI) complexes incorporating ethynyl groups as potential halide chemosensors: an experimental and computational approach. *Supramol. Chem.* **2017**, *29* (11), 922-927.
217. Abdellah, I.; Martini, C.; Dos Santos, A.; Dragoe, D.; Guérineau, V.; Huc, V.; Schulz, E., Calix[8]arene as New Platform for Cobalt-Salen Complexes Immobilization and Use in Hydrolytic Kinetic Resolution of Epoxides. *ChemCatChem* **2018**, *10* (20), 4761-4767.
218. Darensbourg, D. J.; Mackiewicz, R. M.; Rodgers, J. L.; Fang, C. C.; Billodeaux, D. R.; Reibenspies, J. H., Cyclohexene Oxide/CO₂ Copolymerization Catalyzed by Chromium(III) Salen Complexes and N-Methylimidazole: Effects of Varying Salen Ligand Substituents and Relative Cocatalyst Loading. *Inorg. Chem.* **2004**, *43*, 6024-6034.
219. Grimaldi, I.; Santulli, F.; Lamberti, M.; Mazzeo, M., Chromium Complexes Supported by Salen-Type Ligands for the Synthesis of Polyesters, Polycarbonates, and Their Copolymers through Chemoselective Catalysis. *Int. J. Mol. Sci.* **2023**, *24* (8), 7642-7657.
220. Teixeira, F.; Mosquera, R. A.; Melo, A.; Freire, C.; Cordeiro, M. N., Effects of axial coordination on immobilized Mn(salen) catalysts. *J. Phys. Chem. A* **2014**, *118* (45), 10788-10796.
221. Benson, M. C.; Ruther, R. E.; Gerken, J. B.; Rigsby, M. L.; Bishop, L. M.; Tan, Y.; Stahl, S. S.; Hamers, R. J., Modular "click" chemistry for electrochemically and photoelectrochemically active molecular interfaces to tin oxide surfaces. *ACS Appl. Mater. Interfaces* **2011**, *3* (8), 3110-3119.
222. Heinrich, C. D.; Reichstein, P. M.; Thelakkat, M., Synthesis, Surface Grafting, and Fabrication of Ultrathin Polymeric SAMFETs with High Field-Effect Mobility. *ACS Appl. Mater. Interfaces* **2018**, *10* (41), 35441-35448.

223. Paoprasert, P.; Spalenka, J. W.; Peterson, D. L.; Ruther, R. E.; Hamers, R. J.; Evans, P. G.; Gopalan, P., Grafting of poly(3-hexylthiophene) brushes on oxides using click chemistry. *J. Mater. Chem.* **2010**, *20* (13), 2651-2658.
224. Zheng, Y.; Wang, L.; Zheng, S., Synthesis and characterization of heptaphenyl polyhedral oligomeric silsesquioxane-capped poly(N-isopropylacrylamide)s. *Eur. Polym. J.* **2012**, *48* (5), 945-955.
225. Sharma, P.; Moses, J. E., Ethynyldiisopropylsilyl: A New Alkynylsilane Protecting Group and "Click" Linker. *Org. Lett.* **2010**, *12*, 2860-2863.
226. Yamakoshi, H.; Dodo, K.; Palonpon, A.; Ando, J.; Fujita, K.; Kawata, S.; Sodeoka, M., Alkyne-tag Raman imaging for visualization of mobile small molecules in live cells. *J. Am. Chem. Soc.* **2012**, *134* (51), 20681-20689.
227. Kaminsky, C. J.; Weng, S.; Wright, J.; Surendranath, Y., Adsorbed cobalt porphyrins act like metal surfaces in electrocatalysis. *Nat. Catal.* **2022**, *5* (5), 430-442.
228. Hanna, C. M.; Sanborn, C. D.; Ardo, S.; Yang, J. Y., Interfacial Electron Transfer of Ferrocene Immobilized onto Indium Tin Oxide through Covalent and Noncovalent Interactions. *ACS Appl. Mater. Interfaces* **2018**, *10* (15), 13211-13217.
229. Armarego, W. L. F.; Chai, C. L. L., *Purification of laboratory chemicals*. 6 ed.; Elsevier: 2009.
230. Holbach, M.; Weck, M., Modular Approach for the Development of Supported, Mono-functionalized Salen Catalysts. *J. Org. Chem.* **2006**, *71*, 1825-1836.
231. Liu, T. T.; Liang, J.; Huang, Y. B.; Cao, R., A bifunctional cationic porous organic polymer based on a Salen-(Al) metalloligand for the cycloaddition of carbon dioxide to produce cyclic carbonates. *Chem. Commun.* **2016**, *52* (90), 13288-13291.

232. Kondo, A.; Morita, N.; Ishikawa, T.; Yoshida, M.; Moriyama, A.; Wanajo, I. Pyrrolidine derivative. 2019.
233. Hettegger, H.; Sumerskii, I.; Sortino, S.; Potthast, A.; Rosenau, T., Silane meets click chemistry: towards the functionalization of wet bacterial cellulose sheets. *ChemSusChem* **2015**, *8* (4), 680-687.
234. Bazkiaei, A. R.; Wiseman, M.; Findlater, M., Iron-catalysed hydroboration of non-activated imines and nitriles: kinetic and mechanistic studies. *RSC Adv.* **2021**, *11* (25), 15284-15289.
235. Yu, Y. F.; Yuan, D.; Wang, Y. R.; Yao, Y. M., Lanthanide alkoxide complexes stabilized by a novel salen-type Schiff base ligand: Synthesis, structure, and catalysis for the polymerization of lactide. *J. Organomet. Chem.* **2016**, *819*, 37-45.
236. Lanthanides and Actinides in Molecular Magnetism. Layfield, R. A.; Murugesu, M., Eds. Wiley-VCH: 2015.
237. Blagg, R. J.; Ungur, L.; Tuna, F.; Speak, J.; Comar, P.; Collison, D.; Wernsdorfer, W.; McInnes, E. J. L.; Chibotaru, L. F.; Winpenny, R. E. P., Magnetic relaxation pathways in lanthanide single-molecule magnets. *Nat. Chem.* **2013**, *5* (8), 673-678.
238. Marin, R.; Brunet, G.; Murugesu, M., Shining New Light on Multifunctional Lanthanide Single-Molecule Magnets. *Angew. Chem. Int. Ed.* **2021**, *60* (4), 1728-1746.
239. Goldfarb, D., Gd³⁺ spin labeling for distance measurements by pulse EPR spectroscopy. *Phys. Chem. Chem. Phys.* **2014**, *16* (21), 9685-9699.
240. Budker, D.; Romalis, M., Optical magnetometry. *Nat. Phys.* **2007**, *3*, 227-234.
241. Pedersen, K. S.; Ariciu, A. M.; McAdams, S.; Weihe, H.; Bendix, J.; Tuna, F.; Piligkos, S., Toward Molecular 4f Single-Ion Magnet Qubits. *J. Am. Chem. Soc.* **2016**, *138* (18), 5801-5804.

242. Pedersen, K. S.; Dreiser, J.; Weihe, H.; Sibille, R.; Johannesen, H. V.; Sorensen, M. A.; Nielsen, B. E.; Sigrist, M.; Mutka, H.; Rols, S.; Bendix, J.; Piligkos, S., Design of Single-Molecule Magnets: Insufficiency of the Anisotropy Barrier as the Sole Criterion. *Inorg. Chem.* **2015**, *54* (15), 7600-7606.
243. Lucaccini, E.; Sorace, L.; Adelnia, F.; Sanna, S.; Arosio, P.; Mariani, M.; Carretta, S.; Salman, Z.; Borsa, F.; Lascialfari, A., NMR and μ +SR detection of unconventional spin dynamics in Er(trensal) and Dy(trensal) molecular magnets. *Phys. Rev. B.* **2019**, *100* (17).
244. Wang, H.; Gould, P. L.; Stwalley, W. C., Photoassociative spectroscopy of ultracold 39K atoms in a high-density vapor-cell magneto-optical trap. *Phys. Rev. A.* **1996**, *53*, 1216-1219.
245. Malossi, N.; Valado, M. M.; Scotto, S.; Huillery, P.; Pillet, P.; Ciampini, D.; Arimondo, E.; Morsch, O., Full counting statistics and phase diagram of a dissipative Rydberg gas. *Phys. Rev. Lett.* **2014**, *113* (2), 023006.
246. Sushkov, A. O.; Budker, D., Production of long-lived atomic vapor inside high-density buffer gas. *Phys. Rev. A.* **2008**, *77* (4).
247. Pointillart, F.; Cador, O.; Le Guennic, B.; Ouahab, L., Uncommon lanthanide ions in purely 4f Single Molecule Magnets. *Coord. Chem. Rev.* **2017**, *346*, 150-175.
248. Kaczmarek, M. T.; Zabiszak, M.; Nowak, M.; Jastrzab, R., Lanthanides: Schiff base complexes, applications in cancer diagnosis, therapy, and antibacterial activity. *Coord. Chem. Rev.* **2018**, *370*, 42-54.
249. Han, F. B.; Teng, Q. Q.; Zhang, Y.; Wang, Y. R.; Shen, Q., Influence of Schiff Base and Lanthanide Metals on the Synthesis, Stability, and Reactivity of Monoamido Lanthanide Complexes Bearing Two Schiff Bases. *Inorg. Chem.* **2011**, *50* (6), 2634-2643.

250. Long, J.; Habib, F.; Lin, P. H.; Korobkov, I.; Enright, G.; Ungur, L.; Wernsdorfer, W.; Chibotaru, L. F.; Murugesu, M., Single-molecule magnet behavior for an antiferromagnetically superexchange-coupled dinuclear dysprosium(III) complex. *J. Am. Chem. Soc.* **2011**, *133* (14), 5319-5328.
251. Ren, W. S.; Chen, L.; Zhao, N.; Wang, Q. W.; Hou, G. H.; Zi, G. F., Synthesis, structure, and catalytic activity of organolanthanide complexes with chiral biaryl Schiff-base ligands. *J. Organomet. Chem.* **2014**, *758*, 65-72.
252. Sun, O.; Chen, P.; Li, H. F.; Gao, T.; Sun, W. B.; Li, G. M.; Yan, P. F., A series of dinuclear lanthanide(III) complexes constructed from Schiff base and beta-diketonate ligands: synthesis, structure, luminescence and SMM behavior. *CrystEngComm* **2016**, *18* (24), 4627-4635.
253. Matsumoto, K.; Saito, B.; Katsuki, T., Asymmetric catalysis of metal complexes with non-planar ONNO ligands: salen, salalen and salan. *Chem. Commun.* **2007**, (35), 3619-3627.
254. Wang, J. F.; Yao, Y. M.; Zhang, Y.; Shen, Q., Bridged Bis(amidinate) Ytterbium Alkoxide and Phenoxide: Syntheses, Structures, and Their High Activity for Controlled Polymerization of L-Lactide and epsilon-Caprolactone. *Inorg. Chem.* **2009**, *48* (2), 744-751.
255. Xu, X. P.; Yao, Y. M.; Zhang, Y.; Shen, Q., Synthesis, reactivity, and structural characterization of sodium and ytterbium complexes containing new imidazolidine-bridged bis(phenolato) ligands. *Inorg. Chem.* **2007**, *46* (9), 3743-3751.
256. Lapshin, I. V.; Yurova, O. S.; Basalov, I. V.; Rad'kov, V. Y.; Musina, E. I.; Cherkasov, A. V.; Fukin, G. K.; Karasik, A. A.; Trifonov, A. A., Amido Ca and Yb(II) Complexes Coordinated by Amidine-Amidopyridinate Ligands for Catalytic Intermolecular Olefin Hydrophosphination. *Inorg. Chem.* **2018**, *57* (5), 2942-2952.

257. Abinet, E.; Spaniol, T. P.; Okuda, J., Olefin hydrosilylation catalysts based on allyl bis(phenolato) complexes of the early lanthanides. *Chem. Asian J.* **2011**, *6* (2), 389-391.
258. Kapelski, A.; Buffet, J. C.; Spaniol, T. P.; Okuda, J., Group 3 metal initiators with an [OSSO]-type bis(phenolate) ligand for the stereoselective polymerization of lactide monomers. *Chem. Asian J.* **2012**, *7* (6), 1320-1330.
259. Yang, X.; Jones, R. A.; Huang, S., Luminescent 4f and d-4f polynuclear complexes and coordination polymers with flexible salen-type ligands. *Coord. Chem. Rev.* **2014**, *273-274*, 63-75.
260. Wang, X.; Brosmer, J. L.; Thevenon, A.; Diaconescu, P. L., Highly Active Yttrium Catalysts for the Ring-Opening Polymerization of ϵ -Caprolactone and δ -Valerolactone. *Organometallics* **2015**, *34* (19), 4700-4706.
261. Broderick, E. M.; Diaconescu, P. L., Cerium(IV) catalysts for the ring-opening polymerization of lactide. *Inorg. Chem.* **2009**, *48* (11), 4701-4706.
262. Broderick, E. M.; Thuy-Boun, P. S.; Guo, N.; Vogel, C. S.; Sutter, J.; Miller, J. T.; Meyer, K.; Diaconescu, P. L., Synthesis and Characterization of Cerium and Yttrium Alkoxide Complexes Supported by Ferrocene-Based Chelating Ligands. *Inorg. Chem.* **2011**, *50* (7), 2870-2877.
263. Huang, W. L.; Brosmer, J. L.; Diaconescu, P. L., In situ synthesis of lanthanide complexes supported by a ferrocene diamide ligand: extension to redox-active lanthanide ions. *New J. Chem.* **2015**, *39* (10), 7696-7702.
264. Harriman, K. L.; Brosmer, J. L.; Ungur, L.; Diaconescu, P. L.; Murugesu, M., Pursuit of Record Breaking Energy Barriers: A Study of Magnetic Axiality in Diamide Ligated Dy(III) Single-Molecule Magnets. *J. Am. Chem. Soc.* **2017**, *139* (4), 1420-1423.

265. Deng, S.; Diaconescu, P. L., A switchable dimeric yttrium complex and its three catalytic states in ring opening polymerization. *Inorg. Chem. Front.* **2021**, (8), 2088-2096.
266. Yu, I.; Acosta-Ramirez, A.; Mehrkhodavandi, P., Mechanism of living lactide polymerization by dinuclear indium catalysts and its impact on isoselectivity. *J. Am. Chem. Soc.* **2012**, *134* (30), 12758-12773.
267. Zuccaccia, D.; Macchioni, A., An Accurate Methodology to Identify the Level of Aggregation in Solution by PGSE NMR Measurements: The Case of Half-Sandwich Diamino Ruthenium(II) Salts. *Organometallics* **2005**, *24*, 3476-3486.
268. Atzori, M.; Dhbaibi, K.; Douib, H.; Grasser, M.; Dorcet, V.; Breslavetz, I.; Paillot, K.; Cador, O.; Rikken, G.; Le Guennic, B.; Crassous, J.; Pointillart, F.; Train, C., Helicene-Based Ligands Enable Strong Magneto-Chiral Dichroism in a Chiral Ytterbium Complex. *J. Am. Chem. Soc.* **2021**, *143* (7), 2671-2675.
269. Gorczyński, A.; Marcinkowski, D.; Kubicki, M.; Löffler, M.; Korabik, M.; Karbowiak, M.; Wiśniewski, P.; Rudowicz, C.; Patroniak, V., New field-induced single ion magnets based on prolate Er(iii) and Yb(iii) ions: tuning the energy barrier U_{eff} by the choice of counterions within an N3-tridentate Schiff-base scaffold. *Inorg. Chem. Front.* **2018**, *5* (3), 605-618.
270. Kirmiz, A.; Saiki, D. J.; Augustine, M. P., Cavity ring-down observation of Yb(3+) optical absorption in room temperature solution. *Spectrochim. Acta. A Mol. Biomol. Spectrosc.* **2010**, *75* (4), 1211-1217.
271. Brunet, G.; Marin, R.; Monk, M. J.; Resch-Genger, U.; Galico, D. A.; Sigoli, F. A.; Suturina, E. A.; Hemmer, E.; Murugesu, M., Exploring the dual functionality of an ytterbium complex for luminescence thermometry and slow magnetic relaxation. *Chem. Sci.* **2019**, *10* (28), 6799-6808.

272. Buch, C. D.; Hansen, S. H.; Mitcov, D.; Tram, C. M.; Nichol, G. S.; Brechin, E. K.; Piligkos, S., Design of pure heterodinuclear lanthanoid cryptate complexes. *Chem. Sci.* **2021**, (12), 6983-6991.
273. Chen, W. B.; Zhong, L.; Zhong, Y. J.; Zhang, Y. Q.; Gao, S.; Dong, W., Understanding the near-infrared fluorescence and field-induced single-molecule-magnetic properties of dinuclear and one-dimensional-chain ytterbium complexes based on 2-hydroxy-3-methoxybenzoic acid. *Inorg. Chem. Front.* **2020**, 7 (17), 3136-3145.
274. Lefevre, B.; Gonzalez, J. F.; Gendron, F.; Dorcet, V.; Riobe, F.; Cherkasov, V.; Maury, O.; Le Guennic, B.; Cador, O.; Kuropatov, V.; Pointillart, F., Redox-Modulations of Photophysical and Single-molecule Magnet Properties in Ytterbium Complexes Involving Extended-TTF Triads. *Molecules* **2020**, 25 (3).
275. Lin, P. H.; Sun, W.; Tian, Y.; Yan, P.; Ungur, L.; Chibotaru, L. F.; Murugesu, M., Ytterbium can relax slowly too: a field-induced Yb₂ single-molecule magnet. *Dalton Trans.* **2012**, 41, 12349-12351.
276. Liu, T. Q.; Yan, P. F.; Luan, F.; Li, Y. X.; Sun, J. W.; Chen, C.; Yang, F.; Chen, H.; Zou, X. Y.; Li, G. M., Near-IR Luminescence and Field-Induced Single Molecule Magnet of Four Salen-type Ytterbium Complexes. *Inorg. Chem.* **2015**, 54 (1), 221-228.
277. Mandal, L.; Biswas, S.; Cosquer, G.; Shen, Y. B.; Yamashita, M., Anion-driven structures and SMM behavior of dinuclear terbium and ytterbium complexes. *Dalton Trans.* **2018**, 47 (48), 17493-17499.
278. Pointillart, F.; Le Guennic, B.; Golhen, S.; Cador, O.; Maury, O.; Ouahab, L., A redox-active luminescent ytterbium based single molecule magnet. *Chem. Commun.* **2013**, 49 (6), 615-617.

279. Dogaheh, S. G.; Khanmohammadi, H.; Sanudo, E. C., Double-decker luminescent ytterbium and erbium SMMs with symmetric and asymmetric Schiff base ligands. *New J. Chem.* **2017**, *41* (18), 10101-10111.
280. Evans, D. F., The Determination of the Paramagnetic Susceptibility of Substances in Solution by Nuclear Magnetic Resonance. *J. Chem. Soc.* **1959**, 2003-2005.
281. Whitelaw, M. T.; Kennedy, A. R.; Mulvey, R. E., Structural Similarity in a Series of Alkali Metal Aluminates with Heteroleptic tert-Butoxide–Isobutyl Ligand Sets. *Eur. J. Inorg. Chem.* **2020**, (30), 2912-2918.
282. Krause, L.; Herbst-Irmer, R.; Sheldrick, G. M.; Stalke, D., Comparison of silver and molybdenum microfocus X-ray sources for single-crystal structure determination. *J. Appl. Crystallogr.* **2015**, *48* (Pt 1), 3-10.
283. Dolomanov, O. V.; Bourhis, L. J.; Gildea, R. J.; Howard, J. A. K.; Puschmann, H., OLEX2: a complete structure solution, refinement and analysis program. *J. Appl. Crystallogr.* **2009**, *42* (2), 339-341.
284. Sheldrick, G., Crystal structure refinement with SHELXL. *Acta Crystallogr. C* **2015**, *71* (1), 3-8.
285. Sheldrick, G., SHELXT - Integrated space-group and crystal-structure determination. *Acta Crystallogr. A* **2015**, *71* (1), 3-8.